THE UNIVERSITY *of* EDINBURGH

Physics of Bacterial Microcolonies

Dario Dell'Arciprete
(matr.: s1066624)

Thesis submitted in fulfilment of the requirements
for the degree of Doctor of Philosophy
to The University of Edinburgh

Abstract

The growth of bacterial colonies is a very ubiquitous phenomenon occurring in nature and observed in the laboratories. However, there is a limited knowledge on how at the microscopic level these colonies develop and the individual cells spatially organize.

In this thesis, we experimentally investigate the physics of growing microcolonies at the level of the individual *Escherichia coli* (*E. coli*) cells, focussing on the order-disorder evolution and the understanding of it in the context of active matter. Bacterial cells are indeed constantly transducing energy from the environment to move and grow, therefore they behave as active microscopic units, defining an inherently far from equilibrium system.

In Part I, we present a brief summary of passive liquid crystals that provide us with some basic concepts and tools for investigating the bacterial microcolony evolution. Then an overview of the biology of *E. coli* cell is given, both as part of multicellular structures (biofilm) and as individuals. Active matter is then discussed along with some examples of active nematics. This first part ends with the materials and methods used in the experiments and analysis.

In Part II, we provide our experimental results on the study of growing bacterial microcolonies as active nematics. We describe the way a bacterial microcolony evolves from the first mother cell into a layer of hundreds of cells, and we study the global and local orientational order. We find that a transition from an anisotropic to an isotropic phase occurs as the colony increases and that instabilities and topological defects develop, in analogy to the case of an active nematic. We also compare the real system with simulated ones by investigating (*i*) the case of equilibrated configurations with respect to experimental nonequilibrium ones, and (*ii*) long-time behaviour of nonequilibrium analogues.

In Part III, we discuss the buckling of bacterial microcolonies, that is, the transition from a 2D layer of cells to a 3D structure. We investigate the link between the buckling event and the presence of topological defects in the nematic map of the bacterial microcolony, finding that the buckling sites tend to be closer to topological defects with a negative charge. Later, we present some results of buckling in microcolonies composed of mutants lacking some appendages that play a role in the motion in and attachment to the surrounding environment, finding that buckling occurs at earlier times in the case of these mutants than the wild type.

The aim of this work is to show that a growing bacterial microcolony is an interesting model of active matter to experiment on, and that the investigation tools developed for the study of liquid crystals can be useful for describing the evolution of these living systems in mechanistic terms, and for improving the current understanding of nonequilibrium phenomena.

Lay Summary

The formation of a bacterial colony is a phenomenon that has attracted the interest of biologists for many reasons, for instance, the possibility to study its genetic evolution, the way cells communicate with each other, the role played in ecology and in human health. However, our current knowledge of this phenomenon at the microscopic level - that is, how the single cells spatially organize with each other - is limited.

Here we present our work on the growth of *Escherichia coli* bacterial colonies that are imaged under a microscope from the first mother cell to hundreds of daughter cells, resulting in a 2D cell layer that eventually buckles. To interpret their evolution in physical terms, that is, as *living* particles, we establish an analogy with 2D liquid crystals, that is, materials made up of elongated particles – as a model of our pill-shaped bacteria - whose spatial organization/orientation and interaction determine their properties that are between those of crystalline solids and liquids. There is however as a remarkable as evident difference between cells and molecules: bacteria can grow, reproduce and hence move without any external action, by contrast to passive molecules whose dynamics is determined by external applied fields or space constraints. This behaviour of our active particles contributes to a richer dynamics than that of passive liquid crystals.

We show here that a growing bacterial microcolony is an interesting system to experiment on, not only for biologists but for physicists as well, that can be used as a system to test models of nonequilibrium phenomena.

Declaration

I hereby declare that the work presented in this thesis is my own except where otherwise stated. This work has not been submitted for any other degree or professional qualification.

Dario Dell'Arciprete, ...
April 15, 2016

Acknowledgements

I would like to thank Professor Wilson C. K. Poon for his assistance and guidance during my PhD, and EPSRC for providing funds.

I wish also to thank all the people who helped me with the experiments when things were not working as supposed, and those who made clear modelling aspects: Drs Diarmuid P. Lloyd, Davide Marenduzzo, Angela Dawson, Matthew L. Blow, Aidan T. Brown, Jochen Arlt, Vincent A. Martinez, Fred C. D. Farrell, Ottavio A. Croze, Juho Lintuvuori, Bartlomiej Waclaw, Jana Schwarz-Linek, Alexander F. McVey, Dana Vladescu, Alys K. Jepson.

A big thank you to all the people who provided distractions when needed: Giovanni, Nadia, Viviana, Francesca, Alberto, Alex, Giulia, Adriano, Matt, Alys, Laura, Kuba, Elena, Gavin, Martina, Oliver.

Finally, thanks to my family for their unconditional support and ineffable love.

Contents

List of Figures

Chapter 0

Introduction

Active matter is a relatively recent interdisciplinary research field, which brings together scientists from physics, chemistry, and biology. The distinguishing characteristic of the elementary constituents of active systems with respect to passive ones is their capability to use energy, that is, to dissipate it into and to harvest it from the surrounding environment, in order to perform motion or to transform themselves [1].

The experimental, theoretical and numerical investigation of these systems poses big challenges due to their complexity, in terms of the kind of interactions existing between their fundamental units, the wide range of relevant length, time and energy scales. Despite this complexity, active systems show interesting novel properties that make them worth studying, like (*i*) emergent structures from collective behaviour (pattern formation), (*ii*) novel fluctuations such as in number density, (*iii*) order-disorder transition in absence of external fields, (*iv*) unusual mechanical and rheological properties. The variety of systems that fall in this group is very large, including active colloids (*e.g.* Janus particles), biopolymer solutions, amphiphilic systems, membranes and swimming microorganisms [1].

Living systems, from the individual bacterial cell to multicellular organisms, can be interpreted as examples of active matter, with properties such as spontaneous motion, dynamical organization, adaptation and reproduction [2]. Because of the large number of variables that define the state of a cell, we do not have at the moment a theoretical description of the general properties of such living matter. For instance, in a higher multicellular organism like a human, it is possible to find many different types of cell (about 300) and the behaviour of

each cell is affected by many internal and external signals, making the parameter space very large. However, global principles - such as symmetries - constrain the possible dynamical behaviour of cells or even of populations of cells, such as collections of bacteria, fish schools, and bird flocks [3]. Trying to quantify the spontaneous dynamical organization and motion of living systems could help in gaining a better understanding of how these active units respond to these principles, and could also give insights about fundamental biological processes and their mechanistic interpretation.

In this thesis, we investigate an active system represented by a growing colony of bacteria that expands from the first mother cell to hundreds of offspring in a 2D layer. We propose a description of this living system as a new kind of active nematic crystal, that is, as a nonequilibrium anisotropic fluid composed of internally driven elongated units that can grow and reproduce. We focus on (i) the study of the orientational order-disorder transition that corresponds to the change from the anisotropic to the isotropic phase, and on (ii) the buckling of the colony, that is, the abrupt event during which cells move from the layer within which they initially developed into the vertical direction.

In Part I of the thesis, we present the background.

In Chapter 1, to provide background for describing bacterial microcolonies as active liquid crystals, we begin by reviewing some basic aspects of the physics of passive liquid crystals. After having defined liquid crystals, we discuss the isotropic-nematic transition. We then restrict our interest to 2D nematics and conclude this first chapter by describing the deformations and the topological defects that arise in passive nematics due to external fields or boundary conditions.

We move then to Chapter 2 where we discuss biological aspects and introduce the actor of the experiments, that is, the bacterial cell. We provide general information about the role played by bacteria in nature, and then move to smaller systems like communities of bacterial cells in a sessile state, also known as biofilms. Finally, going to even smaller scales, the structure of the single individual cell (with focus on the *E. coli* species) is reviewed, and we discuss methods for genetic manipulation.

Chapter 3 is concerned with active matter, and introduces the point of view

that we adopt for interpreting growing bacterial colonies. First, we give some examples of active matter found in nature that can be studied in the laboratory. Next we restrict our attention to active particles, distinguishing between polar and apolar, extensile and contractile cases, and the occurrence of instabilities in terms of splay and bend that origin from active internal stress. We conclude by discussing some relevant recent works on systems that share some characteristics with ours.

We conclude Part I with Chapter 4, describing the experimental methods we followed, from the initial cultivation of bacterial cells, the ensuing preparation of the sample, and the final imaging techniques - that is, phase contrast microscopy - for recording the time-lapse movies. Furthermore, we discuss the image analysis done to extract basic information (such as position, orientation and dimensions of cells as the system evolves) necessary to derive the results shown in later chapters.

In Part II, we present our experimental results and comparison with simulated systems of bacterial colonies.

In Chapter 5, we begin from the phenomenology of a growing microcolony and then investigate quantitatively the global and local properties of this active system during its transition from orientational order to disorder. This study is based on a liquid crystal approach whereby we study global nematic order parameters, orientational correlation functions, which provide information about the orientational state and its evolution as the colony grows. Instabilities occurring in the living nematics are discussed as well as the emergence of topological defects and their dynamics.

In Chapter 6, we provide an analysis of simulations of 2D bacterial colonies growing onto a substrate. We start by considering the equilibrated case of our active nematics, that is, starting from the same configurations as those of the real colonies for a given number of cells, *in silico* colonies are equilibrated - *via* a Monte Carlo algorithm - so to investigate the differences in the final orientational configurations with respect to the experimental cases (discussed in Chapter 5). Then, we consider the long time behaviour of nonequilibrium *in silico* colony, where we compare the simulated results for the global order and local arrangement with the experimental ones. This allows us to assess what are the basic features of the system in terms of the interactions to take into account to describe it. Finally, we focus on the description of the evolution of cell orientation at the

boundary by introducing a model.

Note that defects play a key role in this work. This is not surprising, because defects are a defining feature of passive liquid crystals[1], but the concept is not restricted only to them. They are indeed studied in other contexts, much different in terms of spatial scale and kind of interactions, like cosmology. This is because defects are a universal feature in systems of broken symmetry, and cosmologists have used the theory of liquid crystals developed by condensed matter scientists to explore the defect evolution of the early universe, contributing later on to the study of defect creation and dynamics in liquid crystals.

In the case of nematics, there exists a unique high symmetry phase, that is the isotropic phase that is invariant under the symmetry group of all rigid rotations (called SO(3)). When a phase transition from the isotropic to the nematic phase occurs, the symmetry is reduced, the simplest nematic being uniaxially symmetric. Since the axis of symmetry is arbitrary, there is an entire set of free energy minima that the system can choose. This corresponds to rapidly cooling down or compressing the isotropic phase into the nematic one, so that nucleation of nematic domains would occur, each one with its own main direction. During this phase it might occur that three domains meet along a line or a point (3D and 2D respectively), along or around which a unique direction of the molecules cannot be determined: that is where a defect is located.

In the case of cosmology, the symmetries are purely internal, being related to some characteristics of the elementary particles, for instance the weak isospin and the colour degrees of freedom, for weak and strong interactions respectively. The group of symmetry is here the group of the standard model that has a more complicated structure than then group of all rotations SO(3). The state that is invariant under this group is the particle-free state of lowest energy (the vacuum), as the isotropic liquid crystal is invariant under rotations.

While the phase transition temperatures in liquid crystals are observed between 240 and 400 K, in particle theory they are predicted to be about 10^{15} GeV $\approx 10^{28}$ K, hence they are so high that they cannot be observed in experiments, but were accessible only in the first instants of the Big Bang, that is, during the first 10^{-35} s of the age of the universe. Hence, in analogy to the cooling of

[1]The simplest kind of liquid crystal that shows uniaxial symmetry is actually named after its defect lines, that is, the dark threads $\nu\eta\mu\alpha\tau\alpha$, that is, nematics.

liquid crystals, cosmologists proposed that, when the cosmos expanded, it started cooling down and experienced the symmetry breaking phase transitions, which finally led to the creation of defects, called *cosmic strings* [4].

In Part III, we focus on the buckling events in the microcolonies, that is, the process whereby cells move outside the 2D layer and explore the third dimension.

In Chapter 7, we investigate a possible connection between the buckling event in bacterial microcolonies and the presence of defects. After describing the observed buckling in our colonies and in other systems, we discuss a simple explanation of the reason some types of topological defects can be related to the buckling site, based on energetic consideration. We conclude by showing some experimental evidence on this buckling site-defects position relation.

In Chapter 8, we discuss our work on the buckling of microcolonies formed by mutants (compared to the wild type case) of *E. coli* bacteria. More specifically, growing colonies of genetically manipulated strains unable to produce appendages used for their motion and interaction with surfaces (that is, flagella and fimbriae) are imaged in order to explore the dependence of the buckling event on the mechanical interactions determined by these appendages, finding that buckling occurs at earlier stage for mutants with respect to the wild type case.

In Chapter 9, we draw conclusions from our work and discuss some other possible experiments for future investigations.

In Chapter A, we provide details of the protocols followed for growing cells and constructing mutants.

Notice to the reader: In the electronic format of the thesis, clickable blue words can be found, redirecting to the glossary; clickable purple-coloured words link to resources on the Internet.

Part I

Background

Chapter 1

Liquid Crystals

This thesis is about understanding bacterial microcolonies as active liquid crystals. For this reason, we first review the physics of passive liquid crystals. This chapter is structured as follows: after the definition and classification of liquid crystals, we discuss the theory proposed by Onsager for describing the isotropic-nematic (IN) transition; we then restrict our attention to 2D nematics and discuss some more recent theoretical and numerical developments that will be useful for later comparison with our system. We move on to describing the continuous deformations occurring in nematics as splay and bends, and conclude with singularities of the nematics field, that is, topological defects.

1.1 What is a liquid crystal?

A liquid crystal (LC) is an intermediate state of aggregation of matter, which shares some mechanical and symmetry properties common to crystalline solids and amorphous liquids [5]. A material existing in such mesophase[1] is both strongly anisotropic in some of its properties and yet exhibits some degree of fluidity. The transition through a mesophase may be caused by changing temperature or by changing solvency - the former case corresponds to thermotropic mesomorphism, the latter to lyotropic mesomorphism.

The investigation of LCs started around 1920 with the works of Friedel [6], and nowadays a myriad of organic compounds are known to form LCs,

[1] LCs are indeed also referred to as mesomorphic phases: *meso* stands for intermediate, *morpho* for form.

finding applications in many contexts, with the most known case being display technology. To better understand what LC is, it is helpful to recall the way a solid and a liquid can be distinguished from each other in terms of their molecular structure, that is, the way their components are spatially organized.

In the case of a solid crystal, the constituent components (either molecules, or group of molecules) are regularly stacked, so that their centres of gravity are located on average on a 3D periodic lattice, characterized by a triplet of basis vectors $\{\mathbf{a}_i\}_{i=1}^3$. If we consider a pattern of molecules located at a point $\mathbf{x}_0$, then the probability of finding an equivalent pattern at point $\mathbf{x} = \mathbf{x}_0 + n_i\mathbf{a}_i, n_i \in \mathbb{N}$ stays finite as $|\mathbf{x} - \mathbf{x}_0| \to \infty$. This can summarized with the following equation:

$$\lim_{|\mathbf{x}-\mathbf{x}'|\to\infty} \langle\rho(\mathbf{x})\rho(\mathbf{x}')\rangle = F(\mathbf{x} - \mathbf{x}')\,, \tag{1.1}$$

where the quantity $\langle\rho(\mathbf{x})\rho(\mathbf{x}')\rangle$ is the density-density correlation function, and $F(\mathbf{x} - \mathbf{x}')$ is a periodic function of the basis vectors, and $\langle\ldots\rangle$ denotes thermal averaging.

In the case of an isotropic liquid, it is not possible to express such probability, except through the average particle density $\bar{\rho}$:

$$\lim_{|\mathbf{x}-\mathbf{x}'|\to\infty} \langle\rho(\mathbf{x})\rho(\mathbf{x}')\rangle \approx \bar{\rho}^2\,. \tag{1.2}$$

An isotropic length scale ξ over which correlations are lost can thus be identified:

$$\frac{\langle\rho(\mathbf{x})\rho(\mathbf{x}')\rangle - \bar{\rho}^2}{\bar{\rho}^2} \sim \exp(-|\mathbf{x} - \mathbf{x}'|/\xi)\,, \tag{1.3}$$

except near criticality where correlations diverge instead.

In the case of a LC, liquid-like disorder exists at least in one spatial direction and, at the same time, some degree of order is also present in the other directions. This anisotropy can correspond, for instance, to the density-density correlation function being dependent both on the modulus $|\mathbf{x}-\mathbf{x}'|$ but also on the orientation of $\mathbf{x} - \mathbf{x}'$ with respect to macroscopically defined axes. The situation is summarized schematically in figure 1.1.

Taking into account such general definition, a further distinction among LCs can be made:

- LCs with no positional order and an anisotropic orientational correlation

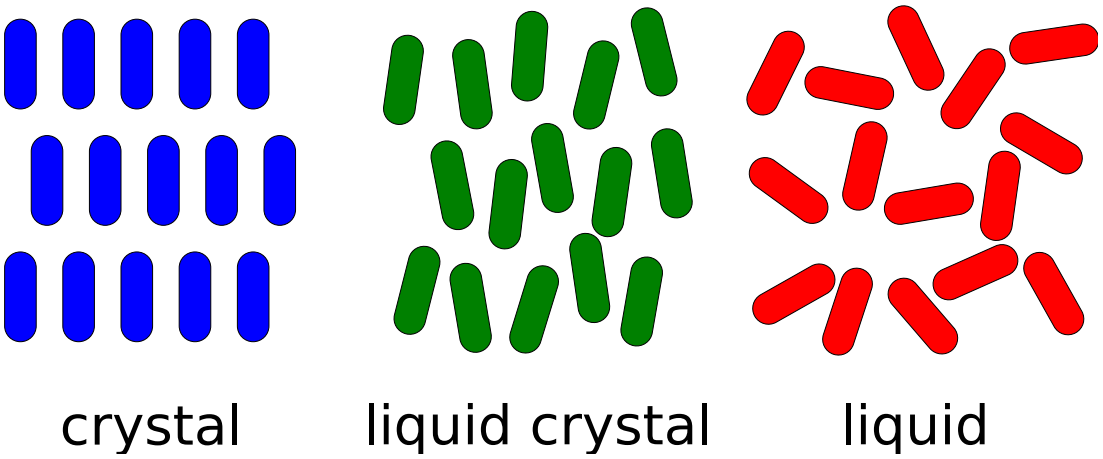

Figure 1.1: Sketch of the molecular structure for a crystalline solid, a liquid crystal, and a liquid. Note the loss of orientational and positional order when moving from solid to liquid: in the intermediate phase of nematics, we still have some orientational order.

function are called nematics. In this case, two length scales ξ_{para} and ξ_{ortho} (considering the alignment of molecules being parallel and orthogonal to a macroscopically defined direction) over which positional correlation decay can be identified;

- LCs formed as a set of 2D liquid layers stacked on each other with a well defined spacing. These kinds of LCs are called smectics;
- LCs which can be viewed as a set of nematic layers stacked on each other with a well defined spacing and a chiral centre. Hence, moving along the normal to the stack, these nematic layers looks twisted of a given (constant) angle. These kinds of LCs are called cholesterics or chiral nematics;
- LCs that can be represented as a 2D array of liquid tubes, and they are called columnar phases.

In figure 1.2, a visual representation of the first three kinds of LCs is provided.

In the following sections, we will focus on the first, simplest example of a LC, that is, the nematic, as this is going to be the reference passive system for the bacterial microcolonies presented in later chapters.

The type of LC structure adopted depends on the molecular structure. Nematics and smectics are often made up of elongated particles, whereas some

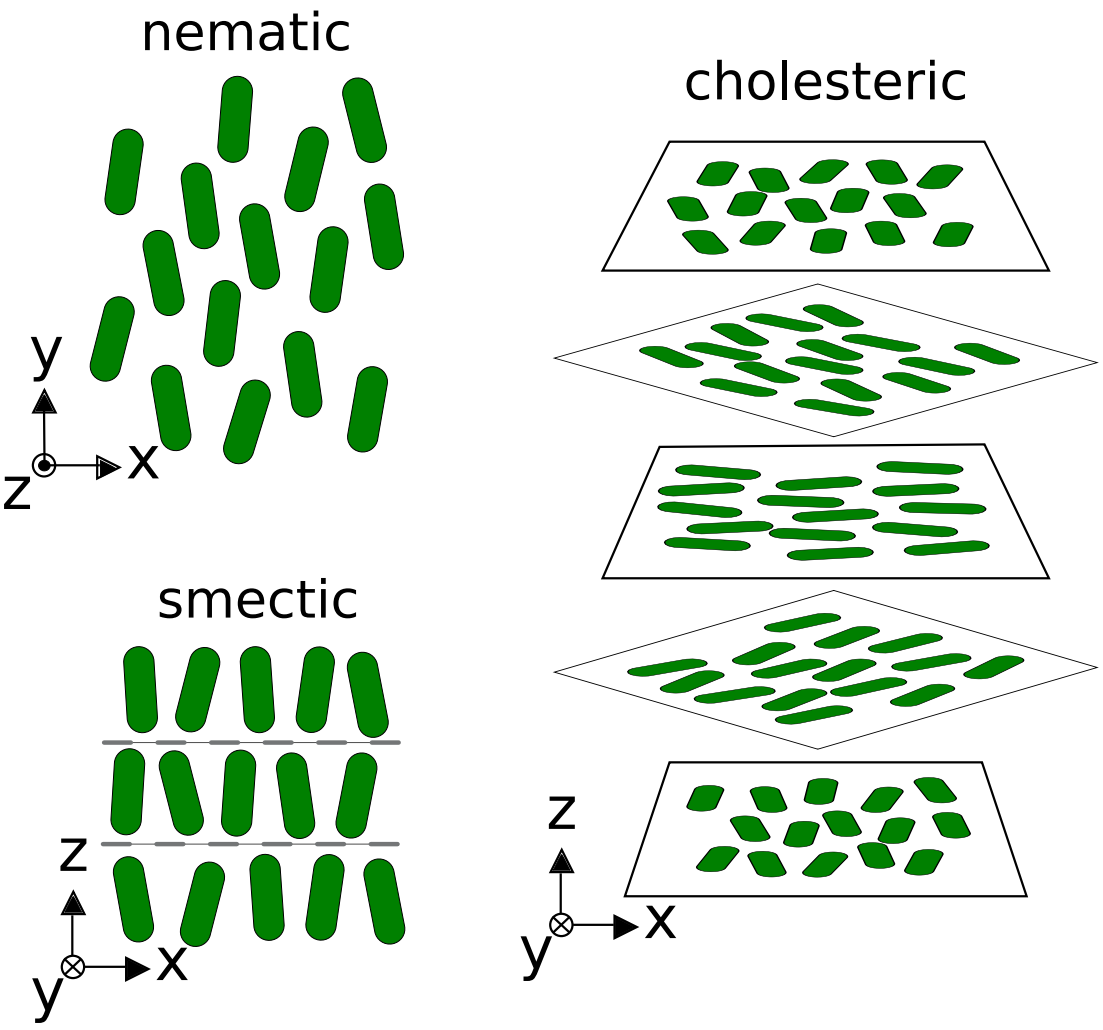

Figure 1.2: Schematics of three of the most common liquid crystalline structures, that is nematics, smectics, and cholesterics.

other nematics and most columnar phases are often made up of disk-like particles. Varying particle shape and external parameters (*e.g.* temperature, solvent, electric field, etc.) can give rise to a wide variety of phenomena and transitions among LCs. On the other hand, each type of phenomenon can be generated using many different realizations of the same basic building blocks. Thus, rods for nematics can be small organic molecules with either a rod-like or disk-like shape, long helical natural or artificial rods, polymers, etc.

As we will see in more detail in the following chapters, *E. coli* bacteria could represent the building block of a novel version of a LC. These bacteria have a rod-like shape (more properly a spherocylindrical shape) and could be thought

as the nematogens of our system.

1.1.1 Symmetries in nematics

The classification of mesophases is based on their translational and orientational symmetry properties. Here, we focus on nematics[2] that display the following features:

1. The centres of gravity of the constituent particles have no long-range positional order. This means that the correlations in position between the centres of gravity of neighbouring particles are similar to those existing in a conventional liquid, aside from the anisotropy in the lengths ξ_{para} and ξ_{ortho} (1.3);

2. By contrast, there is some degree of order in the direction of the particles, that is, an orientational order. They tend to be parallel to some common axis, which is identified by a unit vector, called the director $\mathbf{n}$;

3. The direction of $\mathbf{n}$ is arbitrary in space. In practice, it is imposed by some forces (*e.g.* the boundary conditions of the container walls). This is a situation of broken rotational symmetry; [3]

4. The states $\mathbf{n}$ and $-\mathbf{n}$ of the director are indistinguishable, that is, there is no head-tail distinction for the nematogens, which are therefore apolar.

In summary, nematics are characterized by long-range orientational order and either no (or only short range) positional order. However, there are examples of polar nematics, which are locally nematics but globally polar [7, 8].

1.2 Passive nematics

We now focus on nematics. From previous sections, we learnt that nematics are characterized by anisotropic short-range positional order and long-range

[2] *Nema* is the Greek for thread. Notice that the reference is not to the shape of the elongated molecules they are made up of, but to the thread-like defects that are commonly observed in these materials (G. Friedel gave them the name [6]). These defects are also called disclinations, in analogy to dislocations in solid crystals. We will discuss them in the next paragraphs.

[3] A situation that is reminiscent of a Heisenberg ferromagnet where all the spins tend to be parallel, but where the energy is independent of the direction of the total moment.

orientational order. Thus, when compared to isotropic liquid, they display a lower symmetry, or, in other words, they are more ordered. Now we present ways to quantify such order, along with some models for describing the order-disorder transition.

1.2.1 Quantifying order

The solid-nematic phase transition is characterized by the breakdown of the positional order of the molecules in a regular lattice, but not of the orientational order. Hence, the nematic is liquid-like but not isotropic because of the ability of molecules to slide over one another while still preserving their relative orientation [5, 9].

The aim is then to quantify such change in the order within the LC. In the following subsections, we introduce some quantities for this purpose. As we will see in later chapters, these quantities will remain useful in the understanding of order in bacterial colonies.

The scalar order parameter

The simplest way to quantify order in a nematic is by using a scalar order parameter, which is non-zero in the nematic phase (usually defined to be unity in the full orientationally ordered state), and which vanishes in the isotropic one.

The nematic can be modelled by rigid rods. The axis of each individual rod can be labelled by a unit vector $\mathbf{a}$, whereas the direction of the nematic axis $\mathbf{n}$, that is, the average direction of alignment of the rods, can be taken as the z-axis of the laboratory frame. The rods are assumed to have a complete cylindrical symmetry about $\mathbf{a}$. With θ and ϕ being the polar and azimuthal angles of $\mathbf{a}$ respectively, it holds that

$$\mathbf{a} = (a_x, a_y, a_z) = (\sin(\theta)\cos(\phi), \sin(\theta)\sin(\phi), \cos(\theta))\,. \tag{1.4}$$

A distribution function $f(\theta, \phi)$ can be used to describe the state of alignment of the rods, giving the probability of finding some rods in a small solid angle $d\Omega = \sin(\theta)d\theta d\phi$ around the direction defined by (θ, ϕ). Because of the cylindrical symmetry along the axis of $\mathbf{n}$, the function f depends actually only on the θ angle: $f(\theta, \phi) = f(\theta)$. Furthermore, because of the equivalence of the system

when viewed along the $\mathbf{n}$ and $-\mathbf{n}$ directions, we have that the function f is also π-periodic: $f(\theta) = f(\pi - \theta)$. The function f takes large values around $\theta = 0$ or π (which is the direction of $\mathbf{n}$), and small values around $\theta = \pi/2$. A possible behaviour of the function f is given in figure 1.3.

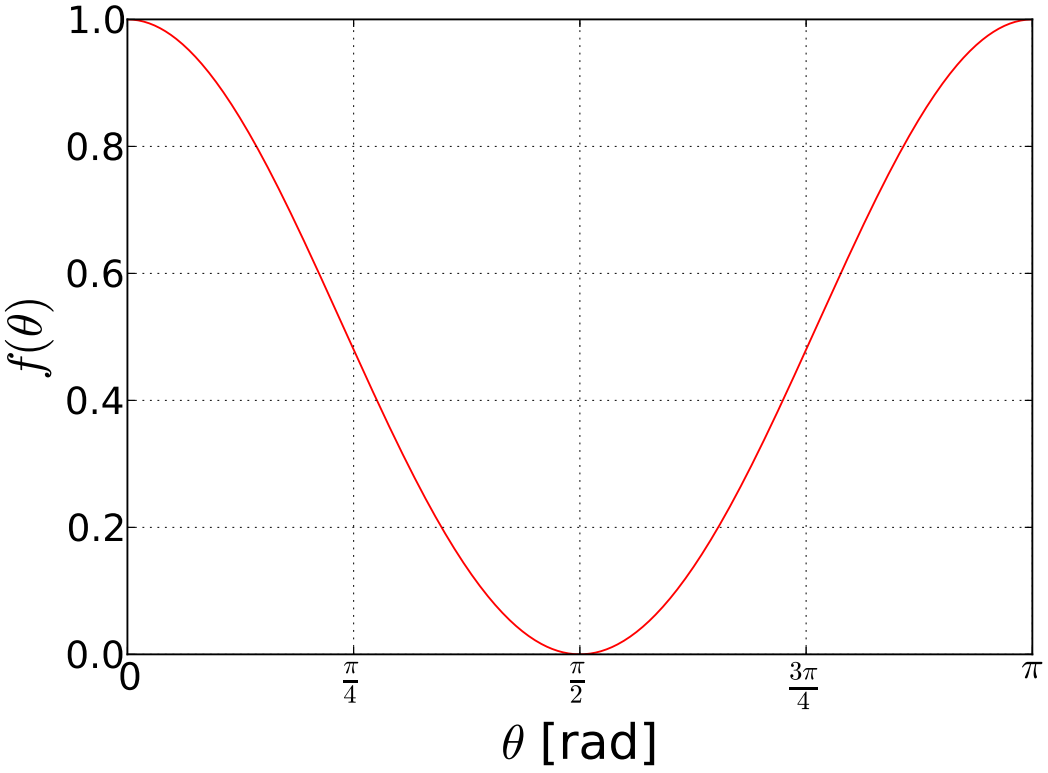

Figure 1.3: Orientational distribution function $f(\theta)$ for a nematic, rescaled between the values 0 and 1.

The function f can represent all the orientations of the nematogens (it is the continuous representation of an orientation histogram for a large number of rods), but it would be preferable to work with a single numerical parameter, that is a scalar, related to this distribution. For instance, a first idea could be to consider the average of all the projections of the directions of the nematogens on the director:

$$\langle \cos(\theta) \rangle_{\text{all rods}} = \langle \mathbf{a} \cdot \mathbf{n} \rangle_{\text{all rods}} = \frac{\int_\Omega f(\theta) \cos(\theta) d\Omega}{\int_\Omega f(\theta) d\Omega}, \tag{1.5}$$

but this quantity vanishes identically as a result of the π-periodicity of f, which

physically means that there is no average dipole. What we can do is to move to higher multipoles, and the first one returning a nontrivial quantity is the averaged quadrupole $\cos^2(\theta)$.[4] The mean value of the quadrupole for a uniform distribution f (which would correspond to a system at high temperature, that is when the particles are oriented randomly) equals $1/3$, whereas when the temperature of the system goes to zero (which correspond to a situation where all the particles are oriented along the director), the $\cos^2(\theta)$ goes to 1, and so the same occurs to the mean. Finally, if $f(\theta)$ was peaked around $\theta = \pi/2$, then the particles would be aligned perpendicularly with respect to the director, and the average quadrupole would vanish. Once rescaled in a suitable way, the order parameter can be defined as follows:

$$Q = \tfrac{3}{2}\left\langle \cos^2(\theta) - \tfrac{1}{3} \right\rangle \in [0,1]\,, \quad \text{3D}\,. \tag{1.6}$$

Thus, for a completely ordered system, $Q = 1$, whereas for a randomly oriented one $Q = 0$. This result holds for 3D systems, and for 2D system it is slightly different as the integration is performed only on θ, the formula being now:

$$Q = 2\left\langle \cos^2(\theta) - 1 \right\rangle \in [0,1]\,, \quad \text{2D}\,. \tag{1.7}$$

The tensorial order parameter

A compact way to describe a nematic in terms of its isotropic-nematic transition and its order degree is to use a tensorial - instead of a scalar - order parameter. The tensorial order parameter is represented by a traceless and symmetric matrix Q:

$$Q_{\alpha\beta} = Q(n_\alpha n_\beta - \tfrac{1}{3}\delta_{\alpha\beta})\,, \quad \alpha,\beta = (x,y,z)\,, \tag{1.8}$$

that, once diagonalized, returns the scalar order parameter Q introduced earlier as the largest eigenvalue, and the director $\mathbf{n}$ as the eigenvector corresponding to such largest eigenvalue; $\delta_{\alpha\beta}$ is the Kronecker delta, for which $\delta_{\alpha\beta} = 1$ if $\alpha = \beta$, 0 otherwise.

[4] Actually, because of the π-periodicity, all the odd moments of the distribution $f(\theta)$ vanish, whereas all the even moments are non-zero and give information about the ordering of the system.

1.2.2 Nematic-Isotropic transition

In this subsection, we give a concise view of the Onsager theory, as the first example of description of the nematic-isotropic transition. We move then on describing some more recent developments in the theory and numerics, restricting our attention to the 2D case.

Onsager model

Onsager developed a theory for explaining the isotropic-nematic transition [10] in a lyotropic[5] LC consisting of hard rods without any forces between them other than the one preventing their interpenetration, that is, only steric repulsion. At low densities, the rods are free to assume all orientations and the system would be in an isotropic state. However, as the density is increased, the rods will find more difficult to assume a random orientation because of the loss of free space where they can re-orient. Hence, intuition suggests that this system should experience a transition from an isotropic to a more ordered anisotropic phase having axial symmetry.

The mathematical calculations are rather complex and based on an exact density expansion for the free energy, which, even in the lowest order, leads to a non-linear integral equation. Because of the difficulty in dealing with this equation, the series is usually truncated after the linear term, implying that the theory is satisfactory only in the limit of very long rods. This hypothesis is evidently inapplicable in our case as the aspect ratio for a bacterium ranges from 3 to 6 (value just after and just before division, respectively). It is however instructive to show how the model describes the isotropic-nematic transition, based simply on increasing the density of particles. In the next section, we will discuss the case of short hard rods in 2D case, which is the simplest possible passive analogue of our active experimental system.

To understand the model proposed by Onsager, it is useful to start from a simpler one made up of hard spheres, where the transition to a crystalline phase is driven by an effective repulsion of entropic origin arising from the effect of excluded volume [11]. We recall first the entropy per atom S_{id} for a perfect gas:

$$S_{\mathrm{id}} = k_{\mathrm{B}} \ln(aV/N)\,, \tag{1.9}$$

[5]From the Greek *lyein*, which stands for to loose, dissolve, set free.

where a is a constant, V the volume of the whole system, and N the number of atoms. If we assign a finite volume b to each atom, then the volume accessible for any given atom is reduced to $V - Nb$, so the entropy changes to

$$\begin{aligned} S &= k_{\mathrm{B}} \ln(a(V - Nb)/N) \\ &= S_{\mathrm{id}} + k_{\mathrm{B}} \ln(1 - bN/V) \\ &\approx S_{\mathrm{id}} - k_{\mathrm{B}}(N/V)b\,. \end{aligned} \tag{1.10}$$

In the last line, the logarithm was expanded assuming a small atom volume fraction. Hence, the corresponding free energy per atom is given by

$$\begin{aligned} F &= F_{\mathrm{id}} + k_{\mathrm{B}}T(N/V)b \\ &= F_0 + k_{\mathrm{B}}T \ln(c) + k_{\mathrm{B}}T c\, b\,, \end{aligned} \tag{1.11}$$

where $c = N/V$ is the concentration of atoms. These results hold in the case of hard spheres.

Onsager developed the anisotropic analogue of the sphere-based system by considering rods. The assumptions are that: (i) the only forces of importance correspond to steric repulsion, in other words the rods cannot penetrate each other;[6] (ii) the volume fraction $\phi = \pi(D/2)^2 L\, c$, where c is the number density of the rods, is much smaller than unity: $\Phi \ll 1$; (iii) the rods are very long, that is $L \gg D$. As it is shown later, since the values of ϕ of interest near the isotropic-nematic transition are such that $\phi L/D \sim 4$, the last two assumptions are related each other.

In the case of hard rods, we have to take into account the fact that rods are elongated, so there is a degree of alignment among them. This degree of alignment can be described by an orientation distribution function $f(\theta)$. First, we have to introduce a new term in eq. (1.11) that accounts for the loss of orientational entropy, given by $\Delta S = -k_{\mathrm{B}} \int f(\theta) \ln(4\pi f(\theta)) d\Omega$. Second, the excluded volume now becomes a function of the degree of orientation: as the degree of alignment increases, the excluded volume decreases. Hence, the third term in the last line of eq. (1.11) changes to $k_{\mathrm{B}}T c\, L^2 D p[f(\theta)]$, where L and D are the length and the width of the rod, respectively, and $p[f(\theta)]$ is the average value of the orientation

[6] The repulsive Coulombic interaction can be included as well with the only effect of increasing the effective size of the rods.

distribution function for two rods that form an angle γ with each other:

$$p[f(\theta)] = \int f(\theta) f(\theta') \sin(\gamma) d\Omega d\Omega' \,, \tag{1.12}$$

Considering now the volume fraction of the rods $\phi = c\,\pi(D/2)^2 L$ and including some constants in the term F_0 in eq. (1.11), we can write the free energy for a system of hard rods as:

$$F = F_0' + k_{\mathrm{B}}T \left[\ln\left(\tfrac{L}{D}\phi\right) + \int f(\theta) \ln\left(4\pi f(\theta)\right) d\Omega + \tfrac{4}{\pi}\tfrac{L}{D}\phi\, p[f(\theta)] \right] . \tag{1.13}$$

In order to find the stable states, it is possible to minimize the free energy in eq. (1.13) by computing its functional derivative with respect to $f(\theta)$ and setting it equal to zero [5]. However, a simpler approach is to consider an approximate solution by assuming a trial function for the distribution $f(\theta)$, and then by minimizing the free energy with respect to a parameter present in the trial function. A possible form would be:

$$f(\theta) \propto \cosh(\alpha \cos(\theta)) \,, \tag{1.14}$$

where α is the parameter that controls the degree of orientation. For $\alpha = 0$ the distribution is uniform: $f = 1/(4\pi)$. However, as it increases, the function develops peaks around the directions $\theta = 0, \pi$ (head-tail symmetry), returning shapes similar to that shown in figure 1.3. These correspond to the anisotropic solutions, that is, the nematic phase.

Therefore, as the degree of order increases, there is an increase in the free energy contribution associated with the loss of orientational entropy, but there is a decrease in the free energy contribution arising from the excluded volume interactions, the relative importance of the two depending on the quantity $\phi L/D$. Hence, as the volume fraction of the rods ϕ increases or as the rods become more elongated, the excluded volume term becomes more important, eventually leading to a phase transition into the nematic state.

For low values of the product $\phi L/D$, the minimum free energy state occurs for a null order parameter $Q = 0$ (as defined in eq. (1.6)), that is, the equilibrium phase is isotropic. However, as the ratio is increased, a minimum appears in the free energy for non-zero values of the order parameter, that is, a nematic phase

is reached.

2D geometry models and particle shape

The Onsager model just presented shows that a 3D system of long hard particles can exhibit an orientationally ordered phase as the density increases and reaches sufficiently high values [10]. More recent theoretical and numerical works focussed on the phase behaviour of 2D hard rod fluids. For instance, Monte Carlo (MC) simulations were used to study the phases of 2D hard rod fluids consisting of spherocylinders in a range of aspect ratio, and confined to lie in a plane [12]. More precisely, because of 2D geometry, the researchers were actually simulating discorectangular particles. The phase behaviour was investigated as a function of the aspect ratio L/D of the particles, where L is the length of the rectangle and D is the width of the rectangle and the diameter of the two half caps attached at the two ends. The range considered was from $L/D \approx 0$ to $L/D \gg 1$ (that is, the thin hard needle limit).

For long rods ($L/D \geq 7$), a transition from an isotropic fluid to a 2D nematic phase was observed when the length of the rods was increased, and the orientational correlation function was found to decay algebraically, suggesting that this phase is characterized by quasi-long range order. Furthermore, by increasing the density of particles with an aspect ratio range as above, the correlation length of nematic fluctuations gradually increased, the system became nematic and the orientational order continued to steadily increase.

For shorter rods ($L/D < 7$), a stable nematic phase could no longer be observed, as the order parameter was found to drop from unity to essentially zero. This results suggests than the short rod systems undergo a transition directly from the solid phase (into which they are prepared) to an isotropic phase (see figure 1.4), which does not contain big orientational domains reminiscent of a nematic phase (which are observed in the isotropic phase for long rod systems, instead). However, particles show a strong local correlation in the positions and orientations, which corresponds to stacks of rods, in which the particles tend to align mainly side-by-side. These stacks appear to become less well developed as the particle length decreases. Hence, locally, this isotropic phase is essentially locked into a solid like structure.[7] This enhanced stability of the isotropic phase

[7]The images of the isotropic phase in Fig. 1.4 indicate that not only are stacks formed,

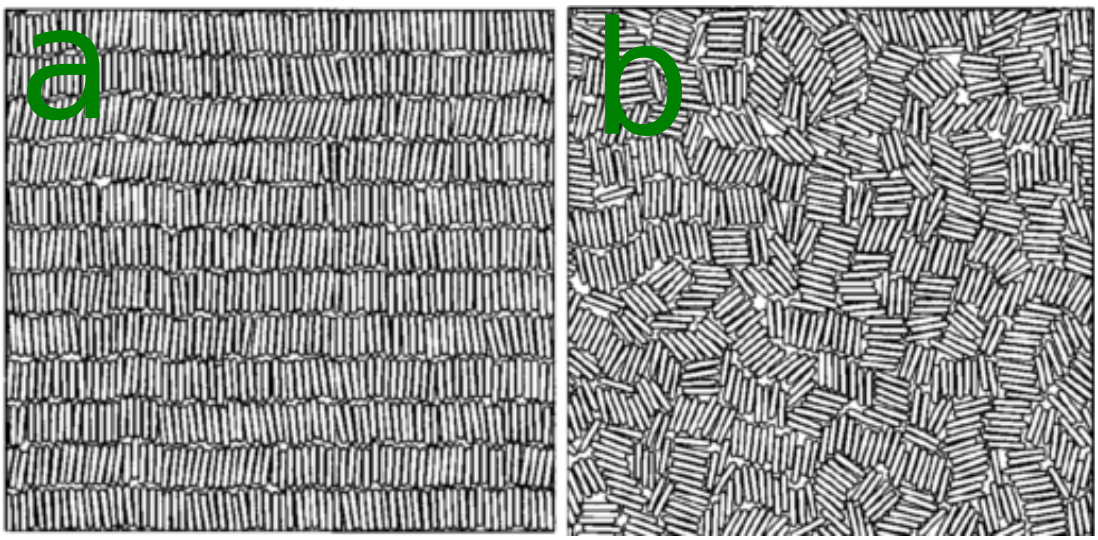

Figure 1.4: From solid (a) to isotropic (b) in a 2D hard rod system. High density phases are highly ordered, both orientationally and positionally. On melting, the system becomes isotropic. Reproduced from [12].

due to the formation of stacks means that the nematic phase does not enter the phase diagram until $L/D \approx 7$. Here, we have a difference from the 3D case, where the nematic phase is observed for rods as short as $L/D = 4$ [14]. Despite the presence of these stacks packed together, there was no evidence of singularities in the director map, that is the presence of point topological defects (later discussed in § 1.4).

Furthermore, different results are found when considering spherocylinders or ellipsoidal particles.[8] Studies of hard ellipses [15] indicate that the nematic is stable for aspect ratios of about 4 and above. The fact that short ellipses do not exhibit a similar isotropic phase to spherocylinders is not surprising, since spherocylinders can pack most effectively side-by-side due to their straight side. In contrast, ellipses aligned side-by-side can roll against each other and therefore it is unlikely that stacks will form and so the isotropic phase observed for spherocylinders is not as favourable as a nematic phase. Thus a small difference in the shape of the particle can lead to rather different phase behaviour.

but that neighbouring stacks appear to align either parallel or perpendicular to each other, a characteristic that defines the tetratic phase [13], in which there are two preferred directions of alignment, but no positional order. However, the decay to zero of the the corresponding orientational correlation functions *vs* the interparticle distance ruled out this hypothesis.

[8] Again, for the 2D case we are interested in, the correct terminology would be discorectangles and ellipses.

1.3 Continuous deformations of nematics

In the case of an ideal uniaxial nematic, the molecules are aligned on average along a common direction $\mathbf{n}$. However, in real cases seen in the laboratory, such an ideal configuration is not compatible with constraints imposed at boundaries, for instance (*i*) the surface of the container of the sample or (*ii*) an external field that is acting on the molecules. The result is that some deformations will occur, hence the order parameter Q will vary in space.

For most situations studied in the laboratory, the distance l over which Q varies considerably is much larger that the molecular dimensions a: typical values are $l \geq 1$ µm and $a \approx 20$ Å. Because of the large ratio l/a, deformations can be described by a continuum theory disregarding the details of the structure on the molecular scale.

We consider then a weakly distorted system ($l/a \gg 1$) in which only the director is position-dependent.[9] This is translated formally into the tensor order parameter in the following way [5] (similar to (1.8) where now the dependencies on position and temperature are explicit):

$$Q_{\alpha\beta}(\mathbf{r}) = Q(T)(n_\alpha(\mathbf{r})n_\beta(\mathbf{r}) - \tfrac{1}{3}\delta_{\alpha\beta}) + O((a/l)^2)\,. \tag{1.15}$$

The distorted state is then described by a vectorial field, that is the field of the director $\mathbf{n}$, with its orientation that varies depending on the position vector $\mathbf{r}$. For the current discussion, it is assumed that $\mathbf{n}$ varies slowly and smoothly in space.

In applying a small distortion ($a\nabla\mathbf{n} \ll 1$) to the nematic, we assume that the only forces of interaction between molecules are short range. A free energy F_d due to the distortion of $\mathbf{n}$ is introduced, with the characteristic that it vanishes when there is no distortion ($\nabla\mathbf{n} = 0 \rightarrow F_d = 0$), and that it can be expanded in powers of $\nabla\mathbf{n}$. Furthermore, the following conditions are imposed on F_d: (*i*) F_d must be even in $\mathbf{n}$ as the states $\mathbf{n}$ and $-\mathbf{n}$ are indistinguishable; (*ii*) F_d does not include any linear term in $\nabla\mathbf{n}$ as terms of such kind are not invariant under rotations; (*iii*) terms in F_d of the form $\nabla \cdot \mathbf{u}$, where $\mathbf{u}(\mathbf{r})$ is an arbitrary vector

[9] This means that changes in density induced by a long-range distortion are negligible.

field, are discarded. [10]

It can then be shown that the distortion energy density F_d has the following form [5]:

$$F_d = \tfrac{1}{2}K_1(\nabla \cdot \mathbf{n})^2 + \tfrac{1}{2}K_2(\mathbf{n} \cdot \nabla \times \mathbf{n})^2 + \tfrac{1}{2}K_3(\mathbf{n} \times \nabla \times \mathbf{n})^2 \,, \tag{1.17}$$

where the Frank elastic constants K_1, K_2, and K_3 are associated with the three types of deformation: splay, twist and bend. These constants are all positive, otherwise the undistorted nematic conformation would not correspond to a minimum of the free energy F_d. In figure 1.5, splay, twist and bend, *i.e.* the three distortions found in nematics, are shown.

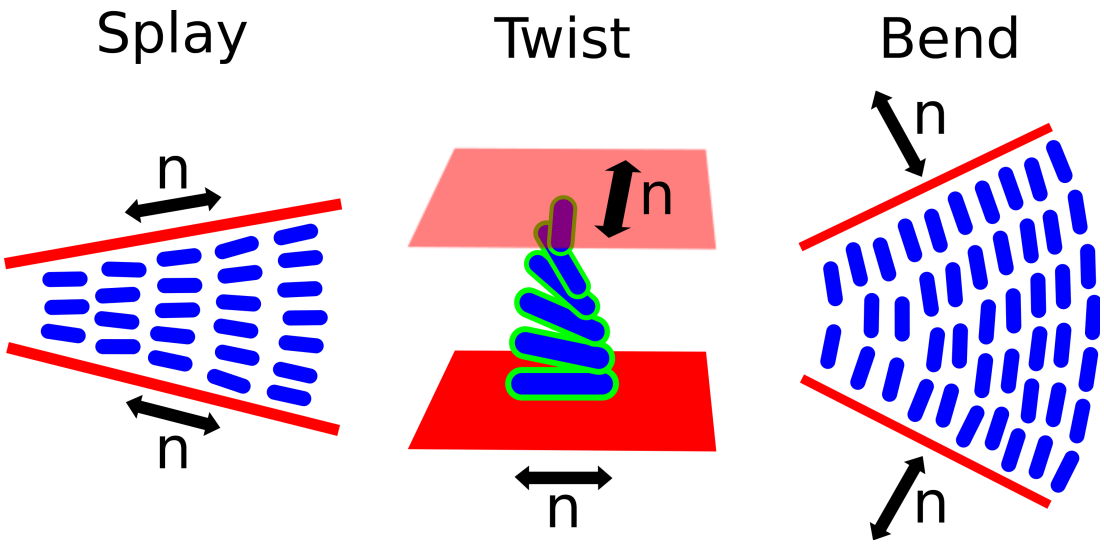

Figure 1.5: A sketch of splay, twist and bend deformations which can occur in a nematic. $\mathbf{n}$ is the director which experiences here the continuous deformations called splay, twist and bend. Because of the lower dimensionality, in 2D nematics, only splay and bend are present.

We observe that for 3D systems a fourth term could be included in eq. (1.17),

[10] This is a consequence of the Green's theorem:

$$\int_V \nabla \cdot \mathbf{u} d\mathbf{r} = \int_S \mathbf{u} \cdot d\boldsymbol{\sigma} \,, \tag{1.16}$$

where the second term is a surface integral, $d\boldsymbol{\sigma}$ being the normal to the surface in each point times and infinitesimal element of surface area. The integral is taken on the limiting surface S of the nematic. Since we are considering only bulk properties we can discard this surface contribution.

that is, the *saddle-splay* term, defined as:

$$K_{24}\nabla \cdot (\mathbf{n}\nabla \cdot \mathbf{n} + \mathbf{n} \times (\nabla \times \mathbf{n})) \,. \tag{1.18}$$

This term is absent in 2D splay (as in our 2D geometry for the bacterial colonies that will be shown later), but present in 3D: in this case, this term behaves as $\sim r^{-1}$, where $r = \sqrt{x^2 + y^2 + z^2}$ is the distance from the centre of the region where the distortion takes place [16]. Little is known at the experimental level about the saddle-splay term [17], however theoretical considerations show [18] that the corresponding moudulus K_{24} is always smaller than those of the splay and twist term, that is, K_1 and K_2.

Furthermore, we notice that F_d is an energy per m^3, $\mathbf{n}$ is dimensionless, hence the constants Ks have the dimension of J/m, that is N. Considering a typical interaction energy U between molecules of the order of 10^3 K or 0.1 eV or 2 kcal/mol or 8.3 kJ/mol, and a molecular dimension a of 15 Å, we expect, from a dimensional argument, that $K \sim U/a \approx 100$ pN.[11] The values of the constants Ks decrease with temperature T, but their ratios stay nearly independent of the temperature.

It is instructive to estimate the distortion energy on the single molecule or nematogen scale, assuming that the typical distortion takes place at some macroscopic length l: this will be roughly $F_d a^3 \sim (K/l^2)a^3 \sim U(a/l)^2$. Since $a \ll l$ (continuum limit), such distortion per molecule is very small.

In many cases it happens that the full form of (1.17) is still too complex to be of practical use - either because the values of Ks are unknown, or because the equilibrium equations derived from (1.17) are too difficult to solve. In this case, a further approximation is done, returning a simpler formula, which helps in understanding qualitatively the nematic distortions. Assuming all the three elastic constants equal ($K_1 = K_2 = K_3 = K$), the distortion free energy can be re-written as

$$F_d = \tfrac{1}{2}K\left[(\nabla \cdot \mathbf{n})^2 + (\nabla \times \mathbf{n})^2\right] \,. \tag{1.19}$$

[11] Such value is comparable to measured values from para-azoxyanisol LCs (usually used for displays) [5]. In most thermotropic LCs, measurements return value of 10 pN.

1.4 Defects: singularities in nematics

In the previous section, we discussed distortions of nematics that involve continuous variations of the director $\mathbf{n}(\mathbf{r})$. However, such distortions can get stronger in such a way that the field $\mathbf{n}(\mathbf{r})$ can no longer be represented by a smooth function of the position vector $\mathbf{r}$ at all points, but singularities appear instead.

The word nematic actually origins from the presence of thread-like structures that can be seen in such kind of LCs between crossed polarisers. In rather thick samples of a nematic, it is common to observe a system of dark, flexible filaments, some floating freely in the bulk, others anchored to one or both the surfaces of the microscope glass slide. The first investigations of defects in nematics were performed by Grandjean and Friedel, who showed that these were genuine features of LCs and not effects due to impurities: they actually correspond to lines of singularity in the molecular alignment, hence the word disclinations[12] introduced later by Frank, as an analogue to the solid crystal case of dislocations [5, 9].

When focussing on a surface, it is possible to see also some singular points - that is, point defects or *noyaux* (nuts) as called by Friedel, on the surface. They can be either point disclinations located at the boundary surface, or lines normal to the plane of the surface (then what is seen is the anchoring of such line to the surface), and both these two cases occur in practice. In most real cases, there are four essential types of point defects, and they are classified through an index s which takes the values $s = \pm\frac{1}{2}, \pm 1$. This value is usually referred to as the topological charge of the defects. To understand such classification, we assume that the director $\mathbf{n}$ is in the plane of the wall (tangential boundary conditions), defining two orthogonal axes (x, y) in this plane, as represented in figure 1.6 for the case of the $\pm 1/2$ charged defects.

The vector $\mathbf{r}$ connects the singularity (red dot) to the observation point, and $\phi(\mathbf{r})$ is the angle between $\mathbf{r}$ and x with $\tan(\phi) = y/x$. The angle between $\mathbf{n}$ and x is $\theta(\mathbf{r})$. Then it follows that on going round the defect,

$$\Delta\theta(\mathbf{r}) = s\Delta\phi(\mathbf{r}) + \text{const.} \tag{1.20}$$

Hence, if we made a loop around the singular point (that is $\Delta\phi = 2\pi$), we would

[12] *Kline* is the Greek for slope.

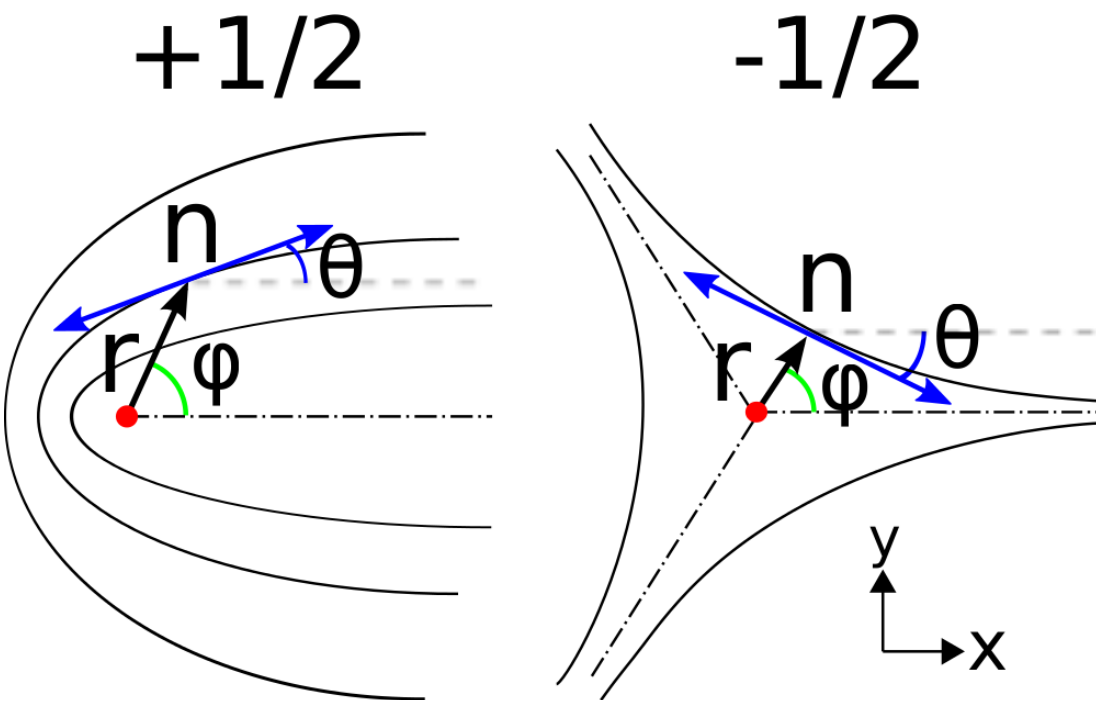

Figure 1.6: A sketch for $\pm 1/2$ charges that are typical of apolar nematics. The sign of the charge is given depending on the sign concordance of the variations between the two angles ϕ and θ; the value of the charge is given by the ratio of the change in the angle θ with respect to the full rotation of 2π of ϕ: so, in this case, it would be $|\Delta\theta/\Delta\phi| = \pi/(2\pi) = 1/2$.

find that the director $\mathbf{n}$ has rotated by $\Delta\theta = 2\pi s$, with $s = \pm 1/2$.

As we will see in Part II and Part III, the features discussed so far of passive nematics - *i.e.* the transition between an ordered and a disordered phase, the deformation of the nematics and the creation of topological defects, are also shared by some biological systems. The differences are however relevant because the constituent particles of a living system, that is, the cells, are inherently not passive: they can sense the environment and respond to it accordingly, and their dynamic is not only the result of an external stimulus (*e.g.* an external field applied to them). Furthermore, they can reproduce, meaning that the number of particles in the system is not conserved and that their shape change on time [19].

We thus introduce in the next two chapters first the bacteria which are the type of particles that we use in our experiments, and then we move to discussing an approach used to interpret biological systems with a physicist's point of view,

known as active matter.

Chapter 2

Bacteria

This thesis is concerned with developing a novel description of a growing colony of rod-shaped bacteria as an active nematic. Therefore, in this chapter, we introduce bacteria. We begin this biology-oriented chapter giving a general introduction to the role played by bacteria in nature, *i.e.* the reciprocal interactions that bacteria have with their surrounding environment, and their relevance to global ecology.

We move on to discuss communities of bacterial cells in a sessile state. The bacterial microcolonies studied in this thesis represent indeed the very early stage of more complex structures of this kind, usually referred to as biofilms. Such communities of bacteria are found in almost every natural environment able to sustain life, even under the most extreme conditions [20].

We then restrict our interest to the structure of the single individual cell, focussing on the particular species of *Escherichia coli* (*E. coli*), which is the one used in the experiments of this work, and one of the best known and most studied model organisms in biology. Finally, we discuss methods for the genetic manipulation of bacteria that have been used in this work in order to construct some *ad hoc* mutants (a more technical description is given in Chapter A).

2.1 Relevance of bacteria

Planet Earth is about 4.5 Gy old, and the first evidence of microbial life can be found in microfossils of prokaryotes present in rocks about 3.9 Gy old. Extensive microbial diversification is believed to have occurred some time later, as rocks 3.5 Gy old (stromatolites) show abundance of microbial formations [21].

In turn, such microorganisms greatly influenced the evolution of the whole planet: oxygenic photosynthesis by cyanobacteria caused O_2 to accumulate about 2.4 Gy ago, eventually leading to the formation of banded iron formations, the ozone shield, and an oxygenated atmosphere, which set the preconditions for rapid diversification of metabolic systems and the evolution of multicellularity [21, 22, 23, 24].[1]

Bacteria represent one of the three major philogenetic domains of cells, the other two being the Archaea and the Eukarya. It is worth recalling that microbial diversity and mass on Earth exceeds that of higher organisms, and that most microbial cells actually reside in the terrestrial and oceanic deep sub-surfaces [21], which, at present, remain mostly unexplored. Bacteria can be beneficial (often essential) or harmful to higher organisms. Agriculture, food, energy, and the environment are all impacted in major ways by these microorganisms [25].

2.2 Biofilms

Bacteria are usually found living together as aggregates in natural environments. These aggregates may contain many different species of cells, so that they constitute microbial communities. Such communities are highly complex entities, both in terms of physical structure and in terms of the biological interactions established among the individual cells (*e.g.* cooperation, competition).

Microorganisms are affected by the surrounding environmental conditions they live in. However, they can also exert a deep impact on their habitats through their activities (*e.g.* the oxygenation of terrestrial atmosphere by cyanobacteria photosynthesis). A relevant bacterial collective phenomenon is the formation of biofilms [26]: these are dense collections of bacterial cells which form on 2D surfaces through a complex life cycle (see figure 2.1). Biofilms are ubiquitous in real world, as bacteria are able to colonize almost every available surface.

They are implicated in a wide variety of diseases and health problems, from cystic fibrosis, through endocarditis to dental plaque; they can grow on hospital equipment and in medical devices [29, 30, 31, 32], with evident

[1] Eukaryotes developed from endosymbiotic events. The modern eukaryotic cell is a chimera with genes and characteristics from both bacteria and archaea: analyses of small subunit rRNA sequence indicate that the ancestors of mitochondria are found in the phylum Proteobacteria, and those of chloroplasts are found in the phylum Cyanobacteria [21].

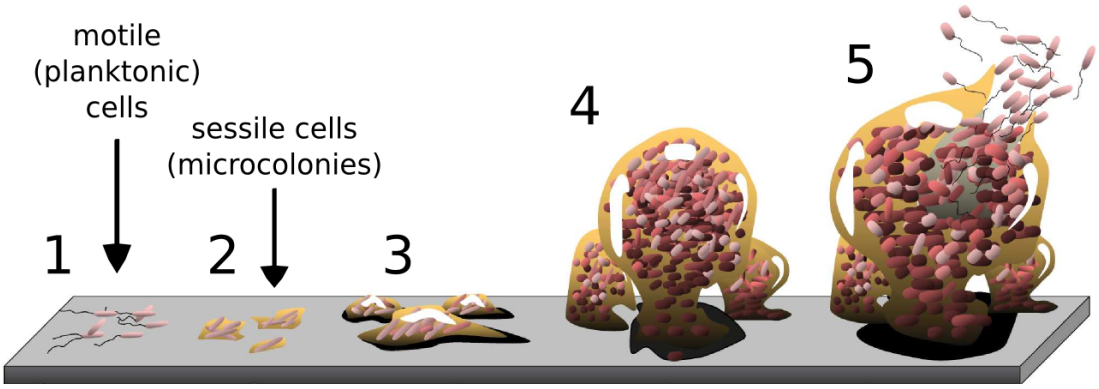

Figure 2.1: The development of a biofilm consists of several stages: (1) cells are initially in a planktonic or motile state. In this stage they explore the surrounding environment and once found a surface, they get stuck to it forming the first small aggregate or microcolonies (2). Then the microcolonies mature (3), initiating the construction of more complex, 3D structures, that is, the actual biofilm (4). Finally, sporulation occurs (5) when the biofilm is fully mature [27], new motile cells are released, and the cycle can restart. Reproduced with modifications from [28].

consequences. Biofilms are particularly troublesome as they exhibit strong resistance to antibiotic agents [33]. They also cause problems in industrial settings, forming on surfaces that obstruct fluid flow or contaminate drinking water.

Despite these negative aspects, biofilms play an essential role in the ecology. Environmental microbiologists have long recognized that complex bacterial communities are responsible for driving the biogeochemical cycling that maintains the biosphere [21]. For instance, they are involved in the degradation of organic matter and environmental pollutants, in photosynthesis, in the fixation of nitrogen, in the cycling of sulphur and many metals. In order to occur, these processes require the combined effort of many single bacterial cells, each cell with its own metabolic capabilities. It is then likely that bacteria forming biofilms could carry out many of these processes [34].

Therefore, biofilms are extremely interesting from the biological point of view, as they represent examples of complex systems where cells can interact chemically and mechanically in order to achieve some communal tasks. For instance, the initial formation of a biofilm involves quorum sensing: when the density of bacterial cells in a given space is large enough, cells will start producing some

chemicals whose result is the activation of genes involved in the formation of biofilm [35].

Cells in a biofilm can undergo phenotypic changes or stages where they can produce substances that allow them to protect the whole community from external agents. Among these materials, are exopolysaccharides, which represent the main constituent of the biofilm scaffolding. Also known as extracellular polymeric substance (EPS) or exopolysaccharide matrix (EPM), these polymers contribute to the development of antibiotic resistance [36]. Biofilms can also exhibit complex structures, such as channels for the transport of nutrient and waste products [37] (see figure 2.2).

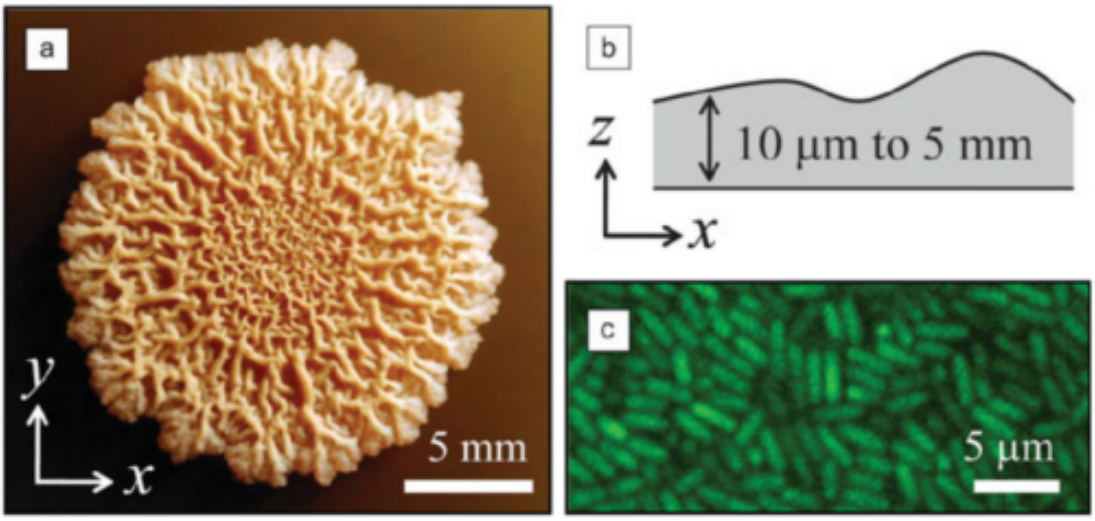

Figure 2.2: A fully developed *Bacillus subtilis* bacterial colony [36] grown on a air-solid surface of agar gel containing water and nutrients. The growing biofilm undergoes radial expansion, and a highly wrinkled morphology is reached when mature (a), with a range in thickness from ten to a thousand times that of a single bacterium (b). In (c), a confocal microscopy image of a bacterial biofilm with individual cells embedded in a viscoelastic extracellular matrix (not fluorescently stained) is shown.

These complex structures are not always due to intercellular chemical signalling. Instead, structures can form because of the mechanical interaction between cells as they grow, and the competition for space and nutrients as they invade new areas, in a fashion that resembles the collective behaviour of flocks of birds or schools of fish [38]. This idea is supported by many computational models of biofilm growth, which exhibit the formation of rather complex architectures

such as branches and channels, even in the absence of any intercellular signalling effects [39, 40, 41, 42]. Experiments where bacteria have been cultured on agar plates gave insights into the pattern formation in biofilms. Even in a simple case where a single bacterial strain is grown onto a surface of agar, a wide variety of complex patterns, depending, for instance, on the amount of nutrient available, can be observed [43, 44]. Interestingly, many of these patterns have similarities to non-living growth processes, such as the growth of crystals or the aggregation of diffusing particles.

Another aspect, as interesting as simple mechanical interactions, is the evolutionary perspective. Cells making up a biofilm are in competition with each other for space and resources, but it might be helpful for them to cooperate instead of behaving selfishly way, for instance by producing EPS and chemicals to break down metabolites in the environment or to protect the whole colony from antibiotics. Actually, spatial structure of biofilms may make cooperation more evolutionarily stable [45], but cooperation will not always be favoured, especially when multiple species are present [46]. Furthermore, the spatial structure present in a biofilms has been shown to affect how likely it is that a beneficial genetic mutation (*i.e.* a mutation that makes the colony grow more quickly) will survive and take over the population rather than dying out due to stochastic nature of the competition between cells [47, 48]. In a pathogenic biofilm, this will affect, for example, how quickly the cells will become resistant to an antibiotic.

2.3 Cell structure

A bacterial cell is made up of many parts interacting with each other and allowing the cell to carry out many activities, such as metabolism, growth, and evolution [21]. Bacterial cells can have many different shapes, and some can transform from one shape to another depending on their habitat and life cycle, the most common shapes being those of rods, cocci, and spirilla. Bacteria are usually smaller than eukaryotes (although some very large prokaryotes are known), the typical dimensions of an approximately spherocylindrical *E. coli* bacterium[2] being 3 µm in length, and 1 µm in width.

[2] *E. coli* bacterium is currently one of best known and studied organisms. It was first identified in the intestinal flora of infants by the German pediatrician Theodor Escherich (1885) who called that species *bacteria coli commune*, and in 1920 it was named after him.

Through the eyepiece of a microscope, a single *E. coli* cells looks like a pill, but, despite such simple look, it stores, reads genetic information in much the same way more complex organisms do. Furthermore, it synthesizes the same kinds of molecular tools for carrying out basic cellular functions. Many of the enzymes designed by *E. coli* cells for harvesting energy or crafting molecular building blocks have structures nearly identical to ours [49]. This is the reason for its importance in the study of biochemical pathways, bacterial viruses, the regulation of gene expression, the genetic code nature, gene replication, protein synthesis and, more recently, the manufacture of proteins of commercial value [49].

The structure of a bacterial cell right next to the cytoplasm - the inside of the cell - is referred to as the cytoplasmic membrane. This is a highly selective permeability barrier, made up of lipids and proteins that form a bilayer. This bilayer is hydrophobic inside and hydrophilic outside. The major functions of a cytoplasmic membrane are selective permeability and transport.

Gram-negative bacteria, such as *E. coli*, have an outer membrane consisting of lipopolysaccharides, protein, and lipoprotein. The gap between the outer and cytoplasmic membranes is called the periplasm, and contains a protein-glycan network involved in transport, sensing chemicals, and other important cell functions. Such a cell wall protects the whole bacterium from osmotic lysis.

Many bacterial cells, including *E. coli*, contain capsules, flagella, pili or fimbriae (see figure 2.3). These structures have several functions, including attachment, genetic exchange, and motility.

In the chapter dealing with mechanical instabilities and mutants (Chapter 8), we will present an investigation of the influence of these appendages on the buckling of microcolonies. In order to observe these effects, we used a wild type strain and some mutants, lacking one or both the flagella and the fimbriae. In the next section, we present the method we use to construct these mutants.

2.4 Horizontal gene transfer

Horizontal gene transfer is the movement of genes between cells that are not direct descendants of one another and it can occur among different species. It allows cells to quickly acquire new characteristics and drive metabolic diversity.

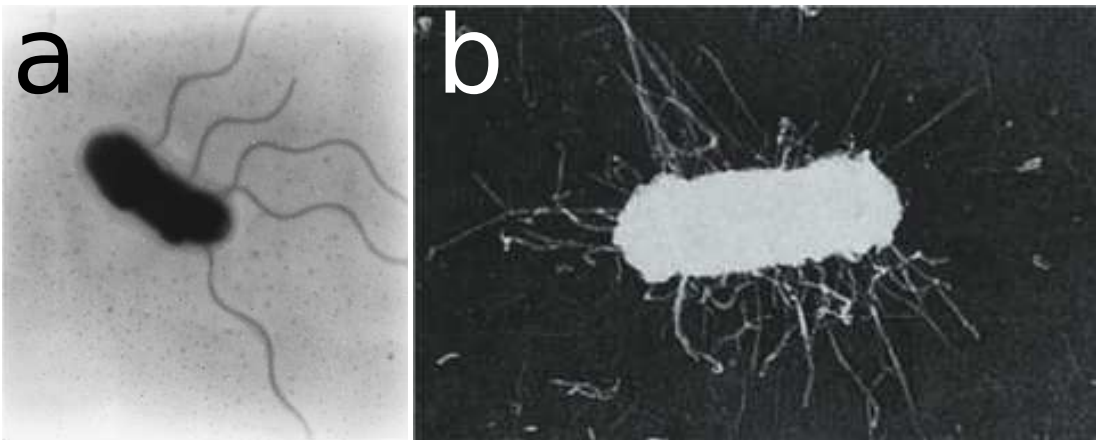

Figure 2.3: (a) Flagella of an *E. coli* bacterium: flagella are the appendages responsible for the self-propulsion of the cell. When united in a rotating bundle (usually 2 to 6 flagella), they produce a thrust force that pushes the whole cell body through the liquid environment (motile state). Reproduced from [49]. Flagellar length is about 10 µm, and the width of the order of 20 nm. Cell width in the picture is about 1 µm. (b) Fimbriae of an *E. coli* bacterium: fimbriae are also known as attachment pili, as they contribute to the adhesion of the cell to surface by direct contact. Fimbriae length spans from 0.5 to 2 µm, with a 20 nm width. Cell width is about 1 µm. Reproduced from [21].

There are three known mechanisms of horizontal gene transfer in prokaryotes: (*i*) transformation, in which DNA released from one cell is taken up by another, (*ii*) conjugation, in which DNA transfer requires cell-to-cell contact and a conjugative plasmid in the donor cell, and (*iii*) transduction, in which DNA transfer is mediated by a virus. These mechanisms lead to the acquisition of new characteristics (either beneficial or detrimental) from which much of the vast diversity of the microbial world derives. They also provide the researchers with tools for genetically modifying bacteria.

We focus in the following sections on the last method, which has been exploited in our work for mutant construction. Since transduction is based on the use of a virus as a vector, we introduce first the P1 virus used in the lab and then the actual method of transduction.

2.4.1 Bacteriophage P1

In nature, wherever there are microbes, there are viruses: an estimate gives a large number of 10^{31} virions - the infectious viral particles - assuming that there

are 10 virions per microbe on Earth [50].[3] A virus is an obligate intracellular parasite that requires a suitable host cell for replication. Once inside the cell, the virus redirects the host metabolism to support its replication.

Bacteriophages (or just phages) are viruses that infect bacterial cells, [4] by far the most abundant (10^7 phages per ml of seawater), the most diverse, and the most dynamic life form [51]. P1 belongs to such a category of viruses that infect *E. coli* and some other bacteria. In our work on the buckling of bacterial colonies, P1 phages have been exploited in the construction of mutants of *E. coli* bacteria.

Phages cannot be seen without specialized equipment as they are very small. However, current imaging methods allow us to unveil the beauty of their typical icosahedral capsids - as one of the five Plato's ideal polyhedra. P1 has a 85 nm diameter icosahedral capsid containing DNA. Attached at one vertex, there is a tail (about 300 nm long, 20 nm width) surrounded by a contractile sheath [51]. Such a tail ends with six tail fibres that are involved in the attachment to the host and in providing specificity.

The genome of P1 phage is moderately large, at around 90 kbp in length [51].[5] The genome is contained in the icosahedral capsid and is a linear double stranded DNA molecule (that encodes for approximately 100 proteins). Once inserted into the host it circularizes and replicates as a plasmid.

The steps by which P1 manages to reproduce by exploiting its host can be summarized as follow:

1. P1 adsorbs onto the target cell membrane through its tail fibre;

2. The tail sheath contracts and the DNA of the phage is injected into the host cell. The host DNA recombination machinery or enzymes directly translated from the viral DNA recombine the ends and circularize the phage genome. At this stage, the phage can either proceed to the lytic phase or enter a lysogenic state.

   During lysogeny, phages behave as temperate viruses, meaning that they do not integrate into the host genome as prophages. The P1 genome is indeed maintained as a low copy number plasmid in the bacterial cell without lysis.

[3] Despite the large number, this would correspond to only 5% of the whole terrestrial biomass, because of their relatively small size.

[4] Literally translated, it means bacteria eaters.

[5] For comparison, T4 virus genome counts about 170 kbp, lambda virus genome 50 kbp, and Ff virus genome 6.5 kbp.

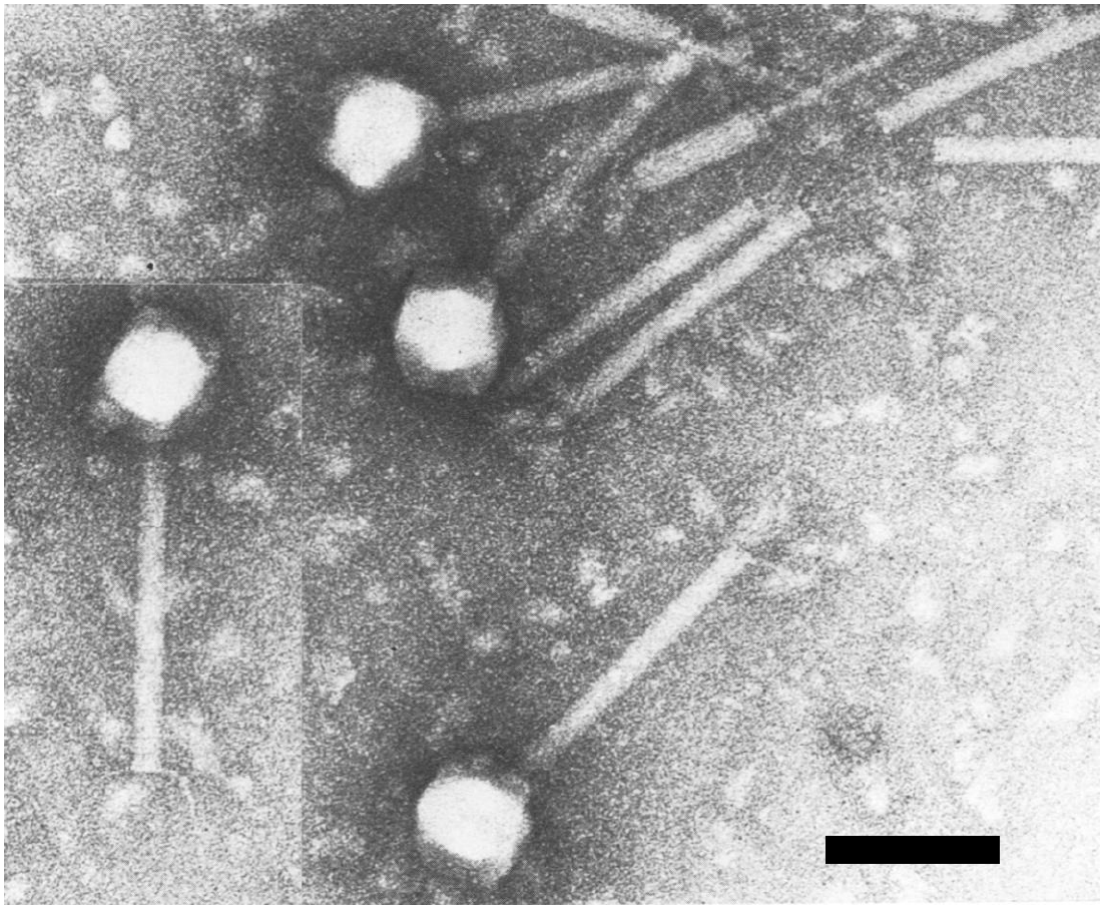

Figure 2.4: P1 phage as seen at the scanning electron microscope. Reproduced from [52]; scalebar is 100 nm.

The other pathway that can be followed by the viral particle is the lytic pathway, whereby the virus redirects host metabolism to support its replication and the assembly of new virions, finally resulting in the destruction of the cell and virions release. This phase can take place just after the injection of prophage into the bacterial host cell or after the induction of the prophage;

3. In both cases, a different form of DNA replication is initiated, called rolling cycle replication. In this process, end to end copies of the P1 genome are generated, which are cut at specific sites at the ends. P1 can also incorporate genomic host DNA at this stage: this is indeed the way viruses are exploited in transduction;

4. An empty procapsid is assembled and packaged with the replicated genome, and viral tail and viral tail fibres are assembled too;

5. Once the complete virions are assembled, the host cell lyses, the viral particles being released.

The process can then restart.

A unique feature of phage P1 is that, once it has injected its DNA into the host cell, its genome is not incorporated into the bacterial chromosome, as it is commonly observed for other phages.[6] Hence, the phage genome exists as a 90 kbp plasmid in the bacterium unlike other phages (*e.g.* the lambda phage) that integrate into the host DNA [52, 53, 54]. Then, the phage genome is partitioned equally into the two new daughter bacterial cells during division.

2.4.2 Transduction

Transduction is an important means of horizontal gene transfer in nature[7] and it is also an important tool in bacterial genetics. Transduction is the transfer of host genes from one bacterium to another by a bacteriophage, which is used as a vector of the mutation.

There are two kinds of transduction: generalized and specialized. We will focus on the former kind, which is the one we used. Microbial geneticists use both generalized and specialized transducing bacteriophages to deliver DNA to target bacterial cells. Transduction can be used to deliver DNA to strains in which transformation and conjugation are not efficient. Bacteriophages can be used to deliver large pieces of DNA to host cells: a typical tailed phage that contains double-stranded DNA can package up to 40 kbp of DNA. The bacteriophages used for transduction in the laboratory are usually nonlytic because bacterial genes have replaced all or some necessary viral genes. To select for a transduction

[6] It is important to observe that viruses can replicate only in their correct host cells. Bacterial viruses, as the bacteriophage P1, have proved useful as model systems because their host cells are easy to grow and manipulate in culture. The attachment of a virion to a host cell is a highly specific process. Recognition proteins on the virus recognize specific receptors on the host cell. Sometimes the entire virion enters the host cell, whereas in other cases, as with most bacteriophages, only the viral genome enters.

[7] Note that not all phages can transduce, and not all bacteria are transducible, but with bacteriophage abundance estimated to outnumber prokaryotic cells by 10-fold in nature, the phenomenon plays an important role in gene transfer in the natural environment.

event, a transducing phage must infect a donor host that has a selectable marker.[8]

Generalized transduction

In our mutant-case study of buckling colonies, we used a generalized transduction for the creation of suitable mutants.

In generalized transduction, virtually any gene on the donor chromosome can be transferred to the recipient, by forming a transductant. When a bacterial cell is infected with a phage, the lytic cycle may occur. However, during the lytic infection, the enzymes responsible for packaging viral DNA into the bacteriophage sometimes package the host DNA, this resulting in a transducing particle. These particles cannot lead to a viral infection because they contain no viral DNA, but they contain the host genome DNA instead, and are said to be defective. On lysis of the cell, the transducing particles are released along with normal virions that contain the virus genome. Consequently, the lysate contains a mixture of normal virions and transducing particles.

When this lysate is used to infect a population of recipient cells, most of the cells are infected with normal virus. However, a small proportion of the population receives transducing particles that inject the DNA they packaged from the previous host bacterium (the donor). Although this DNA cannot replicate, it can recombine with the DNA of the new host (the receiver).

We notice that, because only a small proportion of the viral particles in the lysate are defective and each of these contains only a small fragment of donor DNA, the probability of a given transducing particle containing a particular gene is quite low. Typically, only about 1 cell out of 10^6 to 10^8 is transduced for a given gene. Hence the transducing efficiency in generalized transduction is quite low.[9]

[8] In our case, this selectable marker is represented by an antibiotic resistance cassette, specifically to kanamycin, as discussed in more detail in Chapter A.

[9] By contrast, specialized transduction allows for higher transfer efficiency, but as it is specialized (or restricted), it is selective and transfers only a small, specific region of the bacterial chromosome.

Chapter 3

Active Matter

In this chapter, after explaining what active matter is and presenting its relevant properties, we discuss some examples found in nature and studied in the laboratory. A surprising and fascinating aspect of active matter is how diverse are the systems that belong to this class. We focus then on describing the single constituents of active matter, that is active particles, stressing the difference between polar and apolar cases, then extensile and contractile cases. We discuss the instabilities in terms of splay and bend as consequence of internal active stresses as predicted by theory and observed in experiments. Finally, we review some recent works that represent examples of active nematics and share aspects with our system made up of bacterial microcolonies.

3.1 Properties and examples

Active systems are made up of particles capable of taking energy from the surrounding environment or an internal energy reservoir, and of dissipating it, with the result of performing some movements [1]: it could be either a movement in space of the active particle or a modification of its shape in space (*e.g.* a growth process).

We could think of active matter as a fundamentally, inherently nonequilibrium regime in which we study condensed matter. Three main features common to constituents of all active matter systems can be identified: (i) the energy input takes place directly at the scale of each active particle, hence such a process is

homogeneously distributed through the bulk of the system;[1] (*ii*) self-propelled motion is force-free - the forces that the particle and fluid exert on each other cancel out; (*iii*) any directionality in the motion of an active particle is set by the particle itself, and not by an external field [1].

With the definition of active matter given above and its properties in mind, it is clear then that all living cells could be included into such a class. For instance, examples can be found amongst the simplest forms of life, such as a bacterium growing on a surface or a unicellular alga swimming through some fluid.

Further examples could be observed at an even smaller spatial scale, by looking into such cells, the scale now being of the order of some nm instead of micron-sized bacterial and algal cells: for instance, in eukaryotes, we find the cytoskeleton, that is, the subcellular polymeric scaffolding that regulates transport, adhesion, movement, and division in the living cell. In this system, there are two main nonequilibrium processes that drive the cytoskeleton: (*i*) the adenosine triphosphate-assisted (ATP) polymerization and depolymerization, and (*ii*) the contractility that arises from the ATP-driven movement of motor proteins in specific directions on biofilaments [55]. The cytoskeleton can be mechanically interpreted as a suspension of filaments endowed with active internal forces [56, 57, 58]. We can also move in the opposite direction in spatial range - that is, towards very large systems - and observe collections of cells (microbial communities, suspensions of cells, now at the mesoscopic scale, *i.e.* order of µm-mm) or even macroscopic systems (order of tens of m to km) like flock of birds [59] or fish schools [60, 59] (figure 3.1).[2] This wide spatial range where we can find many examples of systems very different in nature suggests that there are underlying, universal features that are worth investigating.

It is easily noticed by eye that all these systems display some orientational order, which can then be interpreted as an ordered phase of living matter. Such an idea was first numerically implemented by Vicsek. In this model, some interacting particles move at a constant speed and in presence of noise, with the tendency to align their velocity vectors (of fixed magnitude) parallel to those of their neighbours within a given spatial range [65]. The substrate on which or the bulk through which particles move, is inert. After such orientation update, the

[1] Unlike sheared fluids or 3D bulk granular matter, where the forcing is applied at the boundaries.

[2] We could even include some exotic examples like heavy metal concert audiences [61].

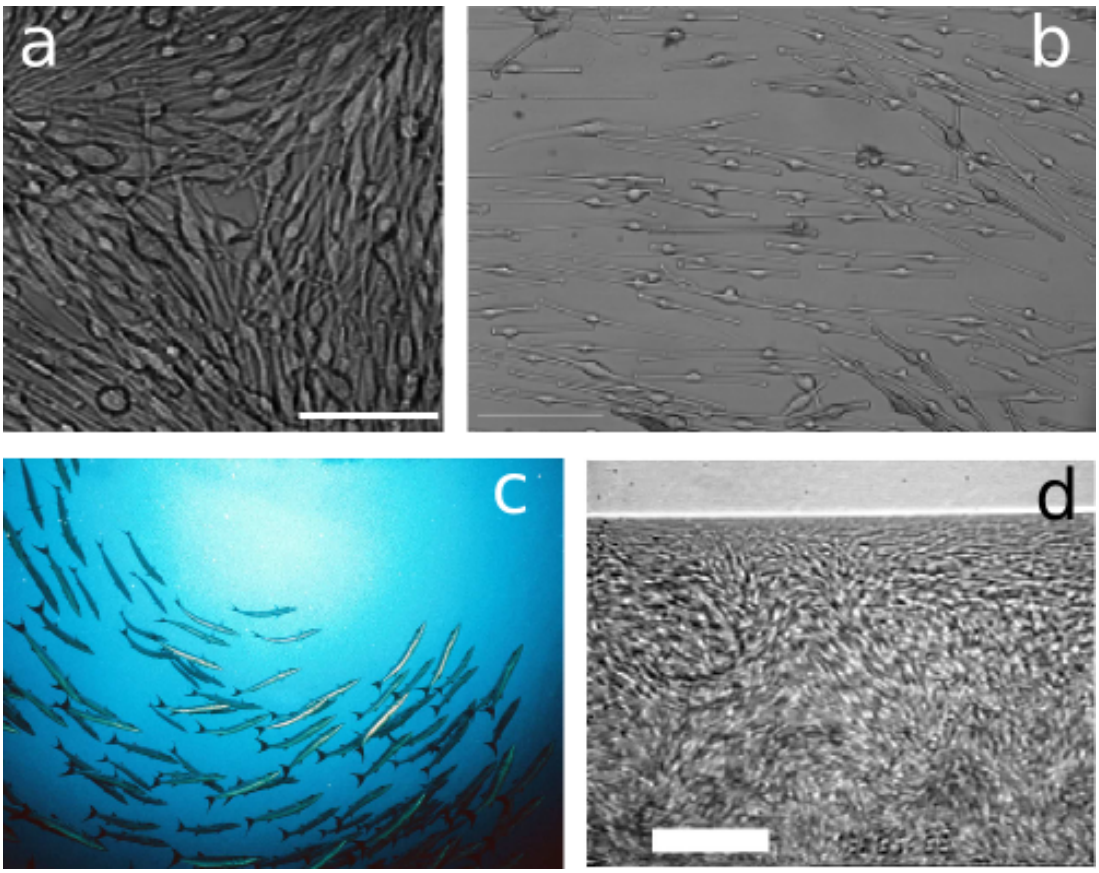

Figure 3.1: Examples of active matter systems: living systems can be included in the group of active systems: (a) and (b) are pictures of melanocytes [62, 63] displaying a -1/2 charge defect and a nematic phase, respectively (scale bars are 100 µm); a (macroscopic) school of barracuda (picture taken by Wolcott Henry, National Geographic) is shown in (c): barracuda may protect themselves against larger predators, such as sharks, by aggregating in schools; in (d), we observe a sort of bacterial turbulence in a drop of bacterial suspension (viewed from the bottom; the white line is the air-water-plastic contact line, scale bar is 35 µm) [64].

particles takes a step in that new direction, and the whole process is repeated to obtain the entire dynamics. A remarkable feature of such a system is that it displays a nonequilibrium phase transition from a disordered state to a coherent flock with long-range order in the particle velocities as the white noise strength is decreased or the concentration of particles is raised (a result which reminds us of lyotropic systems). In figure 3.2, we report the phases which can be observed from such a model [65].

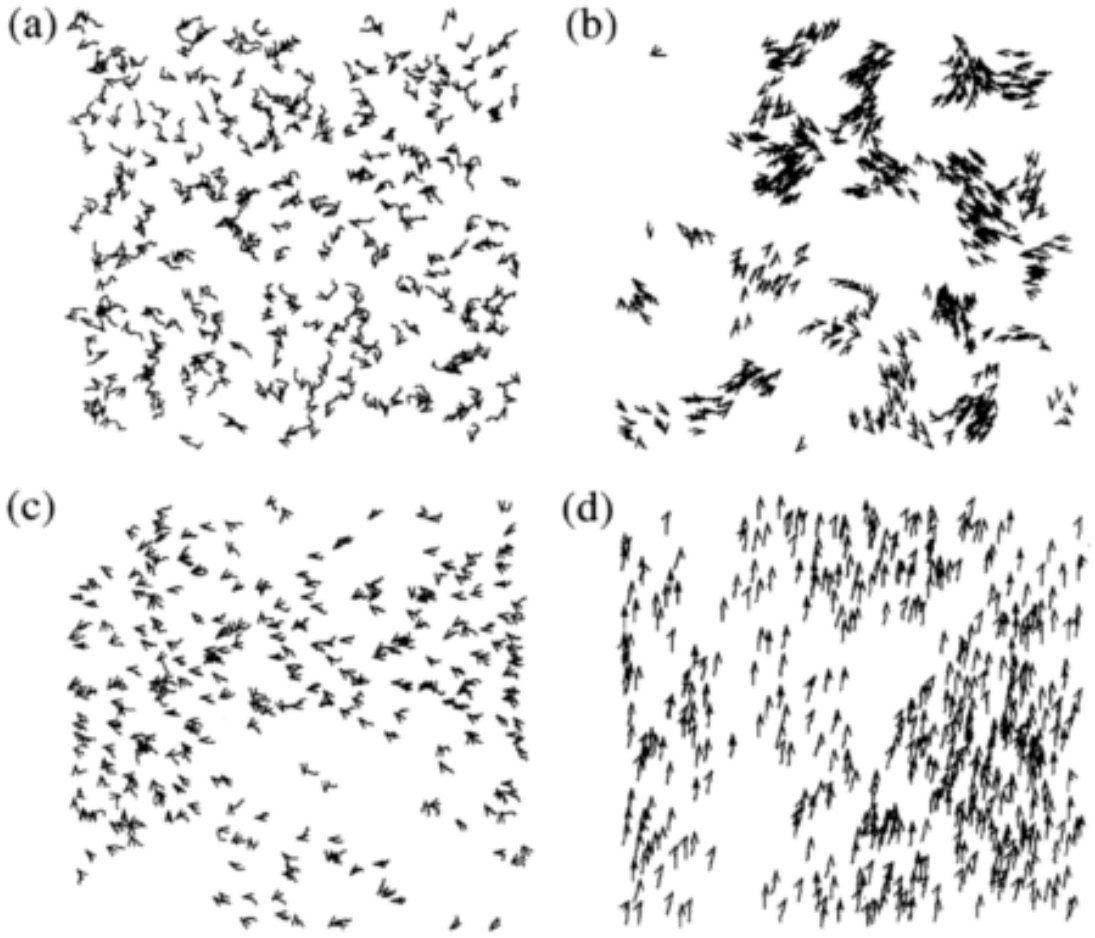

Figure 3.2: Velocities of the particles are displayed for varying values of density and noise. The actual velocity of a particle is indicated by a small arrow, while its trajectory for the last 20 time steps is shown by a short continuous curve. The number of particles is 300 for all cases: (a) picture at initial time, for a square of side L and noise η; (b) smaller densities than (a) ($\approx 4L$, *i.e.* bigger square) and smaller noise ($\eta/20$): particles form groups moving coherently in random directions; (c) same values as in (a), but after some time steps: the particles move randomly with some correlation. (d) higher density ($\frac{7}{5}L$) and smaller noise ($\eta/20$): the motion becomes ordered, exhibiting a nematic phase [65].

This is quite a simple model for an active system and offers also a parallel to a classical system of magnets, which are ferromagnetically interacting through their spins, but with the additional active characteristic that they can move in the direction where they are pointing.[3]

[3]For systems at equilibrium, the Mermin-Wagner theorem [66] states that long range ordered phases (where continuous symmetries are broken) are forbidden in less than 3D. Contrary, for

It is clear that complications arise when the physical properties of the fluid medium - through which the elementary constituents act - are taken into account, that is it is no longer inert: the same active particles can now generate a flow, and this flow can in turn influence the way the particle neighbours behave. This capability of particles to carry permanent stresses that stir the fluid can be formulated in terms of a modified liquid-crystal hydrodynamics [67].

3.2 Polar and apolar active particles

The preferential direction associated with active particles is usually related to the direction along which they move or exert forces on the surrounding environment. Such active particles can be polar or apolar.

Retracing the approach followed by Vicsek, simulations of apolar systems have been performed [68]: each particle is given now an axis, rather than a unit vector, which however tends to align parallel to the mean of its neighbours' axes, again subject to some noise. The particle then takes a small step preferentially along the axis, randomly forward or backward. As the noise or mean interparticle separation is decreased, a continuous phase transition is seen (as well as for the Vicsek polar case) from an isotropic state to a phase with quasi-long-range nematic order of the particle axes. Contrary to the equilibrium case, the density number fluctuations are giant as ΔN grows far more rapidly than N [5]: visually, this corresponds to the formation of particle configurations with strong transient inhomogeneities and banded structures.

Experimentally, apolar active systems have been investigated by many researchers, exploiting active non-living and living constituents. For instance, Narayan *et al.* investigated a collection of vertically vibrated, macroscopic apolar rods (order of mm), studying the deformations of the nematic phase [69, 70], as represented in figure 3.3.

Another apolar system, now involving living agents, has been investigated by Gruler *et al.*, who focussed on melanocytes, *i.e.* the cells that spread pigment in the skin [71]. In their work, melanocytes have been shown to form nematic order *in vitro* as the concentration of cells was increased. The resulting 2D nematic

active systems - *i.e.* in a nonequilibrium regime - long range orientational order shows up also in 2D, as in the relatively simple model of Vicsek, and first explained by Tu and Toner [3].

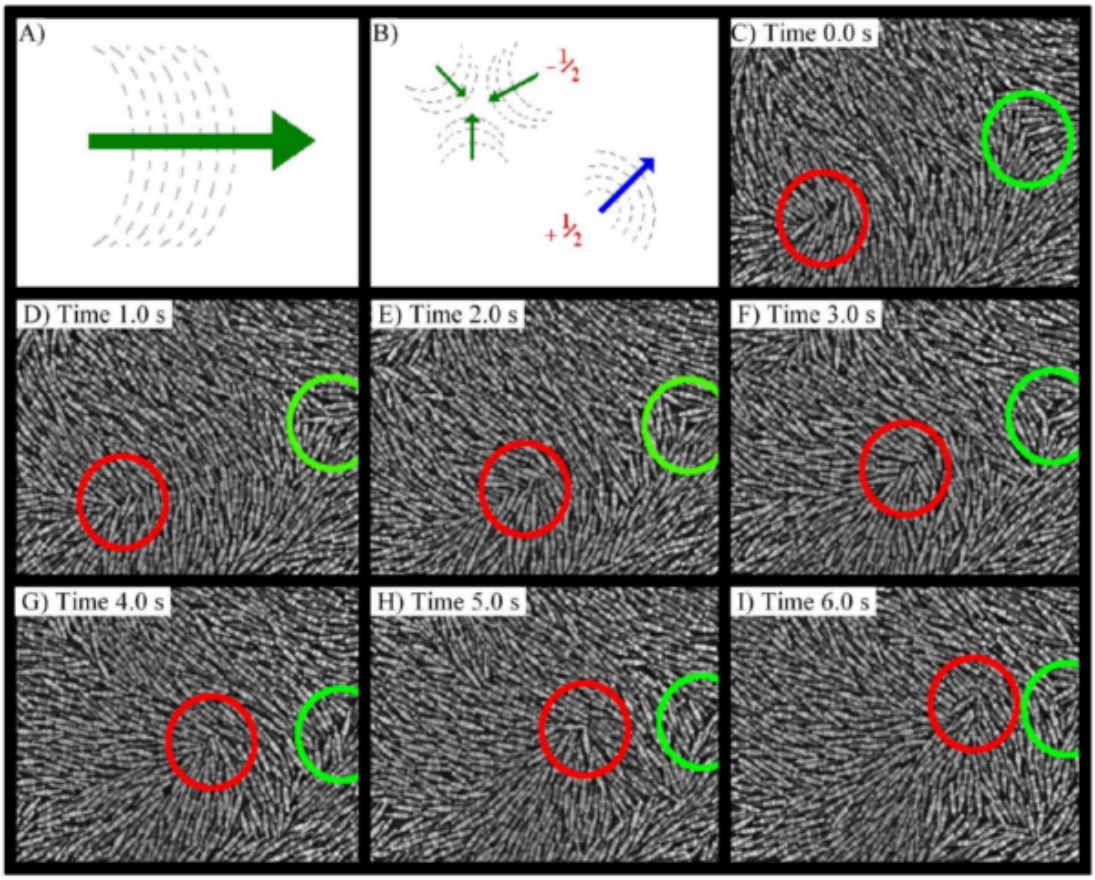

Figure 3.3: Copper rods on a vertically vibrating plane [70]. (A) is the sketch of the current (green arrow) predicted from the theory: such motion arises in response to the curvature of the (bending) distortion in the nematic director field (defined by coarse-graining the orientations of the grey particles); similarly (B) topological defects of strength $\pm 1/2$ are predicted, leading to the same conclusion about their corresponding currents (green and blue arrows). Notice however the radial symmetry of the -1/2 defects contrary to the $+1/2$. It is expected then that the net motion of a -1/2 defect would be null (it should go nowhere or move a little around its centre); (C-I) show the experimental evidence of this theoretical prediction: -1/2 charged defects (green circles) moves very little, while $+1/2$ charged defects (red circles) move substantially and systematically along their polarity.

phase has large regions of oriented cells with occasional topological defects of strength $-1/2$ that reinforce the nematic interpretation (see figure 3.1).

Generally, in the case of polar systems that display some collective motion, all the particles move in the same direction, so that the system has a nonzero drift velocity. Contrary, apolar particles can move collectively in rows or bands,

but with opposite directions: in this case, we end up with a null average velocity of the system. This description is close to what we see in the very early stage of bacterial microcolonies studied in this thesis work, where bacteria are so tight they tend initially tend to slide on each other side, so we cannot identify a direction of collective motion but a mere axis along which motion (in either the two direction) can take place. We will discuss this later in the corresponding Chapter 5 when we will deal with the very early stages (a few cells) of microcolonies. However, we recall that both polar and apolar active particles can form both polar and apolar phases, so there are no implications of (a)polar particles on the creation of (a)polar phases [1].

3.3 Extensile and contractile active particles

The minimal model for an active particle in a fluid is a permanent force dipole as the mutual forces of the swimmer and the surrounding fluid cancel each other by Newton's third law [72]. In the case of swimmers in a liquid environment, activity produces flow, and flow in turn reorients the principal axes of rod-like particles preferentially along the extensional axis [73].

Active suspensions with uniform orientational order are in a state of permanent uniaxial tension or compression, and are therefore intrinsically unstable [74, 75]. For instance, as depicted in figure 3.4, an individual extensile particle pushes fluid out from both ends along its main axis [76]. Contrary, an individual contractile particle pulls fluid in from both ends along its main axis [77, 78].

3.4 Instabilities in active systems

As anticipated in Chapter 1, deformations occur in passive systems when some perturbation alters the orientational state of the constituent particles. In the case of active particles, similar deformations can be seen as well, but now the source of such deformations resides in the same active particles. Furthermore, the state of deformations is not static but dynamic, in the sense that these instabilities in the orientational configuration of cells are changing as long as the particles maintain their activity, which for living cells means as long as they are alive, so there is no equilibrium or relaxation state.

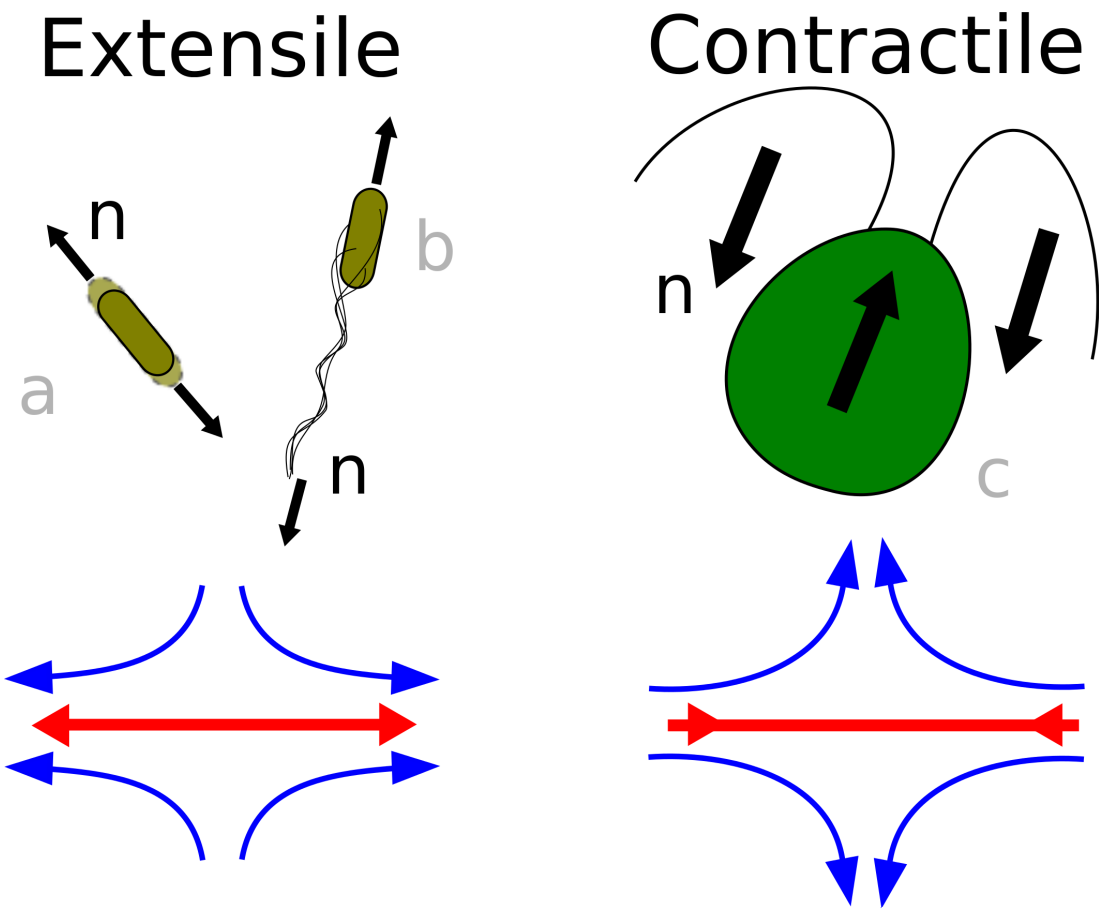

Figure 3.4: Cartoon of extensile and contractile active (living) particles. An extensile particle can be represented as a force dipole with the two components of the forces acting along the same line but outwards (double-head red arrow). A tracer in the neighbourhood of the dipole would be dragged closer and outwards along the direction of the dipole (blue arrows). Examples in nature are given by bacteria, both in their sessile (a, *e.g.* growth) and motile states (b, swimming through a liquid) [76]. A contractile particle can be represented as a force dipole with the two components of the forces acting along the same line but inwards. A tracer in the neighbourhood of the dipole would be dragged inwards along the direction and far from the dipole (blue arrows). An example in nature is given by a unicellular alga swimming through a liquid (c) [79].

In contrast to the situation of a perfectly aligned nematic phase where all the local forces cancel out, in the presence of a deformation, local stresses add up to give a non-zero net force on the surrounding environment and the direction of such force can be found by assuming the extensile or contractile character of the dipolar forces [75]. For instance, if we consider first a perfect nematic order,

the force dipoles would balance each other. However, if we perturb the system by applying a small splay deformation in a system of initially ordered contractile particles (see figure 3.5 (a)), then the density of contractile forces on the left of the splayed pattern would be larger than that on the right (b) [80]. The stress generated in this way causes in turn further splay (c).

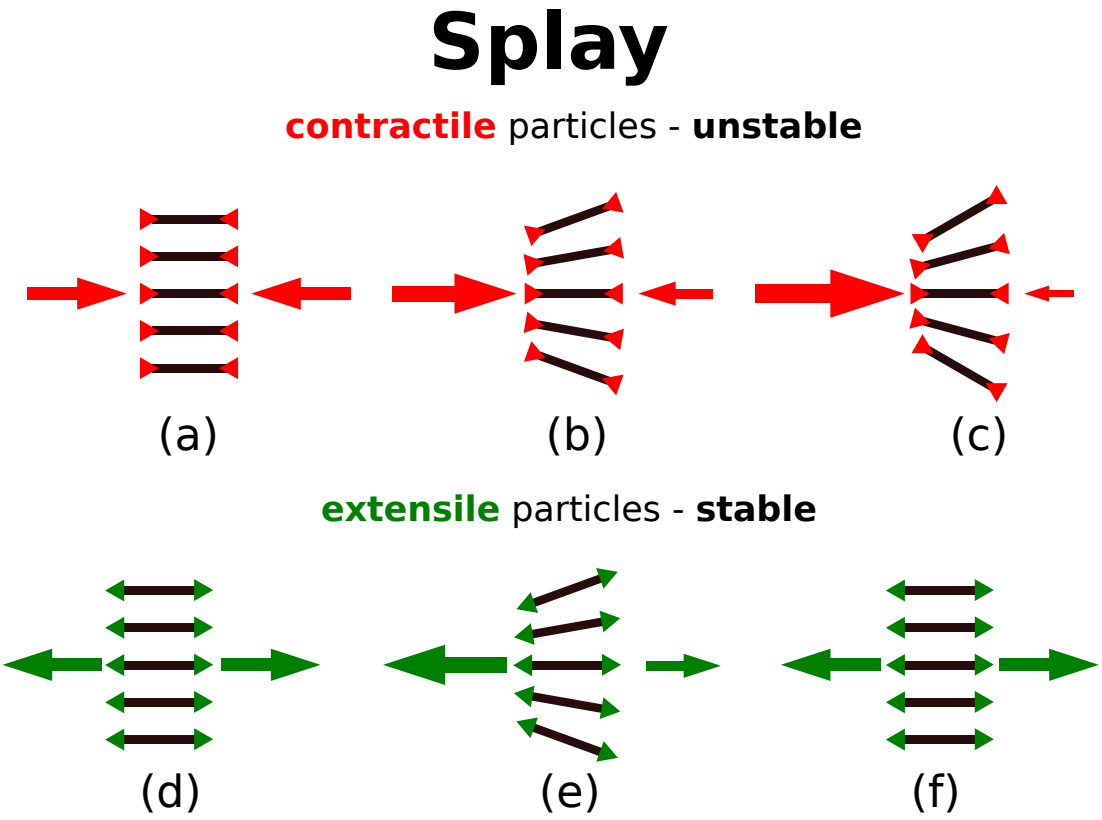

Figure 3.5: Splay deformation in contractile and extensile systems. The former case exhibits instabilities, the latter does not.

By inverting the signs of the force dipoles, that is, by considering extensile particles, we can find that an extensile system is instead stable with respect to splay (see again figure 3.5, (d-f)). However, an extensile system is unstable with respect to bend deformations, so that, once set, the initial small bend deformation would grow (see figure 3.6, (d-f)). Contrary, a contractile system is stable with respect to bend deformation, that is, the small bend deformation would not grow, but be weakened (see figure 3.6, (a-c)).

These instabilities were predicted in early theoretical work [74, 81], supported by experiments [64] and investigated through simulations [82, 83, 84, 85, 86].

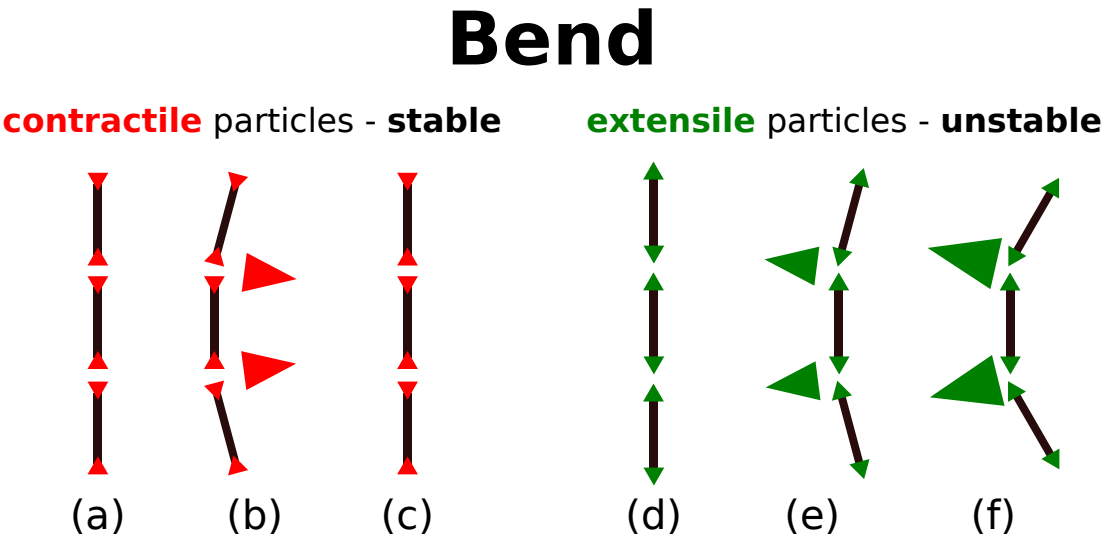

Figure 3.6: Bend deformation in contractile and extensile systems. The latter case exhibits instabilities, the former does not.

Another interesting and general way of interpreting splay and bend deformations in a 2D system is based on a broken symmetry argument [87]:[4] splay and bend produce polar configurations of collections of particles. This is interesting as, although the system could be formed by non-polar individual particles, the orientational deformation experienced by groups of particles generates some local polarity referred to the group. If we add also the absence of time-reversal invariance (due to nonequilibrium regime), that is, broken time symmetry in a driven state, we have that the now curved region must drift in a direction that is defined by the curvature, leading to a current of particles $\mathbf{J}$ with $J_x \propto \partial_y \theta$ and $J_y \propto \partial_x \theta$ in 2D, with (x, y) being the horizontal and vertical coordinates relative to the page, as represented in figure 3.7.

This kind of instabilities is investigated in the following chapters in the context of growing bacterial microcolonies as systems of extensile particles.

[4]The principle, as Curie stated it, is: When certain causes produce certain effects, the symmetry elements of the causes must be found in the effects produced. When certain effects reveal a certain asymmetry, this asymmetry must be found in the causes which give birth to them.

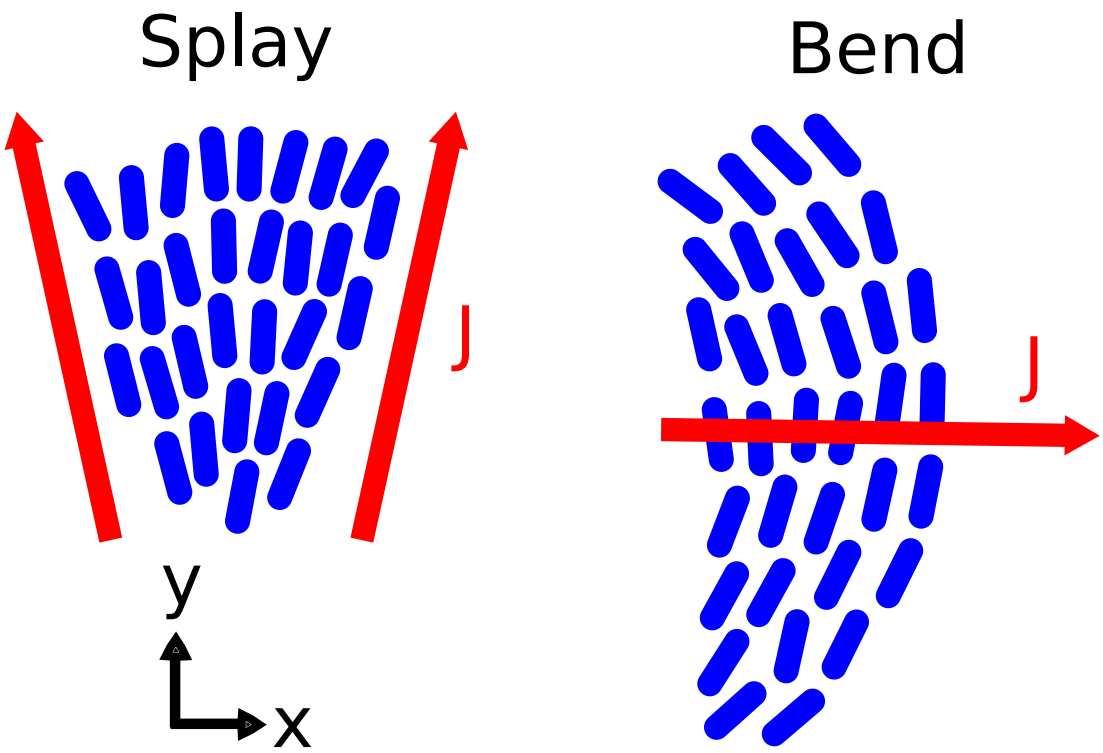

Figure 3.7: In extensile apolar nematics, curvature confers local polarity, hence local motion: the basic concept is that broken orientational symmetries lead to curvature driven fluxes (currents represented as red arrows here).

3.5 Recent works on active nematics

In this section, we discuss two recent works whose subjects share some relevant properties with our system: the first is an experimental work based on microtubule-kinesin bundles confined on a surface, the second is a numerical work based on lyotropic systems.

3.5.1 Microtubule-kinesin bundles

Using extensile microtubule-kinesin bundles as building blocks, researchers have been able to assemble a nonequilibrium analogue of a conventional - *i.e.* passive - LC [88, 89]. In presence of a high concentration of such bundles, an active network forms, exhibiting internally driven chaotic flows, nemato-hydrodynamic instabilities, enhanced transport and fluid mixing. Here, kinesin clusters - that is, the molecular motors that convert chemical energy from ATP hydrolysis into mechanical movement - bind and walk between two aligned microtubules with

different polarity.

However, when these microtubules are confined to a 2D film represented by an oil-water interface stabilized with surfactants, the network forms spontaneously, giving rise to a highly active 2D nematics, that is, a liquid-crystalline monolayer of locally aligned bundles. In this condition, surface streaming flows appear and the microtubule bundles are subject to internally generated fractures, self-healing. Furthermore, generation, unbinding and annihilation of oppositely charged topological defects take place. It is interesting to note that the patterns obtained from this system are qualitatively similar to those observed in other nonequilibrium systems of very different nature, *e.g.* swarming prokaryotic [64, 90, 73, 91] and eukaryotic [92, 93], swimming spermatozoa [94].[5]

More specifically, information about the nature of active microtubule LCs can be obtained through the examination of the structure and the dynamics of their topological defects. Active LCs can have either nematic [68, 96] (*e.g.* monolayers of amoeboid cells or vertically shaken monolayers of granular rods [62, 70]), or polar symmetry (*e.g.* given by motility essays at high concentration [58, 97]), with the latter forming also vortex and aster defects [58, 98].

The researchers working on active microtubule LCs found that the microtubules form topological defects of charge $\pm 1/2$, as shown in figure 3.8. This result is expected because the basic building blocks of these materials are the symmetrically extensile microtubule bundles.

When dealing with LCs at equilibrium, defects are largely static structures whose presence is determined by either internal frustrations or external boundary conditions. By contrast, in this active case, defects exhibit unique dynamics: defects are created when uniformly aligned nematic domains extend, buckle and internally self-fracture. A fracture line exhibits two oppositely charged defects at its ends, and, as the fracture line self-heals, these two defects remain unbound and move, with the possibility of annihilating at later times when encountering other oppositely charged defects. Recently, some authors have also interpreted the $+1/2$ charged defects as active particles [99, 100]. In this spatially extended system, the rates of defect creation and annihilation were balanced, creating steady-state streaming dynamics that could persist for many hours.

[5] Such experimental evidence is corroborated by numerical works based on coarse-grained models of extensile rod-based suspension for which hydrodynamic instabilities are predicted [95].

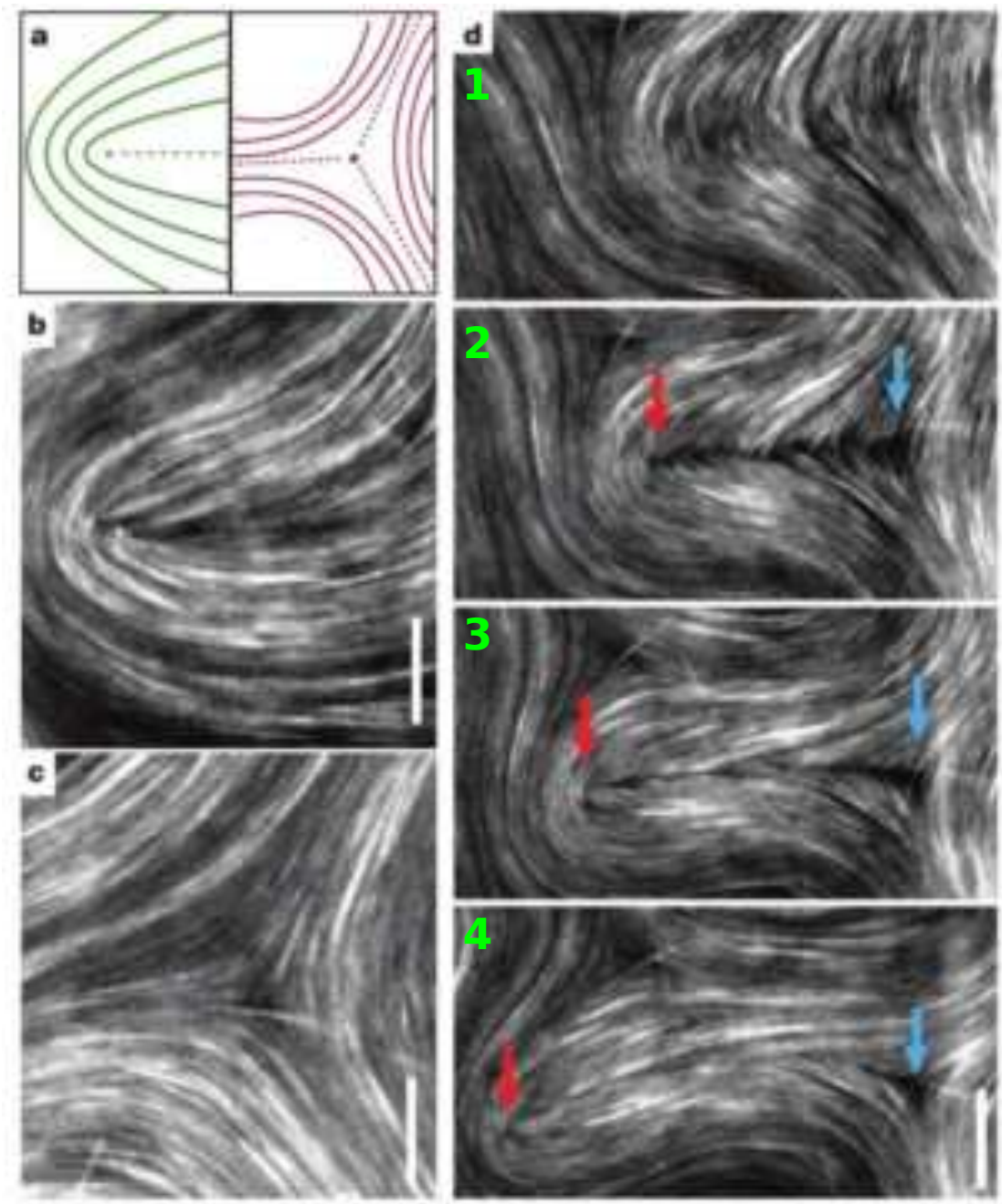

Figure 3.8: Topological defects in microtubule-kinesin suspensions. $\pm 1/2$ charged topological defects (sketched in (a)) are observed as in (b, c). Folding and internal fracture of a nematic domain result in a pair of oppositely charged defects (d1-4). The red arrow indicates $+1/2$ charged defect, the blue $-1/2$. After the fracture line self-heals, the defect pair remains unbound. Scale bar is 20 µm, time-lapse is 15 s [88].

These observations, supported by numerics [101], show how active nematics are fundamentally different from equilibrium ones, in which fractures, internal flows and spontaneous generation and annihilation of defect pairs are not observed.

3.5.2 Lyotropic active nematics *in silico*

In a recent work, researchers reported results from dynamical simulations of a 2D active nematic-isotropic mixture [102], that is, a system consisting of an initial drop (circle) of active nematic, surrounded by an isotropic phase.

Interestingly, they observed during the evolution of the system that the extensile nematic drop elongates in the direction parallel to the director field. To explain this behaviour, it is necessary to consider the active force acting at the interface that includes contributions from gradients in the nematic order represented by the order parameter Q. The active force can be decomposed in the components, perpendicular and parallel to the interface, and it can be shown [102] that the perpendicular component of the active force is given by the following expression:

$$F_{\perp}^{a} = \chi |\nabla Q| (2(\mathbf{m} \cdot \mathbf{n})^2 - 1) \,, \tag{3.1}$$

where χ is the activity ($\chi > 0$ for extensile case), Q is the order parameter, $\mathbf{n}$ the director and $\mathbf{m}$ is the normal to the interface. We observe that in the case of a director parallel to the normal to the surface ($\mathbf{m} \cdot \mathbf{n} = 1$), the active force is positive, that is, the active extensile drop is stretched, or in other words, it elongates where the interfacial alignment is locally homeotropic; in the case of a director perpendicular to the normal to the surface ($\mathbf{m} \cdot \mathbf{n} = 0$), the active force is negative instead, resulting in a compression. Thus, because of this mechanism, the director field is oriented parallel to the interface almost everywhere, except at the ends of the elongated structure (see figure 3.9).[6] The parallel component of the active force contributes by generating a flow at the interface, so that the resulting velocity gradient tends to rotate the director parallel to the interface ([102]).

This phenomenon of alignment of the director parallel with the boundary of the system is similar to what we can actually observe in our system of growing

[6] In the case of a contractile suspension, the drop extends perpendicular to the nematic order, as the forces are reversed.

bacterial microcolonies as we will discuss in more detail in Chapter 6, and also other works have reported it [103, 47]. Here, the phenomenon is referred to as active anchoring because the authors attribute to the active forces present at the nematic-isotropic interface its origin. It is important to notice that, while many simulations incorporate anchoring, *i.e.* a preferred orientation of the director field at the interface explicitly through coupling terms in the free energy, it is not the case for this work. Here, the origin of the anchoring is not thermodynamic, but it is the active stress itself that is responsible for the generation of a preferential orientation, mostly parallel to the interface.

Later on, hydrodynamic instabilities lead to bend deformations, typical of the extensile nematic [1].[7] Eventually, these deformations lead to the formation of $\pm 1/2$ charged defects, as shown in figure 3.9. Depending on their charge, these defects move in a different way. For instance, it is observed that positive half-integer defects migrate into the nematic, a behaviour that is in contrast with bulk active nematics, whereby topological defects of charge $\pm 1/2$ are produced in pairs; whereas negative defects are spread over regions of small curvature. This is interesting as in our growing bacterial colonies we can observe differences in the behaviour of these defects as well, depending on their charge (discussed later in detail in Chapter 5).

[7] In the bulk, this would lead to active turbulence [91].

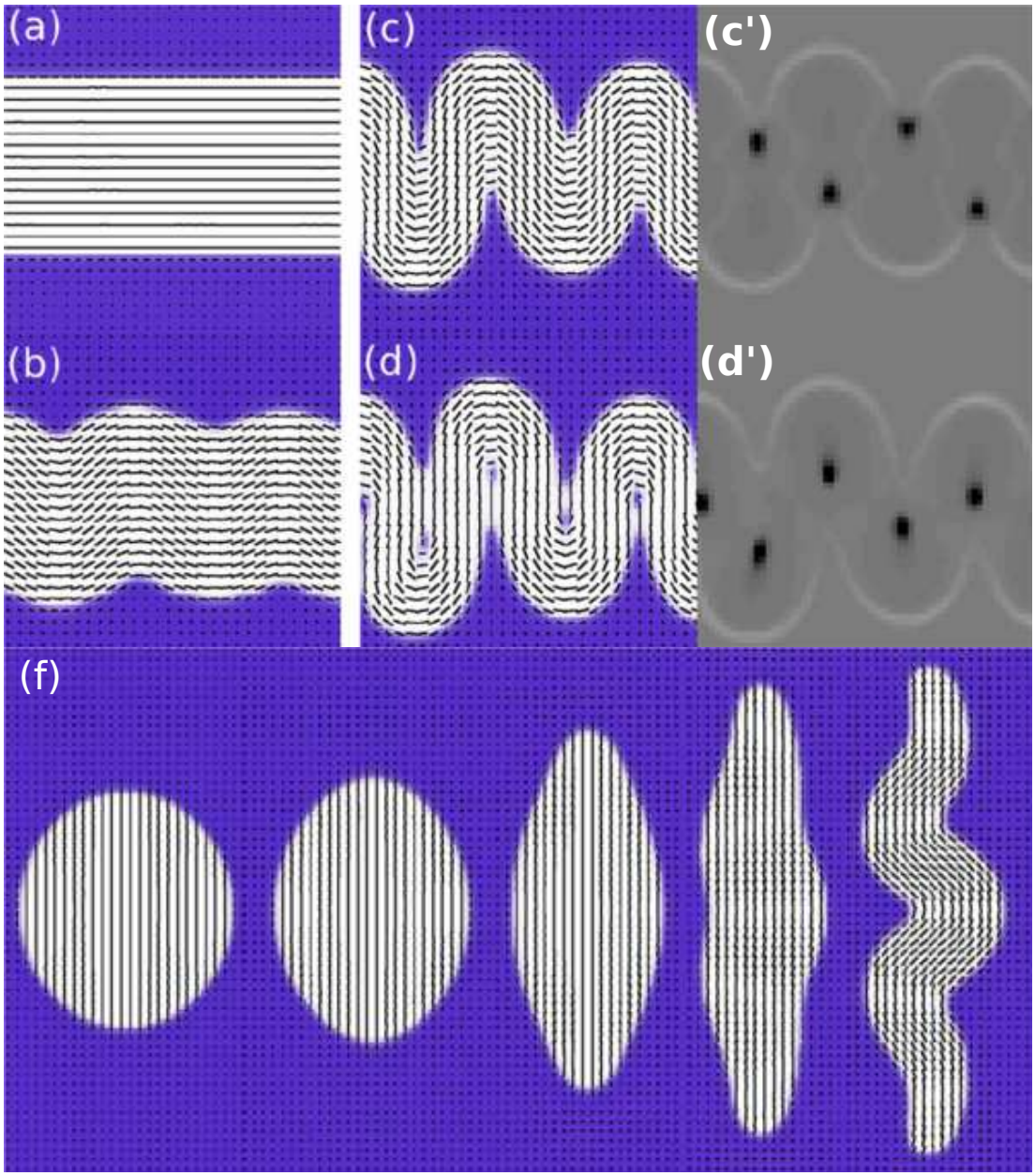

Figure 3.9: Distortions and defects in lyotropic active nematics. The onset of interface instabilities in a band of extensile active nematic results in the formation of defects (sequence (a-d)). Dark points (panels (c') and (d')) correspond to +1/2 charge defects, as obtained from the charge density map of (c) and (d). In (f), the evolution of an initially circular disk of extensile active fluid is shown. The nematic phase is represented in white, the isotropic phase in blue. The black segments represent the director map. The disk extends parallel to the director field, and the surface alignment becomes predominantly parallel to the interface. Reproduced from [102].

Chapter 4

Materials and Methods

We begin this chapter by describing the way bacteria have been cultured. The detailed protocols used for preparing growth media and mutants are given in the appendix. We focus then on the sample preparation and set-up used for imaging it, and performing the time-lapse experiments. We conclude by discussing the methods used for analysing the images that allowed for extracting the fundamental dynamical observables as position, orientation and size of bacteria in the flat geometry.

4.1 Culturing bacteria

In this section, we describe how bacteria are cultured. The way bacteria are cultured depends on the strain used and the aim of the experiment we are interested in. Differences emerge in the choice of growth media, temperature of incubations, oxygenation via sample shaking, use of antibiotics, just to name a few.

The protocol for growing bacteria is divided for the sake of clarity into 3 steps performed over 3 days, starting from the frozen stock to the final bacterial solution ready for the sample preparation. Depending on the strain cultured, antibiotics could be used: in this case, we recall during the protocol the additional steps to be performed in order to obtain such selected culture. All solutions are sterile and techniques are such that they guarantee sterility.

- Day 0 - Bacterial cells (wild-type or one of the three mutants used in this work) from a frozen stock (cryotube) kept at -80 ℃ are struck onto a LB

solid agar Petri dish using a sterile titanium loop, then placed into a static incubator at 30 ℃ for 24 h. For mutant cultures, specific antibiotics are added to the melted agar (thermalized to a temperature of 55 ℃ because of antibiotic sensitivity to temperature) during the preparation of Petri dishes. The reason for using antibiotics is that these mutants are resistant to them, so these specific growth media allow for the selection of the only mutant strain we are interested in (killing all the other unwanted, different cells, which can either derive from a contamination or from mutations). In the experiments, two antibiotics have been used: kanamycin (KAN), whose working concentration is 30 µg/ml, and ampicillin (AMP), whose working concentration is 100 µg/ml;

- Day 1 - After 24 h, if the colonies grew healthy, then bands of individual bacterial colonies looking like pale white spots could be seen. Using again a sterile titanium loop, a single colony - well separated from the neighbour colonies (in the assumption that each colony originates from a single bacterium) - is collected and introduced into a 100 ml flask containing 10 ml of pre-warmed (at 37 ℃) LB medium, simply by shaking the loop tip into the liquid. Then the flask is put into a shaking incubator overnight at 37 ℃, 200 rpm. Again, kanamycin antibiotic is added in case of experiments with mutants at the concentration previously specified;

- Day 2 - 100 µl of the overnight bacterial suspension is pipetted into a second 100 ml flask containing 10 ml of pre-warmed (at 37 ℃) M9 medium (hence a 1/100 dilution). Cells in the exponential phase (optical density at wavelength of 600 nm: $OD_{600} \approx 0.2 - 0.3$)[1] are then diluted to a final concentration of $OD_{600} = 0.001$-0.002: this very small value is suitable for the time-lapse experiment as the agar pad onto which cells are injected has to be scarcely populated: it is necessary to have well-separated bacterial colonies to avoid overcrowding and any possible

[1]Measurements of ODs (using a Hach-Lange DR5000 UV/VIS spectrophotometre) are relative to zero measurement of the medium into which cells are cultured (that is LB or M9), and diluted as many times as necessary to ensure a linear response from the spectrophotometre during the measurement: if the cuvette containing the bacterial suspension was too concentrated, the machine would give a high but non reliable value as it would be working in a nonlinear regime where the intensity of light is not linked to the OD by the usual logarithmic relation: $OD = \log(I/I_0)$.

chemotaxis between growing colonies.

4.2 Preparation of samples for time-lapse experiments

All solutions are sterile and techniques are such that they guarantee sterility.

1. We start by warming up the 2% agarose M9 medium that will form the agar pad onto which the droplet of bacterial suspension at a very low concentration ($OD_{600} = 0.001 - 0.002$) will be injected. Again, when working with mutants resistant to some specific antibiotic, we will add that specific antibiotic with the right concentration to the M9 during its preparation. We usually store such medium in 40 ml Falcon tubes kept in the +4 ℃ fridge. By quickly microwaving a Falcon tube, we can bring the medium to liquid phase and keep it in such phase by putting the tube in a warm water bath (or simply a larger bottle with hot water);

2. We take a standard microscope glass slide (5 cm x 2 cm x 1.5 mm), sterilize it using either the Bunsen flame or a tissue soaked with some ethanol. Then, we attach a sticky frame (Gene Frame by ThermoScientific) to create a suitable space into which inject the melted agar;

3. 400 µl of melted 2% agarose M9 medium are poured into the space created by the frame and - very rapidly - a second sterilized glass slide is put on top of the frame, and a gentle pressure applied. The medium will spread and some of it will come out of the frame, but that is expected as the nominal volume of the space created by the frame is smaller than the 400 µl we injected. The medium will cool down and solidify. It is possible to put it into the fridge to speed up such process;

4. Once the medium has cooled down and solidified, the top glass slide is removed slowly in order to keep the top surface of the medium as flat as possible. Using a scalpel, 3 or 4 bands of the width of about 4 mm are cut on the medium pad, leaving a space between them of about 1-2 mm. Such spaces help in distinguishing between different bands (where

different strains and/or mutants can be inoculated) and also to create oxygen reservoirs;

5. A 1.5-2 µl droplet of the previously-prepared bacterial suspension is poured on the top of each band. The whole sample is tilted several times clockwise and counterclockwise so to spread the content of the droplet along the whole band;

6. After the liquid content of the droplet has evaporated, a microscope coverslip is attached to the sticky boundary of the frame so to seal the whole sample that is now ready for being imaged (see figure 4.1).

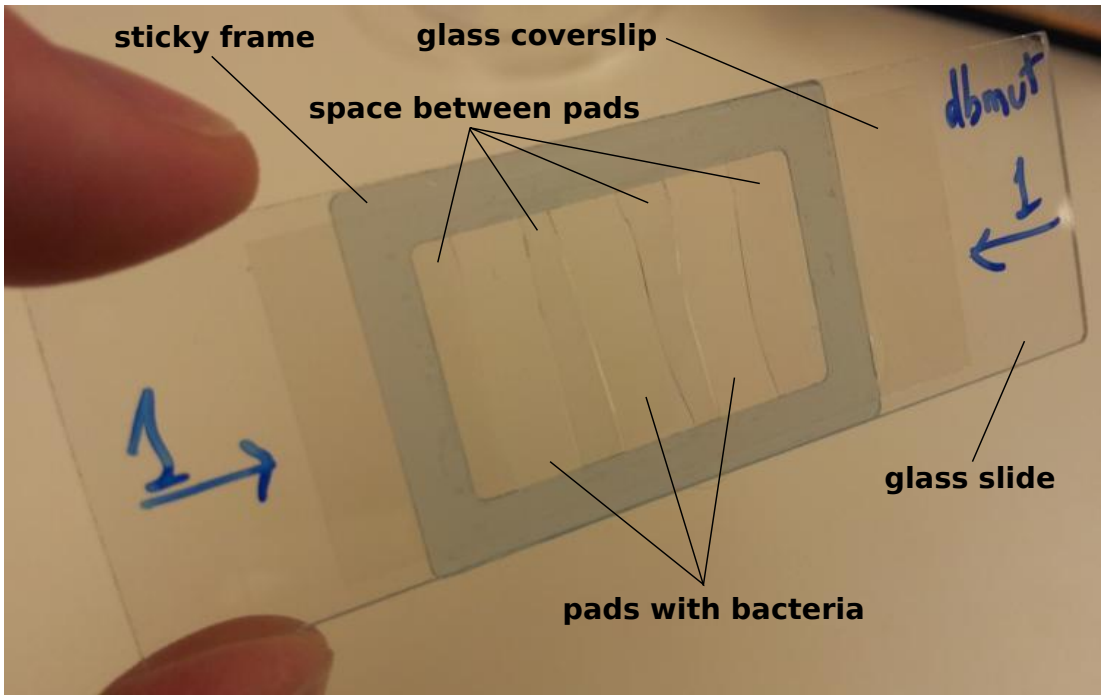

Figure 4.1: Sample for time-lapse microscopy.

4.3 Microscopy techniques

In this section, we describe the general principle of microscopy methods and the set-up used for the time-lapse experiments. More detailed aspects of phase contrast and confocal microscopy can be found in [104, 105].

Phase contrast The working principle of brightfield microscopy is based on the absorption of light by the specimen that we want to image. Depending on the nature of the regions that are being imaged, the amount of light absorbed varies accordingly, and eventually these differences result in the contrast between the regions of interest and the background [104].

However, in the case of bacteria, brightfield microscopy is not effective in giving good imaging as these cells are nearly transparent, that is they absorb very little amount of light. Despite this poor absorption, most biological specimens are still able to modify in a certain way the light rays that pass through them. They can indeed induce a phase shift in these light rays, and for this reason they are usually referred to as phase objects.[2] Phase contrast microscopy is a technique alternative to brighfield that was developed by Zernicke in 1930, which transforms differences in the phase of object diffracted waves to differences in the image intensity.

In order to achieve this transformation, it is necessary (i) to isolate the non-diffracted waves from the diffracted ones emerging from the specimen so that they occupy different locations in the diffraction plane at the back aperture of the objective lens, and (ii) to advance the phase and reduce the amplitude of the non-diffracted waves in order to maximize the differences in amplitude between the object and the background in the image plane. For obtaining such changes in the wave properties, two specific pieces of equipment are required: (i) a condenser annulus and (ii) an objective lens bearing a phase plate or ring.

The condenser annulus is an opaque black plate with a transparent annulus that is positioned in the front aperture of the condenser so that the specimen is illuminated by beams of light emanating from a ring (hollow cone of light). Under conditions of Köhler illumination, non-diffracted waves (that do not interact with the specimen) are focussed as a bright ring in the back focal plane of the objective (that is the diffraction plane). By contrast, waves diffracted by the specimen traverse the diffraction plane at various locations across the entire back aperture. The amount and the location of light depends on the number, size, and refractive index of light-scattering objects in the specimen.

Since the nondiffracted and diffracted light are spatially separated in the

[2] In addition to phase objects, amplitude objects are also recognized, which can produce directly amplitude differences in the image. These differences are detected by the eye as differences in intensity. In this case, specific wavelengths are absorbed by dyes or pigments.

diffraction plane, it is possible to selectively manipulate the phase of the two. Hence, a phase plate or ring - the second specific piece of equipment - is mounted in or near the back focal plane of the objective. The phase plate usually consists of a plate of glass with an etched ring of reduced thickness to selectively advance the phase of the non-diffracted wave by $\lambda/4$ in the case of constructive (positive) phase contrast microscopy (where λ is the wavelength of the light). Furthermore, the same ring is also usually coated with a partially absorbing metal film to reduce the amplitude of the light by 70-80 %, because the non-diffracted wave is much higher in intensity than the diffracted wave (see figure 4.2).

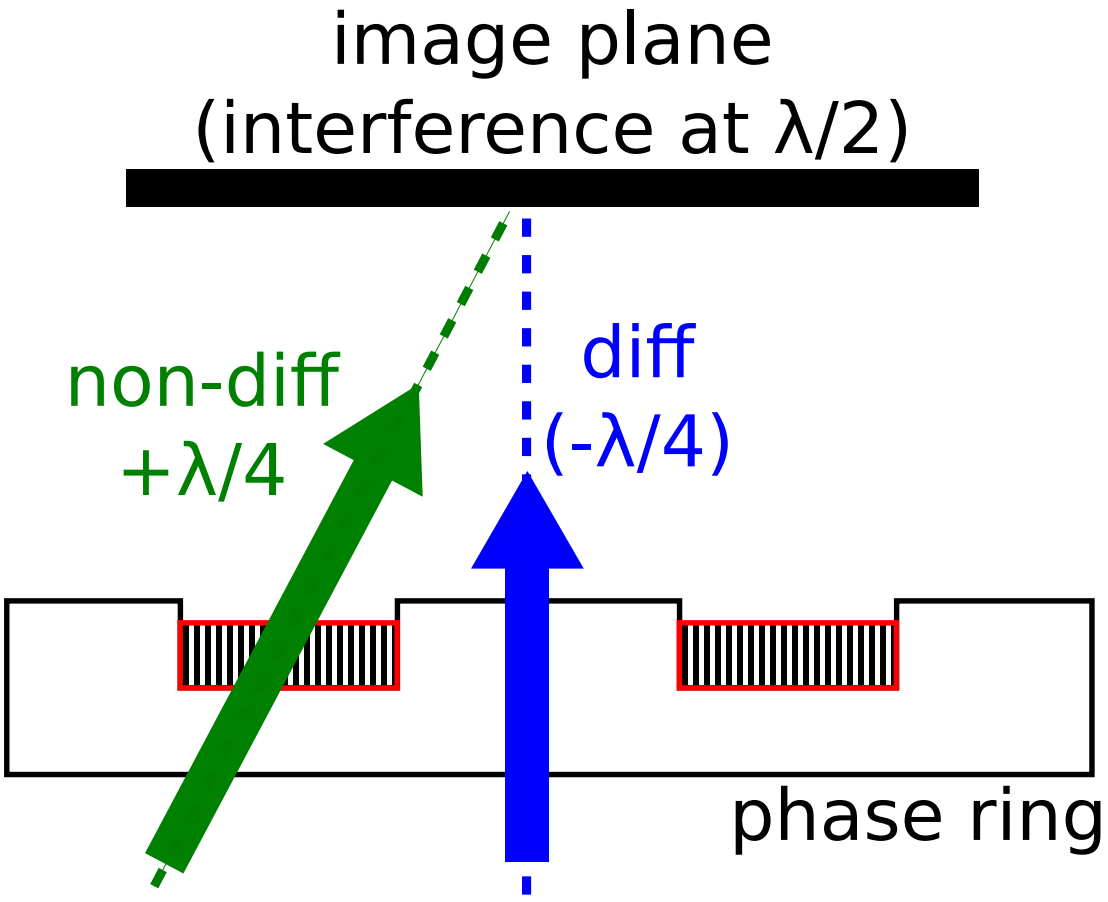

Figure 4.2: Sketch of phase retardation. The phase plate or ring receive the background non-diffracted and diffracted light. The non-diffracted light ray phase is advanced of $\lambda/4$ relative to the scattered one by a ring etched into the phase plate, with a smaller width. Additionally, the intensity of the non-diffracted light is decreased through the a metal film deposited on the ring which absorb about 70% of the wave intensity. The scattered light has been already retarded by $\lambda/4$ during its interaction with the object, hence the overall change is of $\lambda/2$.

The diffracted wave emergent from the object plane is retarded by $\lambda/4$ from the same object, hence increasing the overall path length difference to $\lambda/2$. The final result is that, as the two waves interfere destructively with each other at the image plane, the object of interest is manifested as regions of low intensity, *i.e.* darker regions, against a brighter background.

Phase contrast images can show characteristic patterns of contrast, called phase halos, as a natural result of the phase contrast optical system, in which the observed intensity does not correspond directly to the optical path difference of the object. Phase halos always surround phase objects and may be dark or light depending on whether the optical path through an object is greater or less than that of the medium. For phase objects that appear dark, as the bacteria observed in our experiments, halos result in brighter boundaries. This is the reason why we observe usually brighter boundaries of our colonies. Phase halos occur because the ring in the phase plate in the objective back aperture can also receives some diffracted light from the specimen. Since diffracted waves corresponding to low spatial frequencies pass through the annulus on the plate, they remain $\pi/2$ out of phase relative to the 0th-order non-diffracted light. Hence, the absence of destructive interference by these low spatial frequency diffracted waves causes a localized contrast reversal. Usually, phase halos are excessive for specimens thicker than 5 µm, resulting in a non easy determination of the microorganism boundaries. However, we do not have such a thick layer of bacterial culture: in the case presented in this thesis, the bacterial carpet is 1 µm-thick only, that is, one cell width.

In our experiments, the sample is imaged using a Nikon Eclipse E-800 microscope with a Nikon Plan Apo λ 100x/1.45 Ph3 oil objective in phase contrast settings (see figure 4.3 for a sketch of the set-up and a typical phase-contrast image of a bacterial colony). Minimum illumination intensity is used to minimise photo-damage to the cells; exposure time varied from 20 to 100 ms for each image capture. The time-lapse is set to 1 or 2 minutes[3] and frames were recorded using a Q-imaging Retiga 2000R camera. The microscope used for phase contrast imaging is enclosed into a temperature-controlled box that allows us to keep the

[3]A 1 minute time-lapse corresponds to a better frame rate, but cells are then exposed to light more frequently, and the automated stage moves continuously leading to some early defocussing of the imaged colony because of some errors in re-locating the stage to the previous positions once the cycle of frames has been finalized.

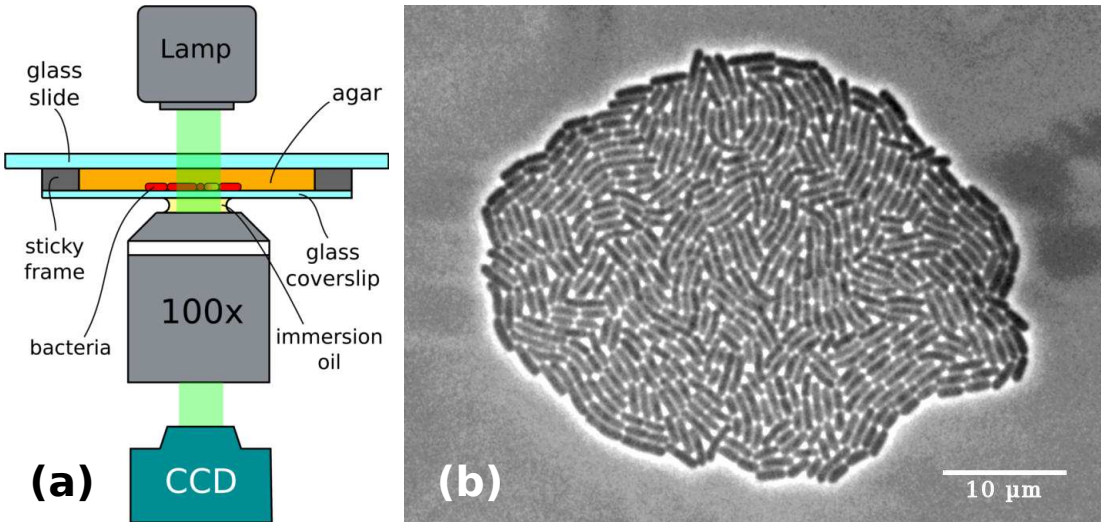

Figure 4.3: (a) Sketch of the phase contrast microscopy set-up used for time-lapse experiments on *E. coli* bacterial microcolonies. The experiments were performed with the microscope being enclosed in a temperature-controlled box (at 37 ℃). (b) Typical phase contrast image of a bacterial colony.

whole sample at a stable temperature of 37 ℃.

Confocal microscopy Although our main method was phase contrast, we also performed a few experiments using confocal microscopy for 3D imaging of the samples used in time-lapse experiments. Confocal imaging is performed using a Zeiss confocal laser scanning microscope LSM 700 with a Zeiss Plan-Apochromat SF20 63x/1.46 oil objective in order to establish the 3D configurations assumed by bacteria. In figure 4.4, we provide an image of GFP *E. coli* bacteria of the same wild-type strain we used in the time-lapse experiments. The agar they are in contact with has been dyed with rhodamine B (0.02% w/v) (red channel) for enhancing contrast with the cells (green channel) and the glass that is the black area in the two side projections.

Images indicate that bacteria are immersed into the agar pad and not onto it: actually, they are compressed when the sample is closed from above with the microscope coverslip, so the cell upper part is in contact with the glass, and the sides and the lower part are embedded into the agar. The yellow spots in the low-right portion of the image represent some dust on the surface of the agar pad.

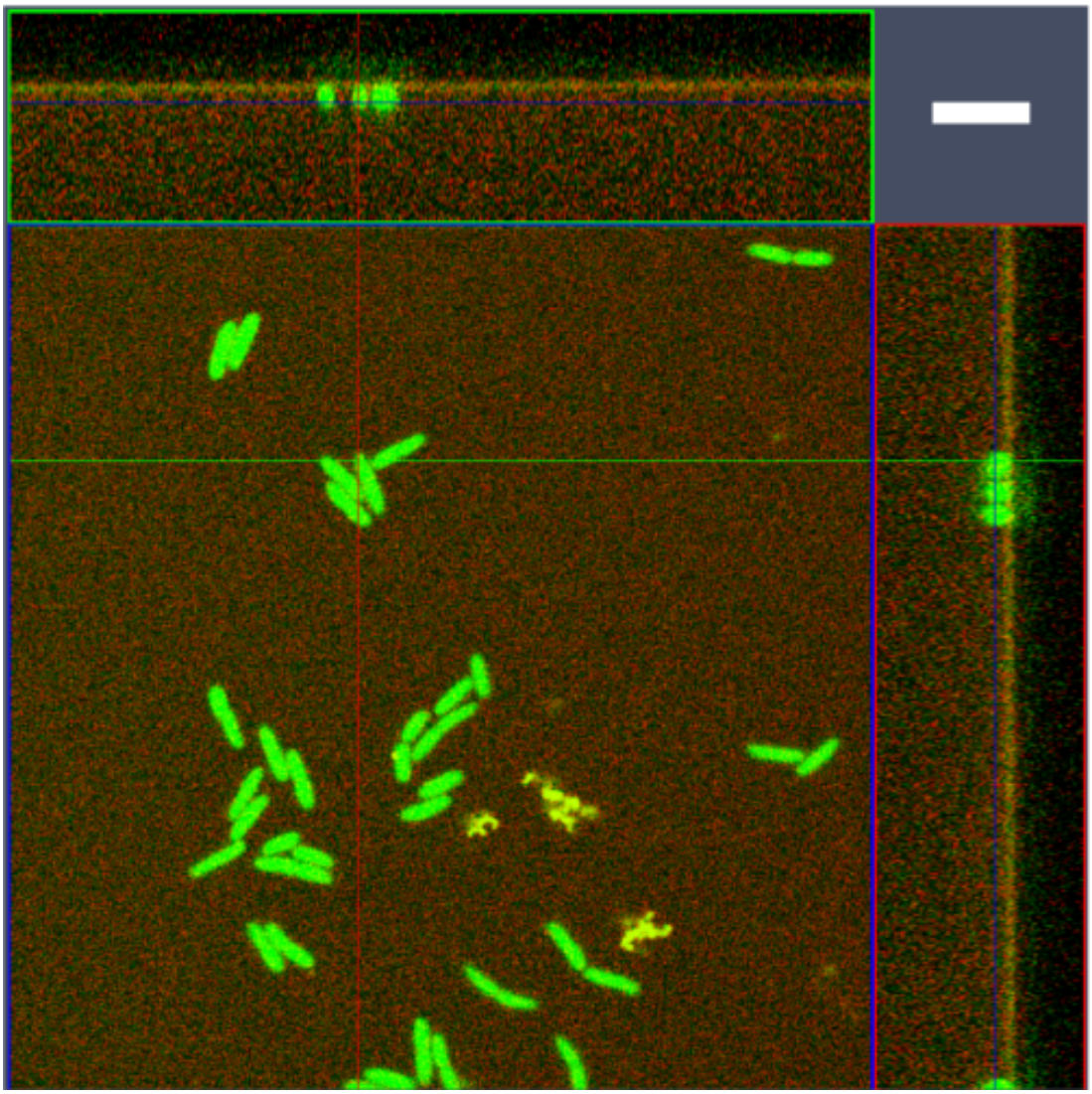

Figure 4.4: Confocal microscope image with side projections. The aim here is to image the spatial configuration assumed by the bacteria once the drop of bacterial sample has been injected onto the agar pad, left dry out and sealed with a microscope cover slip. Scale bar in top-right corner is 5 µm.

4.4 Image analysis

Correction Image analysis is performed using ImageJ. Initially, the frames are cropped to the actual area covered by the colonies at their last stage (the total field of view achievable is at least 3 times larger). Then the frames are adjusted in brightness and contrast, and shift corrected because initially the agar pad, despite being confined between the glass slide and the microscope cover slip, tends to slide. This is due to the changes in temperature: the agar goes from melting temperature (before being poured into the frame) to room temperature during the injection and drying of the cell droplets onto the pad (the whole process takes on average 10 min), and finally to the higher temperature of 37 ℃. Such sliding is limited to a few microns and, as time passes, the pad settles and no longer moves (around a few generations, that is tens of cells). Such correction was performed using an ImageJ macro called StackReg [106]. Furthermore, before segmentation, images are also pre-processed using background subtraction, Gaussian smoothing, or unsharp masks.

Segmentation Finally, frames are ready for being segmented so that the position in the plane, the orientation angle with respect to the reference horizontal axis of the image, and the length of each cell could be extracted. Segmentation is carried out using the Matlab-based Schnitzcells software [107, 108] which returns the morphological features from each cell segmented, such as its size, angle or position within the colony.[4] Through a combination of edge detection, thresholding and watershedding, cells are identified, with the final result given by a mask of the starting phase contrast image, from which centre of mass (c.o.m.) positions, orientations, lengths and widths for all cell are extracted by a backbone fit. See figure 4.5 for an example illustrating the result of segmentation.

This process is fully automated, but for certain images, corrections done manually by the user are needed. Figure 4.6 reports some typical errors it is possible to encounter using Schnitzcells. Typically, errors in segmentation consists of a wrong split of cells (at a wrong time for the mother cell or along the lengths of the two daughter cells) or the identification of speckles as cells. Both errors can be easily corrected manually when dealing with a few-cell colonies, but

[4] The software actually allows for the tracking of the whole colony lineage.

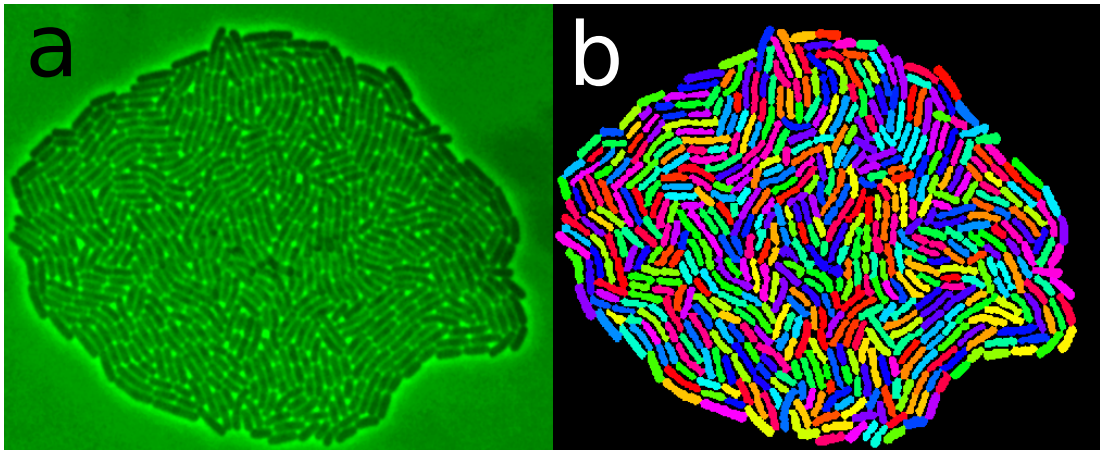

Figure 4.5: Processing of images: (a) phase contrast image as obtained from experiments and (b) the segmented mask after processing with Schnitzcells. Colours are assigned randomly by the program with the only aim to ease the identification of the individual bacteria.

the correction time increases for very large colonies counting hundreds of cells. Generally, better quality images (in terms of good contrast between cells and background) need fewer corrections applied to the corresponding mask.

The Schnitzcells software can process both phase contrast and fluorescence images, and the user has the possibility to set some segmentation parameters, whose choice could depend on the kind of organism being imaged, and other experimental conditions. Despite fluorescence images having a higher rate of success in terms of segmentation processing (that is less correction of the masks needed, because of the better contrast between cells and the background), we used phase contrast images as cells were found to photo-bleach in a relatively short time with respect to duration of the experiments (from the third generation on, images started fading). Using phase-contrast images, we had to correct more frequently the corresponding masks, but we could reach larger colony sizes.

4.5 B-spline for boundary analysis

In order to investigate the orientation of bacteria at the boundary of the microcolonies, a method based on B-spline curves has been employed. We give a brief description of such method and the way we used Mathematica to implement and apply it to our case (whose results are presented in Chapter 6).

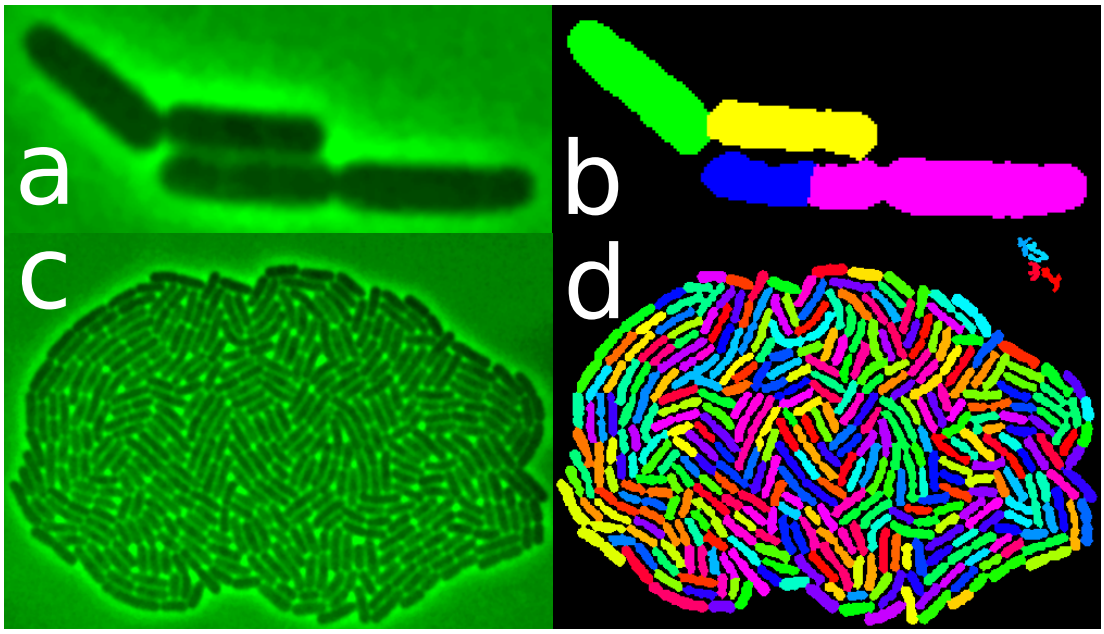

Figure 4.6: Errors in Schnitzcells segmentation mask typically consist of (a-b) wrong splitting of cells (blue and magenta cells are split incorrectly), and/or (c-d) wrong identification of speckles as cells (top right, red and blue objects are not cells, but dust). These can be both corrected manually *via* Schnitzcells software interface.

First, for a given colony, we consider the c.o.m., and the orientation angle (measured with respect to the horizontal axis of the image) of all the bacteria at the boundary of the colony. Such data are available from the phase contrast image using the Schnitzcells software based on Matlab, as discussed in the previous section 4.4. The data are imported and analyzed using a Mathematica script written for this specific purpose. We then use a built-in function provided in Mathematica that allows us to draw a closed, smooth curve - that is, a B-spline - approximating the boundary of the colony, once all the c.o.m. positions of the bacteria, have been ordered either clockwise or anti-clockwise.

The function takes as arguments the c.o.m. points as controls and returns a spline, that is, a numeric function that is piece-wise defined by simpler polynomial functions, possessing a specifiable degree of smoothness at the points where the polynomial pieces are joint with each other.[5] We varied as a test the degree of the polynomial basis used to build the curve by giving as input values larger than 3 (the default degree), but we could not see any important difference and effects on

[5]For the formal definition of the B-spline, see the following link: B-spline MathWorld.

the final results plotted in the orientation histograms. Control weights of control points are all set equal. Once the curve is generated, we compute numerically the tangent vector to such curve close to the corresponding control points. We then consider the angle between the tangent vector and the orientation of the bacterium (modulo π, because if the numerical value of the angle is larger than $\pi/2$, then we have to subtract π). All these angles are then collected and plotted in histograms and averages computed (as illustrated in the corresponding plots shown in figure 6.16).

Part II

Bacterial Microcolonies as Living Nematics

Chapter 5

Experimental results

In this Chapter, we present our experimental work on 2D bacterial microcolonies. We begin with the phenomenology, that is, by describing the growth of a microcolony from the first, single mother cell to hundreds of offspring. We then investigate qualitatively and quantitatively the global and local properties of this active system, basing this investigation on a LCs approach. We explore then the instabilities occurring in a nematic description of the colony, and the ensuing topological defects.

5.1 Phenomenology of 2D growing microcolonies

We experimentally investigate bacterial microcolonies of *E. coli* cells growing in a 2D geometry. We refer to them as microcolonies as we consider only their evolution from the first individual mother cell to about a thousand of cells, that is, between the 9^{th} and the 10^{th} generation. In these observational conditions, colonies reach a typical size of about 50 µm, hence the term microcolonies. Contrary, when fully-developed, a colony grown on agar into a Petri dish looks much larger, that is, of the order of a few mm, counting billions of cells (see Chapter 2 on bacteria for the formation of a macroscopic bacterial colony).

The growth process of a *E. coli* colony is based on the simple binary division of cells that determines an exponential increase in the number of cells on time (see figure 5.1). In figure 5.2, we show the histogram of the doubling times for all the colonies, that is, the time it takes to the colony to double its cell number from the n-th to the $n+1$-th generation. The mean doubling time is 29.24 minutes

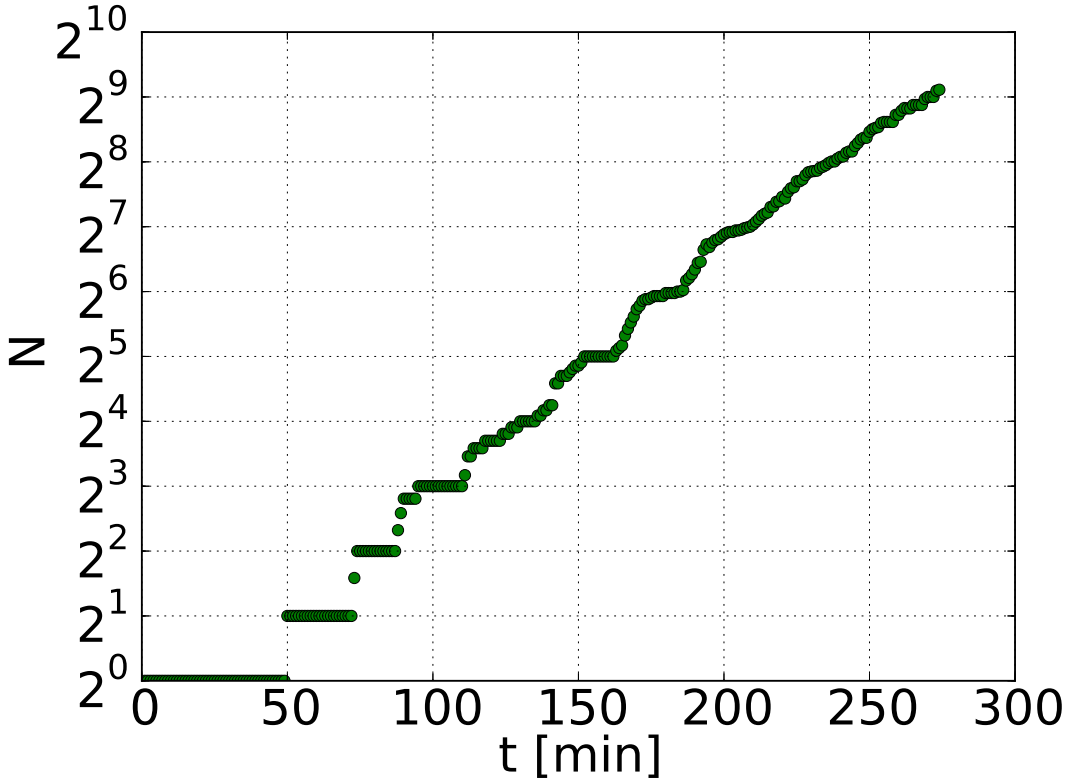

Figure 5.1: The number of cells N as a function of time t in a growing bacterial colony. The growth of the colony is exponential in the time range explored. We observe a sort of step-wise trend for initial times: this is due to cells dividing in synchronization. However, as the colony grows, such synchronization is lost, and the trend looks more similar to a straight line.

with a standard deviation of 7.07 minutes.

In figure 5.3, we show the plot of the mean values with standard deviations for each doubling time among generations, that is from 2 cells to 4, then 4 to 8, and so on, until the 9-th generation corresponding to 512 cells.

We observe that the detection of the division time of the first mother can be problematic for two reasons essentially: first, it is not clear what is the initial (generation) time t_0 of the mother cell; second, even if we assume that the time t_0 of the mother cell is the time from which we start imaging, the mother cell usually divides at a later time than its offspring, that is, a longer 40-50 minutes for the mother cell when compared to the shorter 30 minutes of the offspring, as shown in figure 5.1. This longer time can be due to the stresses the mother cell experiences

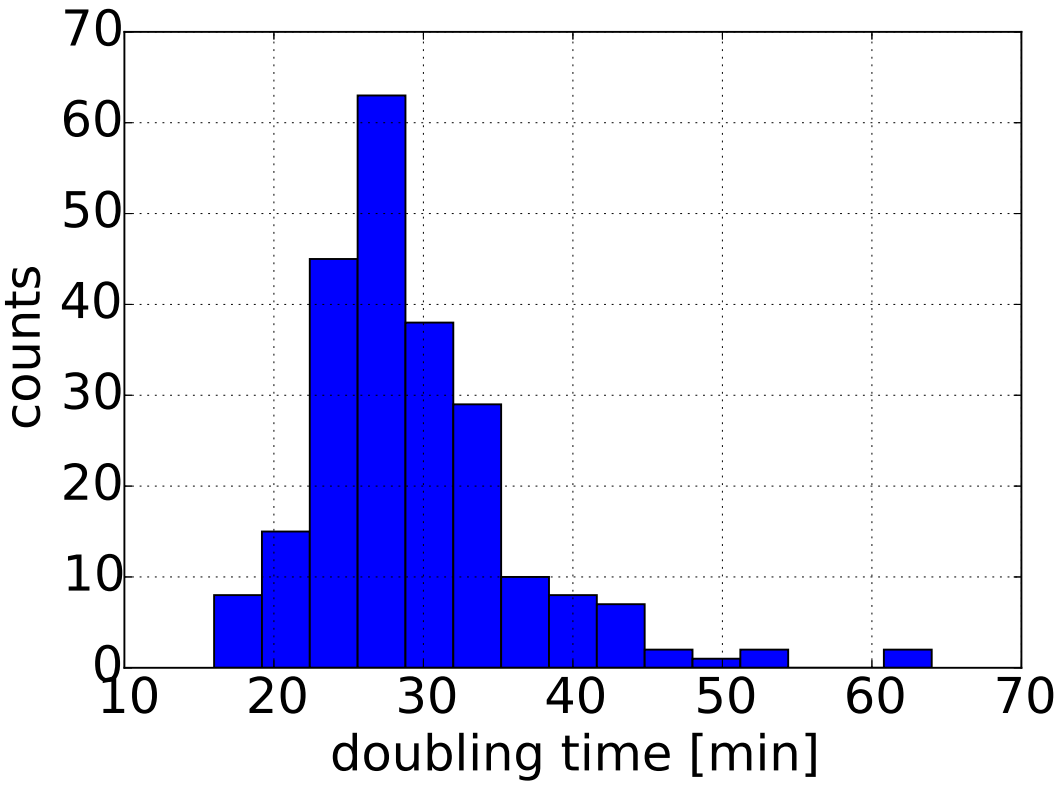

Figure 5.2: Histogram of the doubling times for the bacterial microcolonies.

during sample preparation, first of all the changes in temperature, as it is known that temperature influences the metabolism, hence the growth rate of cells [21, 109]. According to the microbiology protocol we followed (given in details in § 4.1), cells are cultured in a shaking incubator at 37 ℃ in a fresh nutrient medium. Contrary, during sample preparation, cells are handled at laboratory temperature, that is 20-25 ℃, and the droplets, which contain the bacteria and that is injected onto the agar pad, takes about 3 minutes to dry off. Furthermore, the nutrient medium that bacteria are in contact with is incorporated into a jelly substance instead of being in an aqueous medium, thus the intake of nutrient is also based on a different mechanism (either diffusion of the nutrients themselves and the possibility for cells to swim or not depending on the surrounding environment). However, despite these differences, we can see that cells after the first generation tend to grow a little faster and then reach a stable rate, so that the growth results exponential as shown by the linearity of the semi-log plot in figure 5.1.

Considering such limited observational time or spatial scale, the geometry of

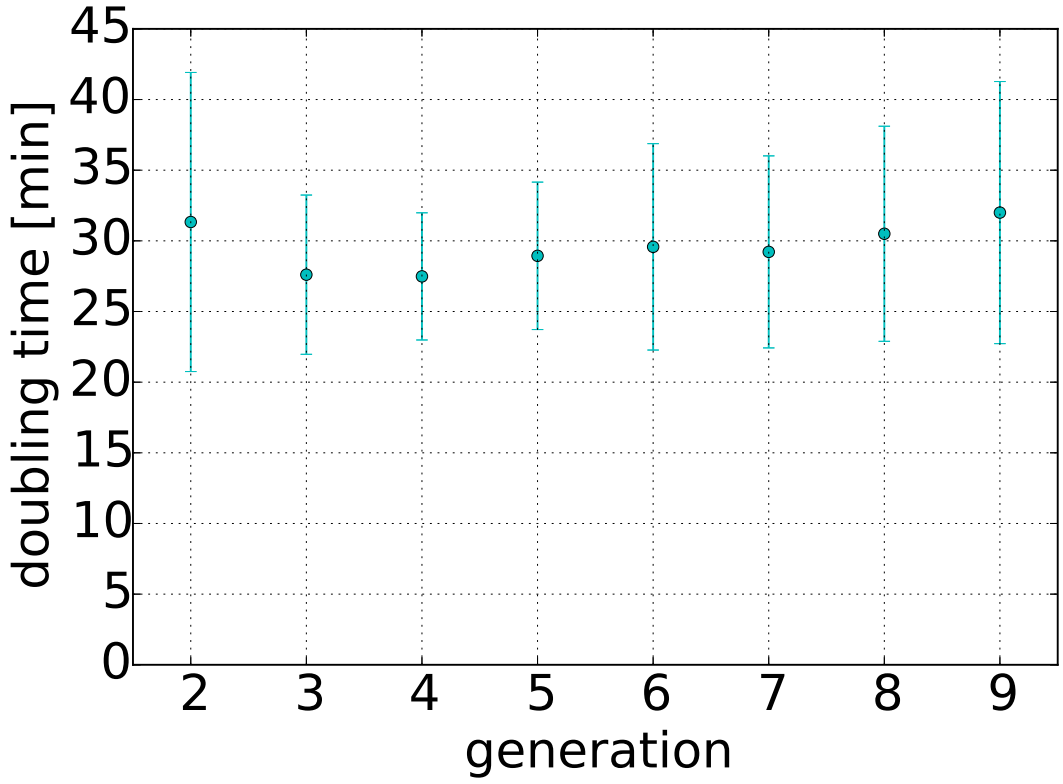

Figure 5.3: Mean values of the doubling times among generations with standard deviations.

the growing colony is well approximated as being 2D, in a sort of *bacterial carpet*, and it is indeed characteristic of such microcolonies, as already shown in figure 4.4. However, for longer times or larger sizes, cells tend to move outside the horizontal plane, invading the third (z) dimension: this is another interesting phenomenon known as buckling of the cell layer whose study is presented in Part III of this thesis.

A montage of frames following the exponential increase of cell number for a typical colony is presented in figure 5.4. The frames have been recorded using a camera attached to microscope in a 3-5 h duration time-lapse experiment, using a standard phase-contrast imaging set-up (more details are given in § 4.3). *E. coli* colony starts from a single mother cell whose shape can be well approximated with a sphero-cylinder, with average length of the major axis of about 3 µm and with a practically constant width of about 0.9 µm.

In figures 5.5 and 5.6, we provide the histogram of the cell lengths for all

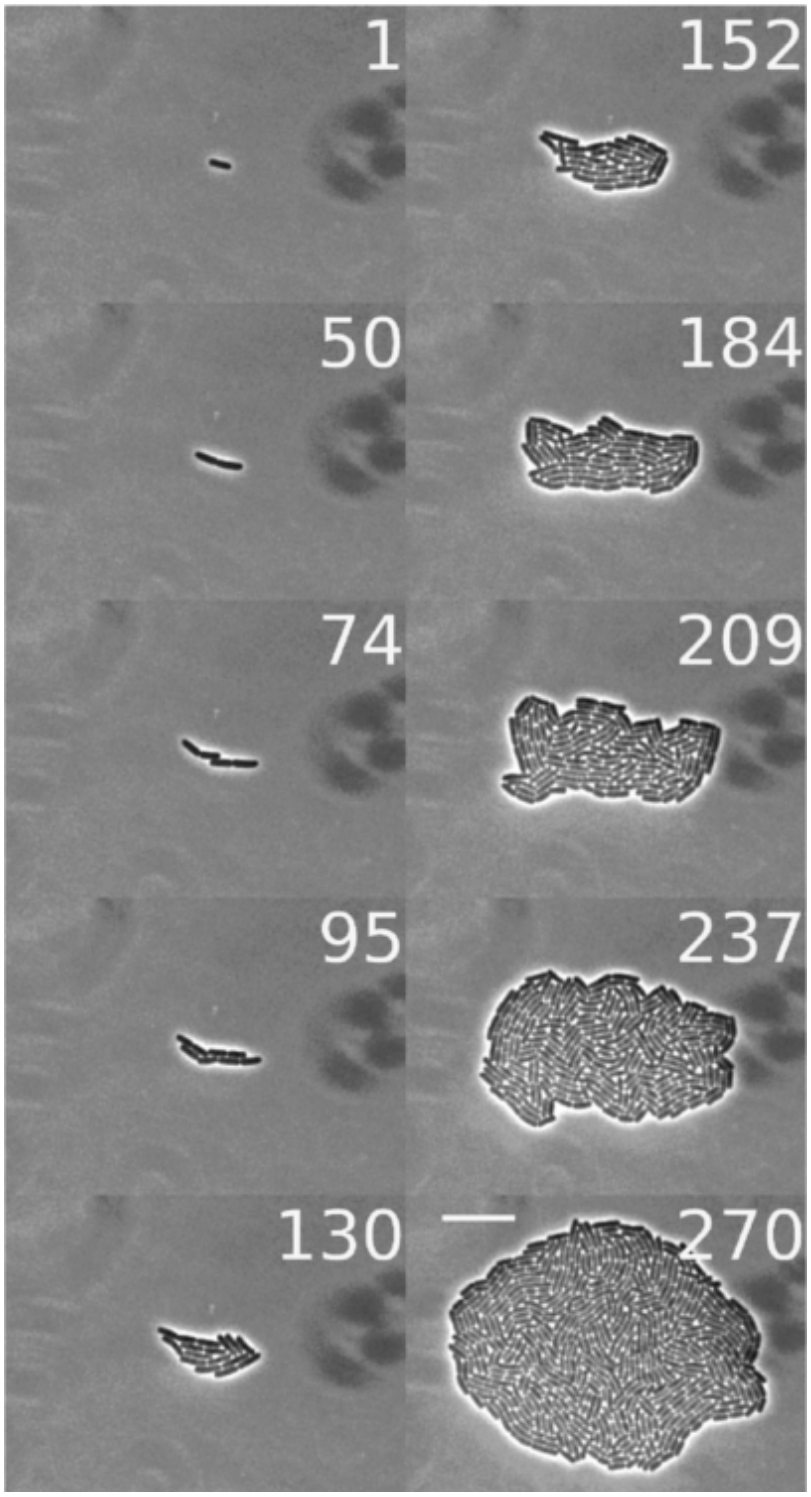

Figure 5.4: A frame montage of a typical 2D growing colony of *E. coli* cells, from the mother cell to about the 9^{th} generation (512 cells). The number in each frame is time in minutes, and the scale bar at the last frame is 10 µm (for all frames).

the 33 colonies analyzed at their last recorded frame (largest colonies), and the average length along with the standard deviations, respectively.

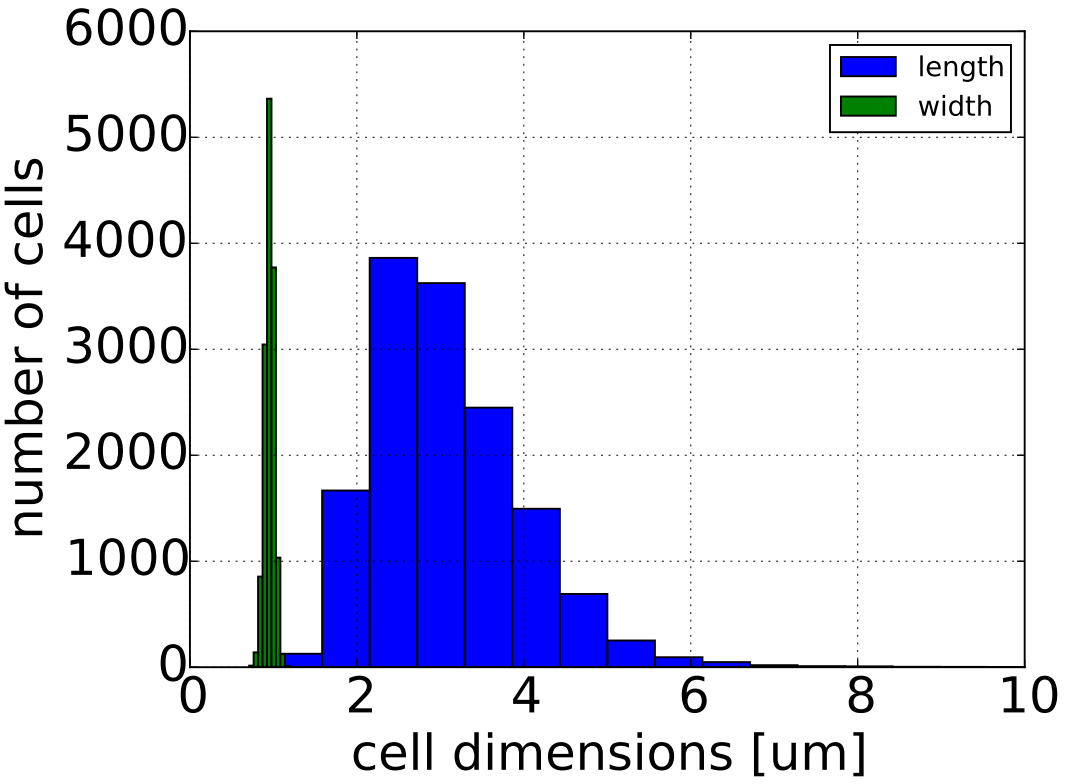

Figure 5.5: Histogram of cell lengths and widths from the 33 colonies analyzed at last frame (total number of cells of the order of 10^4). The histogram of the lengths shows a peak around 3 µm, but longer and shorter cells are measured as well, resulting in a polydisperse system. This polydispersity is due to the fact that cells naturally grow in length and, as the whole colony ages, cells are no longer dividing in synchrony. The histogram of the widths is narrower as bacteria grow along their longitudinal axes, and the peak is around 0.95 µm.

Considering the first few generations only, the colony shape is far from being circular, as most cells grow and keep their alignment close to their neighbouring cells (see figure 5.4).[1] For instance, just after the division of the first mother cell, the two daughter cells execute a rapid movement and move side-by-side the ends that are in contact, as shown in figure 5.7.

This re-arrangement of daughter cells during the early stage of bacterial

[1]In the next sections, we will observe this effect by studying observables that quantify the degree of orientational order.

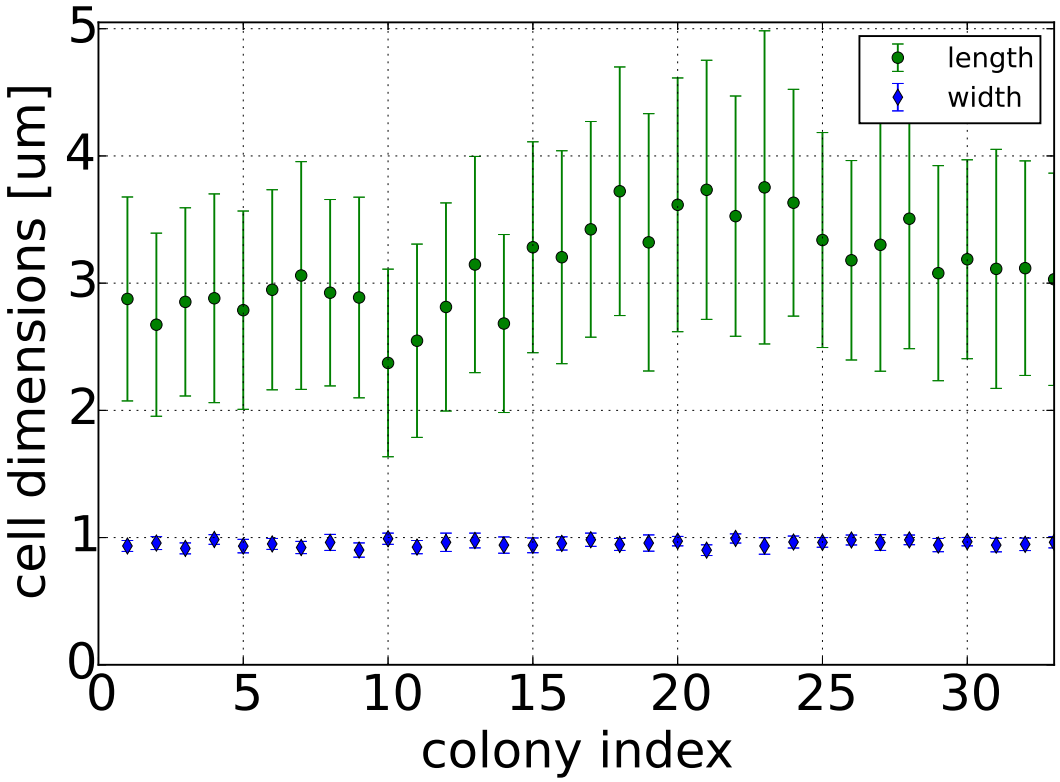

Figure 5.6: Average cell lengths and widths with standard deviations for each of the 33 colonies. The average and the standard deviation of these values are (3.14 ± 0.35) µm for the length, and (0.95 ± 0.02) µm for the width.

division has been observed by other researchers [110]. However, it is important to notice that there are many factors affecting this mechanism of re-orientation. For instance, as shown in [110], the nature of the substrate could affect the way daughter cells move just after division of their mother cell. As a test, they grew cells on a different substrate made up of a gel to which hyaluronic acid was added. This component has the ability to interfere with the adherence of microorganisms, and perturb the attachment of cells. In this different setting, they observed that the side-by-side alignment was largely suppressed, leading to bacteria growing in long chains instead. Additionally, they also examined the role played by some bacterial surface molecules that could tune the interaction with the substrate. By disrupting a specific gene (the lpp gene that encodes a membrane lipoprotein) and hence the production of the corresponding LPP

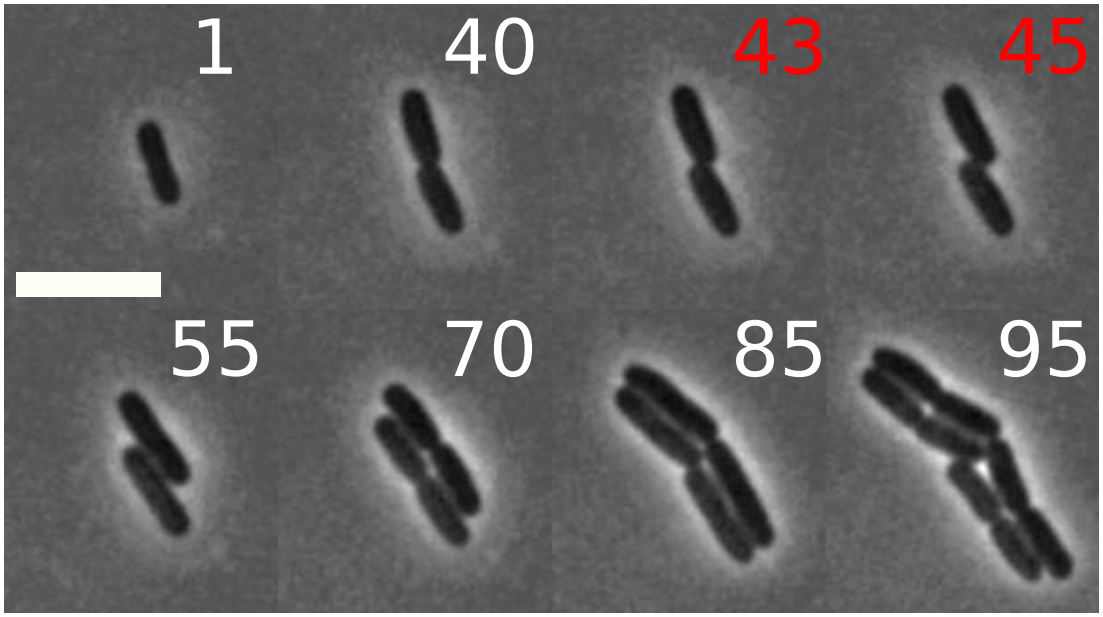

Figure 5.7: Re-orientation of bacteria just after division. When the mother cell divides, the two daughter cells rapidly re-orient, compared to the slower motion characteristic of their growth. The poles of the two cells that are in contact slide along each other, so that cells move from the original direction of their mother cell to two new parallel directions. Numbers in the frames are times in minutes: those in red correspond to the times at which the fast re-orienting movement takes place. It is also possible to notice this re-orientation between frames at minutes 70 and 85. Scale bar (in frame 1, and the same for the other frames) is 5 µm.

protein, they observed that the interaction force with the substrate decreased[2] for cell lacking LPP and non-typical patterns were observed, that is neither sliding side-by-side in parallel nor chains. Hence, these investigations suggests that the early cell patterning is affected by multiple interaction factors, whose origin can be both in the environment and in the cells. We will investigate in a later section in Part III the role played by some appendages present on the bacterial surface, specifically the way mutant cells lacking them grow through the medium with respect to the wild type cell case.

We notice that from our observations there is no evidence for a tendency of the cells to re-orient only on the left or only on the right, being the number of times (a total of 40 cases with a 22 for right and 18 for left) that the daughter

[2] *Via* optical tweezers quantification.

cells re-orient on the right side of their sister equal to the number of times that it occurs on the left. This hypothesis of a possible selected direction of orientation is related to a particular structure that develops into and in contact with the bacterial cell envelope, which is shaped like a helix and is formed by a specific protein called MreB. Recent works [111, 112] showed that as the cell elongates, it also rotates along its major axis, but from our observations this rotation does not seem to contribute to select a particular direction, that is right or left. The daughters then keep growing again side-by-side until they divide again giving birth to other two daughter cells each respectively, hence we end up with 4 cells; the process keeps going on with a base-2 exponential increase.

As the colony cell number increases, such orientational order starting with the mother and kept from the first few daughter cells decreases, so that, for a fully grown colony, there is no longer memory of the orientation of the first mother cell when looking at the offspring of far generations. Despite this loss of orientational order in a global perspective, we will see that the final stages of the microcolonies are also far from being a confused picture of some living rods. Contrary, cells tend to pack in a definite way and form small nematic domains.

Furthermore, during the development of the colony, interesting dynamical phenomena emerge, *e.g.* nematic instabilities and topological defects related to the mechanic interactions between cells, and these are discussed in the next sections. They can be viewed as a characteristic sign of a 2D living nematic, which naturally ends when stresses between cells increase and are no longer contained in the plane where the colony developed at earlier times, eventually leading to the buckling of the bacterial layer. At that moment in the evolution of the colony, the study of the orientational configurations requires different methods from those used in the work presented here, for instance a 3D reconstruction of the bi- or multilayer colony (for instance, through confocal microscopy methods, as done in [113]) and, of course, an even richer set of interactions between cells and between cells and their environment.

5.2 Global order parameter

After the phenomenological description given in the previous section, we now begin investigating at a qualitative and quantitative level the global order-disorder

transition occurring in the microcolonies.

A global description of the nematicity of a LC can be given through a tensorial order parameter Q whose components are defined as follows [5]:

$$Q_{\alpha\beta}(\mathbf{r}) = \frac{1}{N}\sum_{i}^{N}(2\nu_{\alpha}^{i}\nu_{\beta}^{i} - \delta_{\alpha\beta})\delta(\mathbf{r} - \mathbf{r}_{i})\,. \tag{5.1}$$

Here, Greek indices are used for Cartesian components $(\alpha, \beta) = (x, y)$, whereas Latin indices are used for identifying the particles (in our case, the cells); N is the number of cells in the colony at a given time t. We model the bacterial cells as rigid rods that exhibit the symmetry properties that characterize a nematic LC (as discussed in Chapter 1 dealing with LCs, and in Chapter 3 active nematics). Hence, it is possible to describe the order of the colony in terms of a symmetric, traceless[3] tensor [5]: $Q_{ij} = Q_{ji}$, $\mathrm{Tr}(\mathsf{Q}) = 0$.

Because of these properties, the matrix corresponding to the tensor Q can be diagonalised once a proper reference frame in which one of the axes is parallel to the average alignment within all the particles has been chosen. From this diagonalization, the eigenvalues and the corresponding eigenvectors are obtained. The largest eigenvalue of the tensor returns a scalar $Q \in [0, 1]$, which gives the degree of nematicity within the colony: it equals 1 if the cells are all aligned along the same direction, 0 if randomly oriented [5]. The eigenvector corresponding to the largest eigenvalue of the tensor corresponds to the average direction among the cells, also known as the director $\widehat{\mathbf{n}}$. In other words, it is possible to rewrite eq. (5.1) using a simpler notation including the scalar Q and the director $\widehat{\mathbf{n}}$:

$$\mathsf{Q} = Q(2\langle\widehat{\mathbf{n}}\widehat{\mathbf{n}}\rangle - \mathsf{I})\,, \tag{5.2}$$

with

$$Q = \langle 2(\nu\cdot\widehat{\mathbf{n}})^2 - 1\rangle = \langle 2\cos^2(\psi_i) - 1\rangle\,, \tag{5.3}$$

where I is the 2×2 identity matrix, $\langle\ldots\rangle$ denotes average over the cells and ψ_i is the angle between the i-th cell at an angle θ_i with respect to the horizontal axis, and the director $\widehat{\mathbf{n}}$. A sketch of the director and a cell with its angle relative to the director is given in figure 5.8.

[3] This is because the vector ν^i representing the direction of the i-th cell is a unit vector.

Finally, we also notice that

$$\mathsf{Q} = \begin{pmatrix} Q_{xx} & Q_{xy} \\ Q_{xy} & -Q_{xx} \end{pmatrix} = Q \begin{pmatrix} \cos(2\theta_{\widehat{\mathbf{n}}}) & \sin(2\theta_{\widehat{\mathbf{n}}}) \\ \sin(2\theta_{\widehat{\mathbf{n}}}) & -\cos(2\theta_{\widehat{\mathbf{n}}}) \end{pmatrix}, \quad \widehat{\mathbf{n}} = (\cos(\theta_{\widehat{\mathbf{n}}}), \sin(\theta_{\widehat{\mathbf{n}}})) \,. \tag{5.4}$$

Hence, $Q = \sqrt{Q_{xx}^2 + Q_{xy}^2}$, which is useful when implementing in a code such calculation.

In figure 5.8, we present the evolution of Q as the colonies grow, *i.e.* as a function of the number of cells, each point in the plot being obtained as the average over 33 colonies.

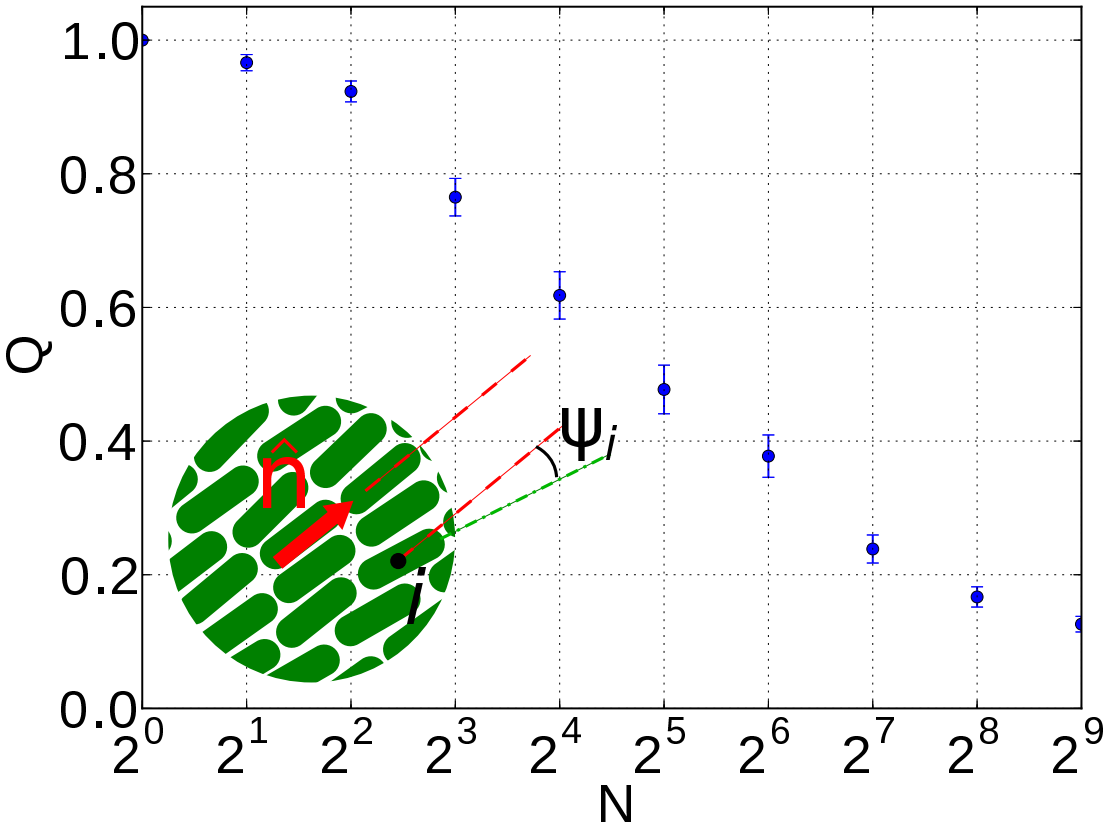

Figure 5.8: The tensorial order parameter Q *vs* cell number N: the nematic degree is quantitatively assessed by measuring Q as the number of bacteria forming the colony increases. The decay from values close to 1 to about 0.1 during the evolution of the colonies indicates that a transition from a nematic to an isotropic phase takes place.

Since colonies can have different growth rates and they can also buckle along the vertical direction at different times, the independent variable with respect to

which is plotted Q is the number of cells N instead of time t. Each value reported in the plot is the result of the average - with its corresponding standard deviation - of the values of Q obtained from the colony frames, which have been binned around the number of cells for each generation, that is 1 cell, 2 cells, 4 cells and so on, in the base-2 exponential. From the plot of Q, we observe that for a small number of bacteria within the colony, the value of the order parameter is high, ranging from 1 for the trivial case of the initial single mother cell to about 0.8 for a 8-cell microcolony. However, as the number of cells N increases, the nematic order decreases as indicated by the smaller values of Q, which range from 0.6 for a 16-cell microcolony to 0.1 for the largest number of cells at the ninth generation, thus revealing that a transition from a nematic to an isotropic state occurs.

5.3 Local orientational correlations

What we get from the quantitative investigation based on the order parameter Q is a global transition from order to disorder. However, this global approach can hide some important aspects of the ongoing processes occurring as the colony grows. For instance, bacteria interact with their neighbours as they are in direct contact, and this means that a local study of the order has to be considered as well to give as a thorough as possible quantitative picture of what is happening in this living system. Moving from a global to a local description, we need also to find some appropriate tools/observables that give such local account of the orientational status of the colony, that is some functions which take into account the orientational correlation of a reference bacterium with respect to all the other bacteria, eventually averaging over all the bacteria present in the colony. This local-order study is then divided here into two parts that are explained in the next two subsections, in terms of the radial and the 2D orientational correlation functions.

5.3.1 Radial orientational correlation function

The radial orientational correlation function ϕ is defined as follows:

$$\phi(d) = \left\langle 2\cos^2(\Delta\theta_{ij}(d)) - 1 \right\rangle , \tag{5.5}$$

where d is the distance between the i-th and the j-th bacterium with an angular difference $\Delta\theta_{ij} = \theta_i - \theta_j$, θ_i and θ_j being the angles of the two bacteria with respect to the horizontal axis of the image; $\langle \ldots \rangle$ denotes average over the cells (see figure 5.9 where a sketch is provided). Such function returns values close to 1 when the correlation between the reference bacterium and its neighbour at distance d is high, that is, if they are very well aligned (the angle difference is small). As bacteria misalign, the value assumed by ϕ tends towards zero. Notice that the π-periodic functional form of ϕ takes into account the nonpolar symmetry of our system: $\nu \rightleftharpoons -\nu$, and also returns value in the unitary range once properly rescaled, as in eq. (5.5).

We considered 154 frames of microcolonies, spanning a cell number range from a minimum of about 150 to a maximum of about 1000 cells. The trends are shown in the plot in figure 5.9, indicating that correlations decay rapidly with the distance between cells, and that the decay is not related to the size of the colony, that is to the number of cells in it, as a colour separation between the correlation functions cannot be seen.

The study of such correlations can give insights about the possible existence of orientational domains into which bacteria are aligned along a preferential direction. Hence, by fitting the curves given in figure 5.9 with an exponential form $a \exp(-d/\xi)$ taken as the decay model, a characteristic or correlation length ξ can be obtained, allowing to quantify the size of the nematic domain, which corresponds to twice ξ. The result of these fits is reported in figure 5.10 along with a linear fit, which returns a slope of 5×10^{-4} µm/cell number, and a y-axis intercept of 2.831 µm. Hence, this suggests the existence of small nematic domains of a diameter of about 6 µm, that is 2ξ.

We thus observe that, despite the global decay order as quantitatively shown by the decay of the tensorial order parameter Q, we find that it is still possible to find local small orientational domains: we can imagine the colony as being divided into subsets, each one with its preferential direction. Such domains do not emerge as a response to an external applied field and are not static. Contrary, their emergence is related to the inherent movement of their constituents and, because of their activity, they are highly dynamic, so they change during time and are continuously redefined. These dynamic states are characteristic of active matter and we will be back with them in a later paragraph (§ 5.4) where we will

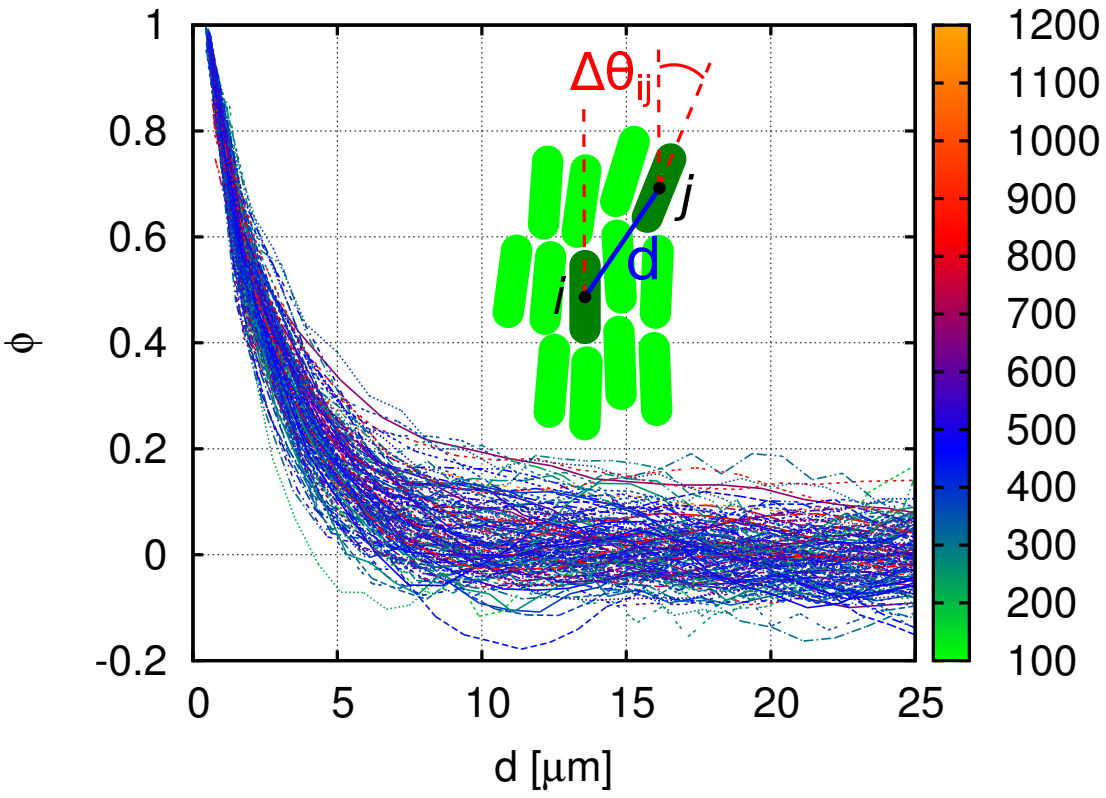

Figure 5.9: Orientational correlation function ϕ *vs* cell-cell distance d, parametrized *via* colony cell number N (colour bar on the right side). This local investigation shows a rapid decay of the correlation that, in the hypothesis of an exponential decay, allows to check for the possible existence of orientational domains and their characteristic size. The number of correlation functions analysed is 154 from the corresponding 154 colonies of different sizes, *i.e.* from about 150 to 1000 cells. The inset sketch is provided for explaining visually how the correlation function in eq. (5.5) is constructed. In figure 5.10, a quantitative assessment of the characteristic domain size is given in terms of the size (number of cells) of the colony.

focus on the orientational instabilities occurring when such domains experience strong deformations.

5.3.2 2D orientational correlation map

As shown and discussed in the previous § 5.3.1, the radial orientational correlation function ϕ is useful when we are interested in looking for possible orientational domains as the colony grows. However, its use can hide some other relevant information because of the implicit radial average assumption we make when

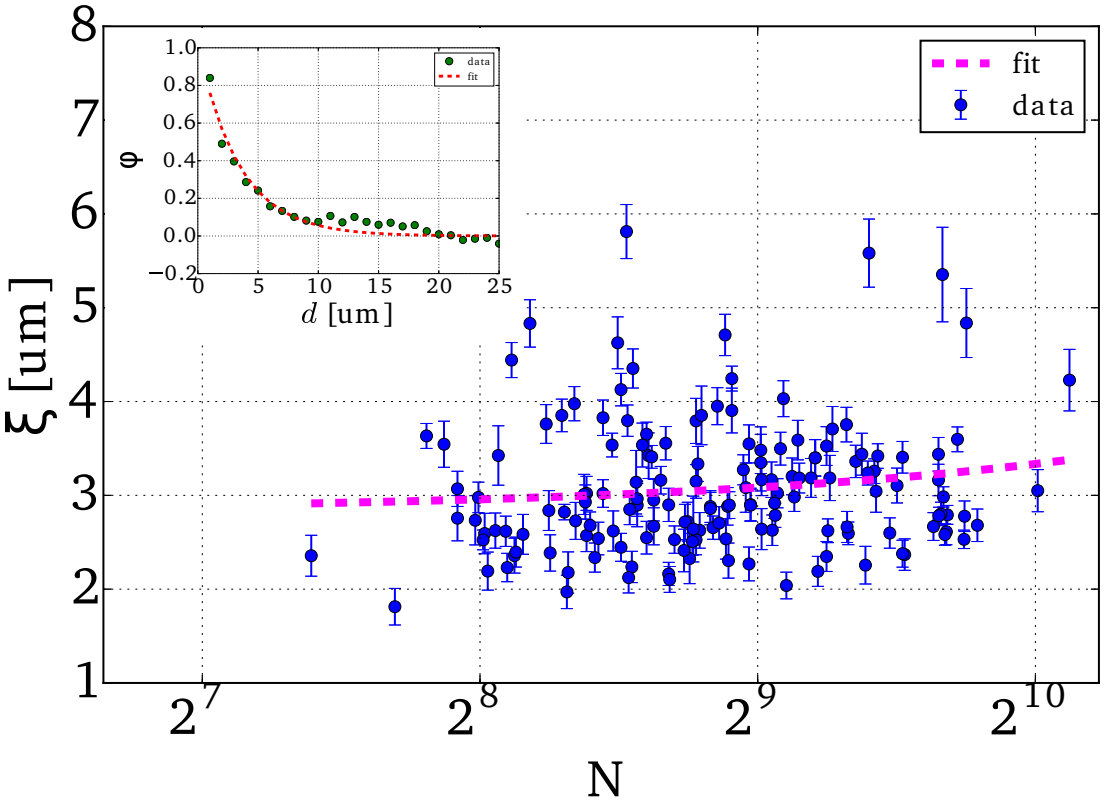

Figure 5.10: Correlation length ξ *vs* cell number N. By fitting the orientational correlation functions (figure 5.9) with an exponential function, the characteristic size of the domains is extracted. Mean value with standard deviation return: (3.07 $\pm$ 0.06) µm, the domain size doubling the correlation length, $l_d \sim 2\xi$. A linear fit of such correlation lengths (green dashed curve) returns a slope of 5×10^{-4} µm/cell number. The y-axis intercept is 2.831 µm. In the inset plot, a typical decay of the orientational correlation function ϕ is shown along with its exponential fit.

using it: actually, our colonies, especially at the beginning of their life, are far from being circular and display quite a high degree of shape anisotropy.

Hence, it would be useful to project the correlation function along each direction in the 2D plane with respect to the main direction defined by the reference bacterium considered for which that individual correlation function is computed, and then average it with all the others obtained from the other bacteria, being each one the new reference bacterium. In this fashion, once a given bacterium is considered in the colony, we can assess how rapidly, in spatial terms, the orientational order is lost in the parallel and orthogonal directions with respect to the long axis of the cell. In order to do so, a 2D local orientational

correlation function can be defined as follows:

$$g_2(\mathbf{r}) = \langle \cos(2(\theta_i(\mathbf{0}) - \theta_j(\mathbf{r}))) \rangle \ , \tag{5.6}$$

where $\mathbf{r}$ is the position vector linking the i-th bacterium with orientation angle θ_i at the origin (being the reference bacterium) and the j-th bacterium at position $\mathbf{r}$ with an angle θ_j; again, $\langle \ldots \rangle$ denotes average over all cell pairs (i, j). The result for a typical colony is shown in figure 5.11. The same behaviour, both qualitatively and quantitatively, is seen for the other 32 colonies.

Several bands of high values (*i.e.* close to 1) occurring in the orthogonal direction ($r_\perp$) can be observed: we can see clearly four bands moving from the origin to larger distances, with the 5^{th} band being almost completely faded out. Such peaks correspond to the presence of bacteria that are well aligned with the reference bacterium. In figure 5.12, the two projections of the 2D map are provided to show more clearly the peaks.

Giving a closer look to 5.11, it is also possible to distinguish some negative values, which are mainly located at the bacterium edge. It is possible to see at least one clear spot on the horizontal axis at 1.5 µm that defines the actual space occupied by the bacterium. This is a steric effect, the average length of the bacteria being actually 3 µm just after the division, with a width varying in a small range between 0.8 and 1.0 µm (see figures 5.5 and 5.6).

We observe that from $g_2(\mathbf{r})$ it is possible to recover the characteristic length obtained from the radial function study presented in the previous paragraph 5.3.1, as this would correspond - on a radial approach - to the average between the extent in the parallel and orthogonal direction of the maxima in $g_2(\mathbf{r})$. Looking at figure 5.11, we can see that in the horizontal direction, high values of $g_2(\mathbf{r})$ are present until a length of 2-3 µm, whereas in the orthogonal direction until 4-5 µm that corresponds to the presence of the last band, hence the average returns a value close to 3 µm, the same as given by the local radial orientational correlation function $\phi(d)$.

We conclude that this pair correlation function shows a marked anisotropy: the order is preserved for a few bacterial widths in the direction perpendicular to the long axis of the reference cell, but it is lost almost instantly along the parallel direction. Such kind of pattern shows some similarities with cybotactic order in LCs, which is sometimes found in the isotropic phase of suspensions of rods, for

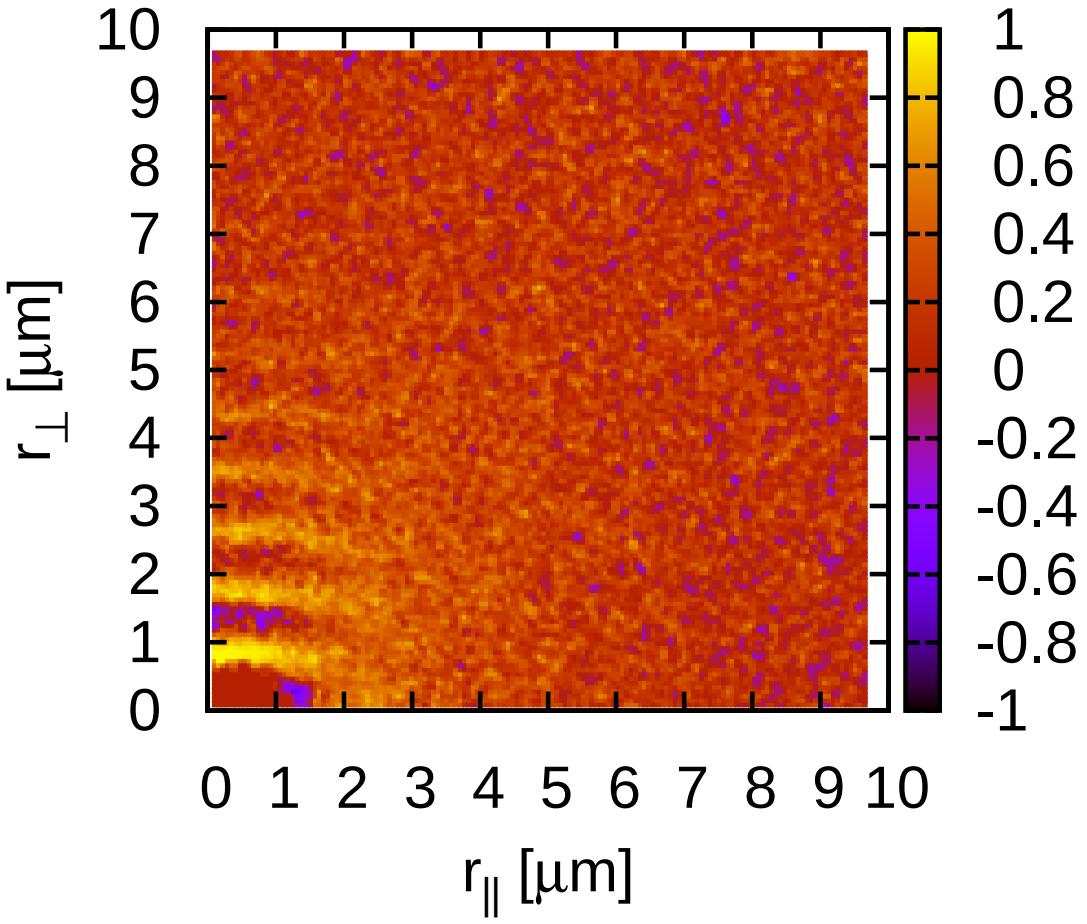

Figure 5.11: 2D orientational correlation function $g_2(\mathbf{r})$ (as defined in (5.6)) from a typical colony. The interparticle vector $\mathbf{r}$ is split into its two components $r_{\parallel}$ and $r_{\perp}$ that are parallel and perpendicular, respectively, to the orientation of the cell (defined by its longest axis) considered at the origin ($\mathbf{0}$). This map indicates that bending is the leading deformation emerging during colony growth, as supported also by theoretical arguments and numerical works (see Chapter 3). Moreover, because of its instability, bending deformation leads to singularities in the director map, *i.e.* topological defects, which are discussed in later sections (§ 5.4).

suitable values of the aspect ratio [114, 115].

Furthermore, this map of orientational correlations gives us insights about the mechanics taking place in the colony: as explained in the introduction Chapters 1 and 3, it is known that bending instabilities are characteristic of systems made up of extensile particles, and the bacteria in these colonies belong to such category. That prediction of bend deformations is actually also suggested from the same map of $g_2(\mathbf{r})$ in figure 5.11. This arises directly from the order in the orthogonal

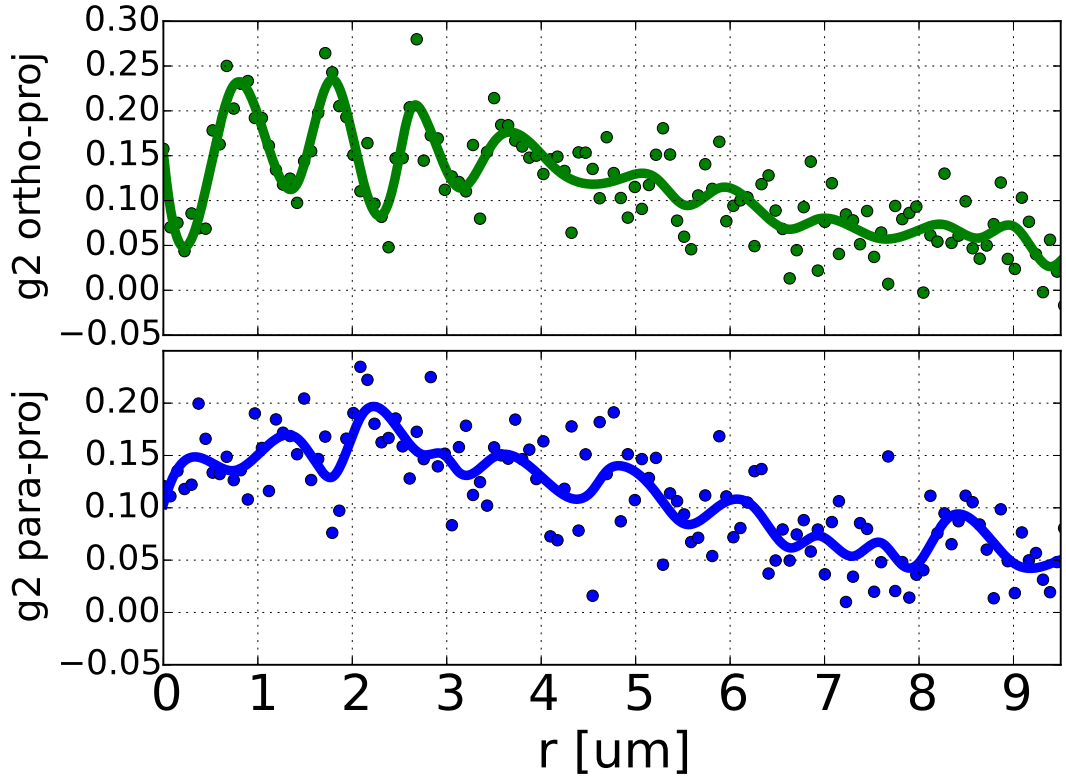

Figure 5.12: Projections of 2D orientational correlation map in the parallel and orthogonal direction with respect to the long axis of the reference cell: the values are computed by averaging over each row (column) of the data matrix for a constant y (x). We observe quite clearly 4 peaks in the orthogonal projection (green), corresponding to 4 bacteria placed side-by-side, which then fades out towards smaller values. For the parallel projections (at bottom in blue), we see by contrary that there are no clear peaks, but an initial range of high values until about 3-4 µm that corresponds to the body of the cell.

direction which prevails on that in the parallel direction, so that bacteria tend to stay better aligned in a side-by-side row than in a head-tail row, and this leads to a bend deformation.

Polydispersity

We can see different decay modes in the 2D correlation map in figure 5.11, depending on the two directions considered, that is, if moving orthogonal or parallel with respect to the bacterium long axis. However, a doubt can come to mind when dealing with growing bacteria, that is, particles that can vary their

length in time. Is the diversity in the orientational correlation decay just an artefact of a system of polydispersed active particles?

In order to answer to this question, we computed again an orientational correlation, but this time measuring the distance in units of number of neighbours, which is independent of the length of individual cells. The result is given in figure 5.13, showing that the decay in the orthogonal direction is slower than that in the parallel direction, being consistent with the 2D map in figure 5.11, hence excluding that the sequence of peaks observed therein is due to polydispersity, but it is due to the actual orientational configuration of the cells, hence the occurrence of bend deformations.

The code used for this analysis was not written by me but it was provided by Dr Juho Lintuvuori in C language. I then used it to analyse the raw data I obtained from the experiments and finally interpreted the results. The program works by considering a reference bacterium and then looking for neighbours in the two directions, parallel and orthogonal to the reference bacterium direction, that is forward/backward and on left/right side of the reference bacterium. Neighbours in these two directions are found into regions of some defined width, that is, the average bacterium width (1 µm, see figure 5.5) when moving forward or backward, and the average bacterium length when moving on the right/left (3 µm).

5.4 Bending instabilities and topological defects

We have seen in the previous sections how it is possible to describe in qualitative and quantitative terms the transition from an orientationally ordered to a disordered state in a growing bacterial microcolony. However, despite the loss of orientational order in a global perspective from the first cell to about hundreds of offspring, we found that, at the local level, cells still exhibit a degree of alignment with the tendency to pack side-by-side.

During the transition from the ordered to the disordered state, there are some other interesting processes happening, which relate to the way the nematic field, corresponding to a coarse-grained description of the orientations of bacterial cell, is deformed. As suggested from previous studies [88, 101] and suggested from the 2D correlation maps (see figure 5.11), the deformations taking place in the microcolonies are bending deformations. Furthermore, when these

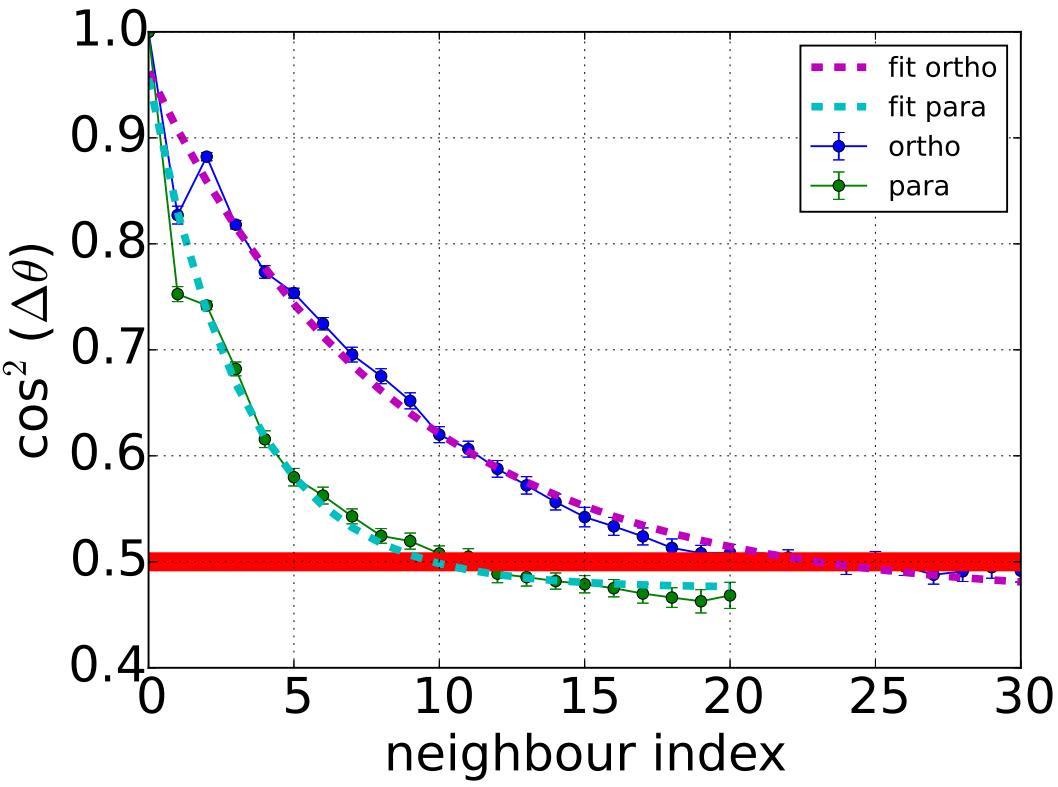

Figure 5.13: Orientational correlation based on neighbour distance (instead of a metric one). As the colony grows, bacteria tend to divide asynchronously leading to configurations where bacteria of different lengths appear (ranging from about 3 to 6 µm). In order to verify that the bending is taking place because of stresses due to the interaction between bacteria, and excluding that is just a mere artefact of polydispersity, the orientational correlation is now given as a function of the number of neighbours of the reference bacterium. The decay is slower in the orthogonal direction than in the parallel one, as shown by the exponential fits from which the correlation lengths in the orthogonal and parallel direction can be extracted, returning $\xi_\perp > \xi_\parallel$, that is, $\xi_\perp/\xi_\parallel \sim 8.5/3$. The dashed red line indicates the mean value for which correlation no longer exists.

deformations become stronger, that is, the nematic fields gets strongly distorted, they eventually lead to the formation of topological defects, which are singularities in the nematic field, that is, points where the director is no longer well defined.

In order to illustrate these two phenomena of deformation and defect emergence, we consider a typical example of a microcolony whose number of cells ranges from the 5^{th} to 7^{th} generation. The phase-contrast images for four time steps are reported in figure 5.14.

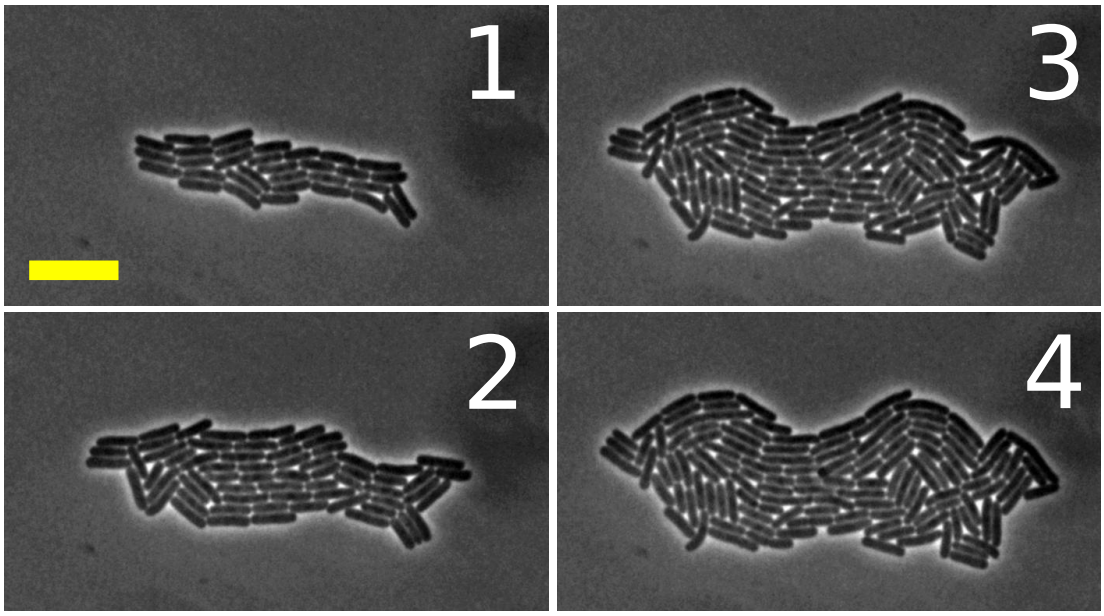

Figure 5.14: Phase-contrast images of a growing microcolony. As cells reproduce by binary division, the overall alignment between cells decreases. Cells start re-orienting, as they are pushed by their neighbours. Scale bar is 5 µm.

For small sizes, that is, a cell number < 30, most cells in the microcolony are oriented along the same direction, hence there exists a high nematic order (see again the plot of the order parameter Q *vs* the number of cells N as in 5.8). However, as the colony grows, cells experience larger re-orientations. For instance, in frame 1 of figure 5.14, there is a very small angular deviation between all the cells (which is reflected in an order parameter Q still close to 1), but moving to frame 2, we can already locate some cells as being orthogonal each other, thus determining a decrease of the order parameter. Finally, when we consider frames 3 and 4, even stronger deformation can be observed, determining now groups of cells that are oriented preferentially in a direction similar to their first neighbours.

5.4.1 Order and director maps with defects

After this qualitative description, it is possible by analysing the images in figure 5.14 to get a more quantitative one, which consists of creating maps of the order parameter. In these maps, regions of small orientational order are represented with dark colours, which then get increasingly brighter as the order increases. In figure 5.15, we report the order parameter maps corresponding to the phase-

contrast images presented in figure 5.14.

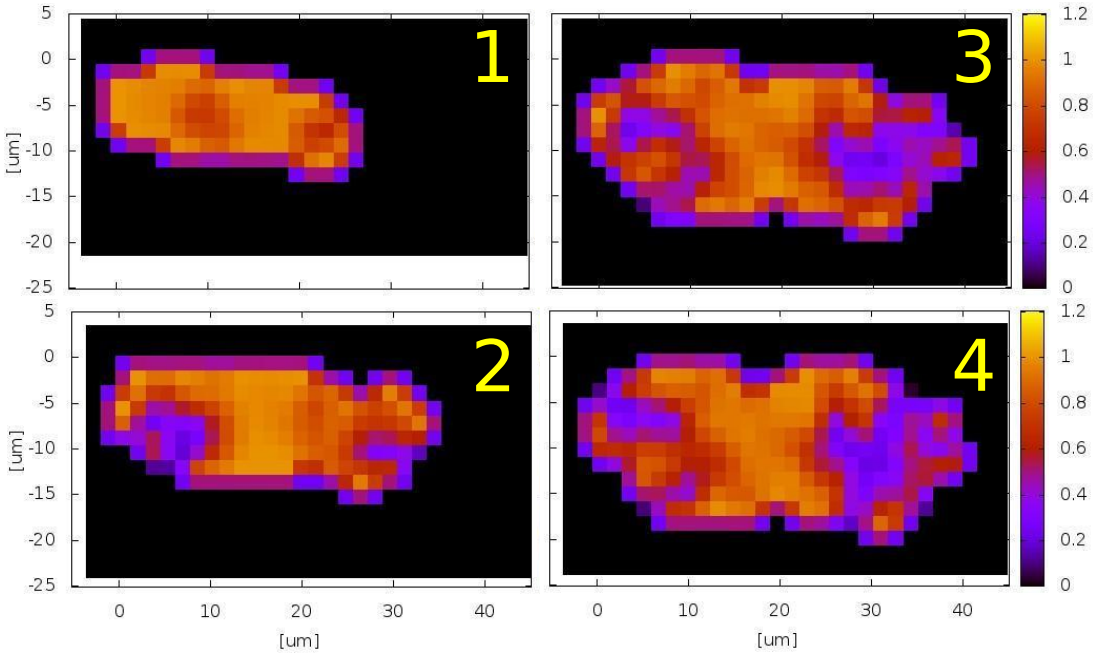

Figure 5.15: Order parameter maps obtained from the images in figure 5.14. Dark purple and orange-yellow regions correspond to low and high nematic order in the microcolony, respectively. Moving from frame 1 to frame 4, it is possible to notice how the order is degraded by looking at the change from a nematic blob with an almost homogeneous colour (1) to a map with darker spots located at the left and right sides (4).

As previously introduced in Chapter 1 and § 3.4, from theoretical and simulation works on active matter, it is known that extensile systems do exhibit unstable bending deformations [67, 74, 75, 116]. Furthermore, if the active particles are extensile (pushers), only positive and negative half-charged topological point defects should be seen for symmetry reasons [2], originating from these bending deformations. As shown in a recent numerical work [101, 117], once generated, these defects can move (actually they can be interpreted as active particles themselves), annihilate each other in case they meet oppositely charged point defects, or get absorbed by the boundary.

In order to provide evidence of the emergence of bending instabilities (in addition to that one provided by the 2D correlation map as discussed in 5.3.2), we plotted the director fields of the microcolonies that are obtained by considering a coarse-grained representation of the cells forming the colonies. These director

maps, used in conjunction with the order parameter maps as shown in figure 5.15, help in identifying the deformations of the colony and the occurrence of topological defects as well, the latter being located at the minima of the order parameter maps.

To obtain the director maps, the colony is divided into several squares creating a grid, assuming a length of their side of 8 µm, so to include at least 20 cells, and being comparable to the correlation length ξ of nematic domain (see again § 5.3.1). Then, the average direction is computed into this square considering all the orientations of the bacteria (with respect to the horizontal axis of the image) therein included, and finally it is assigned to the centre of such square. The operation is repeated for all the squares of the grid. In figure 5.16, we present the director maps corresponding to the images in figure 5.14, and we mark the appearance of defects, both of half charge and opposite signs.

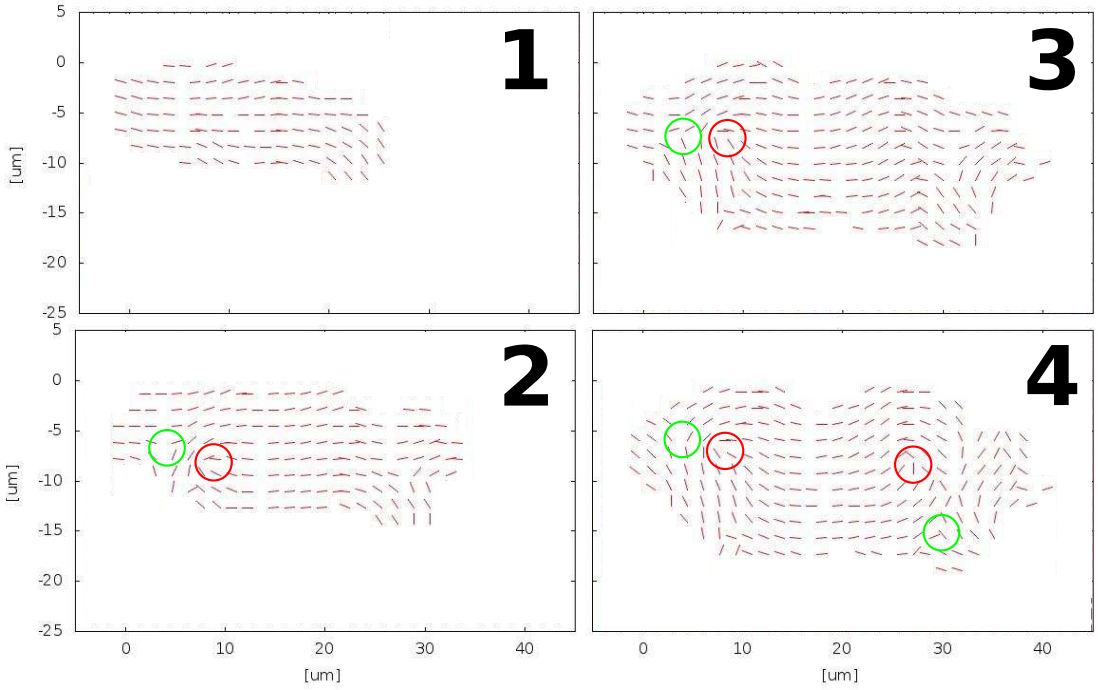

Figure 5.16: Director maps obtained from the images in figure 5.14. In frame 1, we observe a smooth nematic. As the microcolony grows, regions of the nematics start to bend because of the interactions between cells, leading to defects (2-4) of charge $\pm 1/2$. Positive defects are indicated with red circles, negative with green ones.

In figure 5.17, we report a time-lapse of the director map of a colony (the

same colony as in figure 5.4) with $\pm 1/2$ defects. The positive half-integer defects are represented here with red arrows whose direction corresponds to the defect polarity, that is, their axis of symmetry, whereas the negative ones are represented by green dots only.

In principle, topological defects can be detected and tracked by measuring the changes in the orientations of cells around a given point in the colony. However, considering the relatively small number of cells in the microcolonies and the occurrence of some sharp edges at the boundary, it is difficult to unambiguously detect defects in this way. A way to overcome this difficulty is to give a continuum description of the bacterial map, and use a differential form for the topological charge (instead of loop integral including the defect), as suggested in [102]. The $Q_{\alpha\beta}$ tensor given in eq. (5.1) is hence redefined as

$$Q_{\alpha\beta}(\mathbf{r}) = \tfrac{1}{N} \sum_{i=1}^{N} \left(2\nu_\alpha^i \nu_\beta^i - \delta_{\alpha\beta}\right) \times \mathcal{S}_i(l_i, \nu^i) \times \mathcal{S}_i(w, \widehat{\nu}^i)\,,$$

where $\mathcal{S}_i(d_i, \mathbf{v})$ is a smoothing function defined as

$$\mathcal{S}_i(d_i, \mathbf{v}) = \tfrac{1}{2}\left[\tanh\left(\frac{\mathbf{v}^i \cdot \delta\mathbf{r} + d_i/2}{\sigma}\right) - \tanh\left(\frac{\mathbf{v}^i \cdot \delta\mathbf{r} - d_i/2}{\sigma}\right)\right],$$

and $\Delta\mathbf{r} = \mathbf{r} - \mathbf{r}^i$, $\widehat{\nu}$ is the unit vector perpendicular to ν^i, and σ is a smoothing length; l_i is the length of the i-th bacterium, and each cell is assumed the same width. For $\sigma \to 0$, bacteria are resolved as sharp $l_i \times w$ rectangles. We use $\sigma = w$, which returns a good balance between preserving details and smoothing out undulations corresponding to the individual bacteria.

By considering the charge density q [102]:

$$q = \tfrac{1}{4\pi}\left(\partial_x Q_{x\alpha}\partial_y Q_{y\alpha} - \partial_x Q_{y\alpha}\partial_y Q_{x\alpha}\right), \tag{5.7}$$

it is then possible to track the defects by marking the maxima and minima of q, and, in the case of the positive half-integer defects, compute their polarity by measuring $\partial_\beta Q_{\alpha\beta}$ at the maxima.

We can observe from figure 5.17 some of the $+1/2$ defects moving along a direction that is close to the radial expansion of the colony. Thus, we decided to quantify such behaviour for these defects by studying the degree of alignment

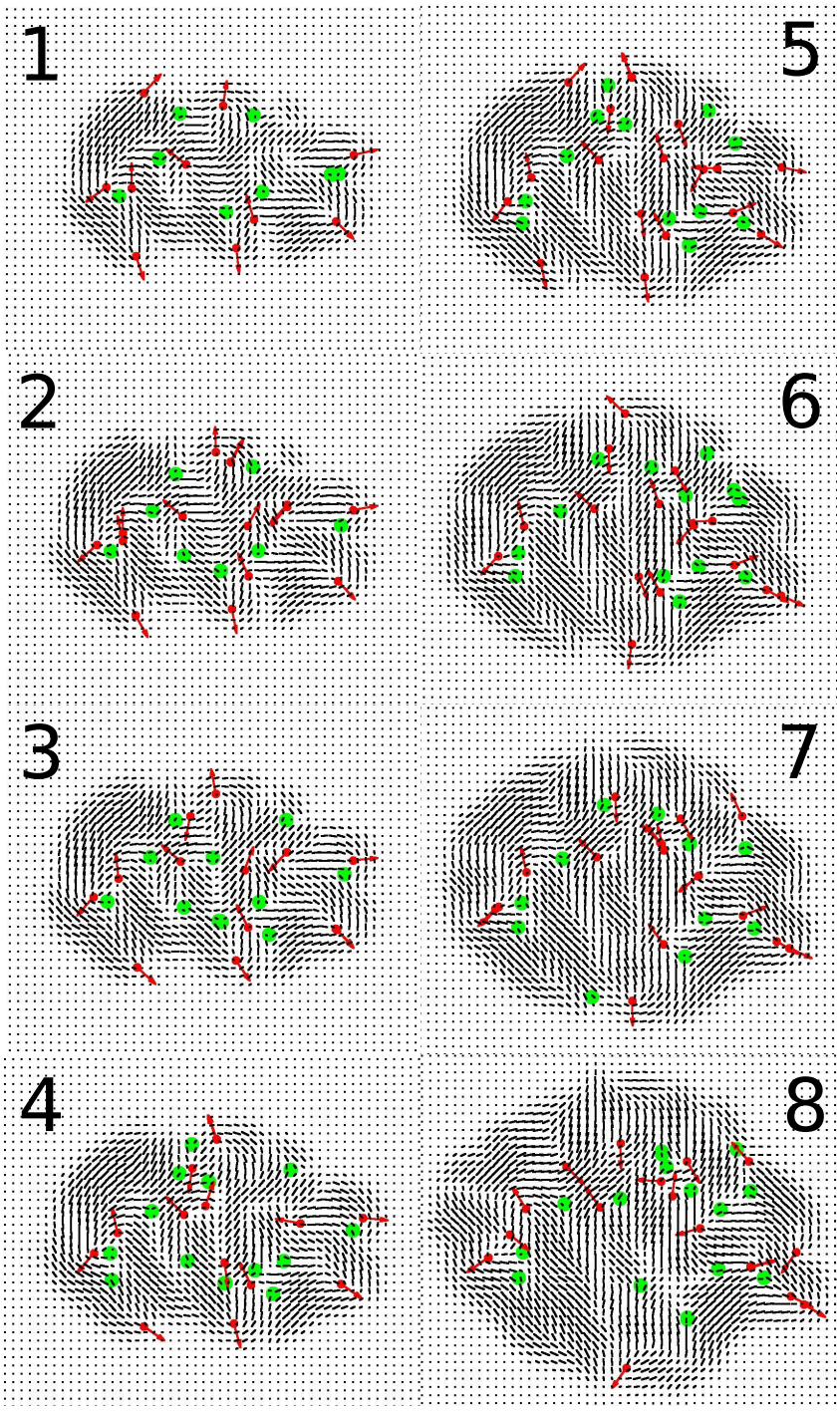

Figure 5.17: Motion of $\pm 1/2$ defects in a colony. The background is represented by the director map. Time step is 5 minutes. Images produced by Dr Matthew Blow.

between their polarity and the radial direction from the centre of mass of the colony, as discussed in the following subsection 5.4.2.

5.4.2 Polarity of +1/2 defects

The nature of topological defects is intimately related to the symmetry of the system. In our system composed of extensile, non-polar active particles, it is possible to observe only half-integer topological defects with opposite charges, that is $\pm 1/2$ [5]. The representations of these two defects are provided in figure 1.6. They are characterized by symmetries of different kinds: the negative half-integer defect displays a trifold rotational symmetry (considering a vertical axis orthogonal to the plane and going through the point defect), whereas the comet-like shaped positive half-integer defect has an axial symmetry with the axis in the 2D plane passing through the singularity point. Because of its axial symmetry, it is possible to assign a polarity to the $+1/2$ defect, which can be represented by a unit vector $\widehat{\mathbf{p}}$ (in the case of the rotationally symmetric $-1/2$ half defect, we cannot assign a polarity).

Contrary to the passive case for which defects annihilate once the system is given time to equilibrate [16], active nematics exhibit defect configurations that occur spontaneously (that is, without applying an external field or imposing boundary conditions), and that can be continuously regenerated by local energy inputs, inherent of the active particles, that is, the bacteria [101, 88]. Recent numerical studies focussed on the dynamics of topological defects occurring in active nematics, showing that it depends on their activity and their extensile or contractile character [101]. For instance, in the case of contractile systems (see section 3.3), researchers observed an enhancement of defect annihilation typical of equilibrated systems, whereas in the case of extensile systems they observed that defects were driven apart from each other, swarming around in the LC, suggesting an interpretation of defects as topologically well-characterized self-propelled particles [101].

The bacterial cells of our colonies can be interpreted as active nonpolar extensile particles, and their dynamics give rise to $\pm 1/2$ charged defects. More specifically, we were interested in analysing the behaviour of the $+1/2$ defects - for which a polarity can be identified - during the expansion of the colony. Hence, we considered the polarities $\widehat{\mathbf{p}}_d$ of these positively charged defects (for all

the colony and for all the frames for each single movie of a colony) and computed the projection with the vector $\Delta\hat{\mathbf{r}}_{d-com}$ that connects the position of the defect with the position of the centre of mass of the colony. In figure 5.18, we report the histogram of such projection $\hat{\mathbf{p}}_d \cdot \Delta\hat{\mathbf{r}}_{d-com} \in [0, 1]$, along with a sketch of the vectors (in the inset).

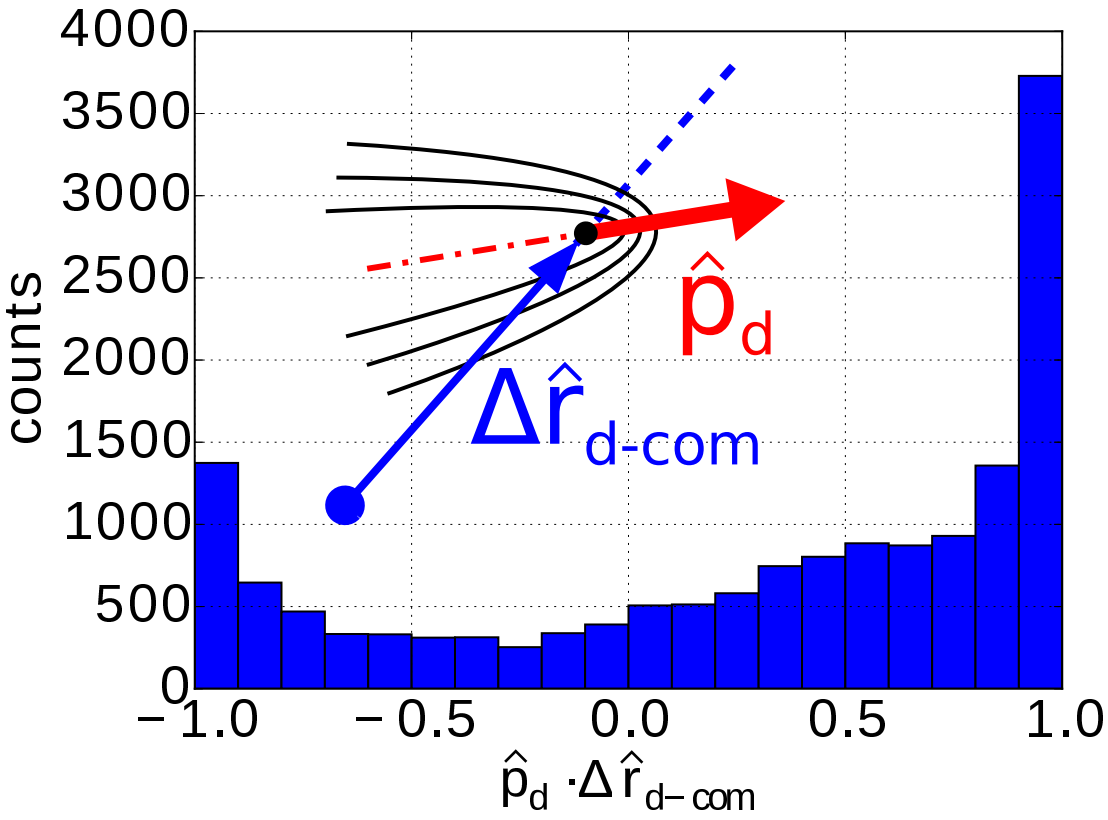

Figure 5.18: Histogram of the scalar product between the polarity of positive half-integer defect ($\hat{\mathbf{p}}_d$) and the radial vector connecting the centre of mass of the colony and the position of the point defect ($\Delta\hat{\mathbf{r}}_{d-com}$). We can observe an asymmetry in the histogram indicating that positively, half-integer defects tend to be aligned mostly along the radial direction and point outwards.

The histogram shows an asymmetry in favour of positive values of such projections, thus indicating that most defects actually are oriented radially - peaks at the extrema ± 1 - and outward - larger peak at $+1$. However, this plot does not tell us about the distribution within the colony of the defects.

In order to understand how the $+1/2$ defects were oriented with respect to their positions within the colony, we considered the distance d of each defect from the centre of mass of the colony, and then plotted the projection as computed

before with respect to that distance d. The result is given in figure 5.19, considering an average values from all the colonies.

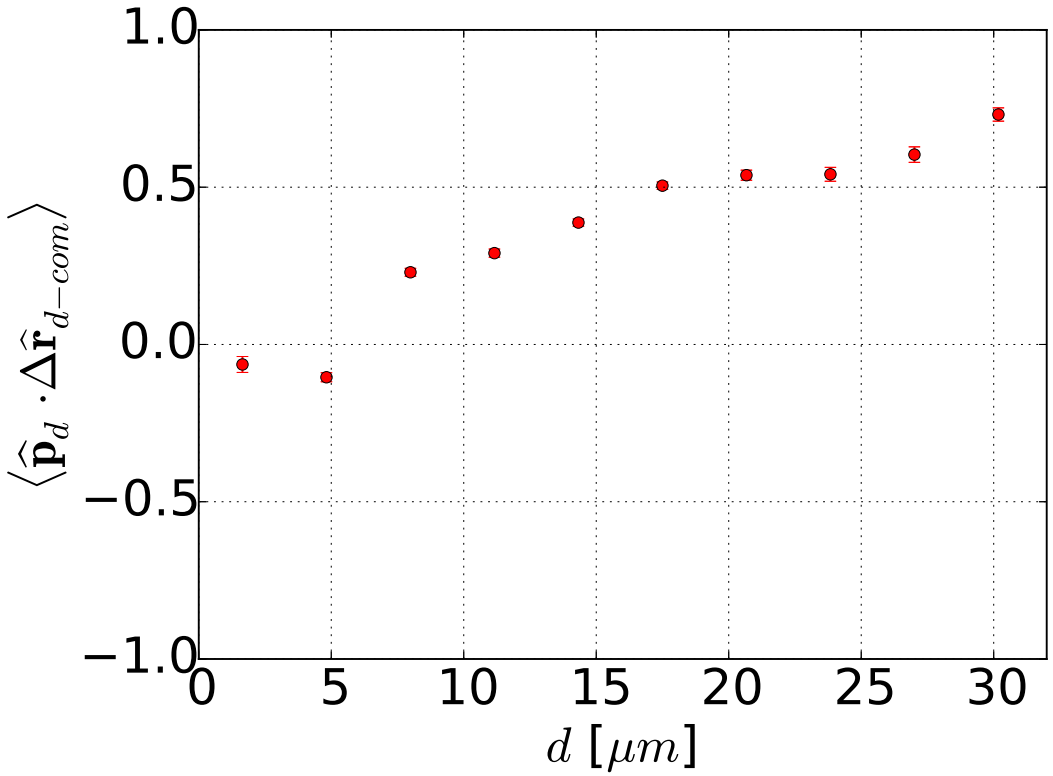

Figure 5.19: Projection between the unit vector of polarity of the positive, half-integer defect and the unit vector connecting the centre of mass of the colony to the defect position, averaged over all the defects detected, as a function of the distance of the defect from the centre of mass. The plot shows that, as the distance of the defects from the centre of mass of the colony increases, also the alignment between their polarity and the radial direction increases.

The behaviour of the projection $\hat{\mathbf{p}}_d \cdot \Delta\hat{\mathbf{r}}_{d-com}$ suggests that as the distance of the defect from the colony centre of mass increases, also the defect alignment with the radial direction increases. So, as the colony expands, these comet-shaped defects tend to point outward radially.

5.4.3 Dynamics of topological defects

As well as the motion of the bacterial cells, it is also interesting and informative to study the motion of the topological defects originated during the growth

of the colony. In order to investigate the defect dynamics, we considered the trajectories of both positively and negatively charged defects, detected and tracked as explained in § 5.4.1, and studied their mean squared displacement (MSD) and their velocity autocorrelation function on time. This investigation allows us to determine if these defects are freely diffusing or are transported by the expansion of the colony.

MSD

The mean squared displacement (MSD) of the trajectories of the topological defects is defined as follows:

$$\mathrm{MSD}(\tau) = \left\langle \left(|\mathbf{r}(t+\tau) - \mathbf{r}(t)| \right)^2 \right\rangle , \tag{5.8}$$

where τ is the delay times, $\mathbf{r}(t)$ is the position vector of the defect at time t, and the angle brackets $\langle \ldots \rangle$ indicate a time average and an ensemble average. The time average means that the squared displacement is averaged over all the possible delay time intervals τ for each trajectory. The ensemble average means that, for a given delay time τ (on which the time average has been already computed), we compute the average of the mean squared displacements from all the trajectories available.

In the case of diffusive motion, the behaviour of the MSD as a function of the delay time is represented by a linear relation, and from the slope of the curve it is possible to extract the diffusion coefficient D; if the MSD saturates to a finite value and shows a concave curvature, then the movement of the particles is in some way constrained. This indicates that the particles cannot freely diffuse away from their starting points; If the MSD increases faster than the linear relation, then the defects are being transported, meaning that, on top of the Brownian motion (erratic movement), these defects have an extra displacement over long time. In this last case of transport, the MSD curve shows a positive curvature, indicating that the dynamics of the defect for long times exceeds the corresponding diffusive case.

In figure 5.20, we report the measured MSDs for both positive and negative defects with linear and quadratic fits.

We observe different behaviours for the positive and the negative defects. In

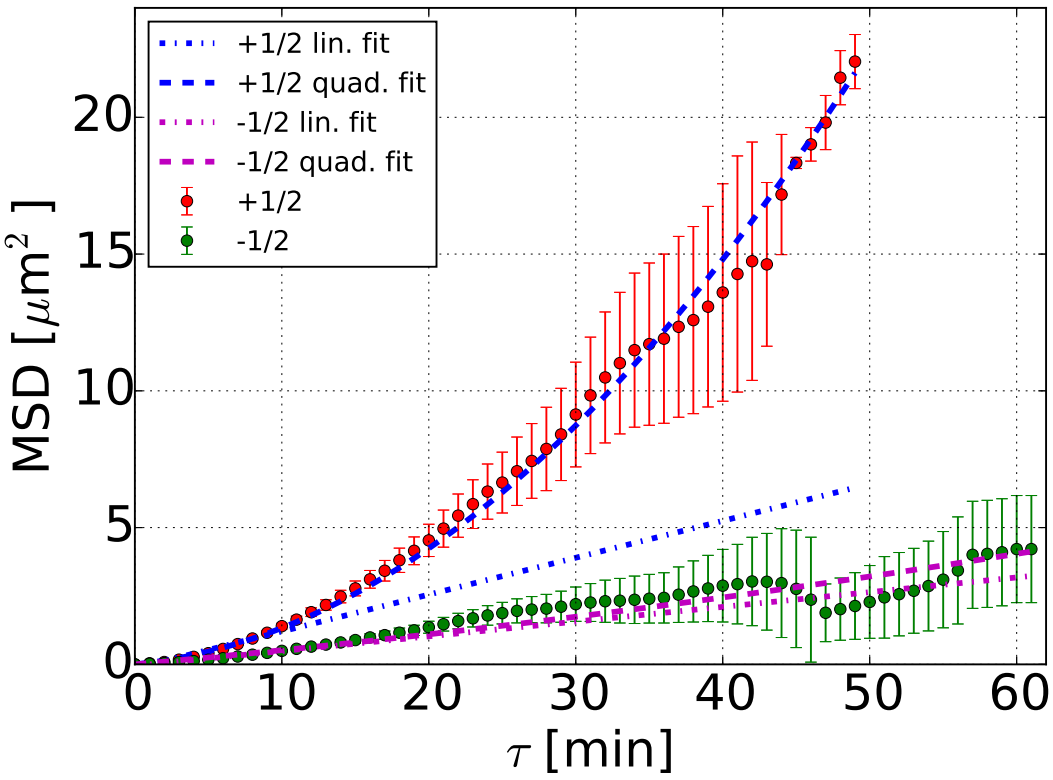

Figure 5.20: Mean squared displacement of positively and negatively half-integer charged topological defects. The quadratic fit label in the legend refers to a quadratic form that includes also a linear term, hence it is a linear plus quadratic fit ($\sim t^2 + t$).

the case of the negative defects, we see a linear behaviour that indicates a diffusive motion, whereas in the case of the positively charged ones, we observe a more than linear trend. A linear and a linear plus quadratic term (parabolic) fits are shown along with the experimental data for both the defects, that is, by using a linear relation $\langle r^2 \rangle \sim 4D_l\tau$ (dash-dot fitting curve), and a linear plus quadratic relation $\langle r^2 \rangle \sim 4D_q\tau + (v\tau)^2$ (dash fitting curve). These two fits are intended to give account of a diffusive or a diffusive plus convected motion of the bacterial cells into the colony.

For the MSD of the negative defects, the linear fit returns a diffusion coefficient $D_{l,-} = 0.0134 \pm 0.0007$ µm^2/s, whereas the parabolic fit returns a diffusion coefficient $D_{q,-} = 0.0122 \pm 0.0008$ µm^2/s and a transport velocity $v_- = 0.0176 \pm 0.0028$ µm/s.

For what concerns the MSD of the positive defects, the linear fit returns a diffusion coefficient $D_{l,-} = 0.0369 \pm 0.0032$ µm^2/s, whereas the parabolic fit returns a diffusion coefficient $D_{q,+} = 0.0135 \pm 0.0010$ µm^2/s and a transport velocity $v_+ = 0.0889 \pm 0.0006$ µm/s.

While the linear and parabolic fits for the -1/2 charged defects are similar (as the diffusion coefficients $D_{l,-}, D_{q,-}$ are), indicating a diffusive motion, in the case of the +1/2 charged defects, we see a clear difference between the two fitting curves, suggesting a directed motion over which a diffusive motion is imposed.

Velocity autocorrelations

In addition to the MSD of the defects, it is also possible to study the velocity autocorrelation function, which gives other complementary information about the particle dynamics. The normalized velocity correlation function is defined as follows:

$$v_{\text{corr}}(\tau) = \langle \mathbf{v}(t+\tau) \cdot \mathbf{v}(t) \rangle \,/\, \langle \mathbf{v}(0) \cdot \mathbf{v}(0) \rangle \ , \tag{5.9}$$

where $\mathbf{v}$ is the velocity of the defect. Like the MSD, the velocity autocorrelation function includes an average on time ($\langle \ldots \rangle$), where τ is the delay time; the average is computed over the increasing delay time. Briefly, this function shows how long a moving particle 'remembers' its previous movements, that is its direction of motion.

In the case of a pure Brownian motion, the displacements of the moving particle are completely uncorrelated, so the velocity autocorrelation should be null for every delay, except for $\tau = 0$. In the case of transport, the autocorrelation is usually above 0 for all the time range considered, showing that on average, a displacement has more chance to occur in the same previous direction over time.

In figure 5.21, we show the plot of the velocity autocorrelation function for both ±1/2 charged defects. We observe that, for both the defect kinds, the velocity autocorrelation function has a small value after the first time step. However, we notice that, for each delay time the values of the velocity autocorrelation function for the +1/2 charged defects are always larger than those of the -1/2 charged ones. Furthermore, the -1/2 defect autocorrelation function tends to zero as the delay time τ increases, whereas the corresponding one for the +1/2 charged defects has always non null and positive values (even at the end). This indicates that, when compared to the -1/2 charged defects,

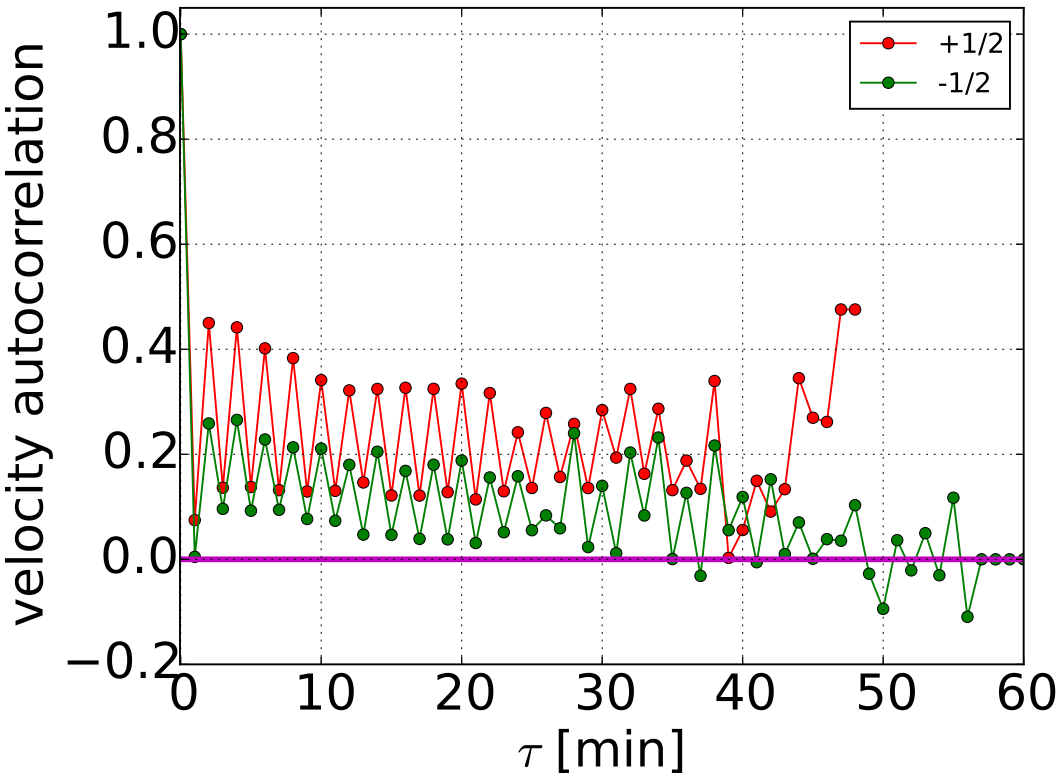

Figure 5.21: Velocity autocorrelation function of positively and negatively half-integer charged topological defects.

the +1/2 charged defects tend to move in a direction that is closer to their previous direction, hence they have some 'memory' of their direction of motion; the negatively charged defects tend instead to lose this memory as time passes, this lacking of memory being consistent with the diffusive motion shown in the MSD behaviour shown in figure 5.20.

5.5 Discussion

We have shown in this chapter that bacterial microcolonies actually exhibit features that are typical of active nematics. From the investigation of the global orientational order that resulted in the decay from an orientationally ordered to a disordered phase, we moved to a local analysis that showed us the existence of some small nematic domains. Furthermore, by investigating the way cells pack within the colony, we could derive the emergence of bend deformations. These

deformations are unstable in our system and lead to the generation of topological defects with defined $\pm 1/2$ charges.

It is interesting to observe that from the analysis of the defect dynamics, we can derive two different behaviours depending on the charge of the defects, that is, on their symmetry properties. For the positive half-integer defect kind, the polarity study indicates that these defects tend to move in the radial direction and that their alignment is stronger the further they are from the colony centre. These results are corroborated by the velocity-velocity correlation function that shows that these defects actually tend to have memory of their previous directions.

This memory is however lacking in the case of the -1/2 charged defects (considering the corresponding velocity-velocity correlation function in figure 5.21). Furthermore, these negatively charged defects have also a different dynamics with respect to the positive ones, showing an essentially diffusive behaviour, instead of a combination of diffusion and transport as displayed by the positive counterpart.

Although, in similar systems, the net displacement of the half-integer negatively charged defects was observed to be null or smaller than that of the positive defects [70], in our case the substrate onto which the defects (of both signs) are developing, is going through a process of expansion, that is, the growth of the colony. Hence, this would suggest that, as for the $+1/2$ charged defects, also the -1/2 charged defects might be expected to display more than diffusive dynamics.

However, this is not what we observed in our experiments and derived from our analysis. A possible interpretation of this behaviour could be related to the limited time during which the colonies are observed and the defects tracked: it could be possible that the -1/2 defect MSD changes from a linear to a more than linear behaviour for longer times than those investigated in the present work. Unfortunately, with the set-up we used, this longer time window cannot be achieved because a second phenomenon - consisting in the buckling of the colony - occurs, changing the geometry of the system from 2D to 3D (this is discussed later in Chapters 7 and 8), hence preventing the tracking of defects.

This represents a limitation to our study, but it suggests also some interesting experiments where the surfaces or the confining geometry surrounding the expanding colony can play a major role and be used to control the way that

expansion takes place.

In this context, we notice that during the preparation of our samples for time-lapse experiments on growing bacterial microcolonies, it happened in some cases that we mistakenly let the bacterial droplet dry for too short a time after its injection on the agar pad. This is a crucial step in the sample preparation as it can lead to different conditions in which the colony grow. If the droplet with a low density of bacteria does not dry completely, the individual bacteria dispersed on the agar pad (sealed on top with a microscope coverslip) can be seen behaving in different ways through the thin liquid layer between the agar pad and the top coverslip. For instance, some of them just move erratically as a Brownian particle, other get stuck to the top glass surface through one or more flagella and start rotating as a clock hand by moving the remaining ones. Others, as represented in figure 5.22, can settle on the agar pad and keep growing and dividing as for the colony for a completely evaporated droplet (see phenomenology as described in section 5.1). In this case, however, because of the presence of the liquid layer, cells are not tightly packed and some cells are even able to escape from the colony by swimming through the liquid. This is shown in figure 5.22, where we focus on a region of interest (blue boundary, then shown in the 8 next smaller frames) in which a cell can be seen swimming from a position at the boundary to another position close to a cell separated from the colony.

Because of this weak packing of cells, more vacancies between cells could be seen with respect to the typical case (see figures 5.4 and 5.14), and a smaller degree of order is expected even from the early stages of the microcolonies.

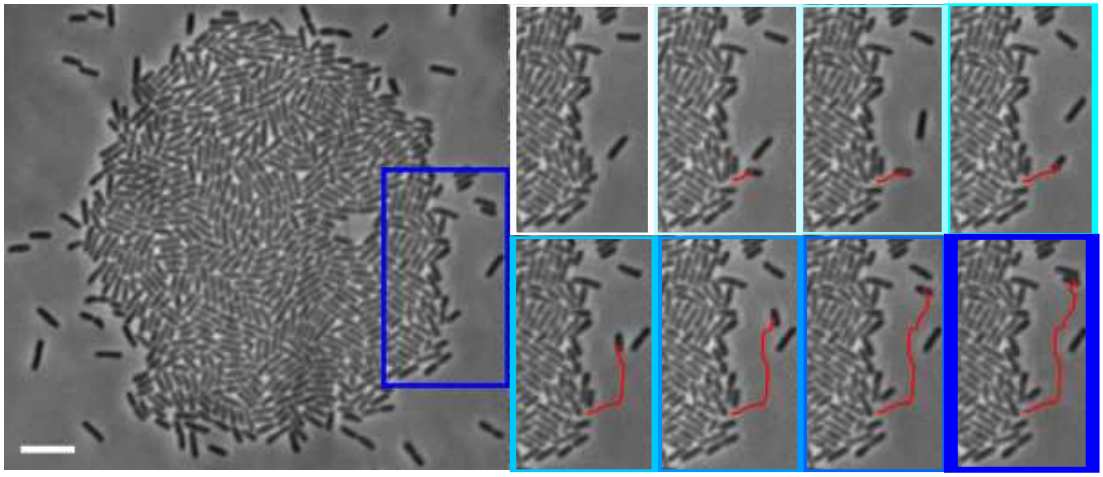

Figure 5.22: Colony growing in presence of some liquid surrounding its boundary. We can observe that bacteria at the boundary tend to be dispersed around the colony and that some are able to swim (see the tracked cell with red line). Scale bar in the first image is 5 µm. The blue region is the region of interest for the next images with a time step of 1 min from one another.

Chapter 6

Comparison with simulations and models

In this Chapter, we first analyse simulations of 2D bacterial colonies growing onto a substrate, and then discuss a model for describing the evolution of cell orientation at the boundary of the colony. These simulations and model are compared to the experimental results of Chapter 5.

For the simulations, we focus on two aspects: (*i*) the nonequilibrium regime and (*ii*) the long-time behaviour. Starting from the same configurations of the real colonies, the simulated colonies are equilibrated through a Monte Carlo simulation in order to investigate the differences with the experimental case. For the long-time behaviour simulations, we compare the results for the global order and local arrangement in simulated colonies with a larger number of cells than the real cases observed in the laboratory: in the latter case, buckling of the cell layer occurs, with the consequence that cells start exploring the third dimension. In simulations, it is possible to constrain cells into the horizontal plane, hence allowing for the analysis of larger cell layer. Furthermore, in the last section, we also discuss a model to interpret the behaviour of cells at the boundary of the colony, and compare the prediction with the experimental results.

The simulations were performed by Dr Juho Lintuvuori (Monte Carlo equilibration) and Dr Fred D. C. Farrell (long-time/large size behaviour). My work consisted in analysing the outputs of these numerical works and in comparing the results with experiments.

6.1 Equilibrium

The bacterial microcolonies studied here can be classified as active systems that evolve in an inherently nonequilibrium regime, the out-of-equilibrium condition being determined not by a heat reservoir or an external applied field interacting with the constituent units, but by the same cells, each one with its own energy reservoir and able to dissipate energy.

Hence, we wondered what would happen if instead of the nonequilibrium regime, the particles would be thermalized, as in the case of an equilibrated system. This case corresponds to a passive thermodynamic model, where the bacterial colony is made up of polydispersed suspension of spherocylinders that are not able to grow or divide. In order to study this case of equilibrium regime, Monte Carlo (MC) simulations have been performed, to thermalize the simulated microcolonies, and observe the final equilibrium configuration.

In the MC simulations, the individual bacterium shape is approximated using a repulsive spherocylinder model [118] by matching the size of the cells to the experimental values. The repulsion between two particles of this kind is modelled using a Weeks-Chandler-Andersen (WCA) potential [119]. The simulations are initialized by reading in the positions and the orientations of the bacteria as obtained from the corresponding experimental colony, further matching the individual bacterial lengths. The spherocylinders are then placed into a circular confinement of radius R_{sim}, so that the overall area fraction is approximately 90-95%. To avoid any of the spherocylinders initially reaching outside of the confinement, their positions are scaled to ensure such that they are all inside, creating artificial overlaps between pairs of particles. The system is then allowed to relax, running the MC simulation (using standard metropolis type acceptance criterion). The simulations are run for a minimum of 10^5 MC sweeps, where each sweep consists of a rotation/translation of each of the particles. A minimum of the WCA potential is then reached, indicating the equilibration of the system.

In figure 6.1, we compare the experimental and the corresponding Monte Carlo equilibrated configurations for a typical colony from generation 5 to 9 (the experimental configurations on the left are the same last five shown in figure 5.4 as phase-contrast images). The colour assigned to particles is a measure of their relative orientation with their neighbours.

In order to quantify the anisotropic-isotropic transition for the equilibrated

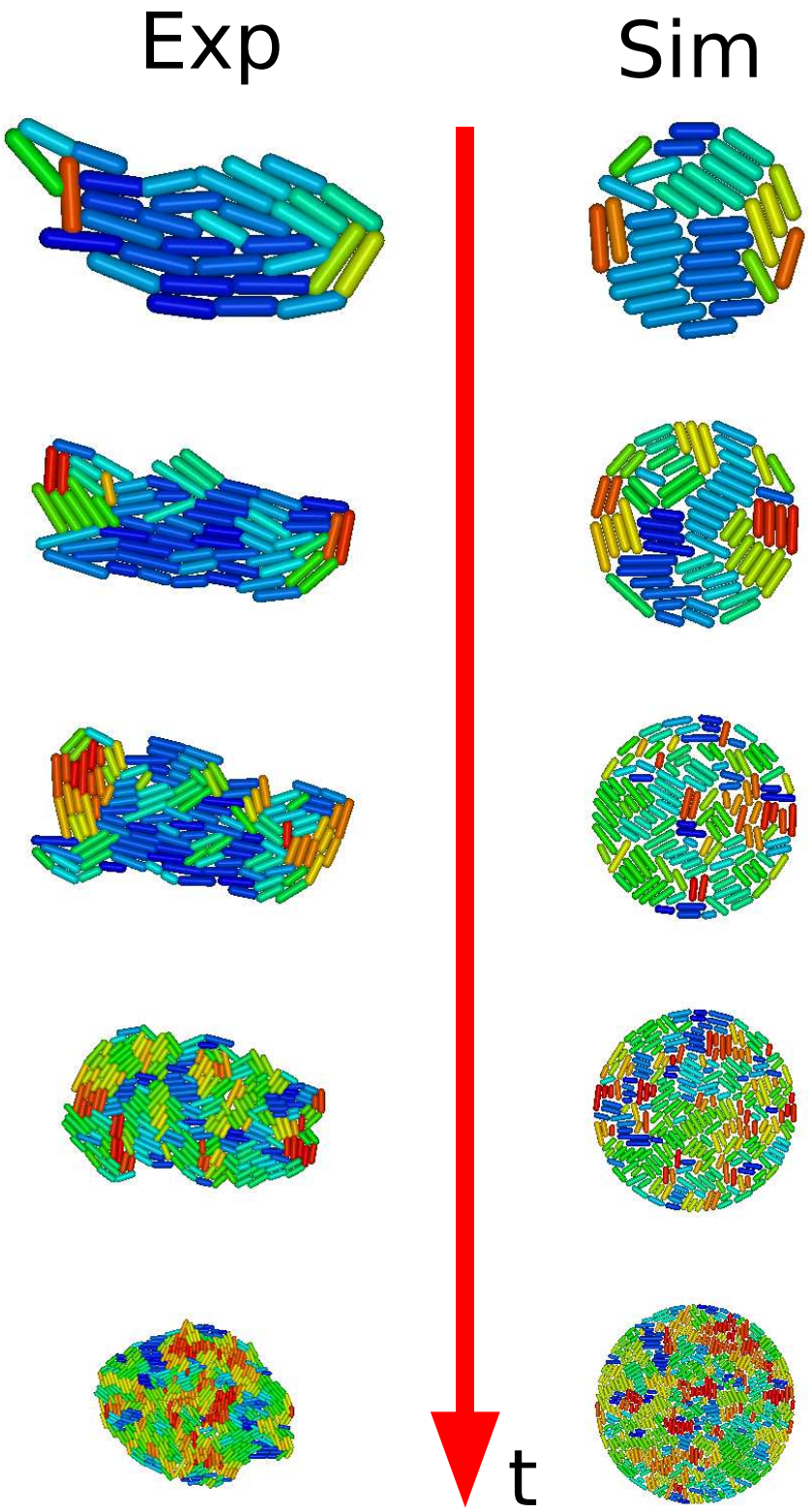

Figure 6.1: Experimental and simulated colony configurations.

case, we computed the order parameter Q (as specified in § 5.2), and compared its behaviour with that of the real configurations. The result is given in the plot in figure 6.2.

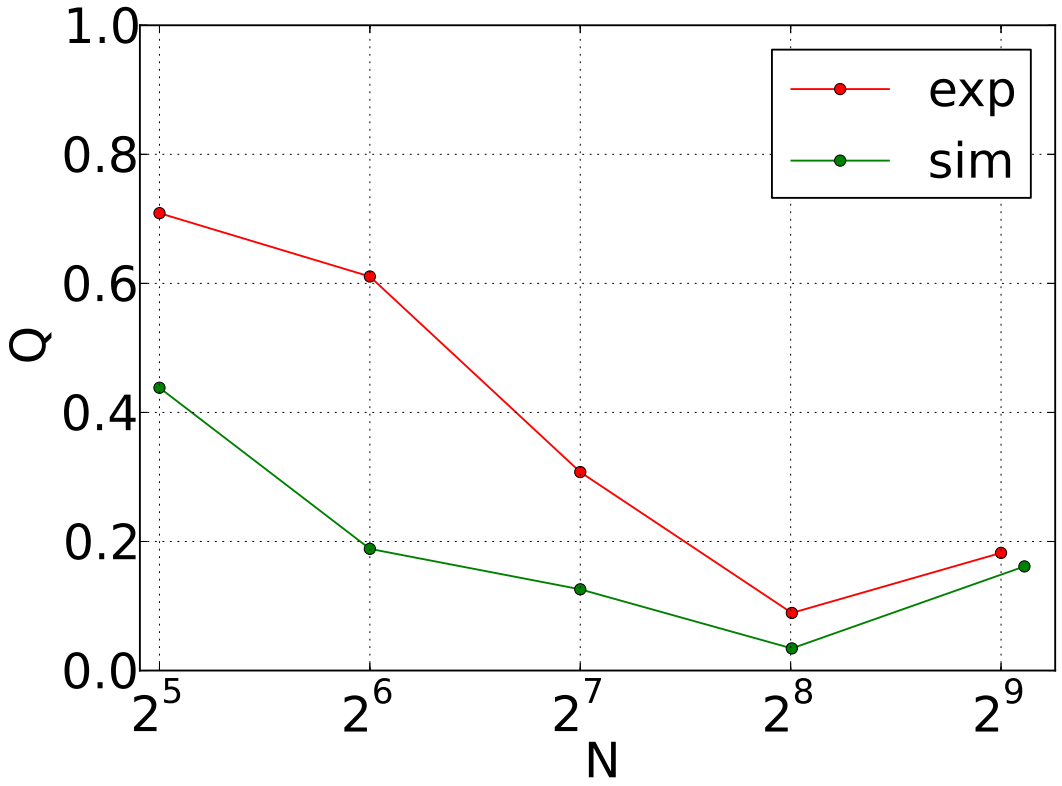

Figure 6.2: Global nematic order parameter Q for real and simulated colonies *vs* the number of cells N. The equilibrated colonies show an earlier decay of nematicity with respect to the real ones, despite the common isotropic phase reached at the end.

Although they both tend to small values ($Q \in [0.1, 0.2]$), the behaviour of Q from the MC simulations shows a quicker decay than that of the experimental nonequilibrium case. Furthermore, from the configurations shown in figure 6.1, it is possible to notice that the local side-by-side packing of cells seems to be enhanced, that is, the stacks are longer. In order to check for this longer stacks, we plotted the map of the 2D orientational correlation function $g_2(\mathbf{r})$, as done in § 5.3.2. The result is given in figure 6.3, where we can see from 1 to about 6 peaks in the orthogonal direction $r_\perp$ with respect to the reference bacterium, whereas for the experimental colonies we were able to see clearly 4 peaks at most.

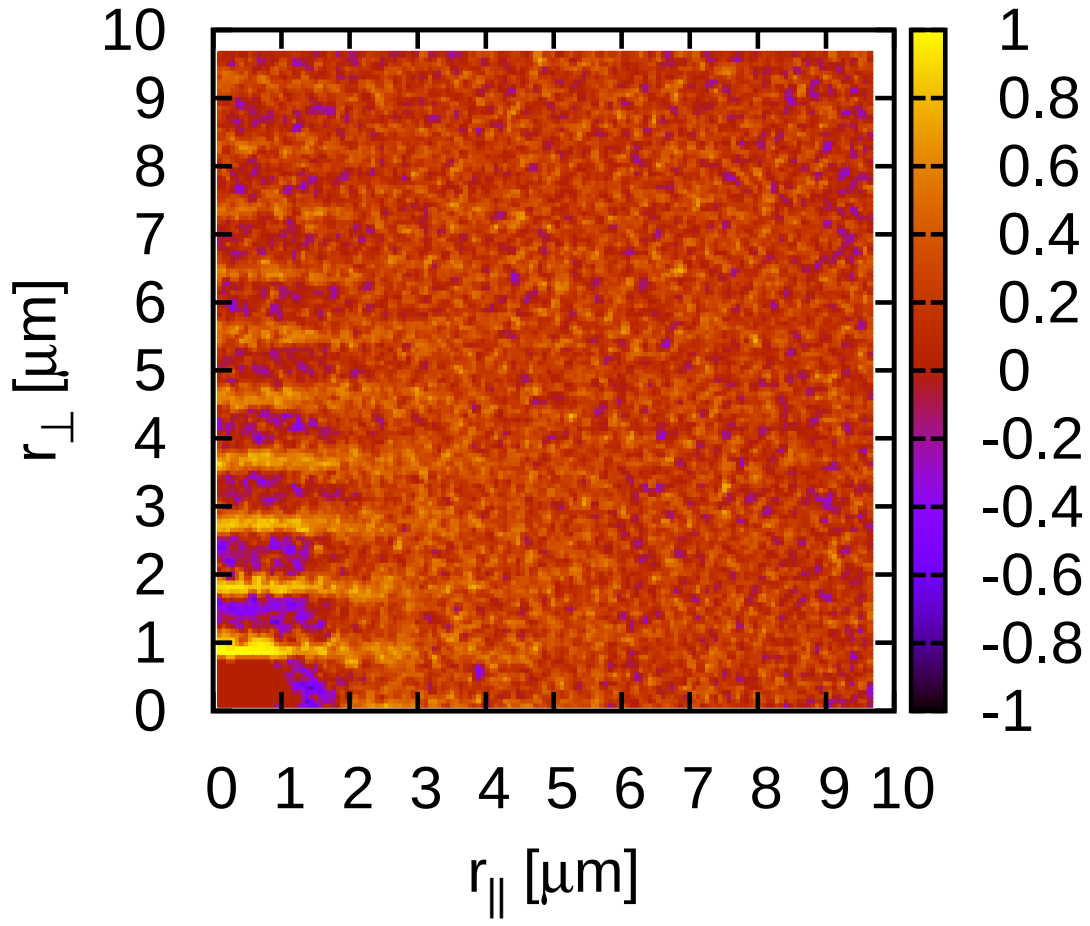

Figure 6.3: 2D correlation map from an equilibrated *in silico* colony. As suggested from the longer stacks of particles shown in figure 6.1, the perpendicular component $r_\perp$ presents 2 more peaks than the real case (see figure 5.11).

In the direction parallel to the longest axis of the reference bacterium we cannot see any change from the real case instead. In order to make the peaks look clearer, we projected the perpendicular and parallel directions and plotted them separately, as reported in figure 6.4.

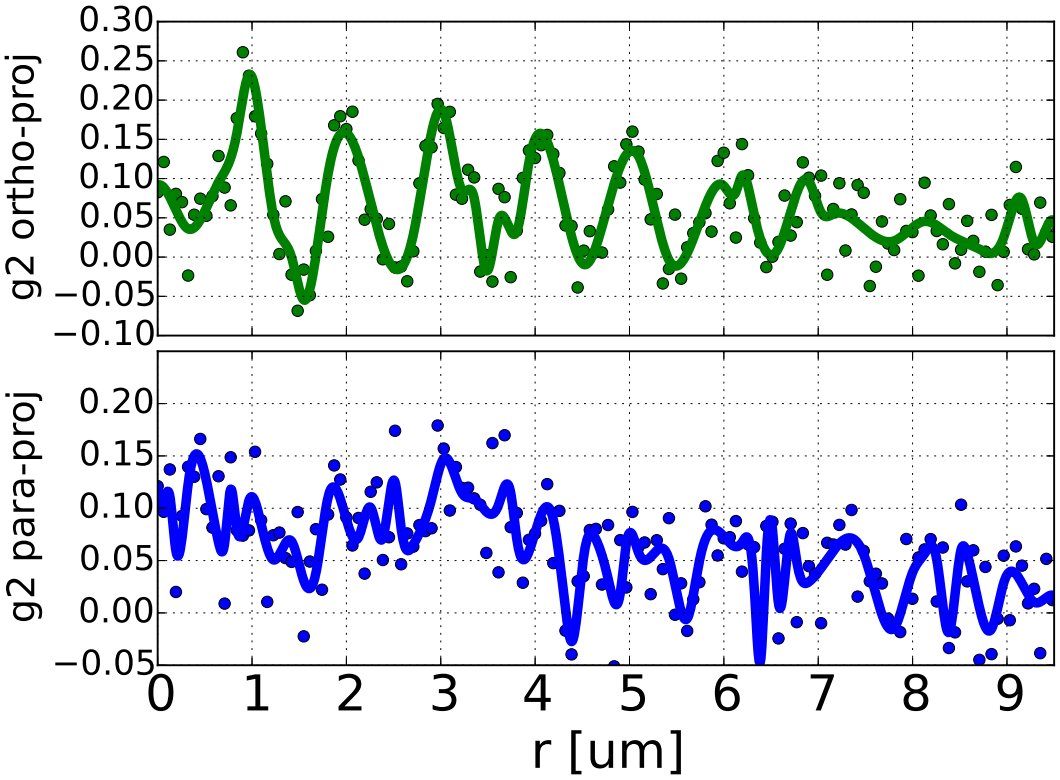

Figure 6.4: Parallel and perpendicular projections of a 2D orientational correlation map from a simulated colony. The values (points) correspond to the average value computed along a row (orthogonal projection) or column (parallel one), whereas the solid line is an interpolating curve. We can observe clearly 6 peaks for the orthogonal projection (green curve), indicating that longer stacks are present in the equilibrated case. For the parallel projection (blue), we cannot see peaks but a larger values in the 0-3 µm range, that would correspond to the bacterial long axis length.

Thus, we observe that for the thermodynamic simulations (corresponding to the equilibrium regime), which take into account volume exclusion but no growth, we do not find a good agreement between the behaviour of the local correlations from these simulations and those from the real cases: in the passive equilibrated case, the correlation length along the perpendicular direction is larger than that

observed in the experiments, in a fashion similar to that observed in unbounded, passive systems as discussed previously in § 1.2.2 (see figure 1.4, [12]). This difference indicates that growth - representing the activity characteristic in our living system - plays a crucial role in determining the nematic order.

6.2 Long-time behaviour

The second kind of simulations analysed was based on an active (nonequilibrium) model where bacteria grow in a 2D space (they are actually modelled as discorectangles) and push against each other, the mechanical interaction being modelled through Hertzian theory of elastic contact [120]. The force between two cells is approximated as a force between two spheres placed along the major axes of the two cells, in such positions that their distance is minimal but the spheres remain within the discorectangles (see figure 6.5) [121, 103].

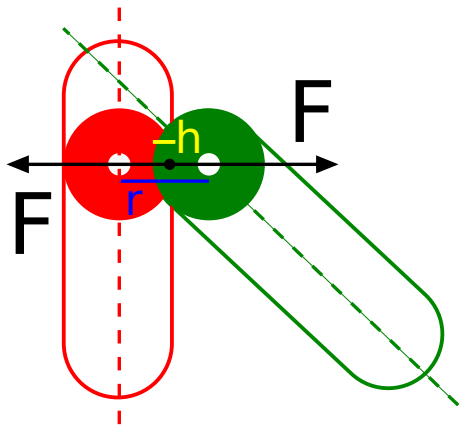

Figure 6.5: Sketch of two discorectangles pushing each other, used to model two cells in contact.

If r is the distance between the centres of the circles and $h = d - r$ is the overlap, with d the diameter of the circles, then the force F is assumed to be equal to $F = E\, d^{1/2}\, h^{3/2}$, where E is a coefficient used to define the strength of the interaction and is proportional to the elastic modulus of the cells [121]. On the assumption of an overdamped dynamics and that every infinitesimal section of the cell experiences a friction force with the surface proportional to its velocity, the equations for the linear and angular velocity of the cells at position $\mathbf{r} = (x, y)$ with an angle θ under the force F, are given by $\dot{\mathbf{r}} = \mathbf{F}/(\zeta l)$ and $\dot{\theta} = 12\tau/(\zeta l^3)$,

where ζ is a constant that describes the friction between the surface and the cell, and τ is the torque on the cell. Note that the assumption that the friction force affecting the cell section is proportional to its velocity is a simplification. Such relation could be indeed more complicated and it is not well characterized experimentally. However, simulations indicate that the details of this force do not make a large difference in the overall behaviour of the colony [121].

Thus, in this model, the first mother cell grows until it reaches a given length l_c, after which it will reproduce by dividing into two identical cells. The length l_c is taken to be similar to the one observed in the experimental case of *E. coli* cells, that is about 6 µm (see figure 5.5 for the histogram of cell lengths in the experimental colonies). Just after the division, the two daughter cells receive a small random perturbation with respect to the initial orientation of their mother cell in order to prevent them from growing in a straight line. Then, the two cells keep growing side-by-side until they divide, hence giving rise to a 4 cell colony. If the process is carried on, the colony would expand at an exponential rate. However, as in real cases, growth is limited by some factors, like the diffusion of nutrients into the colony or the production of waste products within the colony. This limiting effect has been taken into account in the simulations by introducing the dynamics for a limiting nutrient that obeys a diffusion equation. Considering this nutrient depletion, cells consume the nutrient in order to grow, so the growth rate of the cells depends on the concentration of the nutrient, and the same nutrient is depleted by the growth of cells. After a long time, there is no longer nutrient in the middle of the colony, so the cells are no longer able to grow. Only those cells located in a narrow edge shell of the colony are still able to grow, leading to a colony which expands linearly on time [47].

The simulations show that the colony initially becomes disordered, and then develops radial order. To quantify the loss of order, the order parameter Q can be computed. In figure 6.6, we plot the results of Q as a function of the cell number for the experimental and numerical cases.

We observe that qualitatively the decays of Q from the simulation and the experiment are comparable. However, in the simulation we can clearly see a step-like shape (for instance from $N \in [2^4, 2^8]$). This is due to the synchronization with which *in silico* cells divide.

Another aspect, studied and compared to the real case, was the radial order

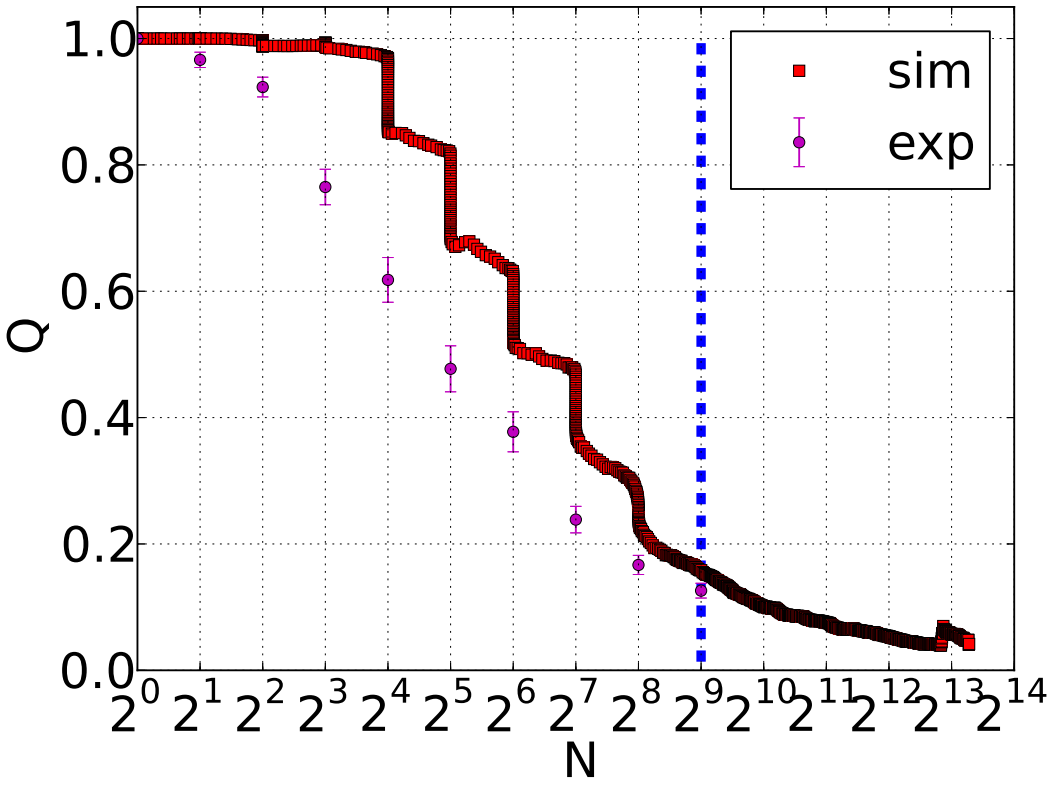

Figure 6.6: Comparison between the global tensorial nematic order parameters for the experimental and the simulated colonies. The dashed blue line represent the largest value of cell number that can be reached in the experimental case, that is between 500 and 1000 cells. Both the curves show a decay towards low values of the order parameter, with the curve from simulations showing a step-like shape due to synchronization in division of cells.

evolution within the colony, which can be quantified by computing the radial order parameter, defined as:

$$P_{rad} = \left\langle 2\cos^2(\theta - \phi) - 1 \right\rangle , \tag{6.1}$$

where $\theta = \arctan(y/x)$ is the angle between the horizontal axis and the vector connecting the centre of masses of the colony and of the individual cell considered, and ϕ is the cell orientation angle. A P_{rad} equal to 1 corresponds to cells oriented perfectly radially within the colony, whereas equal to -1 if cells are perfectly tangential to the colony boundary.

An effect that is characteristic of the case of growing nematics is that the

expansion in the colony tend to align the cells along the direction of the velocity gradient, leading to an ordering effect and a non-zero order parameter. At the level of the single particle, we can imagine a cell at a given angle with respect to a velocity gradient on the direction of expansion of the colony. In the case of a monotonically increasing velocity gradient, the cell experiences a larger force closer to its front than to its back, resulting in a torque that tend to align the cell long axis along the direction of the velocity gradient. Hence, if we consider a cell moving in the flow generated by the other cells, we expect an alignment along this direction (see figure 6.7). The details of this model of alignment are discussed in the next section 6.3.

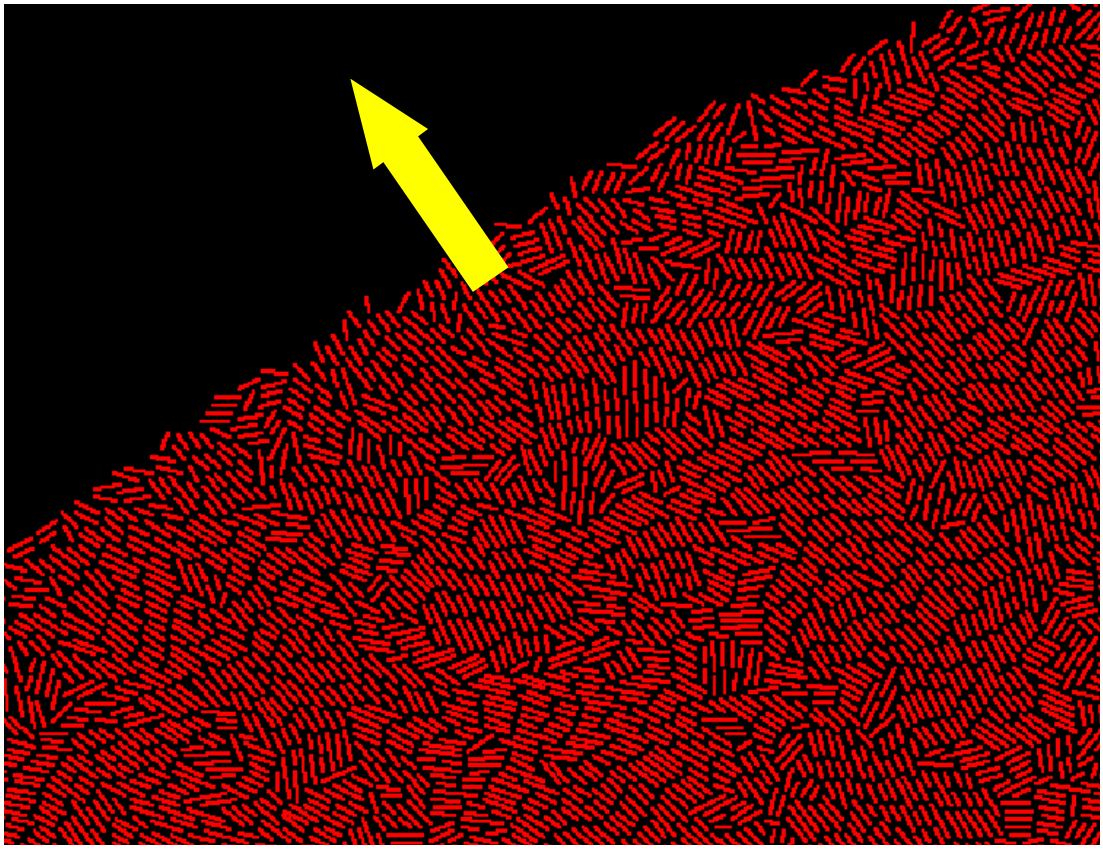

Figure 6.7: A frame from the active particle simulation. The colony is expanding in the direction of the arrow (radial direction). With respect to colonies of smaller sizes, in these long-time simulations, bacteria tend to align along the radial direction or, in other words, the direction of growth of the colony as quantified by measuring a radial order parameter (see figure 6.8).

In figure 6.8, we report the plot of the function P_{rad}. Despite the small

experimental value of the radial order parameter in the case of two cells, we observe that both the experimental and real cases show a qualitatively comparable decay as the number of cells considered is increased. However, it is interesting to notice that in the simulations the radial order starts increasing once reached the 8^{th} generation (2^8 cells). This behaviour will be discussed in the next section dealing with a model for orientation of cells. For the experimental case it is not possible to reach such large numbers of bacteria without incurring in the buckling of the microcolony, which leads to the invasion of cells into the third dimension and the creation of stacked layers of cells.

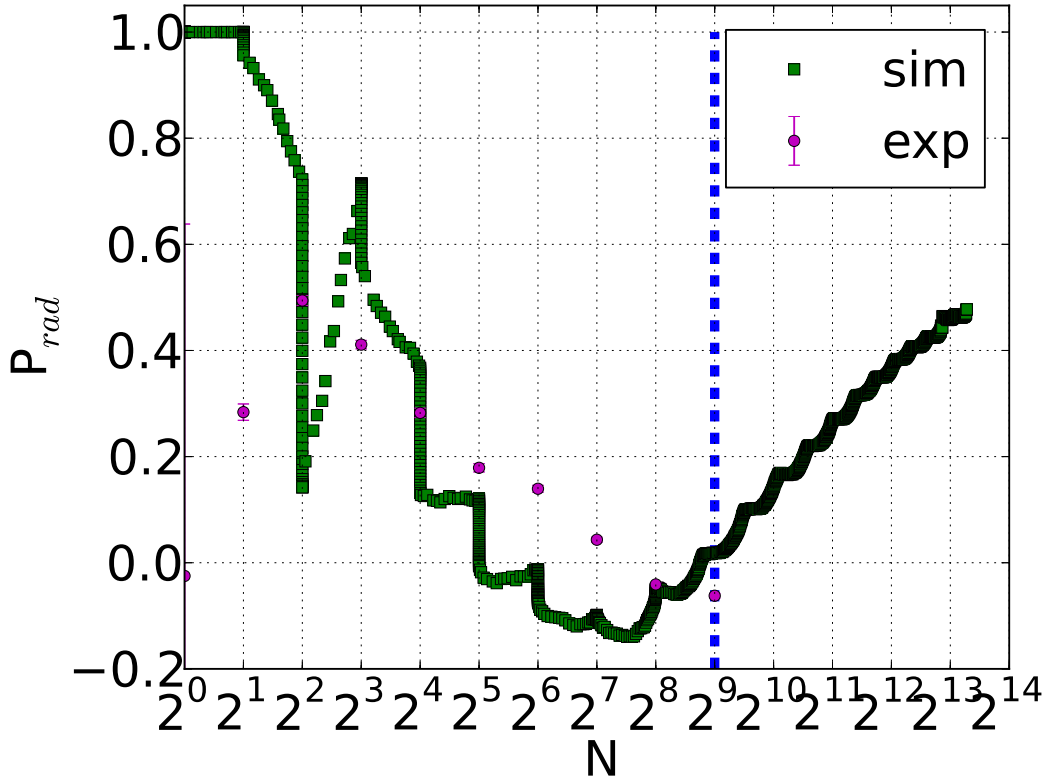

Figure 6.8: Comparison of the radial order parameter P_{rad} for real and simulated colonies. The dashed blue line represents the large colony limit that can be observed in the experiments before buckling occurs. Simulations suggest that as the number of cells increases, the simulated colony shows a first decrease in the radial order, followed by an increase for large colonies.

In addition to the global and radial order, the local arrangement of cells was also investigated by using the 2D correlation function as given in eq. (5.6). The

comparison between experiments and simulations are shown in figure 6.9 for a typical colony of about 500 cells (see figure 5.4).

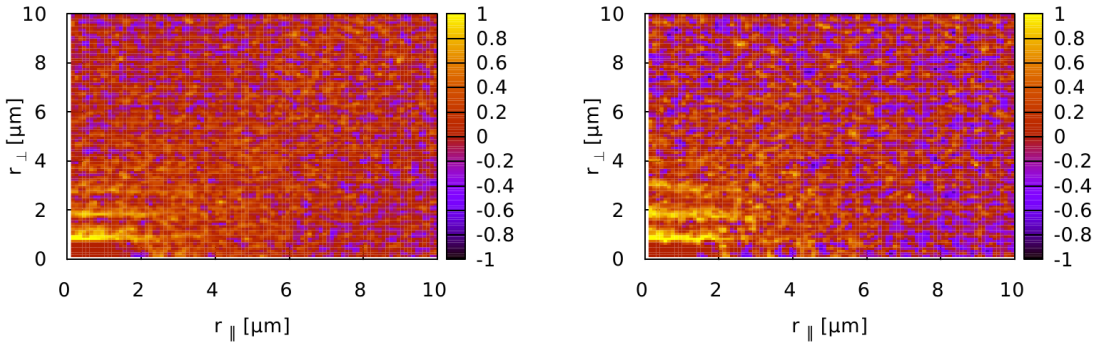

Figure 6.9: Comparison of the 2D orientational correlation functions between experiments (left) and simulations (right) [121]. The two maps look similar: in both we can see peaks spaced of about 1 µm each other, that is the bacterium width. The number of peaks is comparable as well, as we can count 3 peaks quite clearly, the fourth one being almost completely faded out.

The functions look similar for the experimental and the simulation cases in terms of the number of peaks visible along the perpendicular direction, spaced about a micron apart. The cells, as seen previously in § 5.3.2, tend to line up in perpendicular rows and they have a width of about 1 µm. No significant peaks can be observed in the parallel direction.

We observe that some relevant simplifications have been made in this model: for instance, elastic deformations of the cell shape and friction forces between particles are not taken into account, but only friction between cells and surfaces are considered. However, it is remarkable to notice that although these potentially relevant details were not taken into account, the qualitative behaviours of the active model and the real system showed a fair agreement, when considering the order parameters and the 2D orientational correlation maps.

6.3 Boundary orientation model and comparison with experiments

If the behaviour observed for the global nematic order parameter Q is something expected, that is, a monotonic decrease from 1 to small values between 0.1 and 0.2, we see a non-trivial behaviour in the case of the radial order parameter P_{rad}:

after a first decrease, the radial parameter starts increasing at around the 8^{th} generation (figure 6.8) as suggested by simulations. In this section, after a brief presentation of the phenomenology of orientation at the colony boundary, we discuss a model proposed by Dr Davide Marenduzzo in which the increase of P_{rad} can be understood considering that the ordering due to the expansion flow of the colony becomes more and more significant as colony gets larger, leading to a radial ordering of the cells. Finally, the predictions of the model are compared to the results obtained from the experiments by analysing the orientation of cells at the boundary.

6.3.1 Phenomenology

When an active nematic material has an interface, a preferential alignment of the director at the interface can be observed [102]. In this case, the active forces present at the interface are able to generate a flow that in turn causes an 'active anchoring'.

In our case of growing bacterial colonies, a similar effect can be observed at the boundary between the cells and the surrounding environment formed by agar. In proximity of the boundaries, bacteria tend to align orthogonally with respect to the direction of propagation of the colony (for a radial expansion) or, in other words, they tend to align tangentially with respect to the colony boundary, as can be observed in a typical colony in figure 6.10.

Most cells are oriented at an angle that is close to the tangent to the colony boundary, although some outliers at the perpendicular with the boundary can be seen as well, as it is quantified in section 6.3.3. The alignment observed in figure 6.10 can be thought to arise from the growth of the nematic, that is, the colony, through two distinct mechanisms. The first mechanism is of a morphological kind, and it is related to the initial, marked anisotropy of the colony. As can be observed in figure 6.10, the colony has a tendency to elongate along the director in the earlier stages of growth, so that, in a sufficiently ordered colony, the portions of boundary with tangential alignment are stretched along the boundary. At later stages, as the overall orientational order of the colony decreases (*i.e.* when the order parameter Q starts decaying, as in figure 5.8), this mechanism becomes less important, and it is replaced by a second mechanism based on the advance of the colony boundary into the agar that produces torques on the peripheral bacteria,

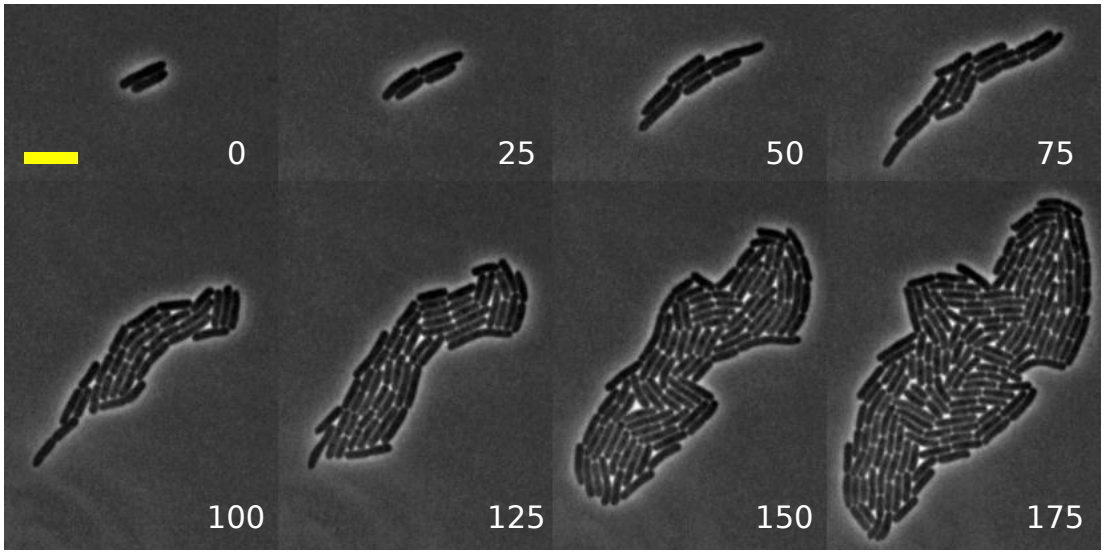

Figure 6.10: Configuration of cells for a small colony. Looking at the cells located at the boundary, it is possible to notice that, as the colony expands, cells tend keep their orientation tangential to the boundary of the colony. The number in each frame corresponds to the time in minutes. The scale bar in yellow in the first frame (time 0) corresponds to 5 µm, and it is the same for all the other frames.

rotating them so that they locally re-orient tangentially to the boundary, in a similar way as observed by Su *et al.* [122].

6.3.2 Model for re-orientation at the boundary

The model is based on some fundamental dynamic variables, which are defined as follow:

- ρ - the bacterial density. In our case of a 2D system, ρ has the dimension of cells/µm^2. However, we will make a further simplification by considering a 1D model, so that the bacterial density is measured in cells/µm;

- $\mathbf{v}$ - the averaged coarse-grained velocity vector of the bacteria in the colony that reduces then to the simpler scalar v in 1D;

- ϕ - the orientation of the cells in the colony with respect to the horizontal axis $\widehat{x}$ of the reference system.

A modified continuity equation that takes into account (i) the conservation of mass and (ii) the growth by bacterial reproduction, is considered:

$$\partial_t \rho + \partial_\beta j_\beta = \alpha \rho \,, \tag{6.2}$$

where the first term on the l.h.s. is the partial derivative of the concentration with respect to time t; the second term on the l.h.s. is the divergence of the current density $j_\beta := \rho v_\beta$ with $\beta = (x, y)$ being the spatial index; [1] finally the term on the r.h.s. is the source of the system, *i.e.* the bacterial reproduction that is assumed to depend on the bacterial concentration and the constant growth rate α. Now we make the ansatz that the cell concentration is constant within the colony, vanishingly abruptly just outside the colony, so

$$\rho(\mathbf{r}) = \rho_0 \theta(\mathbf{r}_0(t) - \mathbf{r}) \,,$$

where ρ_0 is the constant value of the concentration in the colony and $\theta(\mathbf{r})$ is the Heaviside step function, whereas $\mathbf{r}_0(t)$ is the position of the colony boundary at time t (which increases as the colony grows).

We assume that the colony is incompressible which corresponds to a vanishing material derivative of the concentration:

$$\frac{D\rho}{Dt} = (\partial_t + v_\beta \partial_\beta)\rho = 0 \,. \tag{6.3}$$

Hence, using eq. (6.3) in eq. (6.2), a non-null divergence of the velocity field is obtained, which equals the growth rate indeed:

$$\partial_\beta v_\beta = \alpha = \nabla \cdot \mathbf{v} \,.$$

If we make the further simplification of radial symmetry, so that we can move from a 2D to a 1D model, and if we consider a constant growth rate α, then we have that

$$v(y) = \alpha y \,. \tag{6.4}$$

In figure 6.11, we report both the concentration $\rho(y)$ and the velocity $v(y)$.

[1] Here the use of repeated indices means sum over them, *i.e.* $\partial_\beta(\rho v_\beta) := \sum_{\beta=x,y} \partial_\beta(\rho v_\beta) = \partial_x(\rho v_x) + \partial_y(\rho v_y) = \nabla \cdot (\rho \mathbf{v}) = \nabla \cdot \mathbf{j}$.

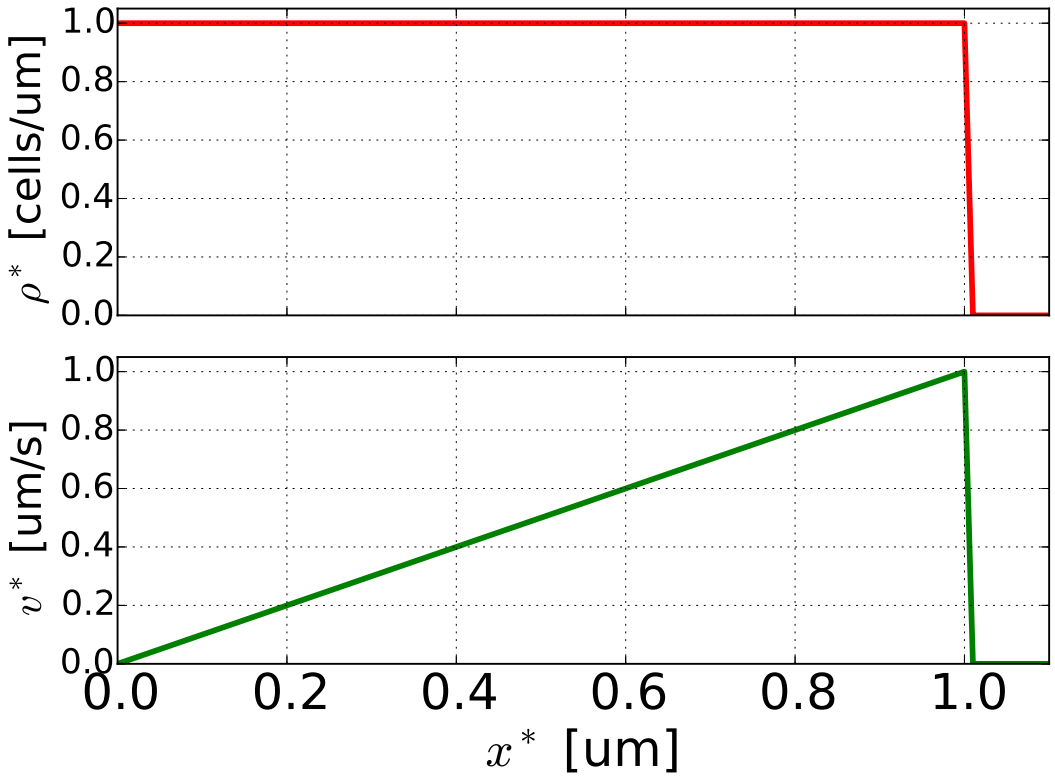

Figure 6.11: Plot of the normalized concentration $\rho^* = \rho/\rho_{\max}$ in the colony and normalized velocity $v^* = v/v_{\max}$.

For what concerns the evolution of the orientation of the single cell at the boundary of an expanding colony, we model the cell as a rigid rod subject to the velocity field $v(y)$. For bacteria, the velocity field is generated by the reproduction process as expressed in eq. (6.4). A sketch of the system is given in figure 6.12.

The equation for the torques acting on the rod reads as

$$\zeta \frac{d\phi}{dt} = \tau \,, \tag{6.5}$$

where ζ [g·m/s] is the rotational friction coefficient and τ is the net torque from the velocity field. The viscous force is given by

$$f(y) = \gamma v(y) \,,$$

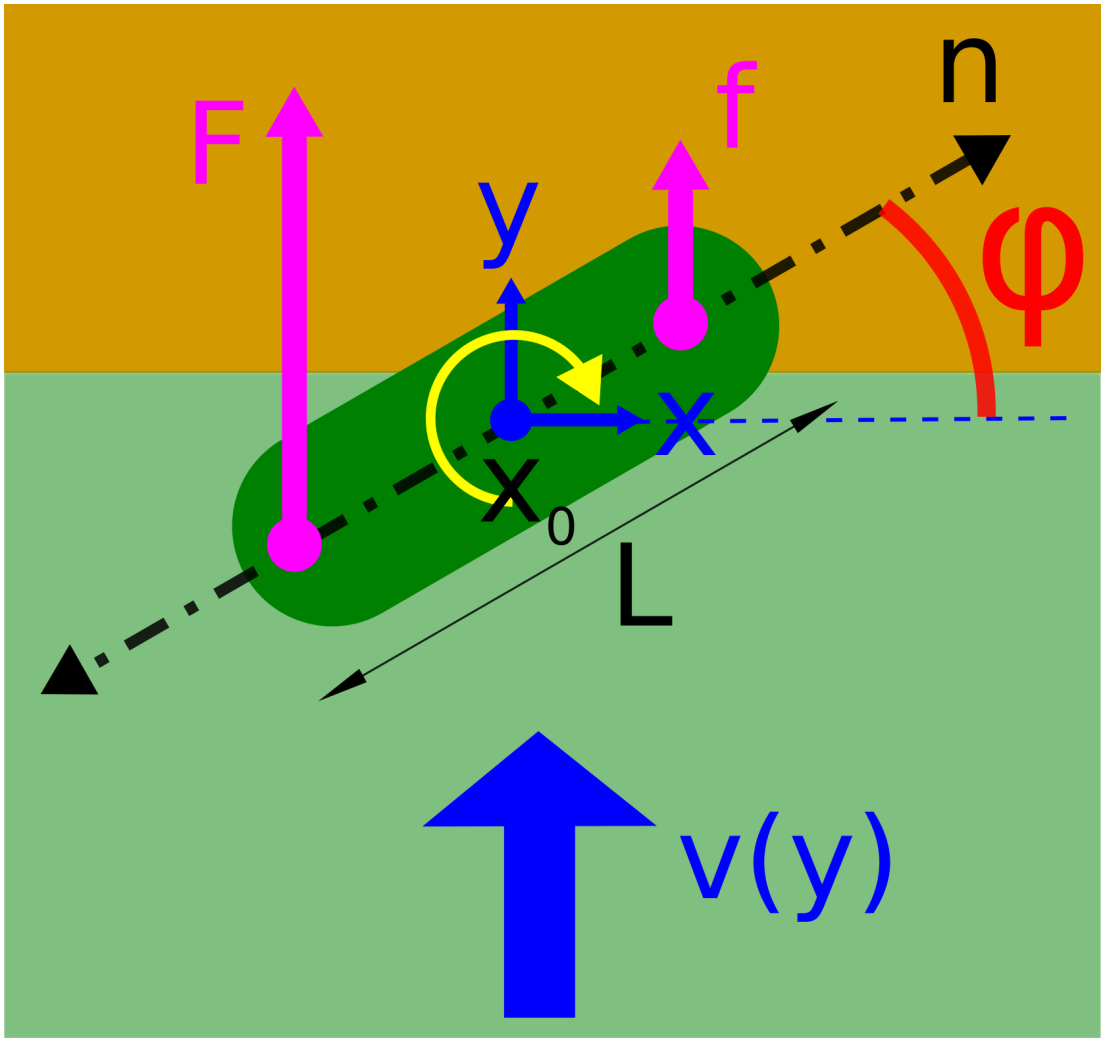

Figure 6.12: A sketch of a cell (modelled as a rigid rod) with length L experiencing torques. Here, $\tau_1 = FB$ and $\tau_2 = fb$; $v(y)$ is the velocity field that vanishes at the colony boundary; $\mathbf{n}$ is the rod unit vector. The application of torques to the rod results in its rotation, here in the clockwise (CW) direction.

with γ [g/s] being the translational friction coefficient. Hence, the net torque is computed along the rod summing up the infinitesimal elements of torque given by the infinitesimal forces times the corresponding arms:

$$\tau = \int d\tau = \int l\cos(\phi)\cdot df = \gamma\cos(\phi)\int_{-L/2}^{L/2} v(y_0 + l\sin(\phi))ldl\,.$$

The Taylor-expansion of the velocity v is given by

$$v(y_0 + l\sin(\phi)) \sim v(y_0) + v'(y_0) l \sin(\phi)\,,$$

with the hypothesis that l is assumed to be much smaller than the spatial length over which velocity changes, and writing $v'(y_0) = (\partial v/\partial y)|_{y=y_0}$. The first term from the the velocity gives a null contribution (integration of an odd function over a symmetric interval, $\sim l$); the second term gives a non-null contribution for the torque which equals

$$\tau = \tfrac{1}{24}\gamma v'(y_0) L^3 \sin(2\phi)\,. \tag{6.6}$$

Finally, inserting eq. (6.6) in eq. (6.5), the evolution equation for a rod experiencing torques in a velocity field is obtained:

$$\dot{\phi}(t) = \Gamma \sin(2\phi(t)) \tag{6.7}$$

where $\dot{\phi} \equiv d\phi/dt$ and

$$\Gamma = \frac{L^3\gamma}{24\zeta}\, v'(y_0)\,. \tag{6.8}$$

The evolution equation (6.7) for the orientation angle ϕ is exactly solvable. First, it is necessary to perform two substitutions by introducing two new variables:[2]

- Substitution 1: $\widetilde{\phi} = 2\phi$;
- Substitution 2: $w = \csc(\widetilde{\phi}) - \cot(\widetilde{\phi})$.

With these substitutions, the integration of eq. (6.7) is reduced to integrals of elementary functions, and the solution reads as

$$\phi(t) = \arctan(Ae^{2\Gamma t}) = \arctan(e^{2\Gamma(t-t^*)})\,, \tag{6.9}$$

where $t^* = \ln(1/A)/(2\Gamma)$ is a characteristic time such that $\phi(t^*) = \pi/4$, and $A = \tan(\phi(0))$. See figures 6.13 and 6.14 for plots of the solution when the characteristic time t^* and the parameter Γ are varied, respectively.

[2] We recall that $\csc(x) = 1/\sin(x)$ and $\cot(x) = 1/\tan(x) = \cos(x)/\sin(x)$.

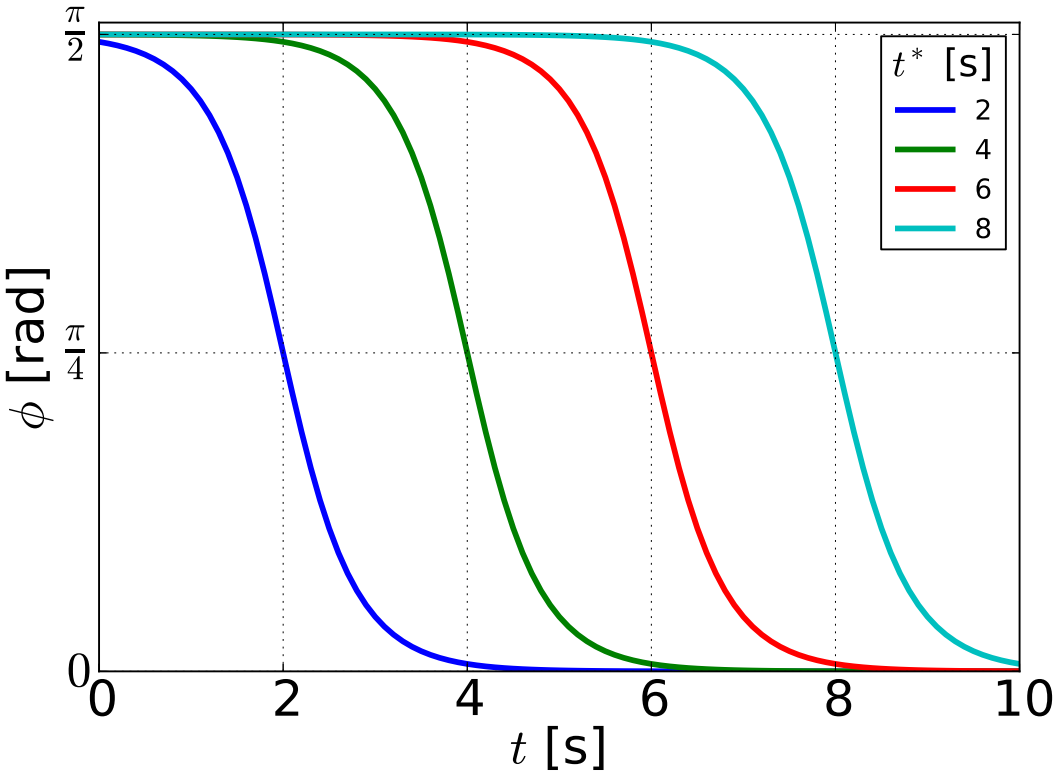

Figure 6.13: The solution ϕ given in eq. (6.9) plotted *vs* time and parameterized *via* the characteristic time t^* for 4 arbitrary values. The characteristic time t^* is the time at which the angle ϕ equals 45 degrees.

The main prediction from the model is that ϕ depends on the values of the parameter Γ: for positive values of Γ, that is a positive velocity gradient $v'(y) > 0$, cells should be oriented orthogonally to the colony boundary or, in other words, radially; for negative values of Γ (corresponding to a negative velocity gradient $v'(y) < 0$), bacteria should align tangentially to the boundary of the colony.

Because of the outward growth of the colony in the plane, the velocity v_y just inside the boundary will be positive (and the velocity gradient too), whereas v_y must vanish just outside the boundary. Thus, the velocity gradient v_y' is negative at the boundary, and the evolution equation for ϕ has a stable equilibrium at $\phi = 0$, corresponding to alignment of the bacteria tangential to the boundary.

We note that this growth-driven mechanism of alignment differs from the shear-driven mechanism that occurs at the interface between an active nematic and isotropic fluid, which also leads to alignment of the director tangential to the

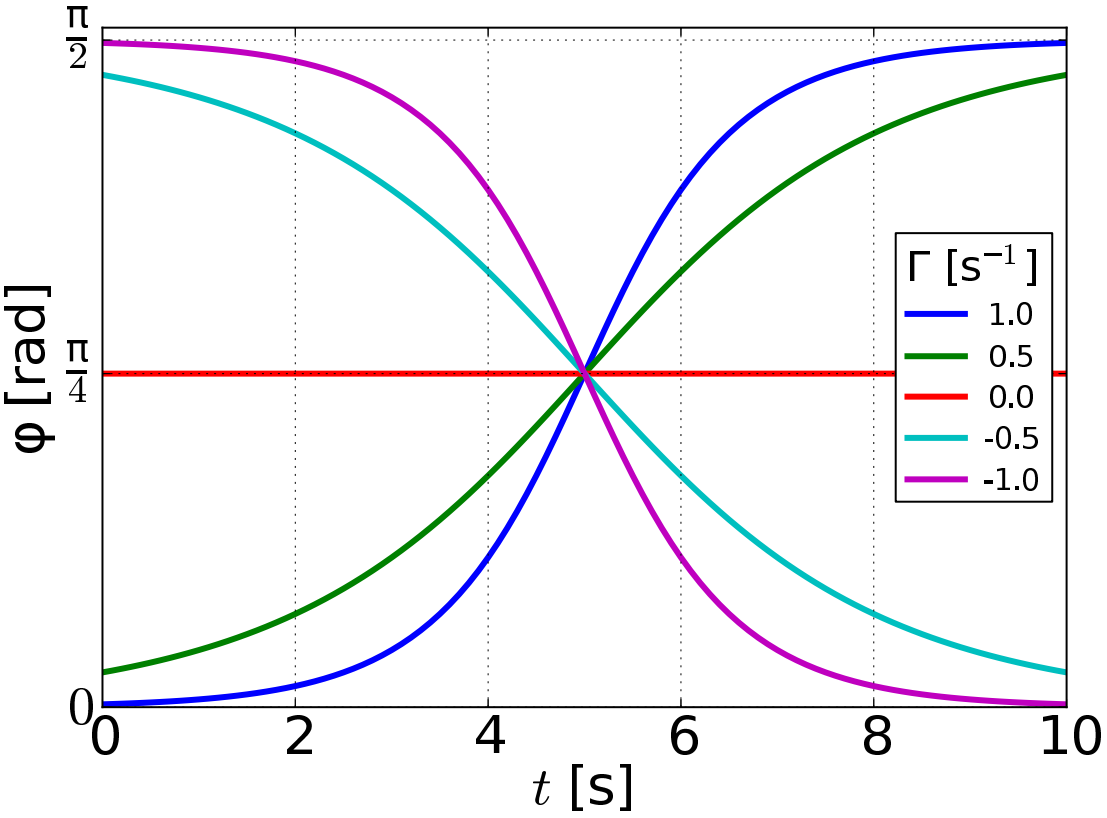

Figure 6.14: Γ is the parameter which discriminates with two opposite possible evolutions for the orientation of the cells: if we consider the inside of the colony, *i.e.* the inner bacteria and those close to the boundary but not at the boundary, then $\Gamma > 0$ as it is directly proportional to the velocity field gradient $v'(y)$, as shown in eq. (6.8). Close to the boundary, the velocity gradient changes abruptly to negative values because the velocity drops down. It is expected then that the bacteria at the boundary tend to reorient tangentially with respect to the colony boundary.

interface for extensile activity [102].

6.3.3 Comparison with experimental results

By analysing the time-lapse movies, we were able to extract the orientations of cells at the boundary and make comparison with the prediction of the model presented in 6.3.2. We detected the angles of the cells with respect to the boundary of the colony by approximating it with a B-spline curve (see § 4.5 for details).

By studying the experimental orientational distribution of bacteria, we

observe that bacteria are actually oriented mainly tangentially to the boundary or, equivalently, orthogonally with respect to the radial direction of growth, as predicted by the model for negative values of Γ and long times (or large cell numbers), which corresponds to the case of a negative velocity gradient at the boundaries.

In order to compute such histogram, we considered the bacteria centroids at the boundary of the colony and used a B-spline curve to fit the boundary, having such centroids as its control points. Then we computed the angle ψ between the vector of the i-th bacterium at the boundary and the tangent to the boundary at the point where the centroid of the bacterium is located.

The histogram of such angle is given in the inset of figure 6.15 for a typical colony, showing a clear asymmetry for small angles, hence suggesting that bacteria align mainly tangentially to the boundary. The same kind of asymmetry is observed for all the other colonies analysed.

We also analysed the evolution of the orientation angle of cells at the boundary, the result being presented in figure 6.16. Here, we plot the mean and the median values of ϕ (that is, averaging over all the angles of the bacteria at a given time) as a function of time t. As indicated by the model in figure 6.14, in the case of a negative velocity gradient ($v'(y) < 0$; for instance, the curves in cyan and magenta ($\Gamma = -0.5, -1.0$)), we should expect a decay of ϕ on time, that is a change from $\pi/2$ to 0. However, this is not what we see in figure 6.16: we observe a constant line around 20 degrees, that is even for the early stage of the colonies when the model predicts instead larger values, that is, radially oriented cells. Hence, we conclude that there is a partial agreement between the experimental data and the prediction provided by the theoretical model, which is limited to long times.

A possible explanation of the practically constant small values of the angle ϕ for short times from the experiment can be searched in the early shape anisotropy showed by all the bacterial colonies, which acts as the main mechanism of control in the orientation of bacteria at the boundary, overcoming the activity induced flow, which takes over at later stages. In this case, most bacteria form elongated structures (see figure 6.10 from time 0 to 125 minutes), so the fraction of bacteria oriented orthogonally with respect to the boundary is small.

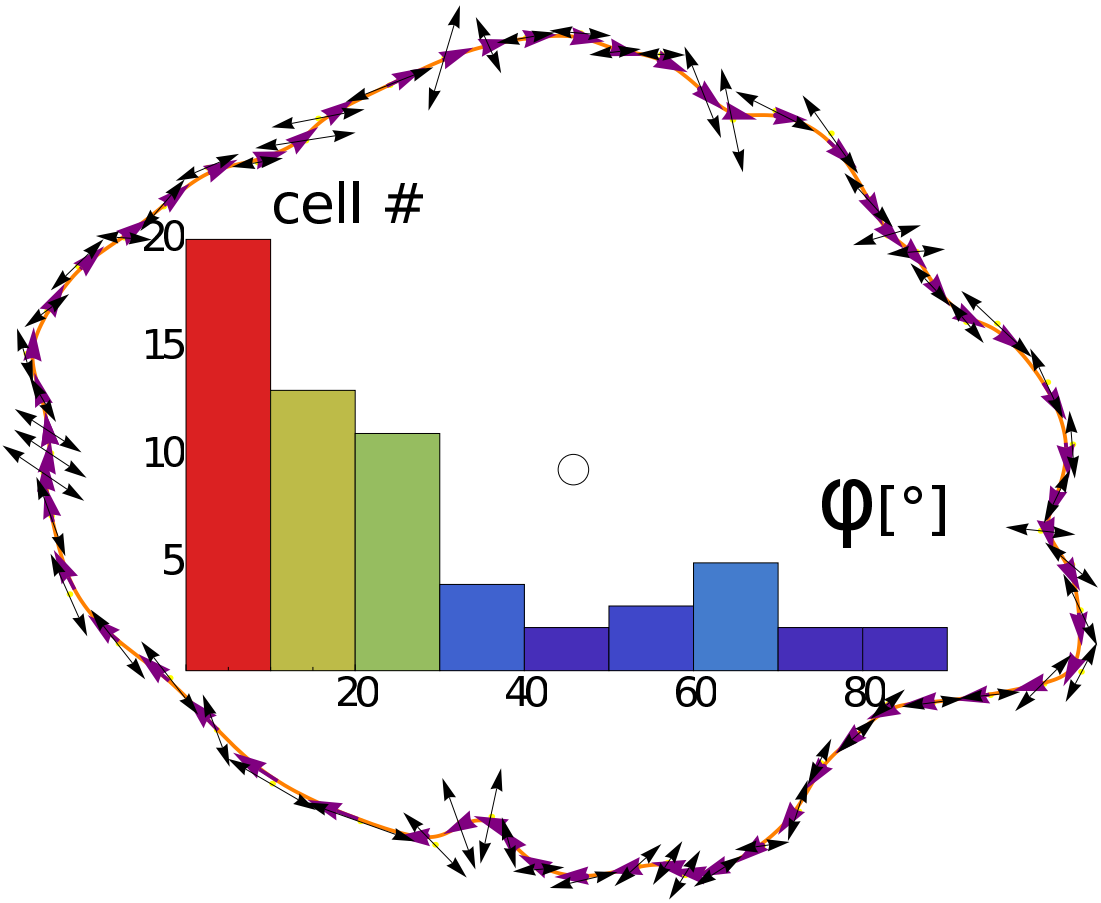

Figure 6.15: Representation of bacteria orientations ϕ (see sketch given in figure 6.12) and tangent to the B-spline curve as an approximation of the colony boundary (for a typical colony), and (inset) the corresponding orientation histogram. Cells are represented by black double-head arrows (because of their nonpolarity, that is $\mathbf{n} \rightleftharpoons -\mathbf{n}$ symmetry); the purple arrows represent the tangents to the B-spline curve (in orange) which approximates the colony boundary. The histogram shows an asymmetry in the distribution of orientations, indicating that most cells tend to align with the tangent of the colony boundary (asymmetry favouring small values of ϕ).

6.4 Discussion

We have shown in this Chapter analyses of simulations and a model that can help in the understanding of the phenomena taking place in this system of bacterial microcolonies.

First, we showed the differences between an active and an equilibrated system by analysing the Monte Carlo simulations of particles that assume initially

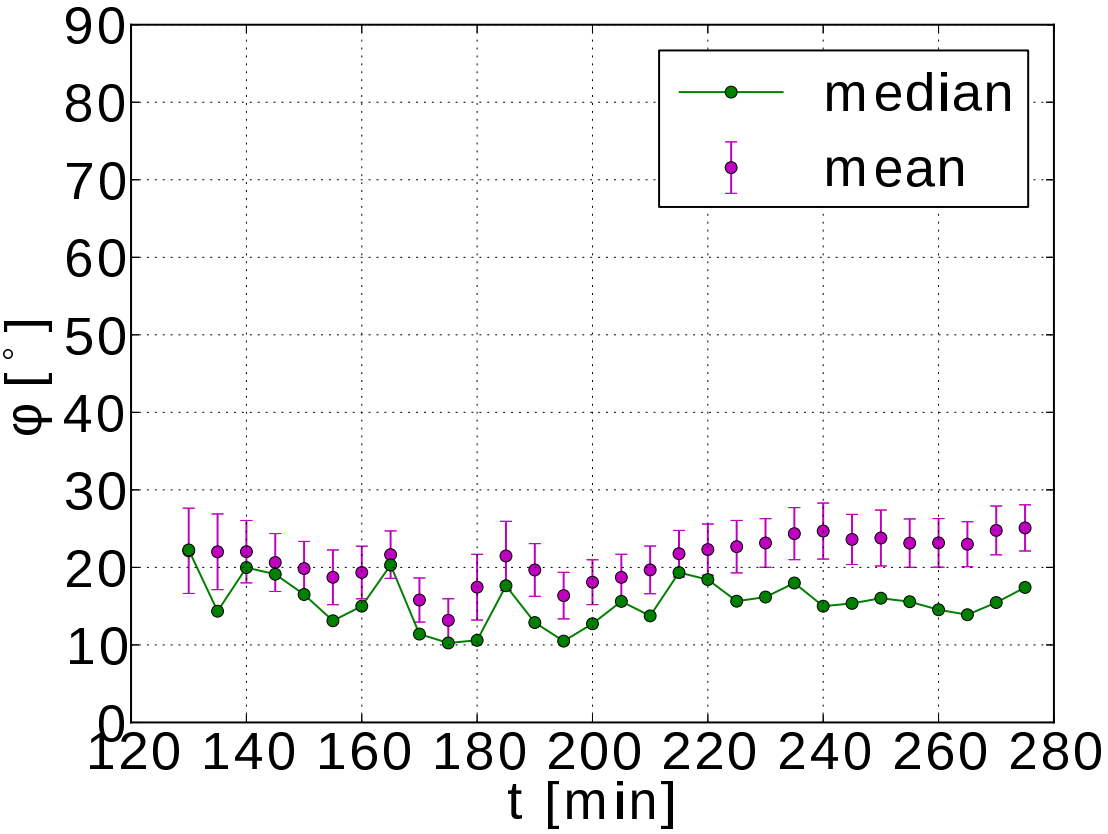

Figure 6.16: The orientation angle ϕ of bacteria at the boundary *vs* time. We do not observe big changes with time of the angle, which is set around 20 degrees.

the same configuration of the corresponding real and out-of-equilibrium case. The difference could be observed in terms of the global order parameter that decreases more rapidly in the case of the simulated/equilibrated microcolonies. Furthermore, another difference is in the behaviour of the local correlations: in the passive equilibrated case, the orthogonal correlation length is larger than the experimental one. These differences indicate that growth - representing the activity characteristic in our living system - plays a crucial role in determining the nematic phase and its deformations.

When we considered the simulations of active particles, we could indeed find an agreement in terms of the 2D correlation maps. The analyses of this second kind of simulations based on active agents also showed an interesting behaviour that cannot unfortunately be investigated with the experimental set-up we used, because of the occurrence of buckling: the radial order quantified through the radial order parameter P_{rad}, after an expected decrease (also observed in the real

case), starts increasing once reached for larger number of cells (around the 8th generation, that is, 256 cells). This result can be understood in terms of the model for cell orientation in the colony, where the (sign of the) gradient velocity controls the evolution of cell alignment with respect to the radial direction of expansion of the colony.

We notice finally that, despite the simplifications made in the model for the simulations of active particles (such as no elastic deformation of the cells and no friction between particles), the qualitative behaviours of the active model and the real system showed a fair agreement.

Part III

Buckling of Bacterial Microcolonies

Chapter 7

Symmetries and Buckling

In this Chapter, we study the relation between the buckling of the bacterial microcolonies and the presence of defects. As we have shown in Chapter 5, the growth of colony is accompanied by the emergence of defects, that is, singularities of the nematic field, a phenomenon that is shared also by the crystalline solids and passive LCs. In the former case of active systems, defects emerge from the inherent activity of cells (growth), in the latter cases, because of quenching, frustration, or application of external fields that control the orientational arrangement of the constituents particles [123]. From the mechanical point of view, defects are region where high stresses can occur and be relieved. Because of these stresses, the bacterial microcolony that forms a single cell layer can eventually buckle into the third vertical dimension when such stresses can no longer be contained in the plane. Here, after describing the observed buckling in our colonies and in other systems, we try to understand the relation between topological defects and buckling *via* an energetic consideration [120]. Then we study our case of half-integer charged defects in bacterial colonies, showing the relation between the position of the buckling point and the position of defects.

7.1 Phenomenology of buckling: transition from 2D to 3D

As introduced in Chapter 5, the mother cell, which is partially immersed into the agarose and in contact with its top surface with the microscope coverslip

(see figure 4.4), grows along its poles in the longitudinal direction and divides, giving rise to two daughter cells. Just after division from the mother cell, the two daughter cells experience a quick flip during which their poles place each other side-by-side, with the consequent elongation taking place along parallel directions of the bacterial bodies. This growth process carries on for the next generations, hence giving rise to a cell layer with its top surface in contact with the microscope coverslip and partially immersed into the agarose. However, because of the lack of space, the bacteria located at the centre of the colony will experience an increasing pressure generated from their neighbours through their own growth. As a consequence, after a given time, the colony will invade the agarose by moving orthogonally with respect to the plane it lies on, that is, some cells in the central region of the colony will move vertically into the agar pad, finding new free space in which to grow [122]. The transition of the colony from a 2D cell layer to a 3D structure is referred to as the buckling event (see figure 7.1), and in the phase-contrast images it can be seen as a darker spot, indicating the layering of cells.

A simple physical interpretation of the buckling can be given by considering a 2D squared lattice, as suggested by Dr Alexander Morozov, in which the sites can be occupied by cells that reproduce by binary division, in a similar fashion to the 'game of life' [124]. Initially a cell is placed on a site and, after its division, one of the four sites surrounding it, can be chosen as the new site of one of the two daughter cells, the other being in the same site of the mother cell. In the case of the square lattice, it is possible to observe that once the fifth generation has been reached, some cells in the centre of the colony are completely surrounded by their neighbours, so there are no longer sites for them where to locate their offspring, and, as a consequence, the third dimension is explored by these cells. The generation number at which caged cells are found - leading to buckling - depends weakly on the nature of the lattice, and in 2D is between 5 and 6 (see figure 7.2).

In the real case of bacterial microcolonies growing on an agar pad, however, the number of divisions after which the cell layer buckles is not necessarily equal to 5, but it is indeed influenced by other factors, for instance the properties of the agar pad where the cells expand on, which can lead to non-monotonic relationship between colony size and agarose concentration [125, 126]. Furthermore, the

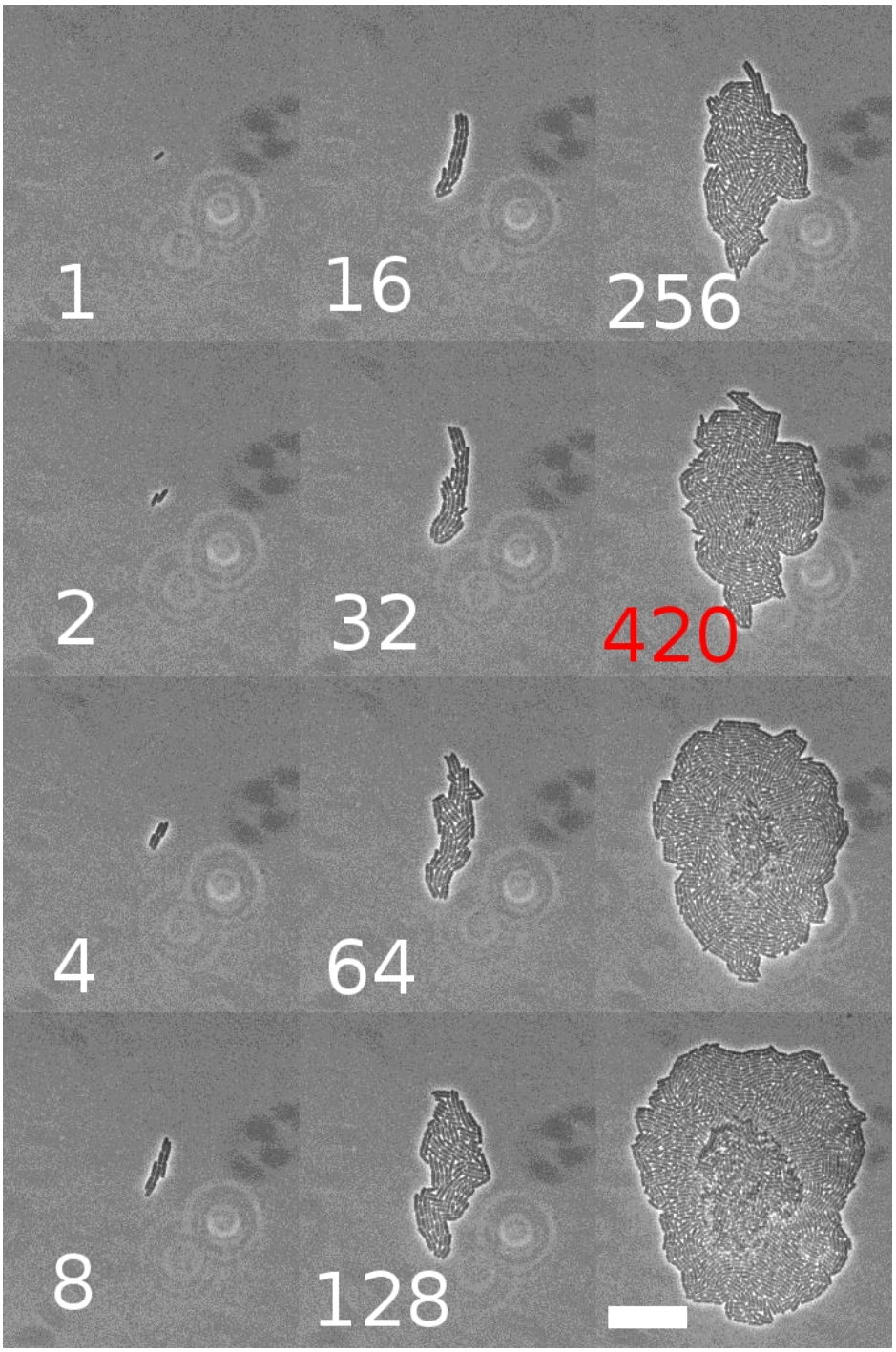

Figure 7.1: Frame montage from a time-lapse experiment in phase-contrast microscopy of a bacterial colony of *E. coli* wild type cells. The number in each frame is the number of cells. The number in red correspond to buckling event after which it is no longer possible to detect the exact number of cells because they overlap each other. Scale bar corresponds to 20 µm (same for all frames).

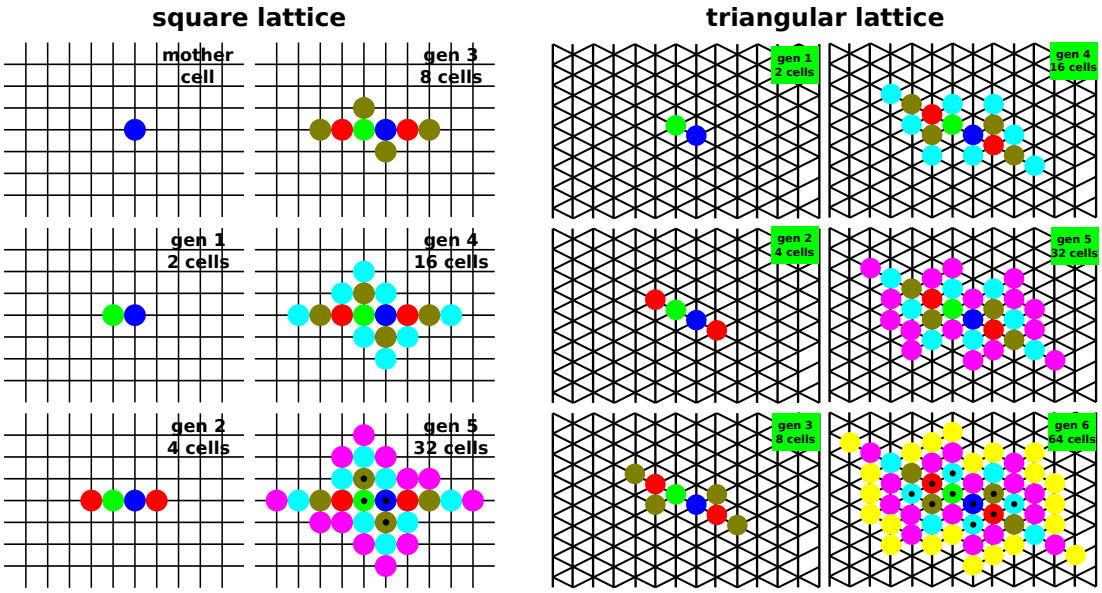

Figure 7.2: Sketch of the Game of life. On the left side, spherical particles populate a square lattice by a binary division process whereby one of the two daughter cells occupies the site of her parent cell, and the other one of the 4 nearest sites. The daughter cells can all find a free site to occupy until the fifth generation is reached: in this case, some of the innermost cells cannot find some more free space, because it has been already occupied by their neighbour cells. The only possible direction for these caged cells to move is to explore the third dimension, hence corresponding to the buckling of the cell layer. The same process happens in the case of the same kind of particles on a triangular lattice but at the sixth generation. The generation number at which buckling occurs depends weakly on the nature of the lattice, and in 2D is between 5 and 6 [124]. This is a simple, physical- that is, steric - reason why a 2D colony would buckle, with innermost cells moving along the direction normal to the cell sheet. However, there are many other factors to consider when dealing with real colonies, such as cell shape other than spheres, the interactions between cells and between cells and the surrounding substrates.

capability of the real cells to push each other and move (not being stuck to the site of the lattice as in the toy model, or under any constriction) on the agarose pad, allows the buckling to happen at later generations.

In these conditions, the buckling can be thought as the result of an increasing pressure generated from the movement of cells and the friction experienced with the substrate. The pressure will accumulate at the centre of the colony because of the collective growth of the cells.

This increase of pressure close to the colony centre can be shown in a simpler

1D model: in this case, the mother cell can be thought to be confined into a rigid squared tube with only side open, allowing for the daughter cells to slide. By considering (i) a pressure spatial gradient proportional to the velocity of the bacteria through a damping coefficient γ: $-dp/dx = \gamma v$, and (ii) assuming the same growth rate $\Lambda = dv/dx$ for all the cells, we have that the pressure increases quadratically when moving from the colony edge to the colony centre.

$$\frac{d^2p}{dx^2} = -\gamma\Lambda \longrightarrow p = p_0 + \tfrac{1}{2}\gamma\Lambda(L^2 - x^2)\,, \tag{7.1}$$

where p_0 is the pressure generated by the agar surrounding the bacterial chain, and L is the length of the bacterial chain. Because of the pressure exerted on the cells by the agarose and the cells themselves, the growth rate could be modelled as a function of the pressure, that is $\Lambda(p) = \Lambda_0(1 - p/p_M)$, where p_M is the maximum pressure beyond which growth stops. For this expression of the growth rate, the solution of eq. (7.1) has the shape of a cosh function with the maximum pressure p_M located at the centre again.

7.2 Buckling as a consequence of topological constraints

There are many external factors that can control the shape of synthetic or living systems and that can lead to a transition towards higher dimensionality, that is from 1D to 2D to 3D. Boundary conditions, external fields (*e.g.* electric fields), surface tension are examples of these external factors, but it is important to notice that the same ordering between the particles forming a given system can play a big role in determining its shape evolution. This is evident in our system made up of cells, that is, active elongated units, which interact by pushing each other during their growth. As observed in the previous Chapters 3 and 5, cells can experience strong re-arrangements and the corresponding director field can exhibit deformations in the form of splays and bends, and, as these deformations turn critical, singularities like defects of a definite charge emerge. Eventually, the colony buckles, with some cells invading the space surrounding the initial cell layer.

It is thus interesting to study the relation between the buckling event and the

presence of topological features [127]. For instance, in some recent works, the patterns formed by elongated particles and their effect on the shape of condensed matter or living systems were studied at the theoretical level: models representing the particle layer as an infinitely thin surface characterized only by its curved shape, and the orientations of the cells represented as a vector field in the plane tangent to the surface have been proposed [128]. The resulting nematic membrane describes flexible sheets incorporating ordered rod-like constituents. Focussing on the possible equilibrium shapes around defects in these deformable nematic membranes, it was shown that the +1 charged topological defects can buckle the nematic layer, and provide also an analytical expression for the profile of the buckled surface [128]. In this context, the central idea is that the stresses among rod-shaped cells that grow in a layer can be driven by the alignment of these cells, regardless of the detailed chemistry of the particles and the surrounding environment, being the same topological constraints able to influence the system shape.[1]

The same phenomenon has been observed experimentally and reproduced in simulations in systems made up of lipid membranes: by lowering the temperature from the LC phase to the gel phase, the vesicles formed by these lipid membranes deform from smooth spheres to disordered and highly crumpled shapes, displaying in the latter state a defect-rich microstructure (see figure 7.3).

Another interesting work pointing to the possible connection between defects and shape changes is the experimental investigation of crack formation and topological defects in lyotropic nematic gels by Islam *et al.* [130]. In this system, the orientational ordering of embedded rods is coupled to an amorphous cross-linked polymer matrix, resulting in the observation of undulations and cusping of the gel side walls. They also observe networks of surface cracks orthogonal to the nematic director field and fissures associated with +1 charged topological defects

7.2.1 Stability of a +1 charged defect: circular symmetry

As we have seen in the previous Chapters 1 and 6, the state of a 2D nematic LC can be described by specifying at each point (x, y) of the plane, the director $\mathbf{n}$, together with its density ρ, pressure p, and velocity v.

[1] More recent work included also the bending rigidity of the particles, so that they could tune the buckling event [129].

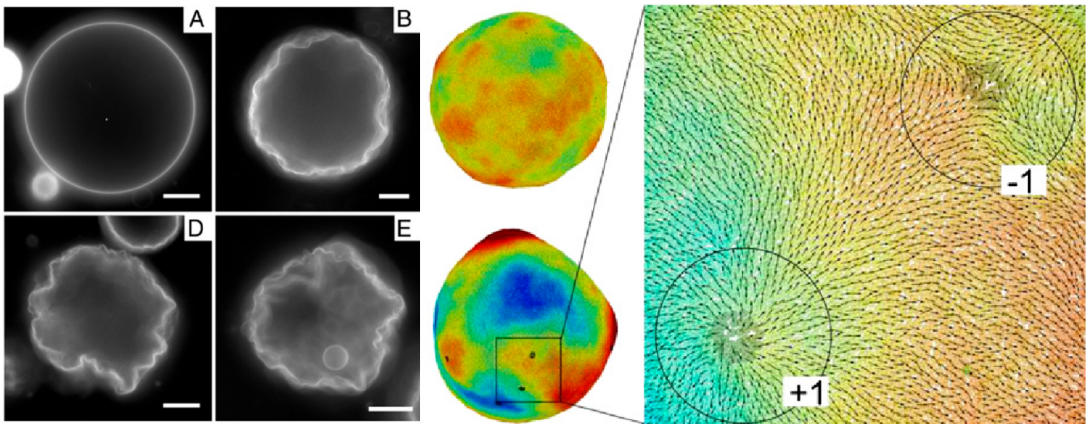

Figure 7.3: Lipid vesicles and topological defects. On the left, fluorescence microscopy images of lipid vesicles in the LC phase (A) at which the shape is well approximated by a sphere, and at the gel phase (B, D and E) after lowering the temperature when the vesicles start showing non-smooth features. Scale bars are 10 µm for all the images. The images in colour are from simulations of the lipid vesicles: the top image corresponds to the simulated vesicle at high temperatures, that is, in the LC phase, the bottom one at low temperatures in the gel phase with black dots representing the topological defects. The zoomed region shows the director field from which the charges of the defects can be assessed, that is ± 1 charges. Colours represent the distance from the centre of mass of the vesicle.

In equilibrium, a nematic at rest under no external forces, including the forces exerted by the boundary walls, is homogeneous, meaning that $\mathbf{n}$ is constant throughout the surface. When deformations of the nematic occur, the direction of $\mathbf{n}$ varies in space, usually assuming that these variations are slow. This means that the characteristic dimensions of the deformation are much greater than the particle dimensions, so that in the modelling the derivatives $\partial n_i/\partial x_k$ are to be regarded as small quantities.

We recall now eq. (1.17):

$$F_d = \tfrac{1}{2}K_1(\nabla \cdot \mathbf{n})^2 + \tfrac{1}{2}K_2(\mathbf{n} \cdot (\nabla \times \mathbf{n}))^2 + \tfrac{1}{2}K_3(\mathbf{n} \times (\nabla \times \mathbf{n}))^2 \,,$$

that describes the deformation energy F_d for a nematic in terms of a quadratic expression in the spatial derivatives of $\mathbf{n}$.

The three quadratic combinations of derivatives are independent, that is, each can be different from zero when the other two are not, and the three coefficients $K_{1,2,3}$ are called the elastic moduli or Frank's moduli of the nematic. Deformations

can then correspond to a pure splay, twist or bend, only if the coefficient K_1 or K_2 or K_3 is nonzero, respectively. In general, the deformation of a nematic includes all three kinds simultaneously.[2]

In the case of strong deformation of the nematic, the director field is no longer varying smoothly, but defects can be observed, representing singularities of the director field. These defects in the nematic represents regions where the stresses between the particles can accumulate and be released, hence it is interesting to study what would happen if a perturbation would take place. As shown in [120, 131], we consider the case of a defect with a circular symmetry, that is +1 charged topological defect in a nematic, which shares the same rotational symmetry of a -1/2 charged defects that we observe in our living nematics.

The representation of a +1 charged defect is given in figure 7.4 where the blue lines represent the direction of the director, developing radially from the centre of the defects, hence conferring the circular symmetry to the defect.

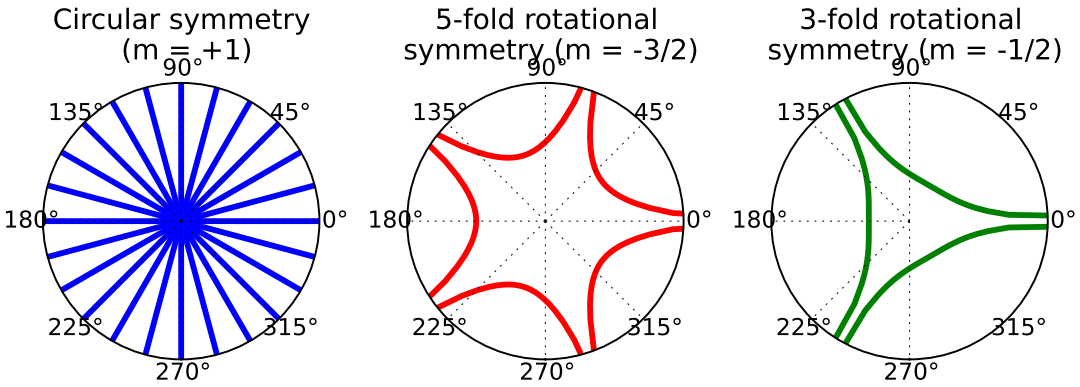

Figure 7.4: Rotational symmetries of topological defects. On the left, a +1 charged defect exhibits a circular symmetry: we can rotate of any angle and get the same shape of the defects. For other defects, like the -3/2 charged defect [132], we still have a rotational symmetry but for only some angular differences, that is $2\pi/5$ rad. In the case of our bacterial colonies, we can observe the -1/2 charged defects (and +1/2 as well) whose symmetry sketch is given on the right: it has a 3-fold symmetry, that is, it looks the same for any rotation of $2\pi/3$ rad.

As the symmetry suggests, it is convenient to describe the unperturbed director field in the region that includes the defect in cylindrical polar coordinates.

[2]In the case of a 2D nematic, there is no twist, because it develops in the direction normal to the nematic plane, that is, it takes place in 3D, thus $\mathbf{n} \cdot (\nabla \times \mathbf{n}) \equiv 0$.

Thus we have the director **n** is given by the following equations:

$$\begin{cases} n_r = 1 \\ n_\phi = 0 \\ n_z = 0 \end{cases}, \tag{7.2}$$

where n_r, n_ϕ and n_z are the radial, angular (in the horizontal plane) and vertical components, respectively.

In order to check the response of this type of defect to perturbations, we apply small rotations to the radial lines, both in the horizontal plane and in the vertical direction. The perturbed director field in the region of the defect can thus be described now as:

$$\begin{cases} n_r = \cos(\Theta)\cos(\Phi) \\ n_\phi = \cos(\Theta)\sin(\Phi) \\ n_z = \sin(\Theta) \end{cases}. \tag{7.3}$$

A sketch of the +1 charged defect with the perturbations applied to the nematic is given in figure 7.5.

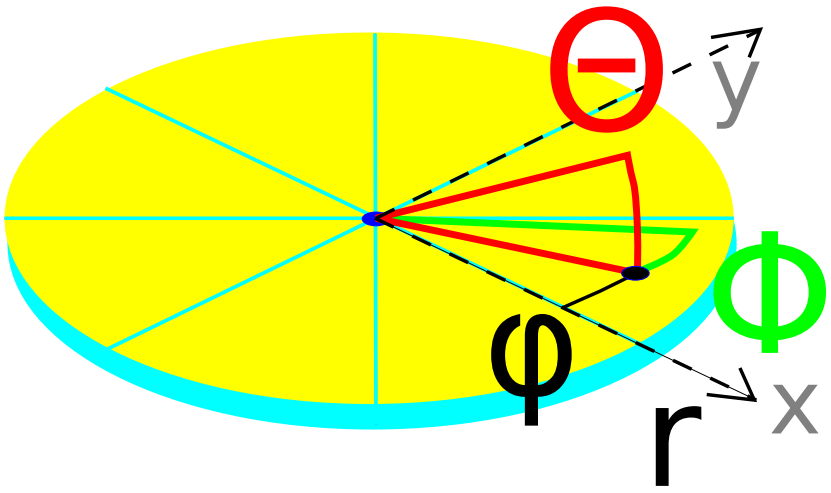

Figure 7.5: Sketch of the perturbed nematic field in the defect region. Only a few lines (in cyan) of the +1 charged topological defect are represented. The two variables Θ and Φ used for describing the perturbation are both functions of the angular coordinate ϕ: $\Theta(\phi)$ and $\Phi(\phi)$.

By considering small perturbations, we can then approximate the previous expression in eq. (7.3) by expanding the trigonometric functions through their

corresponding Taylor's series and by keeping terms until the second order in the variables Θ and Φ, which are functions of the angular coordinate ϕ. The resulting approximated perturbed field is thus:

$$\begin{cases} n_r \approx (1-\Theta^2/2+\mathcal{O}(\Theta^3))(1-\Phi^2/2+\mathcal{O}(\Phi^3)) \approx 1-\frac{1}{2}(\Theta^2+\Phi^2) \\ n_\phi \approx (1-\Theta^2/2+\mathcal{O}(\Theta^3))(\Phi+\mathcal{O}(\Phi^3)) \approx \Phi \\ n_z \approx (\Phi+\mathcal{O}(\Phi^3)) \approx \Phi \end{cases} \tag{7.4}$$

We can now replace the approximated expressions of the director components given in eq. (7.4) into the expression for the deformation energy of the nematics in eq. (1.17), and compute all the derivatives.[3]

Then the energy associated to the deformed nematics can be written as

$$\int F_d \, r dr d\phi = \tfrac{1}{4}R^2 \int \left(K_1\Phi'^2 + (K_3-K_1)\Phi^2 - K_1\Theta^2\right) d\phi \tag{7.6}$$

In the equation eq. (7.6), a term including the coefficient K_2 has not been included since for the 2D nematic there is no twist, and it is also decoupled from from the other two deformations, splay and bend, at the second order calculation; the parameter R is a cut-off that is used to fix the logarithmic divergence arising from the radial integration, and its value can be assumed to be that of the length beyond which the nematic regains its smoothness; the term Φ' stands for $\partial\Phi/\partial\phi$. We can now see that the presence of the term $-K_1\Theta^2$ makes the $+1$ charged topological defect unstable with respect to variations in Θ (that is the small perturbation in the vertical direction), because $K_1 > 0$ and $\partial^2_\Theta(-K_1\Theta^2) < 0$, the other terms being all positive.

This simple analysis shows that in the case of a circular symmetry that characterizes the $+1$ charged defect, a small perturbation in the orthogonal direction with respect to plane into which the deformed director field is confined gives rise to an instability along that direction that corresponds to the buckling

[3] We recall the forms of the divergence and the curl in cylindrical coordinates:

$$\begin{cases} \nabla\cdot\mathbf{n} = \dfrac{1}{r}\dfrac{\partial(rn_r)}{\partial r} + \dfrac{1}{r}\dfrac{\partial n_\phi}{\partial\phi} + \dfrac{\partial n_z}{\partial z} \\ \\ \nabla\times\mathbf{n} = \left(\dfrac{1}{r}\dfrac{\partial n_z}{\partial\phi} - \dfrac{\partial n_\phi}{\partial z}\right)\widehat{\mathbf{r}} + \left(\dfrac{\partial n_r}{\partial z} - \dfrac{\partial n_z}{\partial r}\right)\widehat{\phi} + \dfrac{1}{r}\left(\dfrac{\partial(rn_\phi)}{\partial r} - \dfrac{\partial n_r}{\partial\phi}\right)\widehat{\mathbf{z}} \end{cases} \tag{7.5}$$

of the nematic layer.

This instability is actually not restricted to the case of +1 charged defects, which is characterized by a circular symmetry. Other topological defects show this instability as well, and the reason relies on their symmetry. For instance, as pointed out in [132], the 5-fold rotationally symmetric defect with a corresponding charge of -3/2 is also unstable for the perturbations along its lines of symmetry (see figure 7.4). Hence, in the case of an elastic sheet, the -3/2 charged defect would relieve the stresses that accumulated at its core by buckling into the third dimension, similarly to the case of the +1 charged defect. This observation thus suggests that buckling is a phenomenon that could be expected for any n-fold rotational symmetry where stresses acting along the lines of symmetry tend to concentrate into the core of the singularity: the +1 charged defects represent one of the two extreme cases, that is, when $n = \infty$; the other is represented by a 2-fold symmetry, which is exemplified by the situation of a rod that buckles under compression (see figure 7.6).

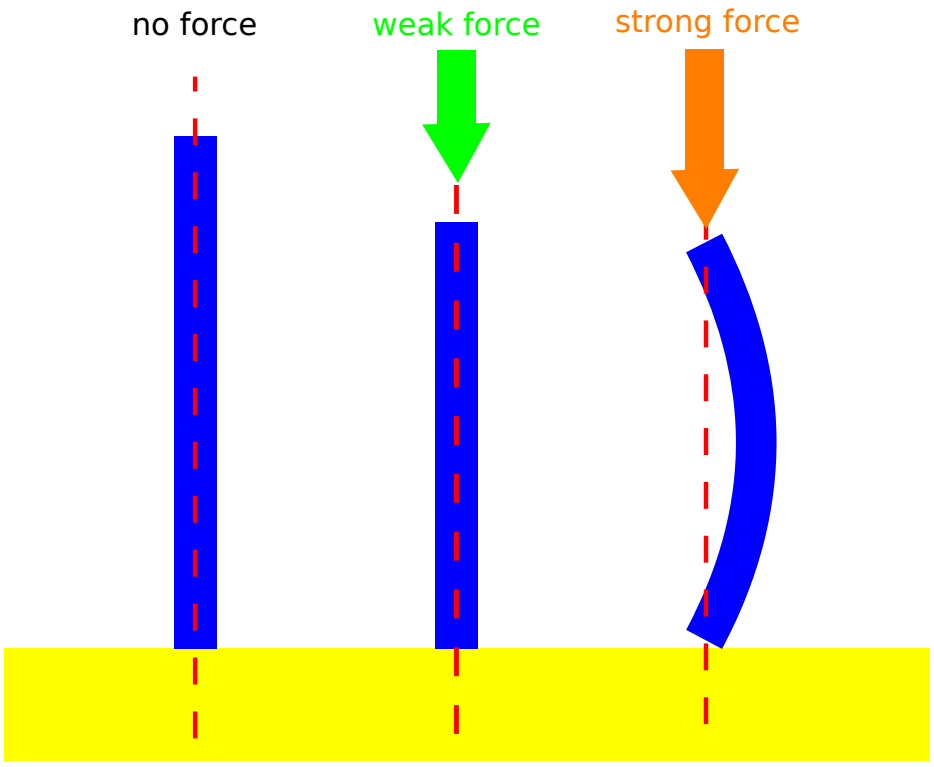

Figure 7.6: Bending rod under compression. As the force applied from above increases, the rod first contracts and then bend. This example represents the simplest case of a 2-fold symmetry.

7.3 -1/2 charged defect locations and buckling point

Considering the previous discussions on the relation between the existence of topological defects in a nematic and the occurrence and location of buckling event, we studied what would happen in the case of growing bacterial colonies. Because of their extensile nature, it is expected that rod-like cells would give rise to singularities in the director field of the nematic with specific charges, that is +1/2 and -1/2 charged defects, which are characterized by an axial and a 3-fold rotational symmetries, respectively (see figures 1.6 and 7.4).

We considered for all the 33 colonies the frames at which the buckling events occurred. In this frames we located the positions of the positive and negative half-integer defects and that of the buckling point. Then we computed the distance from the defects and the buckling point, distinguishing between the charges of the defects. The corresponding plot is given in figure 7.7.

We observe that for large distances we have a larger fraction of +1/2 defects and, *vice versa*, for shorter distances, that is closer to the buckling point, there is a larger fraction of -1/2 defects. This indicates that, although the buckling point is not located precisely onto the core of a -1/2 defects, the buckling region is however likely to be found where there is a larger fraction of -1/2 defects than +1/2.

We also recall that, because of their axial symmetry, hence their polarity, the +1/2 defects tend to better align with the radial direction of colony growth as the distance from the colony centre of mass increases, as shown in fig. 5.18. This suggests that for larger distances a larger fraction of +1/2 charged defects can be expected, as the histogram in fig. 7.7 indicates.

7.4 Discussion

In this Chapter, we investigated a possible link between topology and buckling in bacterial microcolonies, focussing our attention on the location of defects with a positive or negative charge (hence, a given symmetry) and the buckling site.

As a result, we observed that a larger number of -1/2 charged defects can be found close to the buckling site with respect to the number of positively charged

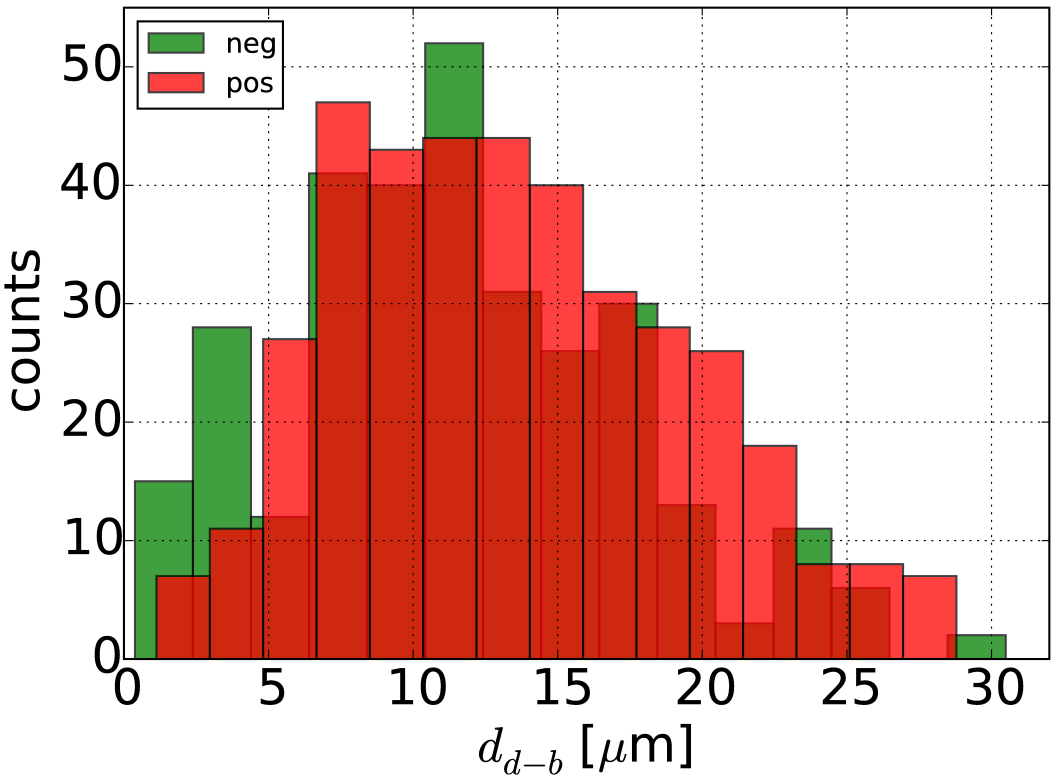

Figure 7.7: Histogram of distances d_{d-b} between defects and buckling point according to the charge of the defects.

defects. We notice that this observation is consistent with the dynamics of defects studied in Chapter 5, whereby -1/2 defects shows a mere diffusive motion with respect to the directed motion of the +1/2 defects (MSD $\sim t^2$) that tend to move radially outward.

It is interesting to notice that this biological system presents similarities with other living and non-living systems existing at different spatial and temporal scales, and that not only the mechanical interactions - for instance, the build-up of pressure - but also the topological properties of the configurations assumed by the elementary entities of the system can determining the dynamical behaviour of the system, that is, in the case here presented, the abrupt transition from a 2D to a 3D geometry *via* the invasion of the agar layer by the cells.

Chapter 8

Buckling and mutants

In this Chapter, we present our experimental work concerning the buckling of microcolonies formed by wild type (WT) and mutant cells of *E. coli* bacterial species. In particular, we compare the case of the WT strain with those of three different mutants lacking appendages that are used by cells to move and attach to surfaces, hence with the capability of tuning the mechanical interactions between the cells themselves and between the cells and the surrounding environment.

8.1 Introduction

One of the most fundamental research topics in biology consists of understanding how 3D multicellular structures assemble together from simpler states of lower dimension, made up of individual cells. Examples are given by the formation and invasion of tissues by skin cancer cells that are initially confined in 2D structures, as in melanomas [133, 134].

The study of the assembly of living systems from 2D to 3D structures is however challenging because many factors can determine the final structure of the organism, and it is not usually easy to separate them. For instance, among these contributions we can recall the mechanical forces acting between cells and the surrounding environment [135, 136], the biochemical interactions between cells [137] and with the matrix [138], cell migration [139], and their death and differentiation [140, 141].

In this context, bacterial microcolonies are interesting model systems for the study of multicellular assembly processes because of some practical advantages.

As we have shown in the Chapter 5, their development can be tracked in the laboratory at the level of individual cells, and they are relatively easy to manipulate at the genetic level [142]. This has lead some authors to suggest that bacterial communities could represent an important test system in the investigation of the role of spatial structure in evolutionary processes, such as the evolution of drug resistance in cancer [143, 144]. Furthermore, these systems can also model practical and ubiquitous situations like the invasion of soft tissue by bacteria growing on the surface of a medical implant (*e.g.* catheter, [26]), or in water pipes [145], teeth and skin [146], in food [147], hence being implicated also in several human pathologies [148].

Here we study growing microcolonies of *E. coli* bacterial cells of wild type (WT) and mutant strains lacking appendages that are responsible for motility and adhesion of cells between themselves and the surrounding environment. We focus on the transition from 2D growth at the interface between a hard surface and a soft agarose pad to 3D growth when the agarose is invaded by cells. We study the colony size in terms of the number of bacteria at the transition for four different strains of bacteria, that is, the WT that is provided with flagella and fimbriae, then the deflagellated, defimbriated, and double knock-out mutant lacking both flagella and fimbriae. Before presenting the buckling size distribution, we discuss briefly the role played by bacterial appendages in the sessile state of our growing microcolonies.

8.2 Role of bacterial appendages

E. coli WT bacteria are characterized by several appendages that are responsible for the interaction, locomotion, and attachment of cells to their neighbours and to the surrounding environment [109].

Flagella are appendages known to be responsible primarily for bacterial locomotion. They are typically 10 µm long helical filaments with a width of the order of 20 nm, which are driven by molecular motors at their base on the bacterial surface and that rotate at a frequency of about 100 Hz, hence propelling the cell through liquid media when bundled together. In the specific case of *E. coli* bacteria, flagella can vary from a number of 2 to 6 [49], and they are distributed all

over the surface.[1] Although being usually regarded only as a motility organelle, the flagellum has been shown to have other functions, for instance they can participate in biofilm formation, protein export [149] and adhesion to other cells and surfaces [150, 151]. Flagella can indeed play a relevant role in bacterial adhesion to and invasion into host cells, as in the case of *E. coli* where flagellin - the major subunit forming the flagellum - and the flagellar cap protein have been reported to function as adhesion elements. Hence, the flagellum itself can be regarded as a potential virulence factor [152].

Pili[2] are hairlike appendages that can be found evenly spread on the surface of many bacteria including *E. coli*. They are more numerous than flagella (order of tens or even hundreds) and shorter in length (about 1-3 µm). Two types of pili are known [109]:

- Conjugative pili - these pili allow the transfer of DNA between bacteria in the process of bacterial conjugation. They are also sometimes called 'sex pili' in analogy to sexual reproduction because the exchange of genes occurs through the formation of mating pairs. A conjugative pilus is typically 10 nm in diameter with a length of about 5 µm;

- Attachment pili or fimbriae - these pili have their external ends capable of adhering to a solid substrate, either other cells or other surfaces, and they are shorter than conjugative pili (about 1-2 µm). The attachment of bacteria to host surfaces is required for colonisation during infection or to initiate formation of biofilms. Mutant bacteria lacking fimbriae are not able to adhere to their usual target. Some fimbriae can adhere to target cells as they can recognize oligosaccharides on the surface of these target cells, other fimbriae bind to components of the extracellular matrix instead. Fimbriae are believed to play a major role with respect to flagella in the interface mechanics of bacteria [109].

[1] Other bacteria as *Pseudomonas aeruginosa* have only one flagellum at one pole, others tens instead, like the *Proteus mirabilis*.

[2] From the Latin (singular) *pilus*, that is hair.

8.3 EPS matrix production in early bacterial colonies

In this section, we want to discuss the role played by the extracellular polymeric substances (EPS), that is, high-molecular weight compounds secreted by many microorganisms (including *E. coli*) under certain conditions, and the possible effects on the buckling.

The main components of EPS is represented by polysaccharides (exopolysaccharides) and proteins, but include other macro-molecules in smaller percentages such as DNA and lipids. These molecules establish the functional and structural integrity of biofilms [153, 154, 26].[3] This means that they can play a role in defining the mechanical properties, for instance, the way bacteria are in contact each other and with the surrounding environment through which they grow and expand as a collective [155].

A polymeric substance called PGA, which is part of the EPS, has been shown to be involved in *E. coli* biofilm formation [156], and that its production is induced by ethanol and high osmolarity, an observation that is consistent with the idea that biofilm formation occurs under stressful environmental conditions [30]. Related works [157, 158] showed that the amount of EPS synthesis within bacterial biofilm depends greatly on the availability of carbon substrates (both inside and outside the cell) and on the balance between carbon and other nutrients. Limitation in nutrients, such as nitrogen, potassium and phosphate, would then promote the synthesis of EPS.

Such stress conditions do not correspond to those that we adopt in our experiments, as we provide nutrients to cells through the agarose pad enriched with M9 medium, maintaining a neutral pH, constant temperature of 37 ℃, and short light exposure during image capture. Furthermore, we observe that *E. coli* bacterium is not the typical model species used in the laboratory for the investigation of EPS role in bacterial aggregates, because it is not an effective producer of EPS. Most EPS studies are performed using other species of bacteria such as *Pseudomonas aeruginosa* [159], and biofilm formation by many *E. coli* strains is characteristically poor *in vitro* as shown in [160].

Furthermore, as observed in [125], the fact that division occurs near the colony

[3] EPS constitutes indeed from 50% to 90% of a biofilm total organic matter.

centre might suggest that it is triggered by biochemical factors secreted by the cells, which might affect their mechanical behaviour (for example, secreted factors can affect motility in *Legionella pneumophila* [161] and *Pseudomonas aeruginosa* [162]) or the physical structure of the agarose. Such factors would be expected to be present at the highest concentration, and for the longest time, near the microcolony centre.

8.4 Observations of buckling in mutant colonies

Experiments are performed using the same set-up as described in Chapters 4 and 5, but considering different cells that have been genetically modified to lack genes that are responsible for the expression of flagella and fimbriae, that is, two kinds of appendages whose function is to provide cells with a propulsion mechanism and surface adhesion capability (see previous section 8.2). The mutants have been obtained starting from the WT strain through transduction as introduced in Chapter 2 and described in the protocol in Chapter 4, thus creating the deflagellated mutant fliF$^-$, the defimbriated fimA$^-$, and the double gene knock-out dbmut.

In the conditions used for the *in vitro* experiments, cells do not show any motility such as swimming, swarming or gliding [163, 164], but they move simply because of the way they push each other during growth. A typical growth and buckling of a mutant strain - in this case for the fimA$^-$ mutant strain - is reported in figure 8.1 as an image sequence. Initially the colony grows from the mother cell to the first two daughters in the same way as seen previously for the WT strain (see section 7.2): the two cells re-align along their longest sides and keep growing in parallel to each other. Growth carries on in a similar way to the WT, but, for a smaller number of cells, it is possible to observe an initial darker spot appearing close to the centre of the colony (frame with 64 cells, in figure 8.1 (number in red)). This darker region corresponds to the buckling site. A similar behaviour is observed for the other two strains used, that is, fliF$^-$ and double mutant knock-out, for 20 colonies for each mutant strain. The distributions of buckling size in terms of cell number present in the colony for all the colony types considered (WT and mutants) are given in figure 8.2.

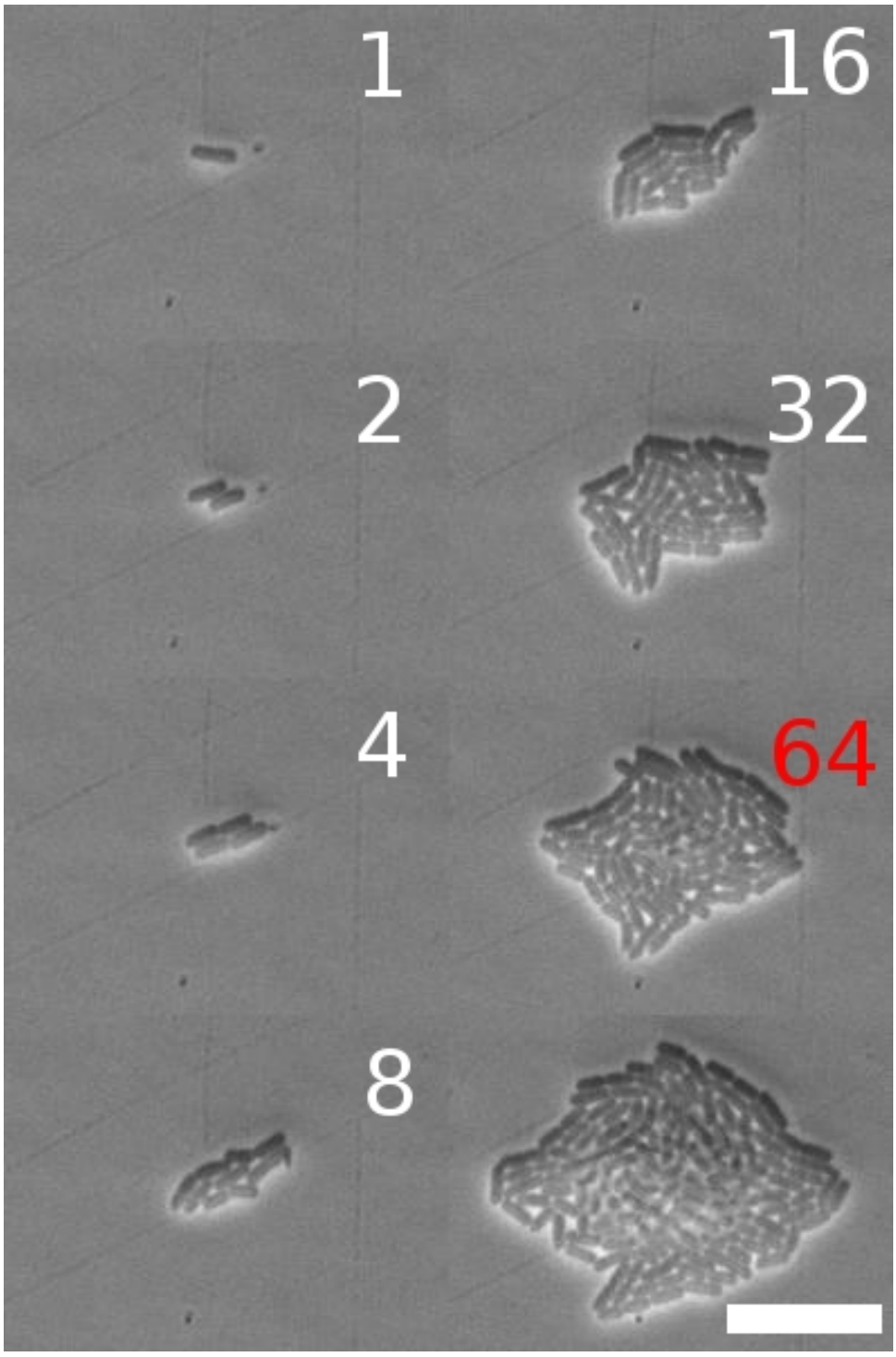

Figure 8.1: Montage of frames from a time-lapse experiment in phase-contrast microscopy of a bacterial colony of *E. coli* fimA^{-} mutant cells. The number in each frame is the number of cells; in red, the one at buckling event. Scale bar at last frame (same for all) corresponds to 10 µm.

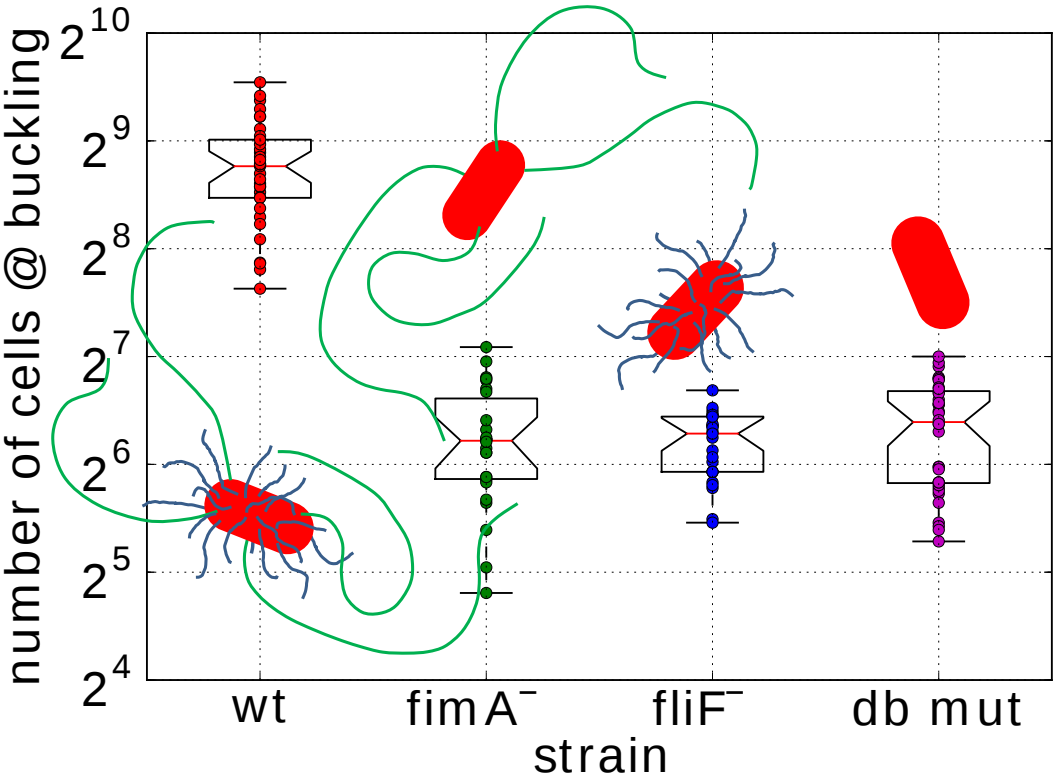

Figure 8.2: Distribution of buckling size among wild type and three mutant cells, with sketches of the corresponding bacterium. The central line (red) of the box represents the median of the data for the strain considered; the bottom and the top of the box are the first and the third quartiles (corresponding to a $\mp 0.675\,\sigma$ when compared to a Normal distribution).

8.5 Discussion

Considering the median of the distributions of the buckling cell number for the mutants, we can see that there is a clear difference from that of the WT provided with all the appendages. In the cases of the mutants, the cells start invading the agarose when they are in a number of about 70, whereas for the WT, the median indicates that buckling should occur when about 400 cells are present in the cell layer. These observations thus indicate that the presence of flagella and fimbriae - as adhesion organelles - can indeed be a relevant factor in triggering the buckling of bacterial microcolonies. It could be useful to think to the appendages as an additional contribution to the mechanics of the bacterial colony: one might think about a network that can increase the intercellular connections and the adhesion

of cells to the surrounding surfaces (both glass and agarose), hence leading to different buckling times and sizes.

Some authors [125], interested in the buckling of *E. coli* colonies, suggested that the transition from 2D to 3D occur because of transformation of inward horizontal forces within the colony into vertical forces, due the presence of small inhomogeneities at the interface. Once the vertically-translated horizontal forces become large enough to overcome the vertical compression force from the agarose layer at the bottom, the bacteria start invading the agarose. In their model [125], they consider bacteria that experience frictional forces acting in the opposite direction of outward radial colony growth, hence the maximal horizontal stress is experienced by the bacteria at the colony centre. Although they consider the presence of spatial inhomogeneities, which can be also represented by the presence of organelles like flagella and pili, they do not consider any adhesion contribution of the cells to the interfaces. That could be done for instance through an anchoring model of the cell: a point on the bacterial surface can be linked to a point on the 2D plane of the glass surface through a spring. As the cell moves, the spring could compress or expand giving rise to an additional force that will add to the frictional forces, eventually tuning the buckling event.

We thus tried to show in this Chapter that, depending on the appendages that cells present on their membrane, the buckling event can be triggered, that is, it can occur at later or earlier times. However, we notice that, despite the specific role played by fimbriae in the adhesion of cells to surfaces, we cannot see relevant differences in the buckling size of the defimbriated fimA$^-$ and the other two mutants fliF$^-$ and double mutant. This indicates that further research is needed in this direction: for instance, an optical method for staining and imaging these appendages would be helpful in identifying their presence and distribution around the individual cell and within the colony; furthermore, the deletion of one gene can be related to the down-regulation of a different gene [150] (for instance, a deflagellated mutant cannot produce flagella, but the production of its fimbriae could be down-regulated, and vice versa). Moreover, it would be useful to repeat the study of the mutant colonies by measuring the corresponding order parameters and by tracking the formation of defects, although from the images and videos that we recorded their emergence seems to be less clear and more difficult to locate; furthermore, it would be useful to measure the volume

fraction of the bacterial colonies of cells with and without appendages, in order to clarify if there is any difference in how well are cells packed depending on their surface morphology. An experimental method for studying the forces between cells, and cells and the surfaces might be based on tracking tracer particles in the agar, as it is routinely done in tracking forces generated by cellular tissues [165, 166].

Chapter 9

Conclusions

We summarize here the main results of this thesis and discuss possible future works that would be a continuation/integration of the present one.

9.1 Summary of results

In this thesis, we showed that a variety of interesting phenomena can be observed when studying at the microscopic level a growing colony of bacterial cells in a 2D geometry.

For instance, we observed

- the transition of the bacterial microcolonies from an orientationally ordered to a disordered global state (in Chapter 5, figure 5.8), quantified through a global order parameter;
- the existence of nematic domains and a side-by-side packing of the cells (in Chapter 5, figures 5.9 and 5.10), as quantified through the use of local orientational correlation functions;
- the occurrence of bending instabilities related to internal stresses due to the fundamental growth process, as indicated from local correlation functions and the order parameter and director maps;
- the development of topological defects with specific charges (in Chapter 5, § 5.4) as prescribed from the symmetries and characteristics of the system, that is, nonpolarity and extensility of the active units, that is, the cells; furthermore, their dynamics;

- the transition from a 2D to a 3D system, consisting in the buckling of the cell layer, that is, the movement out of plane of some cells because of the stresses they experience during colony growth. In this context, we investigated the occurrence of buckling in relation to (*i*) the presence of defects, trying to link the presence of negatively charged defects to the location of the buckling site, and to (*ii*) morphological-physical characteristics of the cells (Chapters 7 and 8), that is, their appendages, showing that buckling can occur at earlier times in their absence.

9.2 Possible future works

We can see many variations of the experiments performed and described in the present work. There is a variety of conditions that can be changed and whose effect might lead to as different as interesting behaviours. For instance, it is possible to consider:

- active units with different physical, morphological, and growth characteristics, for instance, bacteria of different species (not just mutants of an initial wild type);
- a different physics of the boundary conditions. For instance, the surfaces with which cells are in contact during growth can be modified so to tune the physical interaction. A way to do so that is being investigated at the moment in our group, consisting in the functionalization of the coverslip with which the sample is sealed (work of Dr Diarmuid P. Lloyd). Other works, as shown in Grant [125] and currently in the soft matter group at the School of Physics of the University of Edinburgh, focussed on tuning the strength of the viscoelastic medium, that is, the agar, by changing the concentration of agarose [126, 113];
- a different geometry of the boundary conditions. Some recent works, both experimental and numerical focussed on the evolution of active liquid crystals on non-flat surfaces, like spherical an toroidal ones [167, 168];
- external fields, for instance the use of lights (lasers) for controlling the growth of cells, by killing them or by creating fractures (similar to wound healing).

In conclusion, we propose that growing bacterial microcolonies represent a distinct class of active nematics, that is, prescribed-growth active nematics. We hope that our findings will foster a better and more unified understanding of active cellular matter, and possibly contribute to control and mimic it.

Appendix A

Protocols

In the following sections, as an integration to the general descriptions given in Chapter 4 (Materials and Methods), we provide the detailed protocols followed for preparing the media used in the time-lapse experiments and for constructing the mutants.

All solutions are sterile and techniques are such that they guarantee sterility.

A.1 Media preparation

With the quantities reported in the following list, 100 ml of liquid or 2% agarose-based M9 nutrient medium can be produced:

1. Pour 71.8 ml of distilled and de-ionized water in a 100 ml glass bottle;
2. Add 25 ml of 4 x M9 salt;
3. For agarose-based nutrient medium, add 2% (w/v) of agarose (Sigma-Aldrich), that is 2 g of agarose for the final 100 ml of total volume. For liquid nutrient medium, skip this step;
4. Autoclave: the maximum temperature of sterilization is 121 ℃, kept for 20 minutes at least;
5. Let thermalize in a 50 ℃ water bath for 15 minutes;
6. Add 200 µl of 1 M $MgSO_4$ and 2 ml of 20% glucose. Stir until the whole solution looks homogeneous;

7. Add 10 µl of 1 M $CaCl_2$. Precipitates could form when adding $CaCl_2$, hence mix until the whole solution looks homogeneous;

8. For agarose-based nutrient medium, create aliquots using 50 ml Falcon tubes. Store in the +4 ℃ fridge (use within 2 weeks).

A.2 Construction of double knock-out mutants

We provide here the steps concerning the construction of the double knock-out mutant, that is, the fliF$^-$ fimA$^-$ mutant, that is, the deflagellated and defimbriated mutant.

Step 1 - Excision of kanamycin cassette through pCP20 plasmid The parent strain from which the mutant construction process begins is *E. coli* K12 MG1655 fliF$^-$ KAN^R. This strain has the fliF gene deleted and replaced with a KAN cassette, so that this strain is not able to express the flagellar M-ring protein, the basal-body MS (membrane and supramembrane)-ring, and collar protein, which therefore results in a deflagellated phenotype; furthermore, this strain is resistant to the antibiotic kanamycin (which allows then for the selection of that strain during cultivation by using the KAN antibiotic). Since we wish to use kanamycin in subsequent selection steps, our first step is to excise the KAN^R cassette and convert the strain from fliF$^-$ KAN^R to fliF$^-$ KAN^S, that is, from resistant to sensitive.

1. A culture of KAN^R donor cells is grown overnight using LB with KAN antibiotic (30 µg/ml);

2. This strain is transformed with plasmid pCP20 [169]. This plasmid is ampicillin-resistant and it has a temperature-sensitive origin of replication [170]. We select for transformants by growing it at the permissive temperature of 30 ℃ at which this plasmid can replicate. pCP20 expresses an enzyme that can excise the KAN^R cassette;

3. Therefore, during this phase, a fraction of the donor cells will loose their KAN^R cassette. A single colony of these donor cells is picked and an overnight culture is set up: 5 ml of LB in a 20 ml Falcon tube to which

ampicillin (AMP) antibiotic at a concentration of 100 µg/l is added. pCP20 introduces indeed a resistance to ampicillin, hence allowing for selection. The tube is put in the shaking incubator at 30 ℃, 200 rpm;

4. A subculture is prepared the day after again into 5 ml with a 1/100 dilution, until an $OD_{600} \approx 0.1$ is reached (that is, an early lag phase);

5. The temperature is then increased to 42 ℃ and the bacterial suspension left to grow until OD_{600} is between 0.8 and 1.0. This is the restrictive temperature for pCP20 replication, hence plasmids cannot replicate;

6. 50 µl of the culture is then spotted onto an LB plate (many plates can be prepared) and stroke out to obtain individual colonies. Then, the plate is incubated overnight at 37 ℃;

7. Finally, in order to confirm the removal of the KAN cassette and (temporary, plasmid-induced) AMP resistances, three different kinds of plates are prepared using (*i*) LB with AMP (100 µg/ml) so to confirm that pCP20 used for making cells competent has been lost, (*ii*) LB with KAN (100 µg/ml) so to confirm that the KAN cassette has been actually removed, and (*iii*) LB only, which is the last and only kind of plate where we should see bacteria K12 MG1655 fliF$^-$ grow.

The result is the *E. coli* K12 MG1655 fliF$^-$ mutant with the KAN cassette removed, therefore such strain is sensitive to kanamycin (KAN^S) and also to ampicillin antibiotics (AMP^S).

Step 2 - Preparation of P1 lysate P1 lysate is used to infect *E. coli* K12 MG1655 fliF$^-$ (KAN^S AMP^S) strain obtained in Step 1 in order to obtain the desired mutation, that is the deletion of the fimA gene, which is responsible for the expression of the predominant subunit fimA of fimbriae.

For the preparation of the P1 lysate, another bacterial strain that has already the fimA gene deleted is used, and it represents the donor strain. This strain is *E. coli* JW4277 (fimA$^-$ KAN^R), belonging to the Keio single knock-out collection [171], which is based in turn on the parent strain BW25113. This collection is a systematically constructed set of precisely defined, single-gene deletions of all non-essential genes in *E. coli* K-12, where coding regions were replaced with

a kanamycin cassette and primers designed to create in-frame deletions upon excision of the resistance cassette.

In this Step 2, a P1 lysate is prepared in a donor strain that is fimA$^-$ KAN^R. [172]:

1. A fresh culture of the required donor strain JW4277 fimA$^-$ KAN^R is grown overnight in a Falcon tube (20 ml) containing 5 ml of LB. The culture is then re-suspended in 5 ml of fresh LB;

2. 4 Eppendorff tubes are filled with 100 µl of bacterial suspension, 100 µl of $CaCl_2$ (50 mM), 100 µl of $MgSO_4$ (100 mM). 3 out of these 4 Eppendorff tubes are filled with 100 µl of P1 phages at three different dilutions of 1, 10, and 100, using a phage buffer for diluting the stock concentration. The remaining is not filled, representing the control sample. All the tubes are then vortexed and incubated at 37 ℃ for 25 min;

3. 3 ml of melted soft agar (at 47 ℃) are added to each tube, before gently vortexing them, so to avoid bubble formation;

4. The contents are then plated on 4 solid LB plates and incubated upright overnight at 37 ℃ in a static incubator;

5. After the overnight incubation, 2.5 ml of phage buffer are added to each plate showing good lysis (that is, showing clear plaques) and incubated again at room temperature for 15 min;

6. The soft agar with the phage buffer added is then harvested and put into Falcon tubes. A few drops of chloroform are added and the tubes are vortexed thoroughly for 30 s and left to stand for 30 min at room temperature;

7. After a re-vortexing, the tubes are centrifuged and the debris removed;

8. The resulting lysate solution is then stored in the fridge after having added some more few drops of chloroform. Lysate solutions usually last for long time, that is of the order of years.

Step 3 - P1 transduction The P1 lysate prepared as described in Step 2 is used with the recipient strain K12 MG1655 fliF$^-$ KAN^S so to mutate it, that is, to transduce the fimA$^-$ KAN^R into the MG1655 fliF$^-$ KAN^S to obtain at the end the MG1655 fliF$^-$ fimA$^-$ KAN^R. The process is as follows:

1. A culture of the recipient K12 MG1655 fliF$^-$ KAN^S *E. coli* strain is grown overnight in a 20 ml Falcon tube containing 5 ml of LB;
2. The bacterial suspension is then diluted 1/10 in fresh LB with 2.5 mM $CaCl_2$, and allowed to grow for 2 h at 37 ℃ in a shaking incubator (200 rpm);
3. Several Eppendorff tubes are then filled with 100 µl of cell suspension and 100 µl of $CaCl_2$, 100 µl of $MgSO_4$ and sufficient P1 lysate to provide a multiplicity of infection of 1.0. Then, they are incubated at 37 ℃ for 20 min;
4. 200 µl of filter-sterilized 1 M citrate sodium and 500 µl of LB are added to the previous solutions which are then put in the shaking incubator (200 rpm) at 37 ℃ for 30 min in order to permit expression;
5. The contents of the Eppendorffs are then plated onto suitable LB agar plates with KAN antibiotic and incubated overnight in the static incubator at 37 ℃;
6. Then single colonies are picked and plated on new LB Petri dishes with KAN antibiotic to purify them. This step is repeated.

Step 4 - Molecular level PCR phenotype screening The expected phenotype (K12 MG1655 fliF$^-$ fimA$^-$ KAN^R) has been confirmed at the molecular level [142, 173, 174] *via* polymerase chain reaction, performed by Dr Angela Dawson. The polymerase chain reaction is a procedure for amplifying DNA *in vitro* and employs heat-stable DNA polymerases. Heat is used to denature the DNA into two single-stranded molecules, each of which is copied by the polymerase. After each cycle, the newly formed DNA is denatured and a new round of copying proceeds. Hence, after each cycle, the amount of target DNA doubles. As shown in figure A.1, the occurred gene deletion in the fimA$^-$ mutant - starting from the donor mutant fliF$^-$ - can be confirmed. Both primers

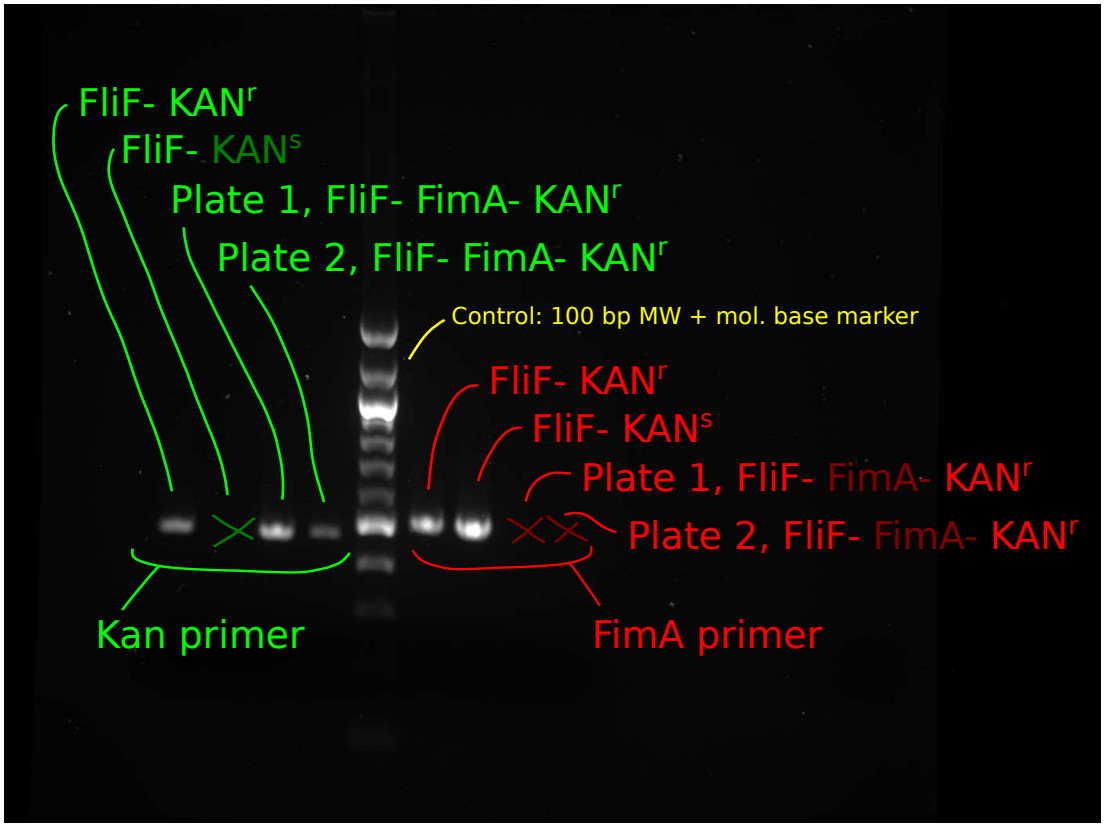

Figure A.1: PCR products after gel electrophoresis: according to the size of DNA fragment, PCR products are dragged to different distances through electrophoresis. The white regions correspond to the products or DNA fragments. In order to make them visible, a dye is used (in this case DNA fragments are SYBR Safe-stained. In this figure, there are 9 lanes along which DNA products are dragged. The long visible lane indicated with the writing in yellow is a control one, obtained using base markers, which returns products for many corresponding pieces of DNA. The remaining lanes, 4 on the left and 4 on the right with respect to central lane, are those related to specific primers we are interested in, that is kanamycin and fimA gene primers.

for KAN resistance and for fimA gene are used in the PCR in order to do such check. For what concerns the KAN primer, the removal of the KAN cassette is checked by comparing the first two bands in the figure (from the left, in the green group of bands): there are clearly some products belonging to the first band, but no products can be identified for the second band (green cross); furthermore, still considering the green group, the presence of the antibiotic resistance in the new mutant fimA$^-$ is confirmed by the presence of products in the next 3rd and 4th

bands. For what concerns the fimA primer, we look at the second group (identified in red): there are products for the first and second band, which correspond to non-mutated bacteria, but no products are visible for the last two bands (red crosses) where the fimA gene has been deleted (that is no fimA primer could attach to it, hence no replication could be initiated).

The whole process described so far, which results in the construction of the desired mutant, is represented schematically in figure A.2.

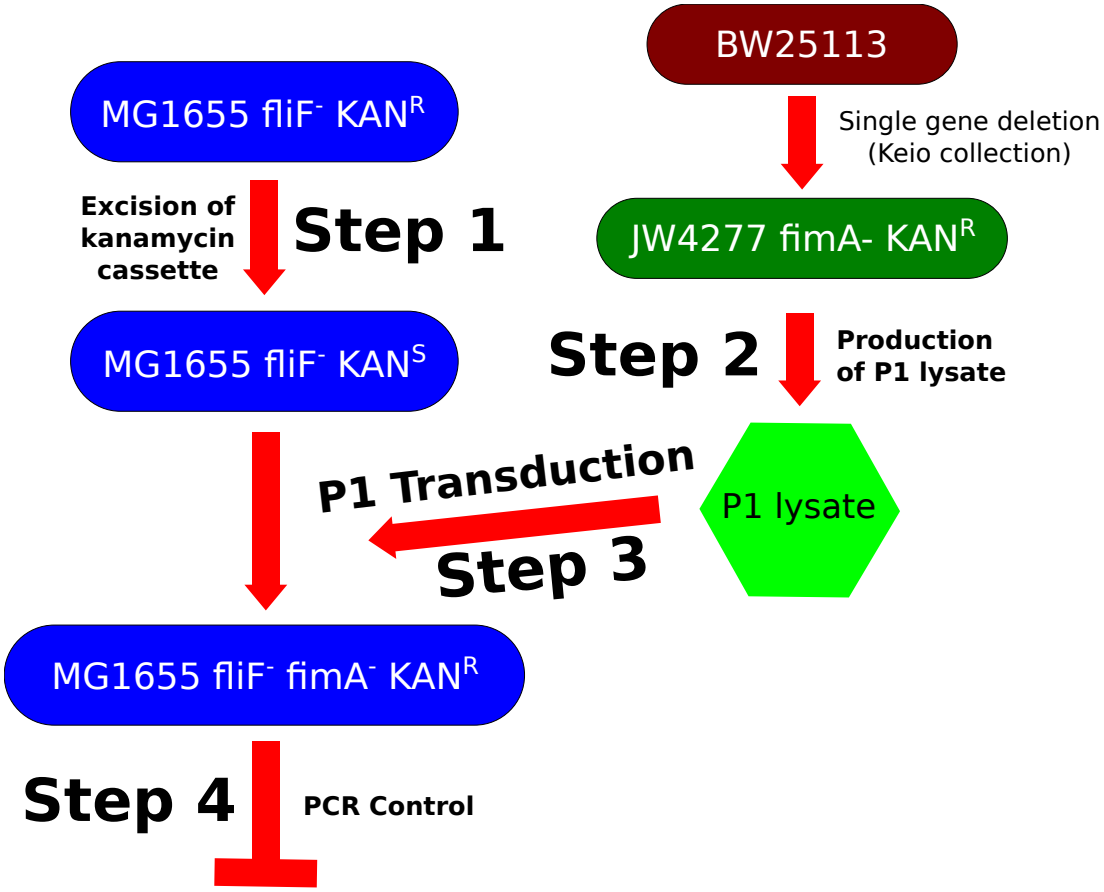

Figure A.2: Steps involved in the production of the double knock-out mutant, that is the deflagellated and defimbriated mutant (refer to subsection 2.4.2 for general aspects of the transduction process).

Glossary

adenosine triphosphate a nucleotide that is the primary form in which chemical energy is conserved and utilized in cells. 38

Archaea prokaryotes distinct from bacteria, with genes and several metabolic pathways more closely related to those of eukaryotes (for instance, some enzymes involved in transcription and translation). A unique aspect of archaea is their reliance on ether lipids in their cell membranes, instead of ester used by both bacteria and eukaryotes. 27

cassette an artificially designed segment of DNA that usually carries a gene for resistance to an antibiotic or some other convenient marker, and is flanked by convenient restriction sites. In other words, a gene, or group of genes, that can be slotted into a specific site. The cassette represents a type of mobile genetic element that contains a gene and a recombination site. An example is the kanamycin cassette which confers kanamycin (an antibiotic) resistance upon that specific bacterial strain. 152

chimera a single organism composed of genetically distinct cells. 26

cybotactic of a liquid crystal, which exhibits spatially extended, short-range orientational order, in such a way that it can be thought as composed of small smectic clusters. 82

Eukarya all eukaryotes: algae, protists, fungi, slime molds, plants, and animals. 27

exopolysaccharide a high-molecular-weight polymer composed of sugar residues and secreted by microorganisms into the surrounding environment. Microorganisms synthesize a wide spectrum of multifunctional polysaccharides including intracellular polysaccharides, structural polysaccharides, extracellular or exopolysaccharides. Exopolysaccharides usually consist of monosaccharides and some non-carbohydrate substituents (such as acetate, pyruvate, succinate and phosphate). 29, 143

kanamycin an antibiotic frequently used in Microbiology. In the Keio collection, that is, a set of single-gene, knock-out mutants for all non-essential genes in *E. coli* K-12 bacterial strain, each deleted gene is replaced with a kanamycin resistance cassette. 53

kbp stands for kilobase pairs. The size of a DNA molecule is expressed as the number of nucleotide bases or base pairs per molecule. For instance, a DNA molecule with 1000 bases is 1 kilobase of DNA. If the DNA is a double helix, then kilobase pairs are used. The bacterium *E. coli* has about 4640 kbp of DNA in its chromosome. Considering that each base pair is 0.34 nm in length along the double helix and that each turn of the helix contains approximately 10 base pairs, then 1 kbp of DNA is 0.34 µm long with 100 helical turns. *E. coli* genome is thus about 1.58 mm long, that is about 500 times longer than the cell itself. 33

lipopolysaccharide (also found abbreviated as LPS) a major component of the outer membrane of Gram-negative bacteria. It is found in the outer leaflet of the bi-layered cell membrane and it is composed of a lipid and a polysaccharide core, extending outward from which are glycan chains (O-antigens). Numerous phages (*e.g.* T3, T4, T7, P2, P22, ϕX174) use LPS as their receptor. 31

lyotropic of a liquid crystal, whose isotropic-liquid crystal phase transition is governed by a change in the density of constituent particles. 38

multiplicity of infection the ratio between the number of phage or virus agents and the infection targets, that is the cells to be infected. 155

nematogen a building block (*e.g.* a molecule, a particle, even a living cell) that is able, in conjunction with other similar constituents, to give rise to a nematic phase, under some physical conditions. Usually, it has a rod-shaped body. 10

osmolarity the capability of a cell to control the influx and outflux of water through its membrane, depending on the concentration of solutes into the cells and the surrounding environment. Water diffuses from regions of high water concentration (low solute concentration) to regions of lower water concentration (higher solute concentration) in the process of osmosis. The cytoplasm of a cell typically has a higher solute concentration than the environment, so the tendency for water is to diffuse into the cell. Under such conditions, the cell is said to be in positive water balance, which is the normal state of the cell. However, when a cell finds itself in an environment where the solute concentration exceeds that of the cytoplasm, water will flow out of the cell. If a cell has no strategy to counteract this, it will become dehydrated and unable to grow. 143

plasmid typically a piece of circular, double-stranded DNA found in many bacteria and archaea that replicates independently of the host chromosome. Plasmids often carry specialization genes that are beneficial for the host in particular circumstances, *e.g.* antibiotic resistance factors. Small plasmids are frequently transferred between hosts, even between hosts in different, but closely-related genera; large plasmids are not mobile and may be in the process of becoming secondary chromosomes. Some bacterial and phage plasmids are linear. Plasmids typically provide factors needed for their own replication; low copy number plasmids also encode a mechanism for their segregation to both daughter cells. 31

polymerase chain reaction the artificial enzymatic amplification of a specific DNA fragment, using repeated cycles of strand separation and replication, more specifically: denaturation, primer annealing and chain extension. 155

primer a strand of nucleic acid that serves as a starting point for DNA replication. Primers are required because the enzyme that catalyses replication, that is, the DNA polymerases, can only add new nucleotides to an existing strand of DNA. Many of the laboratory techniques of biochemistry and molecular biology involving DNA polymerase, such as polymerase chain reaction (PCR), require primers. These primers are usually short, chemically synthesized oligonucleotides with a length of about twenty bases. In other words, a primer is an oligonucleotide to which DNA polymerase attaches the first deoxyribonucleotide during DNA synthesis. 155

prophage the lysogenic form of a bacteriophage, or in other words, the repressed form of bacteriophage DNA in a lysogen; it may be integrated into the chromosome or exist as a plasmid. 33

quorum sensing mechanism whereby bacteria respond to local cell density with the consequence of coordinating gene expression. 28

temperate of a bacteriophage that is capable of establishing a lysogenic relationship with a susceptible host cell; in other words, of a virus whose genome can replicate along with that of its host without causing cell death, in a state called lysogeny (bacterial viruses) or latency (animal viruses); otherwise, not rarely used but less correct, a phage that upon infection chooses between the lytic and lysogenic pathways. 33

virion a bacteriophage genome enclosed within a capsid; an infectious viral particle. 32

Bibliography

[1] S. Ramaswamy. The Mechanics and Statistics of Active Matter. *Annual Review of Condensed Matter Physics*, **1**(1):323–345, 2010. (Cited on pages 1, 37, 38, 43 and 51.)

[2] M. C. Marchetti, J.-F. Joanny, S. Ramaswamy, T. B. Liverpool, J. Prost, M. Rao, and R. A. Simha. Hydrodynamics of soft active matter. *Reviews of Modern Physics*, **85**(3):1143–1189, 2013. (Cited on pages 1 and 88.)

[3] Y. Tu and J. Toner. Long-Range Order in a Two-Dimensional Dynamical XY Model: How Birds Fly Together. *Physical Review Letters*, **75**(23):4326–4329, 1995. (Cited on pages 2 and 41.)

[4] H.-R. Trebin. Defects in liquid crystals and cosmology. *Liquid Crystals*, **24**(1):127–130, 1998. (Cited on page 5.)

[5] P. G. de Gennes and J. Prost. *The Physics of Liquid Crystals*. Oxford Science Publications, 1993. (Cited on pages 7, 12, 17, 20, 21, 22, 23, 41, 76 and 92.)

[6] G. Friedel. The Mesomorphic States of Matter. *Annales de Physique*, **18**:162–174, 1922. (Cited on pages 7 and 11.)

[7] H. R. Brand, H. Pleiner, and F. Ziebert. Macroscopic dynamics of polar nematic liquid crystals. *Physical Review E - Statistical, Nonlinear, and Soft Matter Physics*, **74**(2), 2006. (Cited on page 11.)

[8] H. R. Brand, P. E. Cladis, and H. Pleiner. Reversible macroscopic dynamics of polar nematic liquid crystals: Reversible currents and their experimental consequences. *Physical Review E - Statistical, Nonlinear, and Soft Matter Physics*, **79**(3):1–4, 2009. (Cited on page 11.)

[9] S. Chandrasekhar. *Liquid Crystals*. Cambridge University Press, 1992. (Cited on pages 12 and 23.)

[10] L. Onsager. The effects of shape on the interaction of colloidal particles. *Annals New York Academy of Sciences*, **51**:627–659, 1949. (Cited on pages 15 and 18.)

[11] R. A. L. Jones. *Soft Condensed Matter*. 2002. (Cited on page 15.)

[12] M. A. Bates and D. Frenkel. Phase behavior of two-dimensional hard rod fluids. *Journal of Chemical Physics*, **112**:10034–10041, 2000. (Cited on pages 18, 19 and 108.)

[13] J. A. C. Veerman and D. Frenkel. Phase behavior of disklike hard-core mesogens. *Physical Review A*, **45**:5632–5648, 1992. (Cited on page 19.)

[14] P. Bolhuis and D. Frenkel. Tracing the phase boundaries of hard spherocylinders. *Journal of Chemical Physics*, **106**(2):666–687, 1997. (Cited on page 19.)

[15] J. Cuesta and D. Frenkel. Monte Carlo simulation of two-dimensional hard ellipses. *Physical Review A*, **42**(4):2126–2136, 1990. (Cited on page 19.)

[16] G. Kleman and D. Lavrentovich. *Soft Matter Physics: An Introduction*. 2004. (Cited on pages 22 and 92.)

[17] G. P. Crawford. *Physical Properties of Liquid Crystals: Nematics*. 2001. (Cited on page 22.)

[18] J. L. Ericksen. Inequalities in Liquid Crystal Theory. *Physics of Fluids*, **9**(6):1205, 1966. (Cited on page 22.)

[19] K. D. Young. The selective value of bacterial shape. *Microbiology and molecular biology reviews : MMBR*, **70**(3):660–703, 2006. (Cited on page 24.)

[20] B. C. Christner, J. C. Priscu, A. M. Achberger, C. Barbante, S. P. Carter, K. Christianson, A. B. Michaud, J. a. Mikucki, A. C. Mitchell, M. L. Skidmore, T. J. Vick-Majors, W. P. Adkins, S. Anandakrishnan, G. Barcheck, L. Beem, a. Behar, M. Beitch, R. Bolsey, C. Branecky, R. Edwards, a. Fisher, H. a. Fricker, N. Foley, B. Guthrie, T. Hodson, R. Jacobel, S. Kelley, K. D. Mankoff, E. McBryan, R. Powell, a. Purcell, D. Sampson, R. Scherer, J. Sherve, M. Siegfried, and S. Tulaczyk. A microbial ecosystem beneath the West Antarctic ice sheet. *Nature*, **512**(7514):310–313, 2014. (Cited on page 26.)

[21] M. T. Madigan, J. M. Martinko, K. S. Bender, D. H. Buckley, and D. A. Stahl. *Brock Biology of Microorganisms*. Pearson, 2014. (Cited on pages 26, 27, 28, 30, 32 and 69.)

[22] D. E. Canfield. The Early History of Atmospheric Oxygen: Homage to Robert M. Garrels. *Annual Review of Earth and Planetary Sciences*, **33**(1):1–36, 2005. (Cited on page 27.)

[23] S. A. Crowe, L. N. Dossing, N. J. Beukes, M. Bau, S. J. Kruger, R. Frei, and D. E. Canfield. Atmospheric oxygenation three billion years ago. *Nature*, **501**(7468):535–8, 2013. (Cited on page 27.)

[24] D. E. Canfield, L. Ngombi-Pemba, E. U. Hammarlund, S. Bengtson, M. Chaussidon, F. Gauthier-Lafaye, A. Meunier, A. Riboulleau, C. Rollion-Bard, O. Rouxel, D. Asael, A.-C. Pierson-Wickmann, and A. El Albani. Oxygen dynamics in the aftermath of the Great Oxidation of Earth's atmosphere. *Proceedings of the National Academy of Sciences*, **110**(42):16736–41, 2013. (Cited on page 27.)

[25] N. Christofi and I. B. Ivshina. Microbial surfactants and their use in field studies of soil remediation. *Journal of Applied Microbiology*, **93**:915–929, 2002. (Cited on page 27.)

[26] R. M. Donlan and J. W. Costerton. Biofilms: Survival mechanisms of clinically relevant microorganisms. *Clinical Microbiology Reviews*, **15**(2):167–193, 2002. (Cited on pages 27, 141 and 143.)

[27] E. Ben-Jacob, I. Cohen, and H. Levine. Cooperative self-organization of microorganisms. *Advances in Physics*, **49**(4):395–554, 2000. (Cited on page 28.)

[28] D. Monroe. Looking for chinks in the armor of bacterial biofilms. *PLoS Biology*, **5**(11):e307, 2007. (Cited on page 28.)

[29] J. W. Costerton, K. J. Cheng, G. G. Geesey, T. I. Ladd, J. C. Nickel, M. Dasgupta, and T. J. Marrie. Bacterial biofilms in nature and disease. *Annual Review of Microbiology*, **41**(1):435–464, 1987. PMID: 3318676. (Cited on page 27.)

[30] J. W. Costerton, Z. Lewandowski, D. E. Caldwell, D. R. Korber, and H. M. Lappin-Scott. Microbial biofilms. *Annual Review of Microbiology*, **49**(1):711–745, 1995. (Cited on pages 27 and 143.)

[31] J. W. Costerton, P. S. Stewart, and E. P. Greenberg. Bacterial biofilms: A common cause of persistent infections. *Science*, **284**(5418):1318–1322, 1999. (Cited on page 27.)

[32] G. O'Toole, H. B. Kaplan, and R. Kolter. Biofilm formation as microbial development. *Annual Review of Microbiology*, **54**:49–79, 2000. (Cited on page 27.)

[33] L. R. Hoffman, D. A. D'Argenio, M. J. MacCoss, Z. Zhang, R. A. Jones, and S. I. Miller. Aminoglycoside antibiotics induce bacterial biofilm formation. *Nature*, **436**(7054):1171–5, 2005. (Cited on page 28.)

[34] M. E. Davey and G. A. O'Toole. Microbial biofilms: from ecology to molecular genetics. *Microbiology and Molecular Biology Review*, **64**:847–867, 2000. (Cited on page 28.)

[35] D. G. Davies. The Involvement of Cell-to-Cell Signals in the Development of a Bacterial Biofilm. *Science*, **280**(5361):295–298, 1998. (Cited on page 29.)

[36] J. N. Wilking, T. E. Angelini, A. Seminara, M. P. Brenner, and D. A. Weitz. Biofilms as complex fluids. *MRS Bulletin*, **36**(05):385–391, 2011. (Cited on page 29.)

[37] J. N. Wilking, V. Zaburdaev, M. De Volder, R. Losick, M. P. Brenner, and D. A. Weitz. Liquid transport facilitated by channels in Bacillus subtilis biofilms. *Proceedings of the National Academy of Sciences*, **110**(3):848–52, 2013. (Cited on page 29.)

[38] C. D. Nadell, J. B. Xavier, and K. R. Foster. The sociobiology of biofilms. *FEMS Microbiology Reviews*, **33**(1):206–24, 2009. (Cited on page 29.)

[39] E. Ben-Jacob, O. Schochet, A. Tenenbaum, I. Cohena, A. Czirók, and T. Vicsek. Generic modelling of cooperative growth patterns in bacterial colonies. *Nature*, **368**:46–49, 1994. (Cited on page 30.)

[40] J. U. Kreft, G. Booth, and J. W. Wimpenny. Bacsim, a simulator for individual-based modelling of bacterial colony growth. *Microbiology*, **144**:3275–87, 1998. (Cited on page 30.)

[41] J. B. Xavier, C. Picioreanu, and M. C. M. van Loosdrecht. A framework for multidimensional modelling of activity and structure of multispecies biofilms. *Environmental microbiology*, **7**(8):1085–103, 2005. (Cited on page 30.)

[42] L. A. Lardon, B. V. Merkey, S. Martins, A. Dötsch, C. Picioreanu, J.-U. Kreft, and B. F. Smets. iDynoMiCS: next-generation individual-based modelling of biofilms. *Environmental microbiology*, **13**(9):2416–34, 2011. (Cited on page 30.)

[43] H. Fujikawa and M. Matsushita. Fractal Growth of *Bacillus subtilis* on Agar Plates. *Journal of the Physical Society of Japan*, **58**(11):3875–3878, 1989. (Cited on page 30.)

[44] J. A. Shapiro. The significances of bacterial colony patterns. *BioEssays*, **17**(7):597–607, 1995. (Cited on page 30.)

[45] J.-U. Kreft. Biofilms promote altruism. *Microbiology*, **150**(8):2751–60, 2004. (Cited on page 30.)

[46] J. B. Xavier and K. R. Foster. Cooperation and conflict in microbial biofilms. *Proceedings of the National Academy of Sciences*, **104**(3):876–81, 2007. (Cited on page 30.)

[47] O. Hallatschek, P. Hersen, S. Ramanathan, and D. R. Nelson. Genetic drift at expanding frontiers promotes gene segregation. *Proceedings of the National Academy of Sciences*, **104**(50):19926–30, 2007. (Cited on pages 30, 51 and 109.)

[48] O. Hallatschek and D. R. Nelson. Life at the front of an expanding population. *Evolution*, **64**(1):193–206, 2010. (Cited on page 30.)

[49] H. C. Berg. *E. coli in motion*. Springer, 2004. (Cited on pages 31, 32 and 141.)

[50] W. B. Whitman, D. C. Coleman, and W. J. Wiebe. Prokaryotes: the unseen majority. *Proceedings of the National Academy of Sciences*, **95**:6578–6583, 1998. (Cited on page 33.)

[51] F. Rohwer, M. Youle, H. Maughan, and N. Hisakawa. *Life in Our Phage World: A centennial field guide to the Earth's most diverse inhabitants*. Wholon, San Diego, CA, 2014. (Cited on page 33.)

[52] J. T. Walker and D. H. Walker. Coliphage P1 morphogenesis: analysis of mutants by electron microscopy. *Journal of Virology*, **45**(3):1118–1139, 1983. (Cited on pages 34 and 35.)

[53] G. Cohen. Electron microscopy study of early lytic replication forms of bacteriophage P1 DNA. *Virology*, **131**:159–170, 1983. (Cited on page 35.)

[54] M. B. Łobocka, D. J. Rose, G. Plunkett, M. Rusin, A. Samojedny, H. Lehnherr, M. B. Yarmolinsky, and F. R. Blattner. Genome of bacteriophage P1. *Journal of Bacteriology*, **186**(21):7032–7068, 2004. (Cited on page 35.)

[55] T. Surrey, F. Nedelec, S. Leibler, and E. Karsenti. Physical properties determining self-organization of motors and microtubules. *Science*, **292**(5519):1167–1171, 2001. (Cited on page 38.)

[56] K. Kruse and F. Jülicher. Dynamics and mechanics of motor-filament systems. *European Physical Journal E*, **20**(4):459–465, 2006. (Cited on page 38.)

[57] J. Kierfeld, K. Frentzel, P. Kraikivski, and R. Lipowsky. Active dynamics of filaments in motility assays. *European Physical Journal Special Topics*, **157**(1):123–133, 2008. (Cited on page 38.)

[58] V. Schaller, C. Weber, C. Semmrich, E. Frey, and A. R. Bausch. Polar patterns of driven filaments. *Nature*, **467**(7311):73–7, 2010. (Cited on pages 38 and 48.)

[59] M. Ballerini, N. Cabibbo, R. Candelier, A. Cavagna, E. Cisbani, I. Giardina, V. Lecomte, A. Orlandi, G. Parisi, A. Procaccini, M. Viale, and V. Zdravkovic. Interaction ruling animal collective behavior depends on topological rather than metric distance: Evidence from a field study. *Proceedings of the National Academy of Sciences*, **105**(4):1232–1237, 2008. (Cited on page 38.)

[60] J. Gautrais, C. Jost, and G. Theraulaz. Key behavioural factors in a self-organised fish school model. *Annales Zoologici Fennici*, **2450**(October):415–428, 2008. (Cited on page 38.)

[61] J. L. Silverberg, M. Bierbaum, J. P. Sethna, and I. Cohen. Collective Motion of Humans in Mosh and Circle Pits at Heavy Metal Concerts. *Physical Review Letters*, **110**(22):228701, 2013. (Cited on page 38.)

[62] R. Kemkemer, D. Kling, D. Kaufmann, and H. Gruler. Elastic properties of nematoid arrangements formed by amoeboid cells. *European Physical Journal E*, **1**:215–225, 2000. (Cited on pages 39 and 48.)

[63] R. Kemkemer and V. Teichgr. Nematic order-disorder state transition in a liquid crystal analogue formed by oriented and migrating amoeboid cells. *European Physical Journal E*, **3**:101–110, 2000. (Cited on page 39.)

[64] C. Dombrowski, L. Cisneros, S. Chatkaew, R. E. Goldstein, and J. O. Kessler. Self-Concentration and Large-Scale Coherence in Bacterial Dynamics. *Physical Review Letters*, **93**(9):098103, 2004. (Cited on pages 39, 45 and 48.)

[65] T. Vicsek, A. Czirok, E. Ben-Jacob, I. Cohen, and O. Shochet. Novel type of phase transition in a system of self-driven particles. *Physical Review Letters*, **75**(4):1226–1229, 1995. (Cited on pages 38, 39 and 40.)

[66] N. D. Mermin and H. Wagner. Absence of Ferromagnetism or Antiferromagnetism in One- or Two-Dimensional Isotropic Heisenberg Models. *Physical Review Letters*, **17**(26):1966, 1966. (Cited on page 40.)

[67] R. A. Simha and S. Ramaswamy. Hydrodynamic fluctuations and instabilities in ordered suspensions of self-propelled particles. *Physical Review Letters*, **89**:58101, 2002. (Cited on pages 41 and 88.)

[68] H. Chaté, F. Ginelli, and R. Montagne. Simple model for active nematics: Quasi-long-range order and giant fluctuations. *Physical Review Letters*, **96**:180602, 2006. (Cited on pages 41 and 48.)

[69] S. Ramaswamy, R. A. Simha, and J. Toner. Active nematics on a substrate: Giant number fluctuations and long-time tails. *Europhysics Letters*, **62**:196–202, 2003. (Cited on page 41.)

[70] V. Narayan, S. Ramaswamy, and N. Menon. Long-lived giant number fluctuations in a swarming granular nematic. *Science*, **317**(5834):105–108, 2007. (Cited on pages 41, 42, 48 and 99.)

[71] H. Gruler, U. Dewald, and M. Eberhardt. Nematic liquid crystals formed by living amoeboid cells. *European Physical Journal B*, **192**:187–192, 1999. (Cited on page 41.)

[72] T. Pedley and O. Kessler. Hydrodynamic Phenomena In Suspensions Of Swimming Microorganisms. *Annual Review of Fluid Mechanics*, **24**:313–358, 1992. (Cited on page 43.)

[73] H. H. Wensink, J. Dunkel, S. Heidenreich, K. Drescher, and R. E. Goldstein. Meso-scale turbulence in living fluids. *Proceedings of the National Academy of Sciences*, **109**(36):14308–14313, 2012. (Cited on pages 43 and 48.)

[74] R. Voituriez, J. F. Joanny, and J. Prost. Spontaneous flow transition in active polar gels. *Europhysics Letters*, **70**(3):404–410, 2005. (Cited on pages 43, 45 and 88.)

[75] S. Ramaswamy and M. Rao. Active-filament hydrodynamics: instabilities, boundary conditions and rheology. *New Journal of Physics*, **9**(11):423–423, 2007. (Cited on pages 43, 44 and 88.)

[76] K. Drescher, J. Dunkel, L. H. Cisneros, S. Ganguly, and R. E. Goldstein. Fluid dynamics and noise in bacterial cell-cell and cell-surface scattering. *Proceedings of the National Academy of Sciences*, **108**(27):10940–5, 2011. (Cited on pages 43 and 44.)

[77] M. Polin, I. Tuval, K. Drescher, J. P. Gollub, and R. E. Goldstein. Chlamydomonas swims with two gears in a eukaryotic version of run-and-tumble locomotion. *Science*, **325**(5939):487–90, 2009. (Cited on page 43.)

[78] J. S. Hyams and G. G. Borisy. Isolated flagellar apparatus of Chlamydomonas: Characterization of forward swimming and alteration of waveform and reversal of motion by calcium ions in vitro. *Journal of Cell Science*, **33**:235–253, 1978. (Cited on page 43.)

[79] K. Drescher, R. E. Goldstein, N. Michel, M. Polin, and I. Tuval. Direct measurement of the flow field around swimming microorganisms. *Physical Review Letters*, **105**(16):1–4, 2010. (Cited on page 44.)

[80] G. De Magistris and D. Marenduzzo. An introduction to the physics of active matter. *Physica A: Statistical Mechanics and its Applications*, **418**:65–77, 2015. (Cited on page 45.)

[81] R. Voituriez, J. F. Joanny, and J. Prost. Generic phase diagram of active polar films. *Physical Review Letters*, **96**:028102, 2006. (Cited on page 45.)

[82] J. P. Hernandez-Ortiz, C. G. Stoltz, and M. D. Graham. Transport and collective dynamics in suspensions of confined swimming particles. *Physical Review Letters*, **95**:204501, 2005. (Cited on page 45.)

[83] S. Ramachandran, P. B. S. Kumar, and I. Pagonabarraga. A Lattice-Boltzmann model for suspensions of self-propelling colloidal particles. *European Physical Journal E*, **20**:151–158, 2006. (Cited on page 45.)

[84] D. Marenduzzo, E. Orlandini, M. Cates, and J. Yeomans. Steady-state hydrodynamic instabilities of active liquid crystals: Hybrid lattice Boltzmann simulations. *Physical Review E*, **76**(3):031921, 2007. (Cited on page 45.)

[85] G. Subramanian and D. L. Koch. Evolution of clusters of sedimenting low-Reynolds-number particles with Oseen interactions. *Journal of Fluid Mechanics*, **603**:63–100, 2008. (Cited on page 45.)

[86] D. L. Koch and G. Subramanian. Collective hydrodynamics of swimming microorganisms: Living fluids. *Annual Review of Fluid Mechanics*, **43**(1):637–659, 2011. (Cited on page 45.)

[87] M. P. Curie. Sur la symetrie dans les phenomenes physiques, symetrie d'un champ electrique et d'un champ magnetique. *Journal de Physique*, **3**:393–415, 1894. (Cited on page 46.)

[88] T. Sanchez, D. T. N. Chen, S. J. DeCamp, M. Heymann, and Z. Dogic. Spontaneous motion in hierarchically assembled active matter. *Nature*, **491**(7424):431–434, 2012. (Cited on pages 47, 49, 85 and 92.)

[89] Y. Sumino, K. H. Nagai, Y. Shitaka, D. Tanaka, K. Yoshikawa, H. Chaté, and K. Oiwa. Large-scale vortex lattice emerging from collectively moving microtubules. *Nature*, **483**(7390):448–52, 2012. (Cited on page 47.)

[90] Y. Wu, A. D. Kaiser, Y. Jiang, and M. S. Alber. Periodic reversal of direction allows Myxobacteria to swarm. *Proceedings of the National Academy of Sciences of the United States of America*, **106**(4):1222–1227, 2009. (Cited on page 48.)

[91] J. Dunkel, S. Heidenreich, K. Drescher, H. H. Wensink, M. Bär, and R. E. Goldstein. Fluid Dynamics of Bacterial Turbulence. *Physical Review Letters*, **110**(22):228102, 2013. (Cited on pages 48 and 51.)

[92] M. Poujade, A. Hertzog, J. Jouanneau, P. Chavrier, B. Ladoux, and A. Buguin. Collective migration of an epithelial monolayer. *Proceedings of the National Academy of Sciences*, **104**(41):15988–15993, 2007. (Cited on page 48.)

[93] L. Petitjean, M. Reffay, E. Grasland-Mongrain, M. Poujade, B. Ladoux, A. Buguin, and P. Silberzan. Velocity fields in a collectively migrating epithelium. *Biophysical Journal*, **98**(9):1790–800, 2010. (Cited on page 48.)

[94] I. H. Riedel, K. Kruse, and J. Howard. A Self-Organized Vortex Array of Hydrodynamically Entrained Sperm Cells. *Science*, **309**:300–304, 2005. (Cited on page 48.)

[95] D. Saintillan and M. J. Shelley. Emergence of coherent structures and large-scale flows in motile suspensions. *Journal of the Royal Society Interface*, **9**:571–585, 2012. (Cited on page 48.)

[96] L. Giomi, L. Mahadevan, B. Chakraborty, and M. F. Hagan. Excitable Patterns in Active Nematics. *Physical Review Letters*, **106**(21):218101, 2011. (Cited on page 48.)

[97] L. Giomi, M. Marchetti, and T. Liverpool. Complex Spontaneous Flows and Concentration Banding in Active Polar Films. *Physical Review Letters*, **101**(19):198101, 2008. (Cited on page 48.)

[98] K. Kruse, J. F. Joanny, F. Jülicher, J. Prost, and K. Sekimoto. Asters, vortices, and rotating spirals in active gels of polar filaments. *Physical Review Letters*, **92**:078101, 2004. (Cited on page 48.)

[99] S. P. Thampi, R. Golestanian, and J. M. Yeomans. Velocity Correlations in an Active Nematic. *Physical Review Letters*, **111**(11):118101, 2013. (Cited on page 48.)

[100] F. C. Keber, E. Loiseau, T. Sanchez, S. J. DeCamp, L. Giomi, M. J. Bowick, M. C. Marchetti, Z. Dogic, and a. R. Bausch. Topology and dynamics of active nematic vesicles. *Science*, **345**(6201):1135–1139, 2014. (Cited on page 48.)

[101] L. Giomi, M. J. Bowick, X. Ma, and M. C. Marchetti. Defect Annihilation and Proliferation in Active Nematics. *Physical Review Letters*, **110**(22):228101, 2013. (Cited on pages 50, 85, 88 and 92.)

[102] M. L. Blow, S. P. Thampi, and J. M. Yeomans. Lyotropic Active Nematics. *Physical Review Letters*, **248303**(6):5, 2014. (Cited on pages 50, 52, 90, 114 and 121.)

[103] D. Volfson, S. Cookson, J. Hasty, and L. S. Tsimring. Biomechanical ordering of dense cell populations. *Proceedings of the National Academy of Sciences*, **105**(40):15346–51, 2008. (Cited on pages 51 and 108.)

[104] D. B. Murphy. *Fundamentals of Light Microscopy and Electronic Imaging*. John Wiley and Sons, 2001. (Cited on pages 56 and 57.)

[105] J. W. Goodman. *Introduction to Fourier Optics*. McGraw Hills, 1988. (Cited on page 56.)

[106] P. Thévenaz, U. Ruttimann, and M. Unser. A pyramid approach to subpixel registration based on intensity. *IEEE Transactions on Image Processing*, **7**(1):27–41, 1998. (Cited on page 62.)

[107] M. B. Elowitz, A. J. Levine, E. D. Siggia, and P. S. Swain. Stochastic gene expression in a single cell. *Science*, **297**(5584):1183–1186, 2002. (Cited on page 62.)

[108] J. W. Young, J. C. W. Locke, A. Altinok, N. Rosenfeld, T. Bacarian, P. S. Swain, E. Mjolsness, and M. B. Elowitz. Measuring single-cell gene expression dynamics in bacteria using fluorescence time-lapse microscopy. *Nature Protocols*, **7**(1):80–88, 2012. (Cited on page 62.)

[109] F. C. Neidhardt, J. L. Ingraham, and S. Moselio. *Physiology of the Bacterial Cell*. Sinauer Associates, Inc. Publishers, 1st edition, 1990. (Cited on pages 69, 141 and 142.)

[110] P.-T. Su, P.-W. Yen, S.-H. Wang, C.-H. Lin, A. Chiou, and W.-J. Syu. Factors affecting daughter cells' arrangement during the early bacterial divisions. *PloS one*, **5**(2):e9147, 2010. (Cited on page 73.)

[111] S. van Teeffelen, S. Wang, L. Furchtgott, K. C. Huang, N. S. Wingreen, J. W. Shaevitz, and Z. Gitai. The bacterial actin MreB rotates, and rotation depends on cell-wall assembly. *Proceedings of the National Academy of Sciences*, **108**(38):15822–15827, 2011. (Cited on page 75.)

[112] S. Wang, H. Arellano-Santoyo, P. A. Combs, and J. W. Shaevitz. Actin-like cytoskeleton filaments contribute to cell mechanics in bacteria. *Proceedings of the National Academy of Sciences*, **107**(20):9182–9185, 2010. (Cited on page 75.)

[113] A. F. McVey. *Three-dimensional imaging of bacterial microcolonies*. Ph.D. thesis, 2015. (Cited on pages 75 and 150.)

[114] C. Keith, A. Lehmann, U. Baumeister, M. Prehm, and C. Tschierske. Nematic phases of bent-core mesogens. *Soft Matter*, **6**:1704–1721, 2010. (Cited on page 83.)

[115] X. Xiao and P. Sheng. Generalized onsager theory of liquid crystals. *Physical Review E*, **88**:062501, 2013. (Cited on page 83.)

[116] S. a. Edwards and J. M. Yeomans. Spontaneous flow states in active nematics: A unified picture. *Europhysics Letters*, **85**(1):18008, 2009. (Cited on page 88.)

[117] L. M. Pismen. Dynamics of defects in an active nematic layer. *Physical Review E*, **88**:050502, 2013. (Cited on page 88.)

[118] D. J. Earl, J. Ilnytskyi, and M. R. Wilson. Computer simulations of soft repulsive spherocylinders. *Molecular Physics*, **99**(20):1719–1726, 2001. (Cited on page 103.)

[119] D. Frenkel and B. Smit. *Understanding Molecular Simulations: From Algorithms to Applications*. Academic Press, 2001. (Cited on page 103.)

[120] L. D. Landau and E. M. Lifshitz. *Theory of Elasticity*. Butterworth-Heinemann, Oxford, UK, 1986. (Cited on pages 108, 127 and 134.)

[121] F. D. C. Farrell. *Modelling collective behaviour and pattern formation in bacterial colonies*. Ph.D. thesis, 2015. (Cited on pages 108, 109 and 113.)

[122] P.-T. Su, C.-T. Liao, J.-R. Roan, S.-H. Wang, A. Chiou, and W.-J. Syu. Bacterial colony from two-dimensional division to three-dimensional development. *PloS one*, **7**(11):e48098, 2012. (Cited on pages 115 and 128.)

[123] P. Chaikin and T. Lubenski. *Principles of Condensed Matter*. 1995. (Cited on page 127.)

[124] M. Garned. *Wheels, life, and other mathematical amusements*. 1983. (Cited on pages 128 and 130.)

[125] M. A. A. Grant, B. Waclaw, R. J. Allen, P. Cicuta, and B. Wacław. The role of mechanical forces in the planar-to-bulk transition in growing Escherichia coli microcolonies. *Journal of the Royal Society Interface*, **11**, 2014. (Cited on pages 128, 143, 147 and 150.)

[126] D. P. Lloyd. *Microscopic studies of surface growing bacterial populations*. Ph.D. thesis, 2014. (Cited on pages 128 and 150.)

[127] P. E. Cladis and M. Kléman. Non-singular disclinations of strength S = + 1 in nematics. *Journal de Physique*, **33**(5-6):591–598, 1972. (Cited on page 132.)

[128] J. R. Frank and M. Kardar. Defects in nematic membranes can buckle into pseudospheres. *Physical Review E - Statistical, Nonlinear, and Soft Matter Physics*, **77**(4), 2008. (Cited on page 132.)

[129] M. M. Taniguchi, F. C. Zola, V. G. Guimarães, G. Gonçalves, R. Rossato, and R. S. Zola. Morphology change in nematic membranes induced by defects. *Acta Scientiarum. Technology*, **36**(4):663–668, 1974. (Cited on page 132.)

[130] M. F. Islam, M. Nobili, F. Ye, T. C. Lubensky, and A. G. Yodh. Cracks and topological defects in lyotropic nematic gels. *Physical Review Letters*, **95**(14):1–4, 2005. (Cited on page 132.)

[131] S. I. Anisimov and E. Dzyaloshinskii. A New Type of Disclination in Liquid Crystals and the Stability of Disclinations of Various Types. *Soviet Physics JETP*, **36**(4), 1973. (Cited on page 134.)

[132] N. D. Mermin. The topological theory of defects in ordered media. *Review of Modern Physics*, **51**(3):591–648, 1979. (Cited on pages 134 and 137.)

[133] L. A. Liotta and E. C. Kohn. The microenvironment of the tumour-host interface. *Nature*, **411**:375–379, 2001. (Cited on page 140.)

[134] E. Libby and W. C. Ratcliff. Ratcheting the evolution of multicellularity. *Science*, **346**(6208):426–427, 2014. (Cited on page 140.)

[135] T. Mammoto and D. E. Ingber. Mechanical control of tissue and organ development. *Development (Cambridge, England)*, **137**:1407–1420, 2010. (Cited on page 140.)

[136] E. Marinari, A. Mehonic, S. Curran, J. Gale, T. Duke, and B. Baum. Live-cell delamination counterbalances epithelial growth to limit tissue overcrowding. *Nature*, **484**(7395):542–5, 2012. (Cited on page 140.)

[137] E. M. Pera, A. Ikeda, E. Eivers, and E. M. De Robertis. Integration of IGF, FGF, and anti-BMP signals via Smad1 phosphorylation in neural induction. *Genes & development*, **17**(24):3023–8, 2003. (Cited on page 140.)

[138] P. G. Hodor, M. R. Illies, S. Broadley, and C. A. Ettensohn. Cell-Substrate Interactions during Sea Urchin Gastrulation: Migrating Primary Mesenchyme Cells Interact with and Align Extracellular Matrix Fibers That Contain ECM3, a Molecule with NG2-1ike and Multiple Calcium-Binding Domains. *Developmental Biology*, **194**:181–194, 2000. (Cited on page 140.)

[139] A. J. Ridley, M. a. Schwartz, K. Burridge, R. a. Firtel, M. H. Ginsberg, G. Borisy, J. T. Parsons, and A. R. Horwitz. Cell migration: integrating signals from front to back. *Science*, **302**(5651):1704–9, 2003. (Cited on page 140.)

[140] E. Coucouvanis and G. R. Martin. Signals for death and survival: a two-step mechanism for cavitation in the vertebrate embryo. *Cell*, **83**:279–287, 1995. (Cited on page 140.)

[141] M. Asally, M. Kittisopikul, P. Rué, Y. Du, Z. Hu, T. Çağatay, A. B. Robinson, H. Lu, J. Garcia-Ojalvo, and G. M. Süel. Localized cell death focuses mechanical forces during 3D patterning in a biofilm. *Proceedings of the National Academy of Sciences*, **109**(46):18891–6, 2012. (Cited on page 140.)

[142] J. W. Dale and S. F. Park. *Molecular Genetics of Bacteria*. Wiley-Blackwell, 5$^{\text{th}}$ edition, 2011. (Cited on pages 141 and 156.)

[143] G. Lambert, L. Estévez-salmeron, S. Oh, D. Liao, B. M. Emerson, T. D. Tlsty, and R. H. Austin. An analogy between the evolution of drug resistance in bacterial communities and malignant tissues. *Nature reviews. Cancer*, **11**(May):375–382, 2011. (Cited on page 141.)

[144] P. Greulich, B. Waclaw, and R. J. Allen. Mutational pathway determines whether drug gradients accelerate evolution of drug-resistant cells. *Physical Review Letters*, **109**, 2012. (Cited on page 141.)

[145] A. C. Martiny, T. M. Jø rgensen, E. Arvin, S. r. Molin, A. C. Martiny, T. M. Jø rgensen, H.-j. r. Albrechtsen, E. Arvin, and S. r. Molin. Long-Term Succession of Structure and Diversity of a Biofilm Formed in a Model Drinking Water Distribution System Long-Term Succession of Structure and Diversity of a Biofilm Formed in a Model Drinking Water Distribution System. *Applied and Environmental Microbiology*, **69**:6899–6907, 2003. (Cited on page 141.)

[146] E. a. Grice, H. H. Kong, S. Conlan, C. B. Deming, J. Davis, A. C. Young, G. G. Bouffard, R. W. Blakesley, P. R. Murray, E. D. Green, M. L. Turner, and J. a. Segre. Topographical and temporal diversity of the human skin microbiome. *Science*, **324**(5931):1190–2, 2009. (Cited on page 141.)

[147] B. Carpentier and O. Cerf. Biofilms and their consequences, with particular reference to hygiene in the food industry. *Journal of Applied Bacteriology*, pages 499–511, 1993. (Cited on page 141.)

[148] M. R. Parsek and P. K. Singh. Bacterial biofilms: an emerging link to disease pathogenesis. *Annual review of microbiology*, **57**:677–701, 2003. (Cited on page 141.)

[149] J. C. Conrad. Physics of bacterial near-surface motility using flagella and type IV pili: Implications for biofilm formation. *Research in Microbiology*, **163**(9-10):619–629, 2012. (Cited on page 142.)

[150] J. Haiko and B. Westerlund-Wikström. The role of the bacterial flagellum in adhesion and virulence. *Biology*, **2**(4):1242–1267, 2013. (Cited on pages 142 and 147.)

[151] R. S. Friedlander, H. Vlamakis, P. Kim, M. Khan, R. Kolter, and J. Aizenberg. Bacterial flagella explore microscale hummocks and hollows to increase adhesion. *Proceedings of the National Academy of Sciences of the United States of America*, **110**(14):5624–9, 2013. (Cited on page 142.)

[152] Q. Duan, M. Zhou, L. Zhu, and G. Zhu. Flagella and bacterial pathogenicity. *Journal of Basic Microbiology*, **53**(1):1–8, 2013. (Cited on page 142.)

[153] K. K. Jefferson. What drives bacteria to produce a biofilm. *FEMS Microbiology Letters*, **236**:163–173, 2004. (Cited on page 143.)

[154] P. N. Danese, L. A. Pratt, and R. Kolter. Exopolysaccharide production is required for development of *Escherichia coli* k-12 biofilm architecture. *Journal of Bacteriology*, **182**(12):3593–6, 2000. (Cited on page 143.)

[155] A. Persat, C. D. Nadell, M. K. Kim, F. Ingremeau, A. Siryaporn, K. Drescher, N. S. Wingreen, B. L. Bassler, Z. Gitai, and H. A. Stone. The mechanical world of bacteria. *Cell*, **161**(5):988–997, 2015. (Cited on page 143.)

[156] N. Cerca and K. K. Jefferson. Effect of growth conditions on poly-N-acetylglucosamine expression and biofilm formation in Escherichia coli. *FEMS Microbiology Letters*, **283**(1):36–41, 2008. (Cited on page 143.)

[157] I. W. Sutherland. Biofilm exopolysaccharides: a strong and sticky framework. *Microbiology*, **147**:3–9, 2001. (Cited on page 143.)

[158] M. Ionescu and S. Belkin. Overproduction of exopolysaccharides by an *Escherichia coli* k-12 *rpoS* mutant in response to osmotic stress. *Applied and Environmental Microbiology*, **75**(2):483–492, 2009. (Cited on page 143.)

[159] G. A. O'Toole and R. Kolter. Flagellar and twitching motility are necessary for pseudomonas aeruginosa biofilm development. *Molecular Microbiology*, **30**(2):295–304, 1998. (Cited on page 143.)

[160] X. Wang, J. F. P. Iii, T. Romeo, X. Wang, J. F. P. Iii, and T. Romeo. The pgaABCD Locus of Escherichia coli Promotes the Synthesis of a Polysaccharide Adhesin Required for Biofilm Formation. *Journal of bacteriology*, **186**(9):2724–2734, 2004. (Cited on page 143.)

[161] C. R. Stewart, O. Rossier, and N. P. Cianciotto. Surface translocation by Legionella pneumophila: a form of sliding motility that is dependent upon type II protein secretion. *Journal of bacteriology*, **191**(5):1537–46, 2009. (Cited on page 144.)

[162] M. Fauvart, P. Phillips, D. Bachaspatimayum, N. Verstraeten, J. Fransaer, J. Michiels, and J. Vermant. Surface tension gradient control of bacterial swarming in colonies of Pseudomonas aeruginosa. *Soft Matter*, **8**(1):70, 2012. (Cited on page 144.)

[163] J. Henrichsen. Bacterial Surface Translocation: a Survey and a Classification. *Bacteriological reviews*, **36**(4), 1972. (Cited on page 144.)

[164] R. M. Harshey. Bacterial motility on a surface: many ways to a common goal. *Annual review of microbiology*, **57**:249–73, 2003. (Cited on page 144.)

[165] N. Gjorevski and C. M. Nelson. Mapping of mechanical strains and stresses around quiescent engineered three-dimensional epithelial tissues. *Biophysical Journal*, **103**:152–162, 2012. (Cited on page 148.)

[166] A. F. Mertz, S. Banerjee, Y. Che, G. K. German, Y. Xu, C. Hyland, M. C. Marchetti, V. Horsley, and E. R. Dufresne. Scaling of traction forces with the size of cohesive cell colonies. *Physical Review Letters*, **108**(19):1–5, 2012. (Cited on page 148.)

[167] P. Poulin. Novel Colloidal Interactions in Anisotropic Fluids. *Science*, **275**(5307):1770–1773, 1997. (Cited on page 150.)

[168] I. Musevic, M. Skarabot, U. Tkalec, M. Ravnik, and S. Zumer. Two-dimensional nematic colloidal crystals self-assembled by topological defects. *Science*, **313**(5789):954–8, 2006. (Cited on page 150.)

[169] K. A. Datsenko and B. L. Wanner. One-step inactivation of chromosomal genes in Escherichia coli K-12 using PCR products. *Proceedings of the National Academy of Sciences*, **97**(12):6640–6645, 2000. (Cited on page 153.)

[170] P. Cherepanov and W. Wackernagel. Gene disruption in escherichia coli: Tcr and kmr cassettes with the option of flp-catalyzed excision of the antibiotic-resistance determinant. *Gene*, **5**(158):9–14, 1995. (Cited on page 153.)

[171] T. Baba, T. Ara, M. Hasegawa, Y. Takai, Y. Okumura, M. Baba, K. A. Datsenko, M. Tomita, B. L. Wanner, and H. Mori. Construction of escherichia coli k-12 in-frame, single-gene knockout mutants: the keio collection. *Molecular Systems Biology*, **2**(1), 2006. (Cited on page 154.)

[172] L. C. Thomason, N. Costantino, and D. L. Court. *E. coli* genome manipulation by P1 transduction. *Current protocols in molecular biology*, **1**(17), 2007. (Cited on page 155.)

[173] L. Snyder and W. Champness. *Molecular Genetics of Bacteria*. ASM Press, 3rd edition, 2007. (Cited on page 156.)

[174] J. Sambrook and D. W. Russell. *Molecular Cloning: A Laboratory Manual*, volume 1. CSHL Press, 3rd edition, 2001. (Cited on page 156.)